Opto-Electrical Simulation of Perovskite/Silicon Tandem Solar Cell

ASA optimization of Pvk/c-Si tandem simulation

SET3901: Thesis Project

R.R. Shaikh

Delft University of Technology

TU Delft

Opto-Electrical Simulation of Perovskite/Silicon Tandem Solar Cell

ASA optimization of Pvk/c-Si tandem simulation

by

R.R. Shaikh

Student Name	Student Number
Raiyan Riyaz Shaikh	5267013

to obtain the degree of Master of Science
at the Delft University of Technology,
to be defended publicly on Friday August 5, 2022 at 1:00 PM.

Project duration:	October 12, 2021 – August 5, 2022	
Thesis committee:	Dr. ir. R. Santbergen,	TU Delft, EWI-PVMD Supervisor
	Prof. ir. PTM. Vaessen,	TU Delft, EWI-DCE&S, Professor
	Dr. ir. C. M. Ruiz,	TU Delft, EWI-PVMD Assistant Supervisor
	Dr. ir. PA. Procel Moya,	TU Delft, EWI-PVMD Post-Doc

This thesis is confidential and cannot be made public until August 5, 2023.

An electronic version of this thesis is available at `http://repository.tudelft.nl/`.

TU Delft

Preface

I am grateful to be part of a community that is eager to boost the energy transition towards sustainable energy. Being brought up in Dubai, UAE, a place where sunshine is plenty and climate is warm throughout the year, I always thought about how extreme the climate in Dubai can be especially during the summer. Yet we are blessed with so much power from the Sun waiting to be utilized. It peaked my curiosity into the photovoltaic technologies that can harness the power of the sun to make our lives much easier to live. It lead me on a journey up north to Delft, Netherlands and was able to take part in the SET program and be a member of the Photovoltaic Materials and Devices (PVMD) group at TU Delft to learn more about the solar cell technology and to hone my skills in improving the efficiency of the tandem solar cell devices.

Designing a high efficiency tandem solar cell from scratch is not an easy feat. Speculation, trial and error and previous research in solar cell designing is the first step towards making progress. By working on my thesis project towards optimizing optical and electrical simulation in the perovskite silicon tandem solar cell device, it shortened this work needed into achieving better performance results and helped in kick-starting new ideas into better solar cell designing. I believe that it has opened my eyes into countless possibilities into further research and development in the perovskite silicon tandem solar cell devices. I am grateful to TU Delft and PVMD group for guiding and supporting me to the very end of this thesis project.

I would like to express my gratitude to Dr Rudi Santbergen for allowing me to start this project and give my utmost support me with regards to the structure of this project till the very end. Your incredible suggestions towards optimizing perovskite silicon tandem simulations and your guidance towards better use of GenPro4 really helped with this thesis project.

I am also incredibly grateful to Dr Carlos Ruiz Tobon for being my daily supervisor. Your support and guidance from day one of my thesis project is never forgotten. Our brainstorming and countless trial and errors we made during the optimization of perovskite silicon tandem simulation really took this project to the next level. Our good times inside and outside of academics really helped me develop as a human.

I also appreciate Dr Paul Procel and Prof Peter Vaessen for being my graduation committee members and am grateful to Paul for teaching me the physics and simulation strategies for the tunnel recombination simulations for perovskite silicon tandem.

My special appreciation also goes to the people around me in the Netherlands. My friends here in Delft as well as my friends back home in Dubai. Last but not the least, my utmost gratitude to my family for the unconditional love and support since the very beginning.

R.R. Shaikh
Delft, August 2022

Abstract

Emerging PV technologies like Perovskite has lead to the development of Perovskite/Silicon (Pvk/c-Si) tandem device (Multi-junction device) and has now gained a lot of momentum and attention due to the fact that the tandem device can reach a Shockley-Quisser limit of about 44.1% efficiency. But to speed up its development, a lot of emphasis is made on conducting tandem solar cell device simulations to have get a good idea on the experiments that can be carried out. Solar cell simulations for tandem devices are carried out in advanced 2D/3D solar cell simulators like SETFOS or Synopsys TCAD Sentaurus. These softwares have large computational time and have complex user interface making simulations challenging. There are 1D solar cell simulators like ASA (Advanced Semiconductor Analysis) developed at TU Delft that has less computational time with an easy and intuitive interface. But ASA does not have the appropriate tunnelling models to simulate the tunnel recombination junction characteristics of perovskite silicon tandem devices.

To make ASA a complete software suite for simulating perovskite silicon tandem device, tunnelling models proposed by Ieong et al. is used for both direct and band to band tunnelling. These tunnelling models use basic inputs like band energy data, electrostatic potential data and electric field data for a particular device and outputs the tunnelling generation rate that can simply be added to the continuity equations for electrons or holes during the simulation of the device. A fully fledged algorithm was designed for the automation of the direct tunnelling and the band to band tunnelling process with limited input from the user while using the models proposed by Ieong et al. In simple terms, the algorithm takes in the required input and scans through the device for every interface to check for tunnel contributions and performs calculations when necessary. All necessary conditions are included inside the algorithms to ensure that the simulation is accurately solved.

The validation of the newly developed tunnelling algorithm was commenced for PN junction, Silicon hetero-junction and finally the Perovskite-Silicon tandem device. The JV curve for the above device simulations with and without incorporated tunnelling models was extracted and a comparison was made with literature results and simulation results from other software suites. The newly developed tunnelling algorithms was concluded to be accurate. The JV curve obtained from the ASA simulation showed good agreement with literature results and simulation results from other software suites with error percentages of less than 3% for open circuit voltage, short circuit current and fill factor. With proper tuning of the device layer thickness, texturing on multiple layers for the tandem device and enhancing the mobility of the non-absorber layers for the perovskite top cell, further improvement can be expected in the simulation. These methods can eventually lead to reaching the Shockley Quisser limit of about 35.7% efficiency for the perovskite silicon tandem solar cell even when general opto-electrical losses are taken into account.

Glossaries

Abbreviations

Abbreviation	Definition
PV	Photovoltaics
IRENA	International Renewable Energy Agency
PCE	Power Conversion Efficiency
SQ	Shockley Quisser
PSC	Perovskite Solar Cell
PVK	Perovskite
cSi	Crystalline Silicon
ETL	Electron Transport Layer
HTL	Hole Transport Layer
ASA	Advance Semiconductor Analysis
SHJ	Silicon Hetero-junction
CB	Conduction Band
VB	Valence Band
CBT	Conduction Band Tails
VBT	Valence Band Tails
DOS	Density of States
DB	Dangling Bonds
MOSFET	Metal Oxide Semiconductor Field Effect Transistor
JFET	Junction-gate Field Effect Transistor
TCAD	Technology Computer Aided Design
TAT	Trap Assisted Tunnelling
DT	Direct Tunnelling
BBT	Band to Band Tunnelling
SRH	Shockley Read Hall
TCO	Transparent Conductive Oxide
TRJ	Tunnel Recombination Junction
TJ	Tunnel Junction
JV	Current Density Voltage

Symbols

Symbol	Definition	Unit
$\tilde{r}$	reflection coefficient	[-]
$\tilde{t}$	transmission coefficient	[-]
n	refractive index	[-]
α	absorption coefficient	[-]
A	Absorptance	[-]
T	Transmittance	[-]
R	Reflectance	[-]
q_i^x	flux at interface i approaching from x	[W/m^2]
ε_r	Relative permittivity	[-]
ε_o	Permittivity of free space	[Fm^{-1}]
E_{vac}	Energy at vacuum level of the band diagram	[eV]

Symbol	Definition	Unit
E_C/E_{CB}	Conduction band energy	[eV]
E_V/E_{VB}	Valence band energy	[eV]
E_f/ϕ_f	Fermi level energy	[eV]
E_g/E_μ	Energy band-gap / Energy band mobility gap	[eV]
χ	Electron affinity	[eV]
N_C	Conduction band density of states	[m^{-3}]
N_V	Valence band density of states	[m^{-3}]
N_t	Trap concentration	[m^{-3}]
T	Temperature	[K]
n	Electron concentration	[m^{-3}]
p	Hole concentration	[m^{-3}]
μ_n/μ_p	Electron/Hole mobility	[A/m^2]
J_n/J_p	Current density of electron/hole	[A/m^2]
J_{SC}	Short circuit current density	[A/m^2]
V_{OC}	Open circuit voltage	[V]
FF	Fill Factor	[-]
η/PCE	Power conversion efficiency	[%]
G	Generation rate	[m^{-3}s^{-1}]
R	Recombination rate	[m^{-3}s^{-1}]
Γ	Probability function	[-]
c_n/c_p	Electron/Hole capture coefficient	[-]
e_n/e_p	Electron/Hole emission coefficient	[-]
A^*	Effective richardson constant	[A/m$^2/K^2$]
r	Tunnelling distance	[m]
q	Charge constant	[C]
k_B/k	Boltzmann constant	[JK^{-1}]
h	Plank's constant	[Js]
$\hbar$	Dirac constant	[eVs]
ψ	Electrostatic potential	[V]
ξ/E	Electric field intensity	[V/m]

Constants

Symbol	Value	Unit
q	1.602 x 10^{-19}	[C]
k_B/k	1.381 x 10^{-23}	[JK^{-1}]
h	6.625 × 10^{-34}	[Js]
$\hbar$	6.582 × 10^{-16}	[eVs]
A^*	120	[A/cm$^2/K^2$]
ε_o	8.854 × 10^{-12}	[Fm^{-1}]

List of Figures

1.1 Global Installed Capacity of Renewable Energy by IRENA [22]. 1
1.2 Global Patent Evolution of Renewable Energy by IRENA [21]. 2
1.3 Best Research Cell Efficiency Chart - Emerging PV [35]. 3
1.4 Crystal Structure of a 3D Perovskite [53]. 3
1.5 Common Perovskite Architectures with the ETL marked in grey and HTL marked in yellow [32]. 4
1.6 $FAPbI_3$ based PSC developed by UNIST, South Korea [25]. 5
1.7 Pvk/c-Si architecture developed by HZB, Germany [4]. 6
1.8 Pvk/c-Si architecture developed by EPFL, Switzerland [40]. 6
1.9 Pvk/c-Si architecture used for the simulation in SETFOS. Tunnelling models for the hetero-junctions and the tunnel recombination junctions had to be incorporated for realistic simulations [1]. 7
1.10 JV curve obtained for the Pvk/c-Si simulation conducted in SETFOS [1]. 8
1.11 Pvk/c-Si architecture used for the simulation in AFORS-HET. [20]. 8
1.12 JV curves obtained for the Pvk/c-Si simulation conducted in AFORS-HET a)JV curve for Pvk thickness of 500nm and c-Si thickness of 200um b)JV curve for Pvk thickness of 165nm and c-Si thickness of 200um [20]. 9
1.13 Tandem Perovskite Solar Cell / µcSi solar cell layers [12]. 9
1.14 Tandem Perovskite Solar Cell / µcSi solar cell a)JV curve and b)Band diagram [12]. . . 10

2.1 ASA modelling procedure [51]. 12
2.2 Band diagram of a-Si under equilibrium condition [51]. 14
2.3 2D crustal lattice of a) c-Si and b) a-Si:H [43]. 14
2.4 DOS distribution of electron in a) c-Si b) a-Si:H [43]. 15
2.5 Linear DOS distribution of electron a-Si:H [51]. 16
2.6 Logarithmic DOS distribution of electron a-Si:H [51]. 16
2.7 Simulation flowchart of ASA [51]. 19
2.8 Generation rate due to tunnelling at the contact [18]. 21
2.9 Simple BBT method [30]. 22
2.10 Non-local BBT method [27, 45]. 23

3.1 Illustration of band diagram vs device depth for the direct tunnelling process at the interface x_i. 25
3.2 Illustration of direct a) tunnelling probability b) tunnelling generation rate as a function of device depth for a sample PN junction device with interface x_i at 30 nm depth of device without continuity in the band edges at the interface resulting in a slanted line of the tunnelling generation rate. 27
3.3 Illustration of direct a) tunnelling probability b) tunnelling generation rate as a function of device depth for a sample PN junction device with interface x_i at 30 nm depth of device with continuity in the band edges at the interface resulting in a sharp vertical line of the tunnelling generation rate. 27
3.4 Illustration of band diagram vs device depth for the band to band tunnelling process at the interface x_i. 30
3.5 Illustration of band to band tunnel generation rate as a function of device depth for a sample perovskite/silicon tandem device with tunnel junction interface x_i at 1.47μm depth of device. Forbidden band states are present in between the band edges of VB and CB resulting in zero tunnel generation rate. 32

4.1 Device structure of a simple PN device [7]. 35

4.2 a)Band energy diagram with respect to the position of a simple PN device consisting of conduction band Ec, valence band Ev and fermi level Ef for χ=4.05eV and χ=3.95eV b)Enlarged section of the valence band barrier height at the interface of the PN junction (marked with dotted lines) resulting in tunnelling effects. 36
4.3 JV curve of the PN junction with and without direct tunnelling for the first case of χ=3.95 eV. The newly developed automated DT model shows good agreement with the reference case χ=4.05 eV and the external DT model resulting in similar current voltage characteristics. 36
4.4 Device structure of a simple SHJ device [38]. 37
4.5 Band energy diagram with respect to the position of a simple simple SHJ device consisting of conduction band Ec, valence band Ev and fermi level Ef for each of the layers given in text. Visible barrier heights in the bands leads to tunnelling effects in the device [48, 38]. 38
4.6 JV curve of the Silicon hetero-junction with and without direct tunnelling. The newly developed DT algorithm applied on the base case is in good agreement with the external DT subroutine resulting in similar current voltage characteristics. 39
4.7 Pvk/c-Si architecture developed at HZB, Germany [4]. 40
4.8 Absorptance profile for a entirely flat Pvk/cSi device. [4, 41]. 41
4.9 Absorptance profile for a bottom textured Pvk/cSi device. As compared to the flat absorptance profile as seen in Fig. 4.8, a higher tandem photocurrent is obtained due to light trapping feature in the bottom cell which can improve the short circuit current density when conducting electrical simulations [4, 41]. 41
4.10 a)Band energy diagram with respect to the position of a perovskite-silicon tandem device by Al-Ashouri et al. [4] consisting of conduction band Ec, valence band Ev and fermi level Ef for each of the layers given in text b)Enlarged section of the tunnel recombination junction at the interface of the PTAA and ITO layer (marked with dotted lines) resulting in band to band tunnelling effects. 42
4.11 JV curves based on the perovskite-silicon tandem device by Al. Ashouri et.al. [4] with and without DT and BBT. The newly developed DT and BBT is in good agreement with the experiments resulting in similar current voltage characteristics. 42

5.1 Improved Pvk/c-Si architecture developed at HZB, Germany [46]. 44
5.2 Absorptance profile for an improved Pvk/cSi device. A higher tandem photocurrent is obtained due to micro-sized pyramidal textures below the silicon layer and nano-sized sinusoidal-like texture below perovskite layer [41, 46]. 45
5.3 a)Band energy diagram with respect to the position of an improved perovskite-silicon tandem device by Tockhorn et al. [4] consisting of conduction band Ec, valence band Ev and fermi level Ef for each of the layers given in text b)Enlarged section of the tunnel recombination junction at the interface of the SAM and ITO layer (marked with dotted lines) resulting in band to band tunnelling effects. 46
5.4 JV curves based on the improved perovskite-silicon tandem device by Tockhorn et al. [46] with DT and BBT. The newly developed DT and BBT is in good agreement with the experiments resulting in similar current voltage characteristics. 46

A.1 SRH recombination process between energy level at band-gap and the extended states [44][51] 57
A.2 Sah and Shockley recombination process between energy levels at band-gap and the extended states [39][51] 58
A.3 Reflection and Transmission of incident light on a flat interface [51]. 61
A.4 Reflection and Transmission of incident light on a layer with two interfaces [51]. 62
A.5 Solid angle distribution of light for a rough surface [51] 63
A.6 Reflection and transmission processes for a rough interface [51] 63
A.7 Simulation of incident light for textured surface by a)coherent analysis b)incoherent analysis [51] 64
A.8 A multi-layer structure with the numbering convention for layers and interfaces. a)Optical paths contributing to R, T and A_i b)Net-radiation fluxes. 66

A.9 a) Propagation of light with different angular intervals in a hemispherical form at an interface b) Sub fluxes at interface 1 [41]. 66

B.1 Energy band diagram for a semiconductor/insulator/semiconductor layers [50] 68
B.2 Energy band diagram taking into account the electrostatic potential drop [48] 70
B.3 Non-local BBT method [27, 45] 72

List of Tables

1.1 Current status of the TRJ modelling for different solar cell simulation softwares in the market . . . 10

2.1 Coefficients for the simple BBT model [30, 31] . . . 23

4.1 PN junction electrical parameters [7]. . . . 35
4.2 PN junction performance with and without direct tunnelling. . . . 37
4.3 SHJ junction electrical parameters [48, 38]. . . . 38
4.4 Silicon hetero-junction performance with and without direct tunnelling. . . . 39
4.5 Pvk/cSi tandem electrical parameters by Al Ashouri et al. [4] . . . 40
4.6 Perovskite-Silicon tandem performance comparison with experimental and simulation results [4]. . . . 43

5.1 Improved Pvk/cSi tandem electrical parameters by Tockhorn et al. [46] . . . 45
5.2 Perovskite-Silicon tandem performance comparison with experimental and simulation results [46] . . . 47

B.1 Coefficients for the Hurkx BBT model [15, 31, 45] . . . 70
B.2 Coefficients for the Schenk's BBT model [31, 45] . . . 71
B.3 Coefficients for the Non-local BBT model [31] . . . 73

Contents

Preface i

Abstract ii

Glossaries iii

List of Figures vii

List of Tables viii

1 Introduction 1
- 1.1 Background 1
- 1.2 Perovskite Silicon tandem device architecture 3
- 1.3 Simulation of Pvk/c-Si tandem device in literature 7
- 1.4 Research Gap 10
- 1.5 Objectives 11
- 1.6 Report structure 11

2 Solar Cell Modelling in ASA 12
- 2.1 Optical modelling 12
- 2.2 Electrical modelling 13
  - 2.2.1 Semiconductor equations 13
  - 2.2.2 Density of states models for a-Si 14
  - 2.2.3 Mobilities for crystalline semiconductors 17
  - 2.2.4 Band-gap narrowing for crystalline semiconductors 18
- 2.3 Numerical solution and simulation approach 18
- 2.4 Tunnelling Models 20
  - 2.4.1 Trap Assisted Tunneling 20
  - 2.4.2 Direct Tunneling 21
  - 2.4.3 Band to Band Tunneling 22
- 2.5 Conclusion 24

3 ASA algorithm development for the tunnelling models 25
- 3.1 Newly developed ASA algorithm for Direct tunnelling 25
- 3.2 Newly developed ASA algorithm for band to band tunnelling 30
- 3.3 Conclusion 34

4 ASA validation of the tunnelling models 35
- 4.1 Validation of direct tunnelling using a PN junction 35
- 4.2 Validation of direct tunnelling using a Silicon hetero-junction 37
- 4.3 Validation of band to band tunnelling using a Pvk/cSi tandem 39
- 4.4 Conclusion 43

5 ASA Simulations of PVK/c-Si tandem devices 44
- 5.1 Simulation of an improved version of Pvk/cSi tandem device by Tockhorn et al. 44
- 5.2 Conclusion 47

6 Conclusion and Recommendation 48
- 6.1 Conclusion 48
- 6.2 Recommendation 49

References 51

A Solar Cell Modelling in ASA - additional models 55
- A.1 Electrical modelling - additional models 55

A.1.1 Boundary conditions for ohmic and schottky contacts 55
A.1.2 Recombination-Generation (R-G) statistics 56
A.1.3 Recombination-Generation (R-G) statistics for crystalline semiconductors 59
A.2 Optical modelling - In depth Analysis 59
A.2.1 Lambert-Beer law 60
A.2.2 GenPro1: Optical modelling for flat interface 60
A.2.3 GenPro2: Optical modelling for rough interfaces by incoherent analysis 62
A.2.4 GenPro3: Optical modelling for rough interfaces by semi-coherent analysis . . . 64
A.2.5 GenPro4: Optical modelling using ray and wave optics 65

B Tunnel Recombination Models - additional models 68
B.1 Direct Tunneling 68
B.1.1 Direct tunneling model proposed by Varache et al. 68
B.2 Band to Band Tunneling 70
B.2.1 Band to band tunnelling model proposed by Hurkx et al. 70
B.2.2 Band to band tunnelling model proposed by A.Schenk 71
B.2.3 Non-local band to band tunneling model - version 2 71

C C++ code for the direct tunnelling algorithm 74

D C++ code for the band to band tunnelling algorithm 78

E Input files for the validation of the tunnelling algorithms 85
E.1 ASA input file for the PN junction 85
E.2 ASA input file for the Silicon hetero-junction 86
E.3 ASA input file for the Perovskite-Silicon tandem 87
E.3.1 Genpro input file for the flat Perovskite-Silicon tandem 87
E.3.2 Genpro input file for the bottom textured Perovskite-Silicon tandem 88
E.3.3 ASA input file for the bottom textured Perovskite-Silicon tandem 88

F Input files for the simulation of Pvk/cSi tandem devices 90
F.1 Genpro input file for the improved textured Perovskite-Silicon tandem device 90
F.2 ASA input file for the improved textured Perovskite-Silicon tandem device 91

1

Introduction

1.1. Background

Even as economies sank under the weight of Covid-19 restrictions in 2020, alternative energy sources like solar PV and wind continued to expand fast, and electric vehicles hit new sales records. The future energy economy is predicted to be electric, efficient, networked, and environmentally friendly than the old one [19]. Its rise is the result of a virtuous loop of legislative action and technological innovation, and its low cost are currently sustaining its growth. Solar Photovoltaics (PV) and wind power are presently the cheapest accessible sources of clean energy in most markets. Clean energy technology is rapidly emerging as a major new source of investment and job creation, along with increased competitive market environment [19].

According to International Renewable Energy Agency (IRENA) [22], Renewable energy has added more electricity to the grid each year than fossil fuels and nuclear combined for the past seven years. In 2020, 260 gigawatts (GW) of renewable-based power capacity was additionally built globally as can be seen from Fig 1.1, setting a new high. This is a promising path for the rapid decarbonization of electricity sector [22].

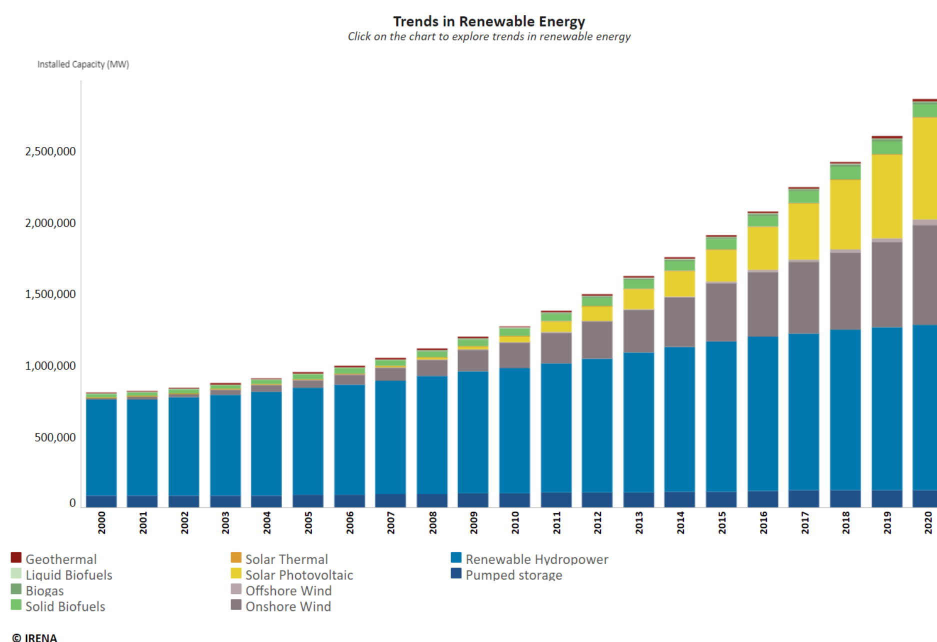

Figure 1.1: Global Installed Capacity of Renewable Energy by IRENA [22].

In 2021, a new high was predicted for worldwide solar PV installations, with almost 117 GW installed,

up nearly 10% from 2020. This rise was attributable to a substantial rebound in utility-scale facilities outside of China, where COVID-19 curtailed PV growth owing to the phaseout of subsidies. To meet deadlines, utility-scale project development is also projected to pick up in India and other major EU markets [17].

In addition to the installed capacities, the innovation and development of the Renewable energy technologies has rapidly increased over past 20 years as seen in Fig 1.2, leading to reduced cost of the technology itself leading to a higher learning curve. It is clear that the Solar PV technologies is leading the evolution of the Renewable energy sector [21].

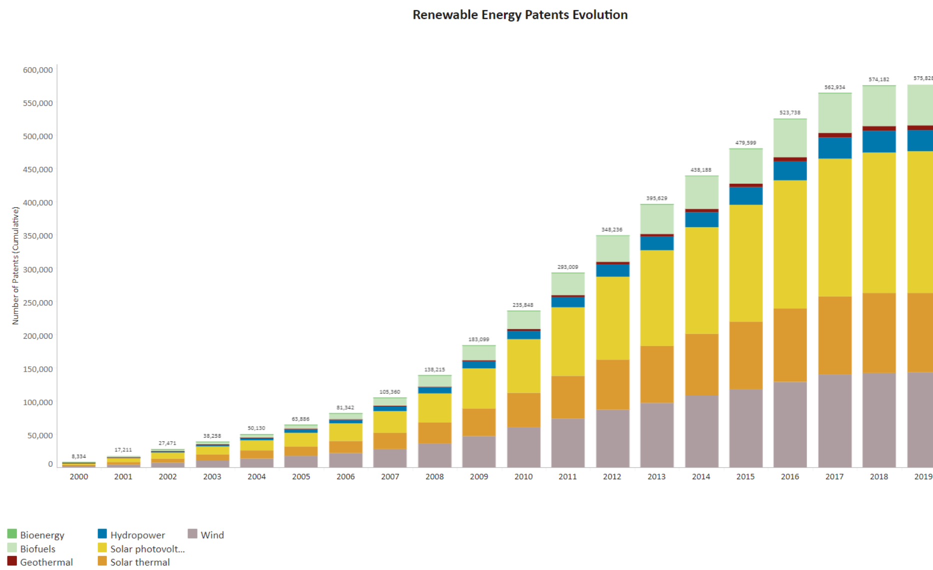

Figure 1.2: Global Patent Evolution of Renewable Energy by IRENA [21].

A semiconductor-based device known as a solar cell is one of the main sustainable energy technology for turning solar energy into electricity. When a solar cell is exposed to sunlight, it transforms the light directly into energy via the process of Photovoltaic effect. However, not all of the light that shines on the cell is turned into energy instead can be lost thermally or optically. The conversion efficiency of transformed sunlight is denoted by the term power conversion efficiency (PCE). The Shockley-Quisser (SQ) limit is the theoretical upper limit of PCE [49]. Increasing the PCE of the PV technologies has always been the main approach in the PV community and its strategies can be briefly summarised. Over 95% of the global installed PV is based on Silicon. The PV industry has swiftly embraced the Passive Emitter Rear Contact (PERC) technology with over 65% of the market share as of 2019 having an 20.3% average PCE and can increase to 22.5% by 2030 [49, 13]. Hetero-junction with Intrinsic Thin layer (HIT) Silicon Solar cell (or in other words silicon hetero-junction (SHJ)) combined with Interdigitated Back Contact technology (IBC) without concentrator developed by Kaneka corporation currently holds the record PCE for silicon solar cell of 26.7% [49, 13]. The remaining 5% of the PV market include the thin film technologies like amorphous Silicon (a-Si) with a maximum PCE of 14% developed by AIST (based on a-Si:H uc-Si:H uc-Si:H triple junction) [13], Cadmium Telluride (CdTe) with a maximum PCE of 22.1% developed by First Solar and finally Copper Indium Gallium Diselenide (CIGS) with a maximum PCE of 23.4% developed by Solar Frontier [13]. However majority of the solar panels on the market are based on single junction solar cell that have a certain SQ limit (for example 32.9% efficiency for silicon of bandgap 1.2 eV) [11].

Extensive research has lead to the development of novel thin film technologies like the Perovskite solar cells (PSC). The PSC technology consisting of organic metal halide has brought a lot of attention in the PV community due to a very steep learning curve leading to a maximum PCE of 25.5% developed by UNIST in 2021, a 21.7% increase in PCE in almost a decade making this technology very promising [35]. Many multijunction solar cell approach has been researched that cross the SQ limitation and substantially increase the PCE than normal single junction technologies. Emerging PV technologies like

Perovskite has lead to the development of Perovskite/Silicon (Pvk/c-Si) tandem device (Multi-junction device) and has now gained a lot of momentum and attention due to the fact that the tandem device can reach SQ maximum of about 44.1% PCE [11]. The SQ limit with general opto-electrical losses can reach upto 35.7% PCE which is still quite promising [11]. The trend of Pvk/c-Si tandem development can also be seen in the Emerging PV section under the "Best Research-Cell Efficiency Chart" from the National Renewable Energy Laboratory (NREL) shown in Fig 1.3[35].

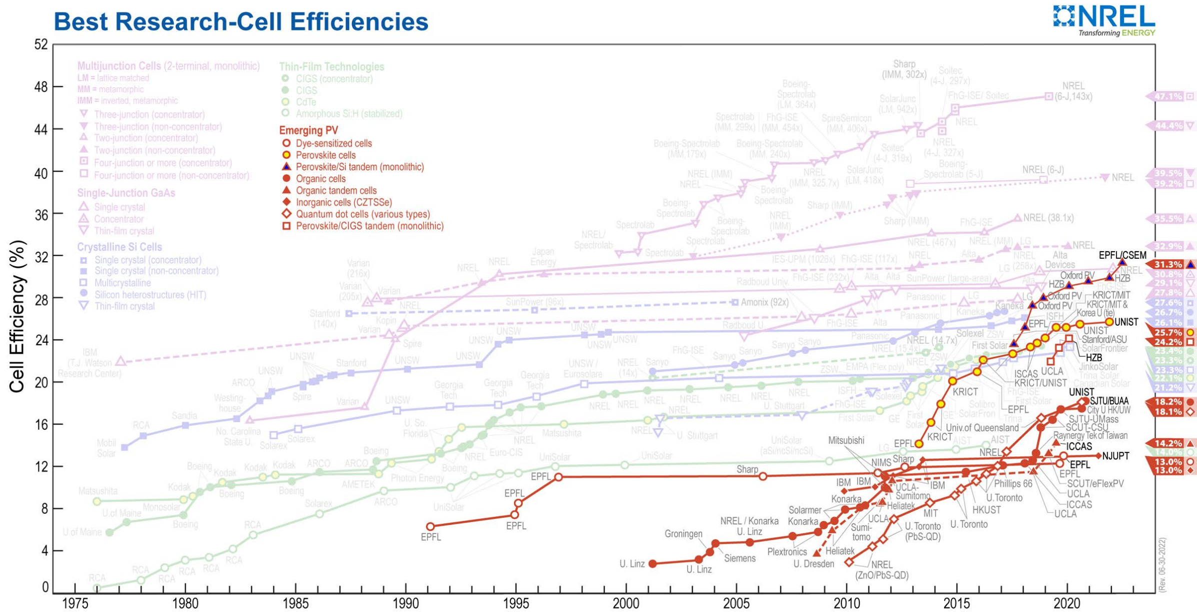

Figure 1.3: Best Research Cell Efficiency Chart - Emerging PV [35].

1.2. Perovskite Silicon tandem device architecture

Perovskites are hybrid organic-inorganic materials with a general chemical formula ABX_3, where A and B are cations and X is an anion, as shown in Fig 1.4. A include organic cations like Methylammonium (MA with a chemical formula $CH_3NH_3^+$) or Formamidinium (FA with a chemical formula $CH(NH_2)_2^+$). Metal cation, such as Pb^{2+} or Sn^{2+}, is represented by B, whereas halide is represented by X. (i.e Cl^-, Br^-, or I^-). Typical Perovskites researched are $MAPbI_3$ and $MAPbBr_3$ as reported by Miyasaki et al. [29]. However high temperature and moisture resulted in stability issues and drop in PCE [2]. This was later resolved by strong encapsulation techniques and ion mixing in the PSC materials like $MAPbI_{3-x}Cl_x$, $MAPbI_{3-x}Br_x$ and $FA_xMA_{1-x}PbI_yBr_{1-y}$ resulting in increased stability and high PCE. With these, the bandgap of PSC can be varied from 1.3 eV to 2.3 eV [2].

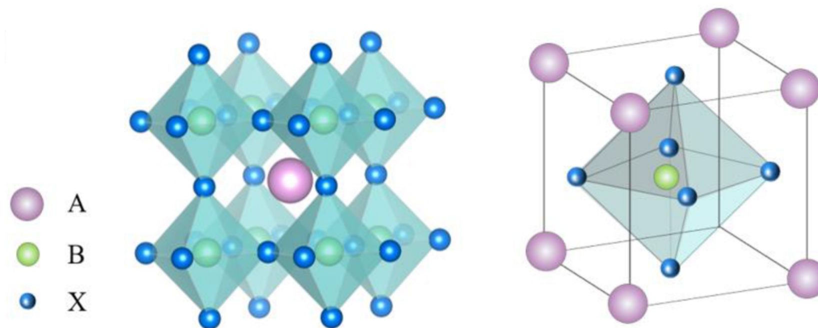

Figure 1.4: Crystal Structure of a 3D Perovskite [53].

Researchers in the PV community are interested in PSC because of its many desirable properties, like higher carrier mobilities, a higher absorption coefficient in the visible light range (400-700 nm) than

c-Si, and a long charge carrier diffusion length with carrier lifetimes ranging from hundreds of nanoseconds to microseconds [16]. Typical PSC architectures are mesoporous, planar (NIP) and inverted planar (PIN). These architectures depend on the deposition sequence of layers on the glass substrate and the type of charge transport layers used. These typical architectures are shown below in Fig 1.5 [32].

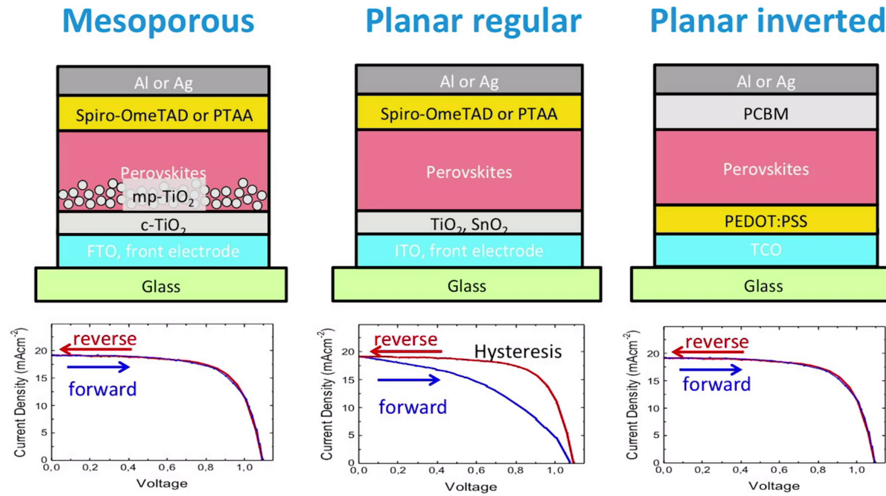

Figure 1.5: Common Perovskite Architectures with the ETL marked in grey and HTL marked in yellow [32].

As seen in the Fig 1.5, the PSC layer (in light red) is sandwiched between electron transport layer (ETL in grey) and hole transport layer (HTL in yellow). These transport layers are responsible for the charge transport from PSC to its respective electrodes in the event of illumination and charge generation [32]. For successful electron extraction, the conduction band (CB) of ETL should be below the absorber's lowest unoccupied molecular orbital (LUMO), while the absorber's highest occupied molecular orbital (HOMO) should be above the valence band (VB). For successful hole extraction, the conduction band (CB) of HTL should be above the absorber's lowest unoccupied molecular orbital (LUMO), while the absorber's highest occupied molecular orbital (HOMO) should be below the valence band (VB) [3]. A perfect HTL would have high hole mobility, low electron affinity, compatible HOMO and LUMO energy levels with Perovskite, high thermal stability, and low costs, whereas an ideal ETL would have high electron mobility, low trap density, wider bandgap, high thermal stability, high transparency, and low costs [3]. Common HTLs include PEDOT:PSS $(poly(3,4-ethylenedioxythio-phene) : poly(styrenesulfonicacid))$, NiO (Nickel Oxide), PTAA $(poly[bis(4-phenyl)(2,4,6-trimethylphenyl)amine])$ [34] and Spiro-OmeTAD $(2,2',7,7'-Tetrakis[N,N-di(4-methoxyphenyl)amino]-9,9'-spirobifluorene)$ [32]. Common ETLs include TiO_2 (Titanium dioxide), SnO_2 (Tin Oxide), ZnO (Zinc Oxide) and PCBM $(phenyl-C_{61}-butyricacidmethylester)$. Common Transparent conductive Oxides (TCO in blue as shown in Fig 1.5) include FTO (Fluorine doped Tin Oxide) and ITO (Indium Tin Oxide) [32, 34].

However it is noticed that some architectures has hysteresis effect in the JV curve (for example planar structures with Spiro-OmeTAD or PEDOT:PSS as HTL and TIO_2 as ETL as shown in Fig. 1.5). These issue are resolved with the use of mesoporous (NIP with meso-porous or mp-TiO_2 nanoparticles in the absorber) or planar inverted (PIN) structure. Furthermore, PCBM is the most often used ETL material because it may reduce the hysteresis caused by trapped charges at the absorber-ETL interface. This is due to the fact that this substance has an excellent interaction with Perovskite [8]. According to a past studies, the use of fullerene (C_{60}) as an ETL also leads in greater charge carrier extraction due to its high mobility and conductivity. It is also studied that C_{60} or monolayer Chlorine also used as a buffer layer between ETL and absorber to reduce the hysteresis effect [8]. Currently the record PCE for a PSC single junction is 25.7%, developed by UNIST in 2022. The PSC si based on $FAPbI_3$ absorber layer with mesoporous structure (NIP configuration with TiO_2 nanoparticles in the absorber layer) as shown in Fig 1.6. The ETL, HTL and TCO is TiO_2, Spiro-OmeTAD and FTO respectively [25].

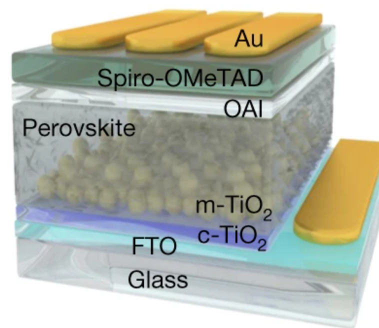

Figure 1.6: $FAPbI_3$ based PSC developed by UNIST, South Korea [25].

If we look at the Pvk/c-Si tandem architecture, the top cell typically consist of a high bandgap PSC (around the range 1.5 eV) and a low bandgap c-Si (around the range 1.12 eV) as the bottom cell. At present, the current record certified PCE for Pvk/c-Si is 31.25% developed by CSEM and EPFL, Switzerland [6]. The architecture is based on a fully textured Pvk/c-Si tandem device with a hybrid solution/vapor processing technique for perovskite. Further details of this architecture was not disclosed as of yet [6]. Looking at the next best tandem device is 29.8% PCE for Pvk/c-Si developed by Tockshorn et al. at the Helmholtz-Zentrum Berlin (HZB), Germany [46]. The architecture is similar to the architecture by Al-Ashouri et al. [4] which shall be discussed soon. The major improvement to this architecture is that the solar cell made up of a nanotextured front side and a dielectric reflector on the back side that reflects infrared light back into the silicon bottom cell absorber. According to the authors, the nanotexturing on one side not only improved light absorption and photocurrent when compared to a reference solar cell without nanotextures, but it also improved the electronic quality of the tandem device slightly and enabled better film formation of the perovskite layers. This is followed by the certified PCE for Pvk/c-Si is 29.5% developed by Oxford PV [36]. However there is currently no public disclosure regarding the device architecture and parameters used. Looking at the next best Pvk/c-Si tandem device is 29.15% efficient tandem device again developed by the Helmholtz-Zentrum Berlin (HZB), Germany [4]. This tandem device will also be simulated in the Advanced Semiconductor Analysis Software (ASA) which is also the objective of this report.

According to Al-Ashouri et al. [4] the architecture shown in Fig 1.7 is summarised as follows. The bottom cell is based on a silicon hetero-junction (SHJ with NIP structure) of 260 μm thick n-type c-Si base (with a bandgap of 1.12 eV) with n-doped nc-SiO_x (nano-crystalline Silicon oxide) and p-doped a-Si (amorphous Silicon) as top and bottom layers for the c-Si base [4]. Intrinsic a-Si is used as buffer layer between the heterojunction layer for good passivation and charge transport between the layers [4]. The top cell is based on the Perovskite (with a bandgap of 1.68 eV) having a composition $Cs_{0.05}(FA_{0.77}MA_{0.23})_{0.95}Pb(I_{0.77}Br_{0.23})_3$ with the deposition of layers on top of SHJ c-Si cell in the order of ITO/HTL/perovskite/(LiF)/C_{60}/SnO_2/IZO/ Ag/LiF. The HTL used here is a self assembled monolayer based on methyl-substituted carbazole Me-4PACz (([4-(3,6- dimethyl-9H-carbazol-9-yl)butyl]phosphonic acid). Here ITO is used as a tunnel recombination junction between the top cell and bottom cell allowing for holes of top cell to recombine with the electrons of the bottom cell [4]. This resulted in the certified Open-circuit voltage (V_{oc}), Short-circuit current (J_{sc}), Fill Factor (FF) to be 1.9 V, 19.26 $mAcm^{-2}$ and 79.52% respectively [4].

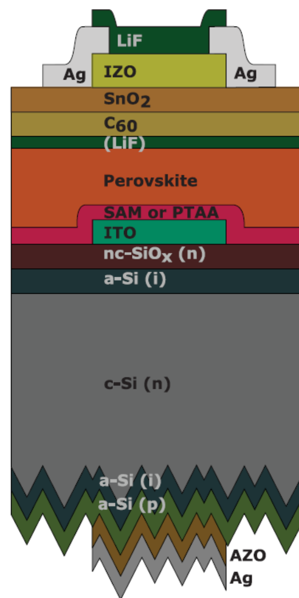

Figure 1.7: Pvk/c-Si architecture developed by HZB, Germany [4].

Other well known Pvk/c-Si architecture include the tandem device developed by EPFL, Switzerland with a PCE of 25.2%. According to Sahli et al. [40], the architecture shown in Fig 1.8 can be summarised as follows. This architecture is based on fully textured monolithic Perovskite/SHJ c-Si tandem device. this device is almost similar to the device developed by HZB, Germany as shown in Fig 1.7. The main difference is the HTL and the tunnel recombination junction employed along with complete texturing of all the layers [40]. Here Spiro-OmeTAD is used as the HTL while p-doped nc-Si:H and n-doped nc-Si:H is used collectively as a tunnel recombination junction to facilitate recombination of holes from the HTL of PSC and the electrons of the n-doped layer from the SHJ c-Si layer and enhance charge carrier recombination in the textured interfaces while employing light trapping techniques [40].

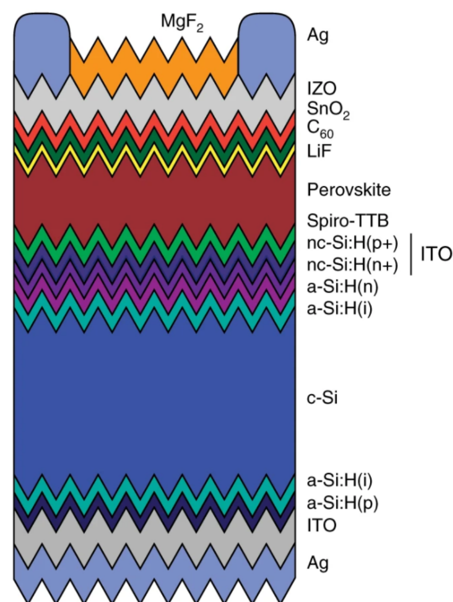

Figure 1.8: Pvk/c-Si architecture developed by EPFL, Switzerland [40].

1.3. Simulation of Pvk/c-Si tandem device in literature

It is noted that many of the recorded efficiencies performance is based on lab scaled solar cells (around $1cm^2$). Scaling up the Perovskite top-cell manufacturing is required to increase the size of the tandem [10]. However, getting high PCE on large-area tandems is a difficult task in and of itself, requiring adherence to current industry standards in terms of material and process manufacture and assembly [10]. Parallel to this, major efforts are still required to fulfill the ever-increasing reliability criteria set by firms international electrotechnical commission (IEC) module certification tests and new ISO tests specifically for PSC [10]. Therefore thorough theoretical research on the optical and electrical characteristics is required even for lab scale PSC/c-Si tandem device before manufacturing and testing due to its inherent expense and time involved.

However, with theoretical background on the opto-electrical characteristics of Pvk/c-Si tandem device or any solar cell technology for that matter, simulation softwares can be created to employ such opto-electrical models in order to replicate almost similar performance results compared to the real-life experimental results. Simulation softwares do exist make use either of the optical models, electrical models or both in order to make near perfect simulations. Well known simulation software include TCAD Sentaurus, ASA, Silvaco, SCAPS, DAMPS, AFORS-HET, SETFOS and others. These softwares differs according to the solar cell technology it can model (c-Si, a-Si, CIGS, CdTe, III-V materials and multijunction solar cells), the modelling method used (Finite element method or Lumped element method), and finally the models used (Electrical models based on 1D, 2D and 3D approach and Optical models based on GenPro 1,2,3 & 4). Throughout this thesis project, the ASA software will be used for the opto-electrical characterization of the Pvk/c-Si tandem device.

Device simulations was frequently utilized in inorganic solar cells such as silicon for understanding device physics and optimum design for efficiency increase. The exciton type is a key distinction between organic and inorganic absorbers. Because the exciton in conventional organic absorbers is Frenkel-type, the binding energy of the exciton must be included into carrier separation in solar cells for correct device modelling, which is difficult [33]. The exciton in the Perovskite material, on the other hand, is a Wannier-type exciton, therefore photo-excited carriers may be treated in the same way as inorganic materials [33]. These two characteristics, namely structural similarity without mesoporous structure and exciton type, allow an existing device simulator for inorganic solar cells to be used to Perovskite solar cells [33].

There are some literatures that have conducted simulations for the Pvk/c-Si tandem device. For instance, according to the simulation conducted by Aeberhard et al. [1], SETFOS was used in the simulation of Pvk/c-Si tandem. A typical Pvk/c-Si tandem device based of NIP Pvk top cell and SHJ c-Si bottom cell was chosen for the simulation and can be depicted in Fig 1.9.

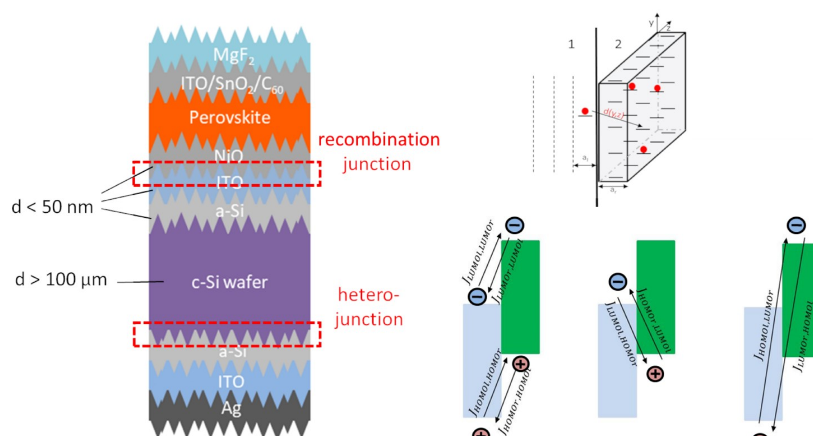

Figure 1.9: Pvk/c-Si architecture used for the simulation in SETFOS. Tunnelling models for the hetero-junctions and the tunnel recombination junctions had to be incorporated for realistic simulations [1].

The optical simulation was based on the transfer matrix method solved along with ray-tracing for the entire device (will be discussed in Chapter 2.1). The electrical simulations utilised standard poisson's equation and continuity equations for electrons and holes (will be discussed in Chapter 2.2). These models were also extended for the hetero-junctions (ETL/Pvk, Pvk/HTL, n-a-Si/c-Si and c-Si/p-a-Si interfaces) and the tunnel recombination junctions. The generation parameters from the optical model were then combined with the electrical models to give a more accurate simulation of the device. The simulations was carried out in 1D environment at STC. The simulation yielded an very good and realistic JV curves and can be seen in Fig 1.10.

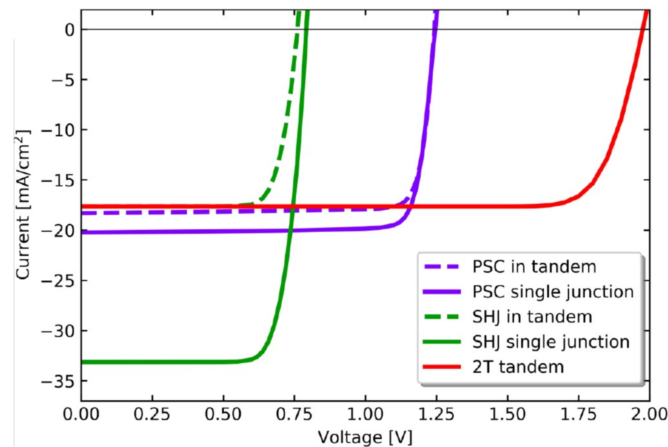

Figure 1.10: JV curve obtained for the Pvk/c-Si simulation conducted in SETFOS [1].

It can be seen in Fig 1.10 that the JV curve of the sub-cells in tandem configuration add up perfectly to the tandem JV curve due to the use of optimized optical and electrical models along tunnelling models incorporated taking recombination losses and other losses into account.

In another literature, AFORS-HET was used in the simulation of Pvk/c-Si tandem device conducted by Iqbal et al. [20]. The device structure was based on PIN Pvk top cell and SHJ c-Si bottom cell as shown in Fig 1.11.

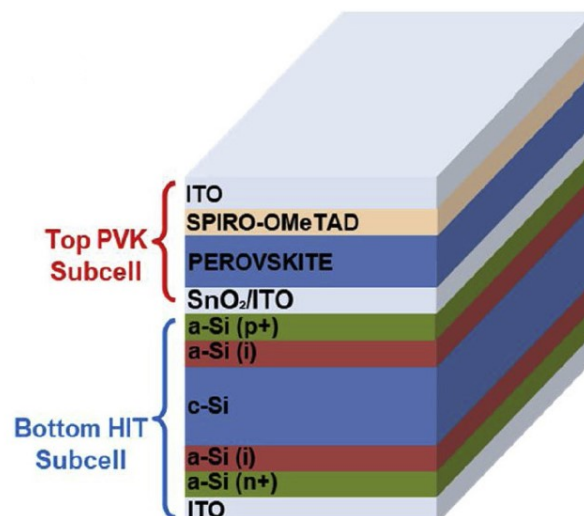

Figure 1.11: Pvk/c-Si architecture used for the simulation in AFORS-HET. [20].

For the optical modelling, simple Lambert-Beer law (will be discussed in Chapter 2.1) for each sub-

cell separately. The electrical modelling was conducted using basic semiconductor equations (will be discussed in Chapter 2.2). All relevant optical and electrical parameters were inserted in the AFORS-HET interface and simulations were carried out in 1D environment at STC. The JV curves for each of the sub-cell were then obtained and can be seen in Fig 1.12.

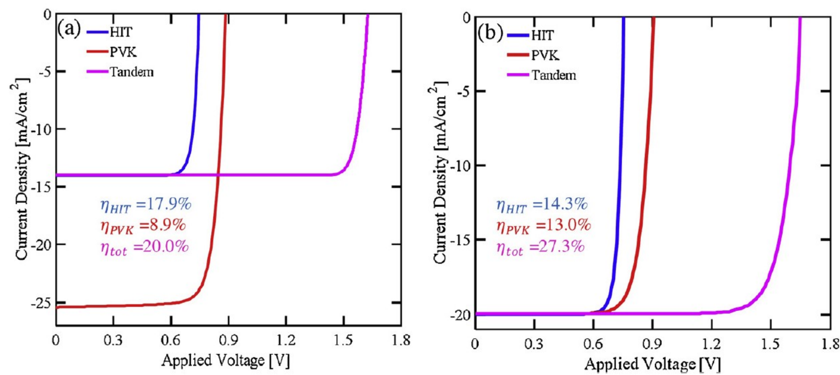

Figure 1.12: JV curves obtained for the Pvk/c-Si simulation conducted in AFORS-HET a)JV curve for Pvk thickness of 500nm and c-Si thickness of 200um b)JV curve for Pvk thickness of 165nm and c-Si thickness of 200um [20].

The JV curve of the sub-cells with different thickness were then added to get the final tandem JV curve. However, experimental validation was carried out for each sub-cell and not for the tandem device.

For the PVMD thesis [12] conducted by J.G Godoy, a simulation was carried out for the Perovskite/micro crystalline Silicon tandem device which incorporated the tunnel recombination junction as shown in the Fig 1.13 below:

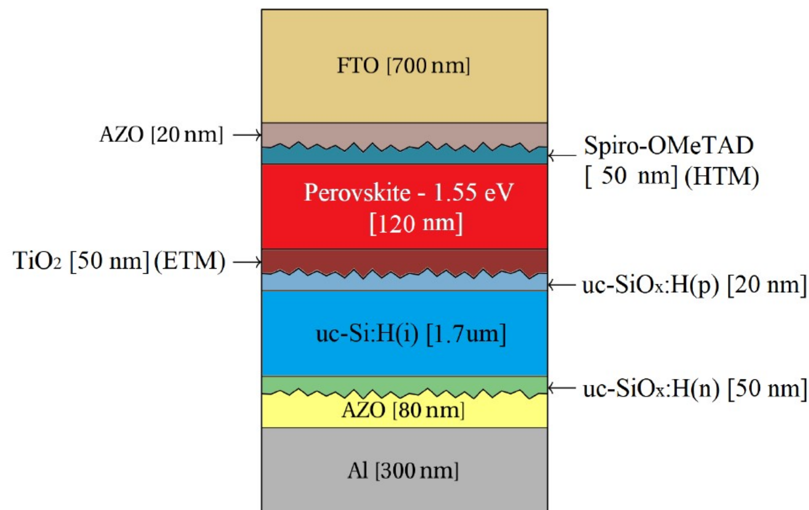

Figure 1.13: Tandem Perovskite Solar Cell / µcSi solar cell layers [12].

The tunnel recombination junction was achieved by doping the TiO_2 and uc-SiO_x:H(p) layers. Since appropriate tunnelling models were not included inside ASA, trap assisted tunnelling had to be used. However, convergence in the solution was not achieved despite fitting the trap states for each of the layers [12].

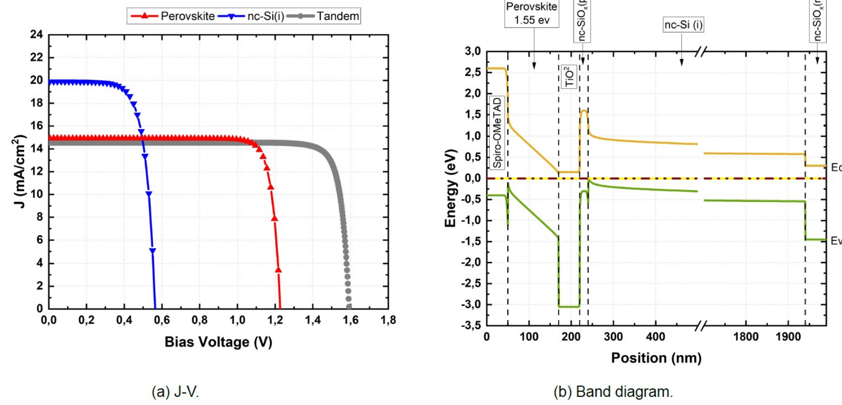

(a) J-V. (b) Band diagram.

Figure 1.14: Tandem Perovskite Solar Cell / µcSi solar cell a)JV curve and b)Band diagram [12].

As a result, the tandem JV curve was obtained from the combination of single sub-cell JV simulation and concluded as it is [12]. In the below table, we present the current status for the multi-junction tunnelling capabilities of solar cell simulation softwares. By the end of this project, the ASA software may become a complete one-dimensional solar simulation suite that can produce similar solar cell performance results as compared to advanced simulation softwares like TCAD Sentaurus.

Table 1.1: Current status of the TRJ modelling for different solar cell simulation softwares in the market

	Direct	Band to Band	Trap Assisted	Multi-Tunneling
ASA	☑	☑	☑	☑
Sentaurus	☑	☑	☑	☑
ATLAS	☑	☑	☑	☑
AFORS-HET	☑	x	☑	x
DAMPS	☑	x	☑	x
Quokka	☑	x	x	x
SCAPS	☑	x	☑	x
PC1D	x	x	☑	x

1.4. Research Gap

So far, most of the literature on simulation presented here are commenced on 1D solar cell simulators due to inherent simplicity and fast simulation times compared to 2D or 3D simulators like TCAD Sentaurus or Silvaco Atlas. However, as seen in the simulation conducted by Aeberhard et al. [1], material properties for the electrical simulations were difficult to find and had to be fitted with experimental results in order to replicate real device performance. Also, complete opto-electrical simulation is numerically challenging as huge difference in solar cell performance is noticed due to layer thickness modification of Pvk/c-Si tandem leading to potential convergence issue. Also, the tunnelling models used in the simulation is not explained clearly in this literature, so question of accuracy of the simulation arises.

In other literatures on Pvk/c-Si simulation like the one conducted by Iqbal et al. [20] carried out the simulations for each subcell and combined the JV curves to obtain the tandem device performance. As a matter of fact, most of the tandem simulations in literature are based on individual sub-cell simulations that were carried out in most of the 1D simulators (including ASA) and was combined to obtain the tandem JV curve. Comparing real tandem device performance to these kind of simulations is not realistic since tunnelling losses are not incorporated in the simulation. Furthermore, possible optical losses and parasitic absorption can occur in the tunnelling layer with poor interface passivation that can lower the performance of the tandem device but are not accounted for in the simulation.

Hence there is little literature on the electrical modelling of Perovskite/Silicon tandem, meaning that there is limited information on the parameters used for simulation [33]. Since we will use ASA software for this thesis project, single junction Perovskite or SHJ c-Si can be simulated in ASA accurately. However no appropriate tunnelling models exist in ASA as per version 5.0. Trap Assisted Tunnelling (or TAT) model alone cannot work with Pvk/c-Si tandem as the trap density and defects of Perovskite HTL/ETL are low compared to the n-doped or p-doped a-Si:H leading to inefficient tunnel recombination with very poor convergence in the solution as seen in Godoy's thesis [12]. Instead, the trap parameters need to be fitted to simulate real life tunnelling effects.

Because appropriate models and parameters for the entire device is limited, study of Pvk/c-Si tandem device performance and its losses may be less accurate or incorrect. The parameters for the multijunction simulation need to be user defined and the software needs more input to identify the number of junctions where tunnelling will take place making the user experience less friendly.

1.5. Objectives

We know that there is only little literature on the electrical modelling parameters of Pvk/cSi tandem. Furthermore, ASA currently has TAT recombination which does not work accurately for Pvk/cSi modelling [52]. Therefore, the main objectives of this thesis project are:

1. To understand the solar cell modelling approach in ASA and the tunnel recombination models that can be incorporated in the source code for the simulation of multi-junction devices
2. To develop an algorithm (C++ code) that can automatically detect and process the tunnelling models in ASA for Pvk/c-Si tandem device or any device in general.
3. To validate the algorithm (C++ code) with experimental or other simulation results.
4. To perform further simulation of the Pvk/c-Si tandem device in ASA to optimize its performance.

1.6. Report structure

The report's structure is as follows. In Chapter 2, we will look at the typical modelling setup for a solar cell in ASA. The existing optical and electrical models followed by the tunnelling models in existing literature are briefly discussed in this chapter. In Chapter 3, the development of an algorithm for the tunnelling models will be explained followed by its validation using other simulation or experimental results in Chapter 4. In Chapter 5, further opto-electrical simulation of Pvk/cSi tandem device will be conducted in ASA to improve its performance. This is then followed by the final Chapter 6 with conclusion and recommendation for this project.

2
Solar Cell Modelling in ASA

In this chapter, we shall focus on the first objective of this thesis project to understand the solar cell modelling approach in ASA and the tunnel recombination models that can be incorporated in the source code for the simulation of multi-junction devices. The ASA software is a 1D, steady-state device simulator that allows you to analyze and optimize semiconductor devices made of a variety of semiconductor materials with different band structures [51]. A general overview of the most important optical models models utilized in ASA is explained in Section 2.1 followed by the electrical models in Section 2.2 including the tunnel recombination models that can be used together. A simulation approach and the solver in ASA is then briefly explained with a use of a simulation flowchart in Section 2.3.

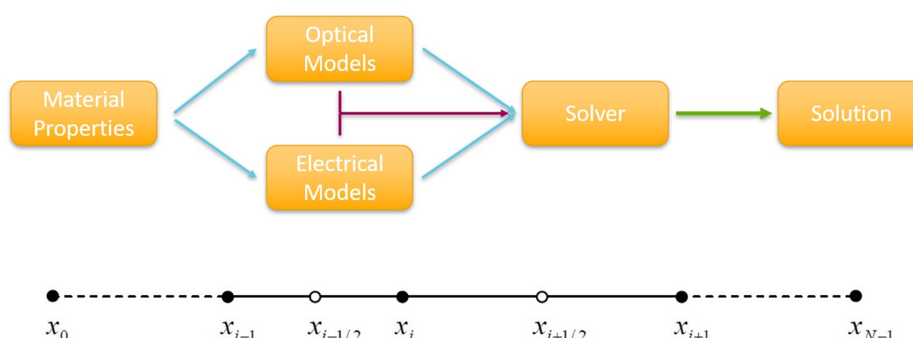

Figure 2.1: ASA modelling procedure [51].

As shown in Fig 2.1, the modelling in general starts with first defining the materials properties and grid definition. Certain optical and electrical models can then be performed over the defined material properties and mesh using a solver. Results like JV curve and other performances can be extracted and verified.

2.1. Optical modelling

One of the main goals of any semiconductor device is to maximize the light absorption when light is introduced to the semiconductor material. The optical generation rate G_{opt} is an important parameter to obtain the generation rate profile of a solar cell device. A typical semiconductor device can have multiple layers (both thin and thick layers with a certain complex refractive indices) with or without texturing. In this thesis project, the Genpro1 and Genpro4 optical models will be mostly used for the simulations and validations of Pvk/cSi tandem devices. These models are explained in detail and can be referred to in the Appendix A.2 due to the fact that these models are not directly involved in finding the tunnelling contributions and is out of scope for this project.

There are other optical models in literature and in the ASA manual that can be used in the simulations of tandem devices [51]. In general, The major input parameters for optical simulation with GenPro models in ASA are the layer thicknesses, complex refractive indices of layers, scattering levels that determine diffused components (Haze), and Angular distribution functions of scattered light (ADF). For this project we will be using GenPro1 model for a fully flat solar cell devices like PN junction and the silicon hetero-junction and later use the GenPro4 model for flat and textured interfaces for the Pvk/c-Si tandem device [51].

2.2. Electrical modelling

The differential transport equations that constitute the model's foundation are described in this section. This comprises of mathematical description of the energy band diagram, a density of states distribution for a-Si that includes defect states, and recombination-generation characteristic models [51]. However, the boundary conditions, contacts and the generation recombination characteristics are not explained here but can be referred from the Appendix A.1.

2.2.1. Semiconductor equations

A mathematical description of semiconductor device operating under non-equilibrium situations is represented by the fundamental set of semiconductor equations that is typically used by every solar simulator [51, 43]. These include the Poisson Eq. (2.1), the continuity equations for electrons and holes (shown in Eq. (2.2) and Eq. (2.3) respectively):

$$\nabla \cdot (\varepsilon \nabla \Psi_{vac}) = -\rho \tag{2.1}$$

$$\frac{\partial n}{\partial t} = \frac{1}{q} \nabla \cdot \vec{J}_n + G - R \tag{2.2}$$

$$\frac{\partial p}{\partial t} = -\frac{1}{q} \nabla \cdot \vec{J}_p + G - R \tag{2.3}$$

where ε is permittivity of the semiconductor, Ψ_{vac} is the potential related to the local vacuum level, ρ is the space charge density, n and p are the electron and hole concentrations in the extended conduction and valence bands, $\vec{J}_n$ and $\vec{J}_p$ are the electron and hole current density, t is time, G is the generation rate, and R is the recombination rate, respectively. $\frac{\partial n}{\partial t}$ and $\frac{\partial p}{\partial t}$ are the time rate of change of the electron and hole concentration respectively. The current density of electrons and holes given in Eq. (2.4) and Eq. (2.5):

$$\vec{J}_n = \mu_n n \nabla E_{fn} \tag{2.4}$$

$$\vec{J}_p = -\mu_p p \nabla E_{fp} \tag{2.5}$$

where μ_n and μ_p are the electron and hole mobilities respectively, and E_{fn} and E_{fp} are the electron and hole quasi-Fermi energy level. When we look at a typical energy band diagram of a typical semiconductor material like as shown in Fig 2.2, band properties play an important role in the performance of the device given by the minimum energy of the conduction band (CB) E_c, the maximum energy of the valence band (VB) E_v and the mobility gap E_μ (also called band gap for c-Si) [51, 43]. These energies can be expressed in terms of vacuum energy E_{vac} as shown in Eq. (2.6) and Eq. (2.7):

$$E_c = E_{vac} - q\psi - \chi \tag{2.6}$$

$$E_v = E_{vac} - q\psi - \chi - E_\mu \tag{2.7}$$

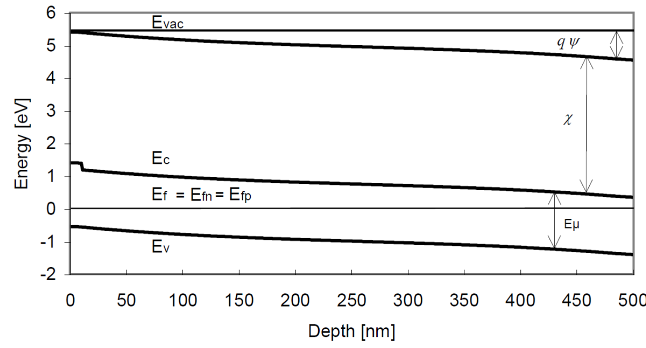

Figure 2.2: Band diagram of a-Si under equilibrium condition [51].

The Maxwell-Boltzmann approximation is then used for the carrier concentrations for electrons and holes as a function of quasi-Fermi level and the density of states (DOS) of VB and CB [51, 43], given by N_v and N_c respectively, resulting in the following Eq. (2.8) and Eq. (2.9) respectively:

$$n = N_c \exp\left(\frac{E_{fn} - E_c}{kT}\right) = N_c \exp\left(\frac{E_{fn} - (E_{vac} - q\chi)}{kT}\right) \tag{2.8}$$

$$p = N_v \exp\left(\frac{E_v - E_{fp}}{kT}\right) = N_v \exp\left(\frac{(E_{vac} - q\chi - E_\mu) - E_{fp}}{kT}\right) \tag{2.9}$$

This can also be written in the form of E_{fn} and E_{fp} as shown below in Eq. (2.10) and Eq. (2.11).

$$E_{fn} = E_c + kT \ln\left(\frac{n}{N_c}\right) = E_{vac} - q\psi - \chi + kT \ln\left(\frac{n}{N_c}\right) \tag{2.10}$$

$$E_{fp} = E_v - kT \ln\left(\frac{p}{N_v}\right) = E_{vac} - q\psi - \chi - E_\mu - kT \ln\left(\frac{p}{N_v}\right) \tag{2.11}$$

2.2.2. Density of states models for a-Si

The structure of amorphous silicon differs from crystalline silicon due to its irregular lattice with random orientation compared to c-Si as shown in Fig 2.3. In general, Silicon has a coordination number of 4, meaning that one atom can be bonded by 4 other atoms. Due to the chaotic arrangement a-Si, some of them can form three bonds instead of four, with a fourth valence electrons free of any bonds, in other words known as dangling bonds [51, 43].

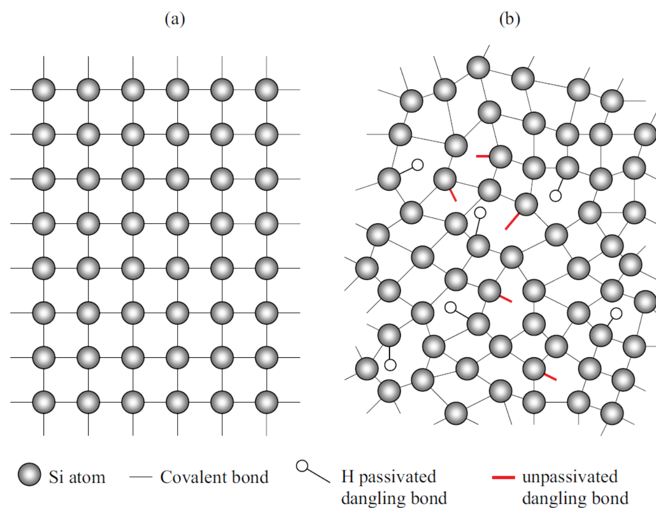

Figure 2.3: 2D crustal lattice of a) c-Si and b) a-Si:H [43].

The electronic density of states is the number of states per energy level that are accessible for electrons to occupy (DOS). It calculates the energy distribution of charge carriers in conjunction with the probability distribution function of electrons inhabiting these states. The periodic and regular lattice orientation of c-Si results in well-defined energy bands with a forbidden band gap in between with almost zero DOS due to the fact that very few defect exists in c-Si [51, 43]. On the other hand, due to irregular lattice with random orientation and bond lengths, a-Si does not have well defined or sharp energy bands like c-Si. Due to higher defects, many band states exist over a range of energies in the form of exponentially decaying band tails (valence band tails (VBT) and conduction band tails (CBT)) and defect states (due to dangling bonds (DB)) with non-zero DOS in between the VB and CB (also known as extended states) and VBT and CBT [51, 43]. The band energies of a typical a-Si can be shown below in Fig 2.4.

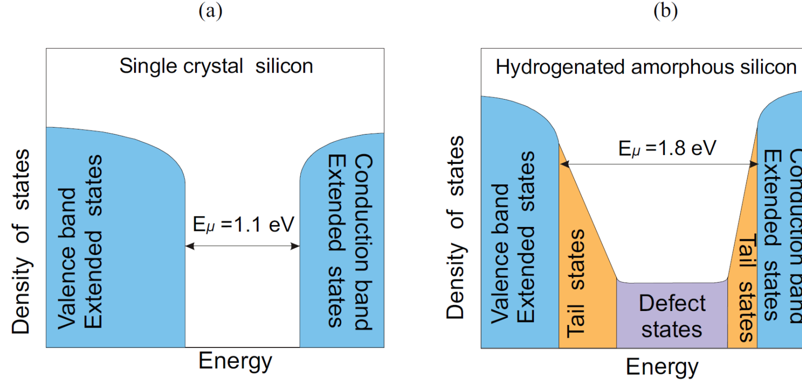

Figure 2.4: DOS distribution of electron in a) c-Si b) a-Si:H [43].

As seen in Fig 2.4, Due to the lack of a clearly defined band gap in a-Si:H, the gap is characterized in by the transition from extended to localized states, also referred to as the mobility gap. The optical gap on the other hand, which describes the least energy, a photon must have to excite an electron from the VB to the CB, is not always equal to the mobility gap [51, 43]. Carriers in the extended states VB and CB have similar energies and can pass into neighbouring states. Tail states, such as VBT and CBT, and defect states, such as DB, are confined states with little or no energy overlap with neighbouring states. As a result, carriers in these states are restricted in their movement and are effectively confined. These carriers will eventually be re-emitted to their respective bands, or they will reunite when another carrier of opposite charge is captured [51, 43]. The DOS distribution as a function of band energy for the CB, CBT, VB and VBT is given below in the following equations:

$$N_{CB}(E) = N_c^0\,(E - E_c)^{1/2} \tag{2.12}$$

$$N_{CBT}(E) = N_c^{\text{tail}}\ \exp\left[-\left(\frac{E_c^{\text{tail}} - E}{E_{c0}^{\text{tail}}}\right)\right] \tag{2.13}$$

$$N_{VB}(E) = N_v^0\,(E_v - E)^{1/2} \tag{2.14}$$

$$N_{VBT}(E) = N_v^{\text{tail}}\ \exp\left[-\left(\frac{E - E_v^{\text{tail}}}{E_{v0}^{\text{tail}}}\right)\right] \tag{2.15}$$

In the above equations, N_c^0 and N_v^0 describe the parabolic distribution of DOS of CB and VB respectively with E_{c0}^{tail} and E_{v0}^{tail} indicating the characteristic decay energy of CBT and VBT respectively. N_c^{tail} ,E_c^{tail} , and N_v^{tail} ,E_v^{tail} are the DOS and band energy respectively for the edges between the extended states and the tail states for CB and VB as shown in Fig 2.5.

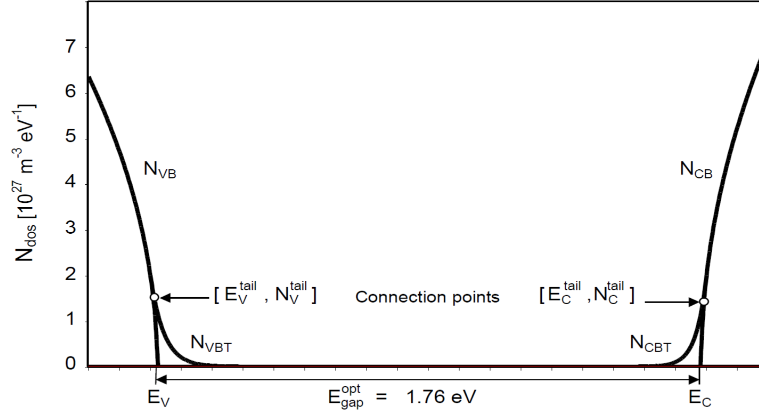

Figure 2.5: Linear DOS distribution of electron a-Si:H [51].

It is important to note that unlike the c-Si, the difference in E_c and E_v correspond to the optical bandgap. The mobility bandgap on the other hand for a-Si is given by Eq. (2.16)

$$E_\mu = E_c^{\text{tail}} - E_v^{\text{tail}} = E_c^{\text{mob}} - E_v^{\text{mob}} \tag{2.16}$$

When we look at the DB distribution, two defect groups exist, namely donor-like states ($DB^{+/0}$) and acceptor-like states ($DB^{0/-}$) with its respective energy levels $E_{DB}^{+/0}$ and $E_{DB}^{0/-}$ [51, 43] represented in the form of a Gaussian distribution as shown in band diagram of a-Si:H on a logarithmic scale in Fig 2.6. the mathematical description of the DOS of DB states is given by:

$$N_{DB^{+/0}}(E) = \frac{N_{DB}^{tot}}{\sigma_{db}\sqrt{2\pi}} \exp\left[-\frac{\left(E - E_{DB}^{+/0}\right)^2}{(2\sigma_{db}^2)}\right] \tag{2.17}$$

$$N_{DB^{0/-}}(E) = \frac{N_{DB}^{tot}}{\sigma_{db}\sqrt{2\pi}} \exp\left[-\frac{\left(E - E_{DB}^{0/-}\right)^2}{(2\sigma_{db}^2)}\right] \tag{2.18}$$

$$N_{DB^{0/-}}(E) = N_{DB^{+/0}}(E + U) \tag{2.19}$$

$$E_{DB}^{0/-} = E_{DB}^{+/0} + U \tag{2.20}$$

where U is the correlation energy, N_{DB}^{tot} is the total density of defects, and σ_{db} is the standard deviation of the DOS distribution.

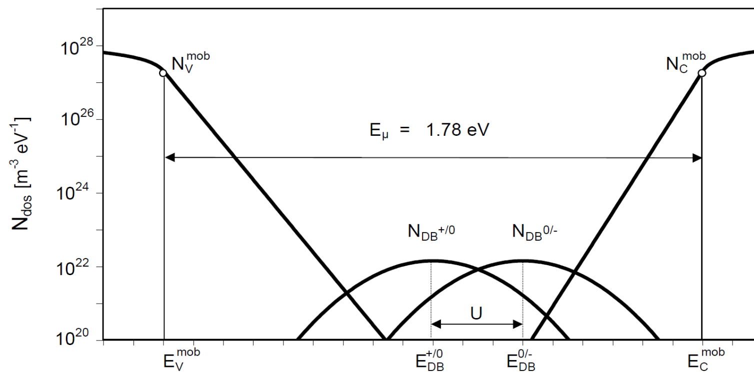

Figure 2.6: Logarithmic DOS distribution of electron a-Si:H [51].

However, this DB states does not have information on its origin. Defect pool model of Powell and Deane is hence used [37]. It is based on the DB and weak bonds like Si-Si or Si-H bonds. It goes by

the following assumption that VBT corresponds to the energy distribution of weak bonds (Si-Si or Si-H) and the available defect sites (also called defect pool) $P(E)$, uses a Gaussian distribution given in Eq. (2.21):

$$P(E) = \frac{1}{\sigma_{dp}\sqrt{2}} \text{exp}\left[-\frac{(E-E_{dp})^2}{2\sigma_{dp}^2}\right] \tag{2.21}$$

where σ_{dp} and E_{dp} are the standard deviation and the mean energy of the Gaussian defect pool respectively. The energy distribution of DB defect states (for donor like states in this case) can be rewritten as:

$$N_{DB^{+/0}}(E) = \gamma\left[\frac{2}{F_{eq}^0(E)}\right]^{\rho kT/E_{v0}^{tail}} P\left(E + \frac{\rho\sigma_{pd}^2}{E_{v0}^{tail}}\right) \tag{2.22}$$

$$\gamma = \left[\frac{N_v^{\text{tail}}\, 2\left(E_{v0}^{\text{tail}}\right)^2}{\left(2E_{v0}^{\text{tail}} - kT\right)}\right]^{\rho}\left[\frac{i_H}{2c_H}\right]^{\rho-1} \text{exp}\left(\frac{-\rho}{E_{v0}^{\text{tail}}}\left[E_P - E_v^{\text{tail}} - \frac{\rho\sigma_{pd}^2}{2E_{v0}^{\text{tail}}}\right]\right) \tag{2.23}$$

$$\rho = \frac{2E_{v0}^{\text{tail}}}{\left(2E_{v0}^{\text{tail}} + i_H kT\right)} \tag{2.24}$$

where c_H is the total hydrogen concentration in a-Si:H, i_H the number of Si-H bonds (i_H=0,1 or 2) and ρ relates to the i_H dependence. F_{eq}^0 is the equilibrium occupation function of neutral DB and can exist in the form of donor DB or acceptor DB given in the following equations:

$$F_{eq}^+ = \frac{1}{Z} \tag{2.25}$$

$$F_{eq}^0 = \frac{2}{Z} \text{exp}\left(\frac{E_f - E}{kT}\right) \tag{2.26}$$

$$F_{eq}^- = \frac{1}{Z} \text{exp}\left(\frac{2E_f - 2E - U}{kT}\right) \tag{2.27}$$

$$Z = 1 + 2\,\text{exp}\left(\frac{E_f - E}{kT}\right) + \text{exp}\left(\frac{2E_f - 2E - U}{kT}\right) \tag{2.28}$$

It is important to note that the DB distribution depends on Fermi level E_f and its profile is calculated at the freeze-in temperature which is usually above the deposition temperature and is given by Eq. (2.29):

$$E_{v0}^{\text{tail}\ 2}(T) = E_{v0}^{\text{tail}\ 2}(T=0) + (kT)^2 \tag{2.29}$$

For more information on the principle working of the density of states for a-Si:H and its defect distribution, kindly refer to the latest ASA manual [51, 43]. The equations mentioned above for the density of states models for a-Si will be used in the simulation of HIT c-Si bottom cell.

2.2.3. Mobilities for crystalline semiconductors

The mobility can be calculated from temperature and local doping concentration or can be set to a fixed value and be described by the following Eq (2.30) [51]:

$$\mu(x,T) = \mu_{\text{min}} {T_{rel}}^{\beta_1} + \frac{(\mu_0 - \mu_{\text{min}})\, {T_{rel}}^{\beta_2}}{1 + \left(\frac{N_D(x)+N_A(x)}{N_{ref}{T_{rel}}^{\beta_3}}\right)^{\alpha {T_{rel}}^{\beta_4}}} \tag{2.30}$$

where β_x and α are the empirical material constants, $N_D(x)$ and $N_A(x)$ are the donor and acceptor doping concentration, μ_0 is the mobility of the intrinsic material at 300K and T_{rel} is equal to $(T/300)$. The mobility is reduced at high electric fields to account for the saturation velocity of the electrons and is given by Eq (2.31):

$$\mu_{HF} = \frac{\mu_{LF}}{\sqrt{1 + \left(\frac{\mu_{LF} E}{v_{sat}}\right)^2}} \tag{2.31}$$

where v_{sat} is the saturation velocity, μ_{LF} is the mobility at low electric fields and E is the local electric field.

2.2.4. Band-gap narrowing for crystalline semiconductors

Due to heavy doping effects, a shift in CB and VB edge is noticed leading to band-gap narrowing [51]. The shift in the band edges is given by the following equations:

$$\Delta E_c(x) = -E_{\text{bgn.ref}} \frac{N_D(x)}{N_D(x) + N_A(x)} \left[\ln\left(\frac{N_D(x) + N_A(x)}{N_{\text{ref}}}\right) + \sqrt{\ln^2\left(\frac{N_D(x) + N_A(x)}{N_{\text{ref}}}\right) + \frac{1}{2}} \right] \tag{2.32}$$

$$\Delta E_v(x) = E_{bgn.ref} \frac{N_A(x)}{N_D(x) + N_A(x)} \left[\ln\left(\frac{N_D(x) + N_A(x)}{N_{ref}}\right) + \sqrt{\ln^2\left(\frac{N_D(x) + N_A(x)}{N_{ref}}\right) + \frac{1}{2}} \right] \tag{2.33}$$

where $E_{\text{bgn.ref}}$ is the slope for CB and VB.

2.3. Numerical solution and simulation approach

In ASA, power conversion is regarded to be in steady state ($\frac{\partial n}{\partial t}$ and $\frac{\partial p}{\partial t}$ is zero) and the simulation is done in one dimension (with respect to the depth of the device x). Also assumption that $dE_{vac}/dx = 0$ and the Einstein relation $D_{n,p} = kT\mu_{n,p}/q$ is used [51]. The basic semiconductor equations from (2.1) to (2.3) is manipulated further resulting in the following set of equations:

$$\begin{cases} \frac{\partial}{\partial x}\left(\varepsilon_0 \varepsilon_r(x) \frac{\partial}{\partial x}\psi(x)\right) + \rho(x) = 0 \\ \frac{1}{q}\frac{\partial}{\partial x} J_n(x) + G(x) - R(x) = 0 \\ -\frac{1}{q}\frac{\partial}{\partial x} J_p(x) + G(x) - R(x) = 0 \end{cases} \tag{2.34}$$

The above equations will then be solved with space charge density ρ and the modified equations of (2.4) and (2.5) as shown below:

$$\begin{cases} \rho(x) = q\left(p(x) - n(x) + p_{loc}(x) - n_{loc}(x) + N_d(x) - N_a(x)\right) \\ J_n(x) = q\mu_n(x)E(x)n(x) + kT\mu_n(x)\frac{\partial}{\partial x}n(x) \\ J_p(x) = q\mu_p(x)E(x)p(x) - kT\mu_p(x)\frac{\partial}{\partial x}p(x) \end{cases} \tag{2.35}$$

Here $p_{loc}(x)$ and $n_{loc}(x)$ are the localised carrier concentration. The grid points or mesh of small units is created for the device structure in order to solve the Poisson equations and the continuity equations for each unit. Hence a spatial discretization is created for the three semiconductor equations leading to 3×N nonlinear algebraic equations with 3×N unknowns where N is the number of gridpoints. Boundary conditions are set for x=0 and x=L (Ohmic or Schottky contacts boundary conditions can be referred from the Appendix A.1.1 and the ASA manual) [51].

Difference methods, interpolation methods and Gummel's integral method can be used to create a complete and accurate set of semiconductor equations for all the grid points. These equations are then solved iteratively using Gummel's method or Newton's method. For a brief description, the Gummel's method solves the 3 basic semiconductor equations in one variable sets separately achieving faster and accurate convergence to the required solution but with less precision while the Newton's method solves 3 basic semiconductor equations simultaneously in one single variable set with extremely precise convergence to the solutions but at a cost of increased simulation time. These methods can be referred from the ASA manual as it's theory is beyond the scope for this project [51]. Finally with all parameters of the device layers, the simulation of the device can be represented in the following flowchart algorithm in Fig 2.7:

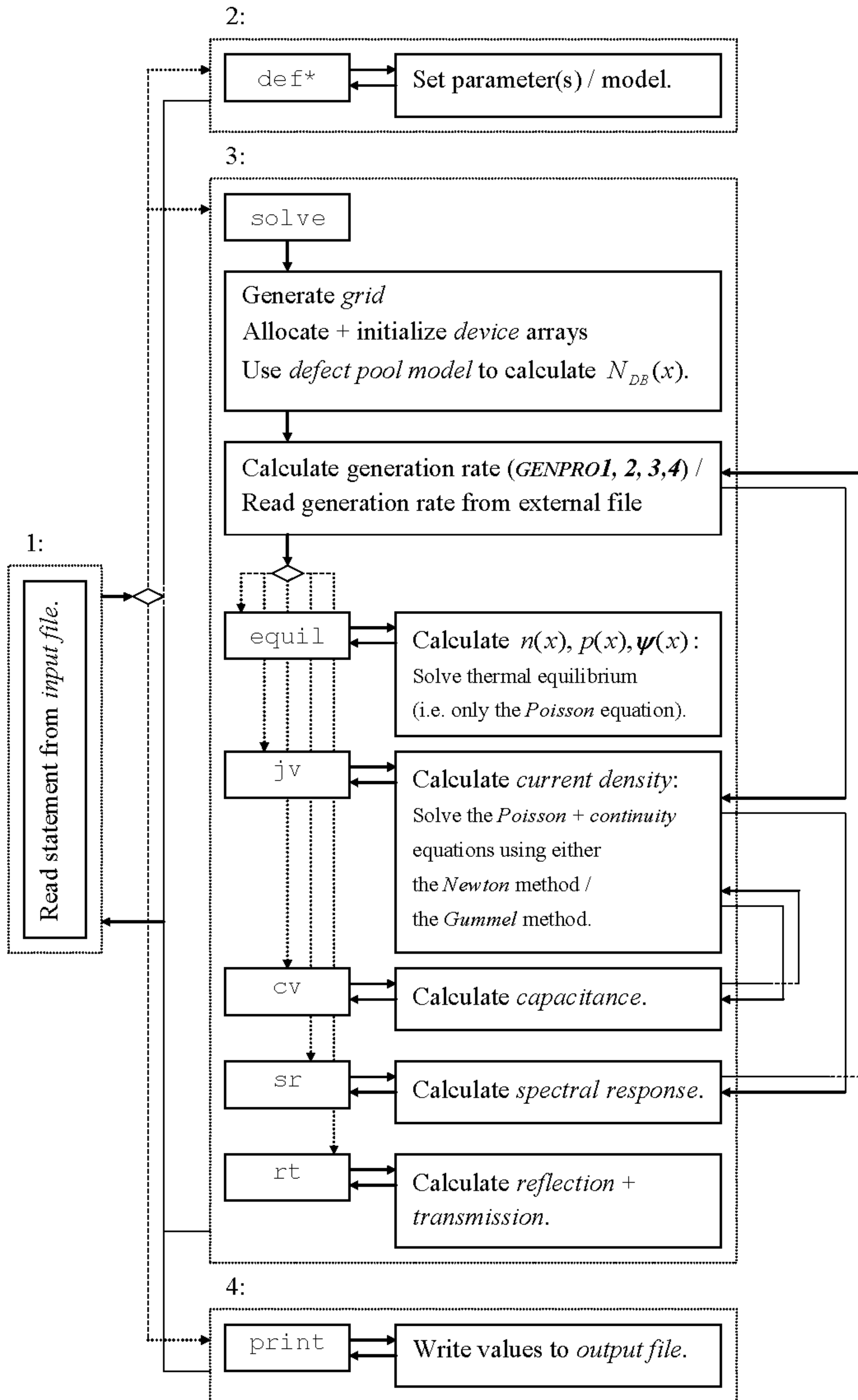

Figure 2.7: Simulation flowchart of ASA [51].

2.4. Tunnelling Models

The tandem performance of the Pvk/SHJ c-Si in reality is not as straightforward as simply combining the JV as seen in Chapter 1.3. Real multi-junction devices need a so called "Tunnel Junctions" in order to facilitate proper charge carrier between bands of different layers and should have low optical and electrical losses between two sub-cells of the tandem device. It was first used in 1980 by Bedair et al. [5] on the Aluminum-Gallium-Arsenide (AlGaAs) top cell and Gallium-Arsenide (GaAs) bottom cell. Tunnel junctions in general are PN junctions with high doping and narrow depletion regions. Without these junctions, the p layer of the top cell and the n layer of the bottom cell would create a PN junction in the reverse direction (reverse bias condition) significantly lowering the voltage of the tandem device. With high doped region of the n and p layer of the tunnel junctions, the electron in the CB of the n layer can tunnel through and recombine with the holes in the VB of the p layer. A good tunnel junction should have high bandgap than the bottom sub-cell to prevent parasitic absorption, high mobility for effective charge transport and good lattice matching with the top and bottom cell to reduce recombination losses.

To simulate real tandem devices, we need to incorporate appropriate tunnel recombination models into ASA and solve them along with the basic semiconductor equations simultaneously. In literature, there are several tunnelling models, of which most of the models were used for the simulation of transistors like MOSFETS and JFETS [18], and some specifically for solar cells in the solar cell simulators like SCAPS, AFORS-HET and TCAD Sentaurus. In general, these tunnelling models can be categorised based on the principle of tunnelling method and are given by:

1. Trap Assisted Tunneling (TAT)
2. Direct Tunneling (DT)
3. Band to Band Tunneling (BBT)

Some of these categories may have various sub-models depending on the mathematical approximations used in these models. However for this section, we shall focus on specific models, like direct tunnelling by Ieong et.al. [18], simple band to band tunnelling [30] and non-local band to band tunnelling [27, 31]. Other models can be referred to from the Appendix B

2.4.1. Trap Assisted Tunneling

At the moment, the tunnelling model that is incorporated in ASA is the TAT model. This model is mainly used for charge tunneling through defect rich layers like p or n doped a-Si. It is mainly used in the simulation of micromorph tandem devices. The TAT model incorporated in ASA uses the Delft method, that takes into consideration the basic TAT model by Hurkx et al. [14] and enhanced carrier transport in the high field region of the tunnel recombination junction (TRJ) [52]. The recombination rate at the trap is calculated using a modified SRH formula in this model. In the region of the tunnel recombination junction, this formula is utilized to compute the recombination rate at the CBT and VBT, as well as the DB defect states. This is given by Eq. (2.36):

$$R_{tat} = \frac{N_t\left(1+\Gamma_n\right)\left(1+\Gamma_p\right)\left(c_n c_p n_0 p_0 - e_{n.0} e_{p.0}\right)}{\left(1+\Gamma_n\right)\left(c_n n_0 + e_{n.0}\right) + \left(1+\Gamma_p\right)\left(c_p p_0 + e_{p.0}\right)} \tag{2.36}$$

where n_0 and p_0 is the electron and hole concentration in the CB and VB respectively at the trap position, N_t is the concentration of traps, c_n and c_p are the capture coefficients of the electrons and holes respectively, $e_{n,0}$ and $e_{p,0}$ are the emission coefficients of the electrons and holes respectively, $\Gamma_{n,p}$ are the electric field dependent factors and R_{tat} is the TAT recombination rate. Due to tunneling from other positions to the trap, the field dependent parameters $\Gamma_{n,p}$ relate to the electron and the hole concentration in the CB and VB respectively to the effective electron (n_t) and hole (p_t) concentrations that are available for recombination at the trap position. The analytic equations for $\Gamma_{n,p}$ also takes into consideration the local electric field and the likelihood of an electron and hole tunneling to a trap. The same factor affects the effective emission coefficients $e_{n,t}$ and $e_{p,t}$ as well [51]. These are given by the following equations:

$$\frac{n_t}{n_0} = \frac{e_{n.t}}{e_{n.0}} = 1 + \Gamma_n \tag{2.37}$$

$$\frac{p_t}{p_0} = \frac{e_{p.t}}{e_{p.0}} = 1 + \Gamma_p \tag{2.38}$$

The TAT model accommodates for greater recombination rates in high field locations, but the tunneling transport through localised states to recombination sites is ignored. To take this into account, effective extended state mobility of electrons ($\mu_{n,eff}$) and holes ($\mu_{p,eff}$) in the high electric field regions which includes all the the electron states above and below the mobility edge is used in the current density Eq. (2.4) [51]. The modified current density which includes all the states is given by Eq. (2.39):

$$J_n = \mu_{n.eff} n_{ext} \cdot \frac{dE_{fn}}{dx} \tag{2.39}$$

In the area of high electric field at thermal equilibrium, the effective extended state mobility is determined by Eq. (2.40):

$$\mu_{eff} = \mu_{ext} \cdot \exp\left(\frac{|\xi|}{\xi_0}\right) \tag{2.40}$$

where $\xi_0 = 2x10^5 V/cm$ and ξ is the intensity of electric field at thermal equilibrium.

2.4.2. Direct Tunneling

In DT method (also called quantum tunneling method or intra-band tunnelling), the electrons/holes from one semiconductor material band-edge can tunnel through the forbidden states of the insulating layer and cross the other side of the insulating layer to the same band edge (CB-CB/VB-VB) of similar energy states of another semiconductor material.

Direct tunneling model proposed by Ieong et al.

This DT model was used in the tunneling of electrons and holes in the MOSFET device in the Silicon and Silicide interface as shown in Fig 2.8 and charges can be tunnelled in either direction [18].

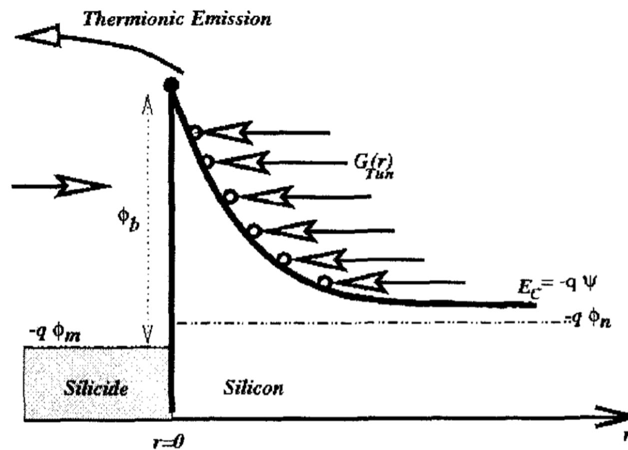

Figure 2.8: Generation rate due to tunnelling at the contact [18].

The working of this model is such that the recombination or generation process is converted from the tunnelling current. The local tunneling generation rate, given by $G_{Tun}(r)$, depends on the potential profile along the tunneling path (represented by the circular nodes in Fig 2.8) and the local Fermi level ϕ_n. The tunneling integral over distance and energy may be turned into a double integral over distance alone, making this possible [18]. The local generation rate associated with tunneling may be linked to the local tunneling current J_{Tun}, which is provided in the Eq (2.41).

$$G_{Tun}(r) = \frac{1}{q}\nabla \cdot J_{Tun} = \frac{1}{q}\frac{dJ_{Tun}}{d\psi} \cdot \nabla\psi = \frac{dJ_{Tun}}{d\varepsilon} \cdot \vec{E}, \vec{E} = -\nabla\psi, \epsilon = -q\psi \tag{2.41}$$

where $\vec{E}$, ϵ and ψ are the electric field, energy level and electrostatic potential respectively. The tunneling current from Silicon to Silicide metal and vice versa can be given in the following equation:

$$J_{Tun,S-M} = A^*T^2 \int_{\varepsilon}^{\infty} \Gamma(r) \ln \left[\frac{1}{1 + \exp\left((\varepsilon' - E_{fn}) / k_B T \right)} \right] d\varepsilon' \tag{2.42}$$

$$J_{Tun,M-S} = A^*T^2 \int_{\varepsilon}^{\infty} \Gamma(r) \ln \left[\frac{1}{1 + \exp\left((\varepsilon' - E_{fm}) / k_B T \right)} \right] d\varepsilon' \tag{2.43}$$

where $\Gamma(r)$ is the probability of the charge carrier to tunnel through the interface, $E_{fn} = -q\phi_n$ is the electron quasi Fermi level of Silicon layer, $E_{fm} = -q\phi_m$ is the Fermi level of the Silicide metal, A^* is the Richardson constant and T is the temperature in Kelvin [18]. The total or the net tunnelling current is given below in Eq. (2.44):

$$J_{Tun} = J_{Tun,S-M} - J_{Tun,M-S} \tag{2.44}$$

With Eq. (2.44), Eq. (2.41) can then be rewritten as:

$$G_{Tun}(r) = \frac{A^*T}{k_B} \vec{E} \Gamma(r) \ln \left[\frac{1 + \exp\left(-q\left(\psi - \phi_n \right) / k_B T \right)}{1 + \exp\left(-q\left(\psi - \phi_m \right) / k_B T \right)} \right] \tag{2.45}$$

The tunnelling probability is expressed by using the Wentzel-Kramers-Brillouin approximation, also known as the WKB method [18]. The tunneling probability $\Gamma(r)$ can then be given by Eq. (2.46):

$$\Gamma(r) = \exp \left[-\frac{2}{\hbar} \int_0^r \sqrt{2m\left(\phi_b/q + \phi_m - \psi(x) \right)} dx \right] \tag{2.46}$$

where m is the electron tunnel mass, ϕ_m is the metal work function of Silicide and ϕ_b is the barrier height of the interface between Silicide and Silicon. Once the tunnel generation rate is found, the term can be added to the continuity equation from the basic semiconductor equations to include tunnelling effects [18].

2.4.3. Band to Band Tunneling

In BBT method (also called inter-band tunnelling or zener tunnelling), the electrons/holes from one semiconductor material band-edge can tunnel through the forbidden states of the insulating layer and cross the other side of the insulating layer to a different band edge (CB-VB/VB-CB) of similar energy states of another semiconductor material. There are different models related to band to band tunneling given in literature, but we shall focus on few models that are have simple and accurate expression for the tunneling parameters [31, 45].

Simple band to band tunneling model proposed by J.J.Liou

This BBT method is based on the simplified version of Kane's tunnelling model [27] and Keldyshs's tunnelling model [28]. This model is time independent and uses Schrödinger equations in an environment with uniform electric field. This model's most striking flaw, when compared to sophisticated models, is that they anticipate a non-zero generation rate due to tunnelling even in equilibrium [30]. A simple illustration of BBT method can be shown in Fig 2.9 and its generic equation for the generation rate due to tunnelling can be given below in Eq. (2.47):

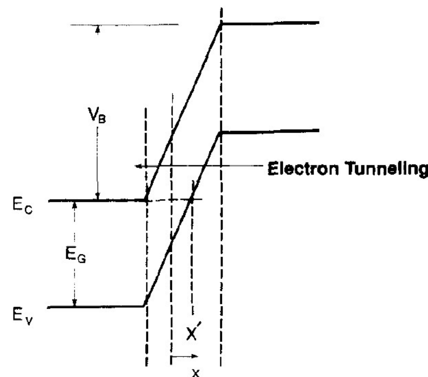

Figure 2.9: Simple BBT method [30].

$$G_{BBT-Simple} = AE^P \exp\left(-\frac{B}{E}\right) \tag{2.47}$$

where E is the electric field strength. Depending on the type of BBT tunneling (direct BBT or phonon-assisted BBT), the parameter P takes the values 1, 1.5 or 2. The coefficients A and B relate to the electron concentration with its tunnelling probability and the electric field properties at the tunnelling site and its values can be represented in the Table 2.1:

Table 2.1: Coefficients for the simple BBT model [30, 31]

P	A	B
1	1.1e27 $cm^{-2}s^{-1}V^{-1}$	2.13e7 Vcm^{-1}
1.5	1.9e24 $cm^{-1.5}s^{-1}V^{-1.5}$	2.19e7 Vcm^{-1}
2	3.4e21 $cm^{-1}s^{-1}V^{-2}$	2.26e7 Vcm^{-1}

Non-local band to band tunneling model
The band-to-band tunneling models presented so far in this section determine a recombination-generation rate at each point purely based on the local electric field value. As a result, they are referred to as local tunnelling models. One must account for the spatial variation of the energy bands in order to represent the tunneling process more precisely [27, 45]. One must also consider the fact that the generation and recombination of opposing carrier types do not occur in the same spatial location and can depicted in Fig 2.10 for a reverse biased pn junction where the tunneling mechanism is believed to be elastic [27, 45]. Tunneling current may be obtained at forward bias for degenerately doped p-n junctions, resulting in negative differential resistance in the forward I-V curve. Non-local BBT model can allow for modelling of this forward and reverse tunnelling currents [27, 45].

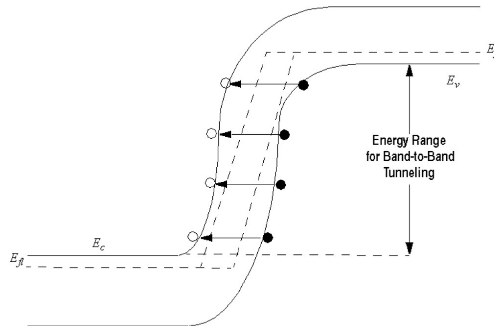

Figure 2.10: Non-local BBT method [27, 45].

We now that energy band profile dynamically determines the tunnelling path. This model also does not require the user to specify the non-local mesh. The tunnelling path is therefore determined with the following assumptions. The tunnelling path starts from the VB in the non-local active region. The path is then a straight line in the direction opposite to the VB gradient at the start point. The energy for tunnelling is equal to the VB energy at start point and is also equal to the CB energy plus band offset at the end point where the path ends at CB [31]. However, small modifications are made to consider both tunnelling scenarios (i.e if the tunnelling starts from VB or CB and ends at CB or VB respectively)

Let us consider a tunnelling path of length $2r$ starting from position $x = u$ and ending at position $x = l$ with $x = 0$ at the interface of tunnelling. holes are generated at the VB and electron generated at the CB. BBT processes include direct BBT or phonon-assisted BBT. The tunnelling process uses the same concept of Ieong's direct tunnelling model where we have a tunnelling probability based on WKB approximation [18, 31]. The probability of charge carriers tunnelling from conduction band CB to valence band VB and vice versa is given by the following equations:

$$\Gamma_{CV}(u,\varepsilon) = T_{CV}(l)T_{CV}(u)\left[\frac{-2}{\hbar}\int_0^u \sqrt{2m_c(r)\left|\varepsilon - E_{CB}(r)\right|}\Theta\left[\varepsilon - E_{CB}(r)\right]dr\right] \tag{2.48}$$

$$\Gamma_{VC}(u,\varepsilon) = T_{VC}(l)T_{VC}(u)\left[\frac{-2}{\hbar}\int_0^u \sqrt{2m_v(r)\left|E_{VB}(r) - \varepsilon\right|}\Theta\left[E_{VB}(r) - \varepsilon\right]dr\right] \tag{2.49}$$

where $T_{CV}(r)$ and T_{VC} are the transmission coefficients of tunnelling at position r from the interface. By default these are set to 1 when we know that tunnelling will happen. m_c and m_v are electron and hole tunnelling mass respectively at position r. ε is either the CB energy or VB energy on the other side of the barrier with respect to the CB or VB energy at position r [18, 31]. For Eq. 2.48 ε is the VB energy on the other side of the barrier while for Eq. 2.49 it is the CB energy on the other side of the barrier with respect to r. Θ is the heaviside function that outputs 1 if the argument is greater than 0 and outputs 0 if the argument is less than or equal to 0. This serves as a check if tunnelling from CB to VB or vice versa is possible or not. $\hbar$ is the dirac constant in eV. Finally the generation of electron in the CB or hole in the VB due to band to band tunnelling can be given from the following equations [18, 31]:

$$\begin{aligned} G_{CB} = {} & \frac{A\Gamma_{CV}}{2qk_B}\left[T_n(u) + T_p(l)\right]\left[\left|\frac{\partial E_{CB}(u)}{\partial u}\right|\Theta\left[\frac{\partial E_{CB}(u)}{\partial u}\right]\left|\frac{\partial E_{VB}(l)}{\partial l}\right|\Theta\left[\frac{\partial E_{VB}(l)}{\partial l}\right]\right] \\ & \times\left[\left[1 + \text{exp}\left(\frac{-q\left(E_{fn}(u) - \varepsilon\right)}{k_B T_n(u)}\right)\right]^{-1} - \left[1 + \text{exp}\left(\frac{-q\left(E_{fp}(l) - \varepsilon\right)}{k_B T_p(l)}\right)\right]^{-1}\right] \end{aligned} \tag{2.50}$$

$$\begin{aligned} G_{VB} = {} & \frac{A\Gamma_{VC}}{2qk_B}\left[T_p(u) + T_n(l)\right]\left[\left|\frac{\partial E_{VB}(u)}{\partial u}\right|\Theta\left[\frac{\partial E_{VB}(u)}{\partial u}\right]\left|\frac{\partial E_{CB}(l)}{\partial l}\right|\right] \\ & \times\left[\left[1 + \text{exp}\left(\frac{-q\left(\varepsilon - E_{fp}(u)\right)}{k_B T_p(u)}\right)\right]^{-1} - \left[1 + \text{exp}\left(\frac{-q\left(\varepsilon - E_{fn}(l)\right)}{k_B T_n(l)}\right)\right]^{-1}\right] \end{aligned} \tag{2.51}$$

where A is the effective Richardson constant, q is the elementary charge, k_B is the Boltzmann constant, $T_n(r)$ $T_p(r)$ are the temperature of the layer at position r from the interface [18, 31].

2.5. Conclusion

The objective of this chapter was to understand the modelling approach used in the ASA software. The fundamental electrical and for a typical solar cell simulation have been explained in this chapter. Additional electrical and optical models can be referred to from the ASA manual or from the Appendix A and B. The fundamental electrical models are necessary for the processing of the band energy diagram, electrostatic potential and electric field for a particular solar cell device.

The band energy diagram, electrostatic potential and electric field are then used for the Direct tunnelling model by Ieong et al [18], simple band to band tunnelling model [31] and non-local band to band tunnelling model [18, 31] as discussed above for which the generation rate due to tunnelling can be extracted and added to the continuity equations of Eq 2.2 and Eq 2.3 for electrons and holes respectively and achieve convergence for the final device performance (JV curve, Fill Factor etc).

3

ASA algorithm development for the tunnelling models

This chapter will focus on the second objective which is to design an algorithm that can run the tunnelling models as effectively as possible. Moreover, we would like to introduce a new implementation method that can automate these algorithms with minimal input requirements from the user. If properly done, the simulations can happen without the user having to specify the tunnelling requirements and the computer can decide that aspect without any difficulties. In the following sections, we shall discuss the algorithms used for the direct tunnelling process and the band to band tunnelling process (based on the models as discussed in Section B.1 and B.2). Please note that these algorithms needs to be processed after the poisson's simulation and before the continuity equation simulations (see Section 2.3) for proper convergence to be achieved.

3.1. Newly developed ASA algorithm for Direct tunnelling

For any algorithm, we have an input, the process and the output. The important input parameters for the direct tunnelling process is the layer thickness (entire device depth and thickness of each layer), the tunnelling mass (for electrons and for holes separately), the band energy values, the electrostatic potential values, the electric field values and finally the temperature. These inputs are directly related to the equations we have seen in the Section 2.4.2 and are stored in certain variables.

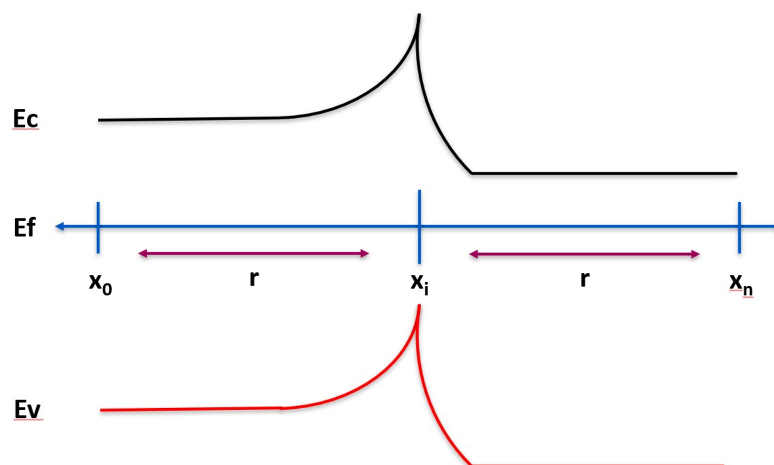

Figure 3.1: Illustration of band diagram vs device depth for the direct tunnelling process at the interface x_i.

The above figure will be used as a reference for the algorithm development. Please note that this figure is only for illustration purpose and does not represent any real device. The first step is identify-

ing the the interfaces (x_i) along the device length (grid points from x_0 to x_n) and calculating the band energy difference at ith and i+1 grid-point of CB or VB separately. It is noticed that the energy difference becomes large when moving towards the interfaces. This large energy difference constitutes to a barrier height ϕ_b (as per Eq. 2.46) and its interface location along the device is stored in a separate variable. The barrier height and its location is independent of the number of the grid-points along the device and will give the same result regardless.

The next step is to run a scan through the entire device for n number of times (ie. for n interfaces) with the help of two for loops as per C++ syntax. So for a sample device with 100 grid-points and 5 interfaces, the two for loops scans through all 100 grid points for 5 times resulting in the total number of simulation steps processed by the algorithm to be 500. At each device (grid-points) scan, certain conditions are checked to ensure smooth operation while checking for the tunnelling contributions in the device with respect to a particular interface x_i. Below are the following conditions:

1. If the current simulation grid point is before the interface grid-point x_i.
2. If the current simulation grid point is after the interface grid-point x_i.
3. If the current simulation grid point is exactly at the interface grid-point x_i.

If the current simulation grid point is before the interface grid-point x_i., the parameters related to the current grid-point (from Eq. 2.45 and Eq. 2.46) such as the tunnelling distance r (from the current grid point to the interface), barrier height ϕ_b for the interface x_i, the electric field E, the tunnel mass m and the fermi level ϕ_n are found and stored in separate variables. On the other hand, the fermi level ϕ_m is the fermi level on the other side of the interface (ie. in this case, the right hand side of the interface x_i) at the distance r. Its grid point will be twice the tunnelling distance r from the current grid point. This value is found and again stored in a separate variable. In addition, the electrostatic potential values from the current grid point to the interface are stored in a vector form since it will be used in the integration term with respect to $\psi(x)$ of the tunnelling probability Eq. 2.46. Trapezoidal integration method is used for the integration term in Eq. 2.46 and the calculation method for the tunnelling probability is done separately in a different function. Please note that a Richardson constant of 120 $A/cm^2/K^2$ was set as default based on the research by C.R. Crowell [9] and it is material dependent. The value can be modified from the code as per the user's device configuration. With all the necessary parameters available, the generation rate due to direct tunnelling at the current grid point as per Eq. 2.45 is calculated in a different function and the respective value is stored in a matrix for that particular grid point and interface.

If the current simulation grid point is after the interface grid-point x_i (as shown in Fig. 3.1), all the parameters discussed above (the tunnelling distance r, barrier height ϕ_b, electric field E, tunnel mass m, fermi level ϕ_n and electrostatic potential $\psi(x)$) are extracted at the current grid point with respect to the interface x_i. On the other hand, the fermi level ϕ_m, will be the fermi level at the other side of the interface (ie. in this case, the left hand side of the interface x_i) at twice the tunnelling distance r from the current grid point. If the current simulation grid point is exactly at the interface grid-point x_i, all the parameters including the fermi level ϕ_m are extracted at the current grid point. Here, the tunnelling distance r will be zero. Tunnelling probabilities for general device configurations ranges from 0-1 where at the interface, the maximum tunnelling probability of 1 can be achieved (as shown below in Fig. 3.2.a). Tunnelling generations on the other hand can vary depending on the strength of electric field and the energy of the barrier (as shown below in Fig. 3.2.b). In general, the the shape of the graphs for the tunnelling probabilities and tunnelling generation rate will look like as shown in Fig 3.2.

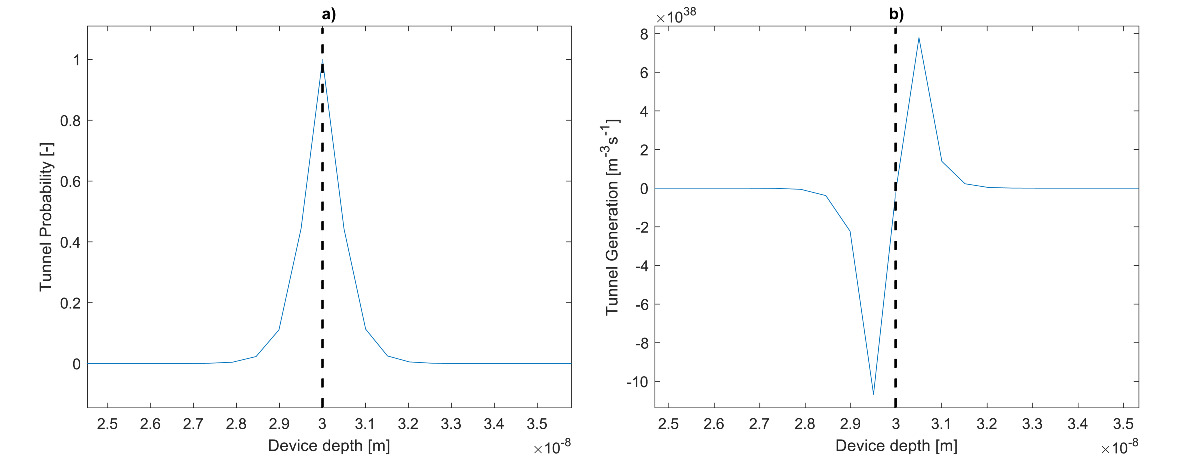

Figure 3.2: Illustration of direct a) tunnelling probability b) tunnelling generation rate as a function of device depth for a sample PN junction device with interface x_i at 30 nm depth of device without continuity in the band edges at the interface resulting in a slanted line of the tunnelling generation rate.

It is interesting to note that in Fig 3.2.b, when there is positive generation on one side of the barrier, there will always be negative generation (recombination) on the other side of the barrier. By the shape of the graph, one can know the direction of charge carrier tunnelling which in this case is towards the left hand side of the barrier.

In addition to the conditions mentioned previously, there are other conditions to consider to ensure error free calculations of the tunnelling contributions, these are:

1. If the grid points are continuous or discontinuous.
2. If the parameter extraction goes out of bounds.

For the first condition, a check on the continuity of the grid points is carried out at the interfaces between two layers. By continuity, we mean that the grid point at the interface will have parameters of both the layers taken into account. At the moment, the ASA software does not taken this continuity into consideration, hence we have a slanted shaped line in the tunnel generation rate at the interface as seen in Fig 3.2.b. However, the newly designed algorithm also takes continuity into consideration so that in the future if ASA is updated to take continuity into account, this algorithm will still work perfectly. This will result in a sharp vertical line in the tunnel generation rate as seen in the below Fig 3.3.b.

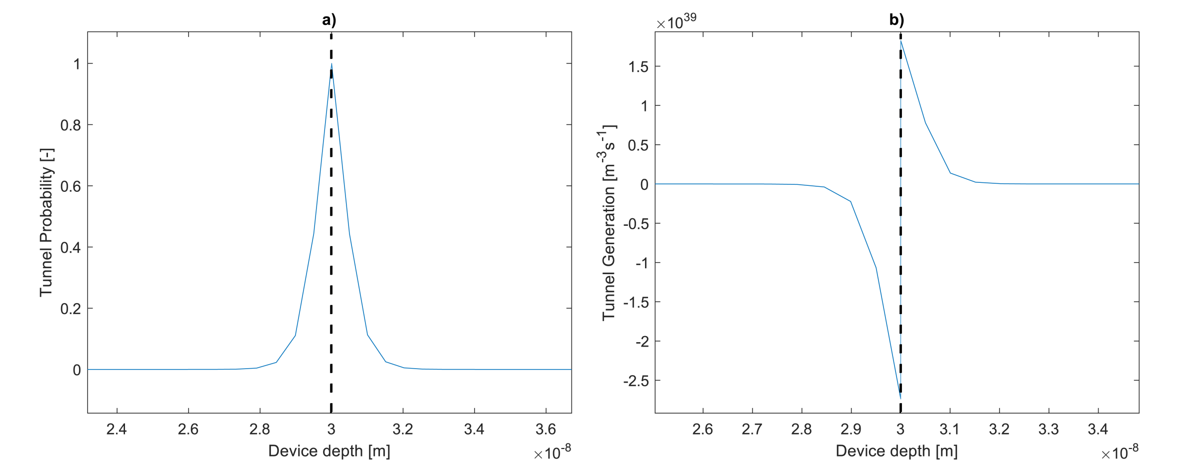

Figure 3.3: Illustration of direct a) tunnelling probability b) tunnelling generation rate as a function of device depth for a sample PN junction device with interface x_i at 30 nm depth of device with continuity in the band edges at the interface resulting in a sharp vertical line of the tunnelling generation rate.

The second condition is applied when the tunnelling parameters are extracted for the calculation of the tunnel generation. This is especially important for the fermi level on the other side of the barrier ϕ_m. There are cases where, at the current grid point, all the parameters are found except for the fermi level ϕ_m, due to no grid points existing on the other side of the barrier. This can happen if twice the tunnelling distance from the current grid point goes beyond the depth of the entire device resulting in no energy found. In that case, the fermi level ϕ_m is set to zero and the rest of the calculations are processed. This is important as the algorithm will generate an error if the fermi level ϕ_m is an empty variable.

The entire parameter extraction and calculations for the tunnel generation is done for every grid point and the process is repeated again for every interface. The reason is that each grid point has different tunnelling contribution and interacts differently for each interface along the device. The calculation is done for the conduction band and valence band separately since direct tunnelling is an intra-band tunnelling process. All the tunnel probabilities and the tunnel generation values are stored in a mxn matrix (m grid points and n interface), one for CB and one for VB.

Finally the generation rates of all the interfaces are added together for every grid-point and stored in a vector list which can be then printed as a final text file result with three columns (Depth x.....Generation rate CB.....Generation rate VB) and is later added to its respective continuity equations. A C++ code for this algorithm can be found in Appendix C for reference. A flowchart briefly explaining the algorithm can be shown in figure below:

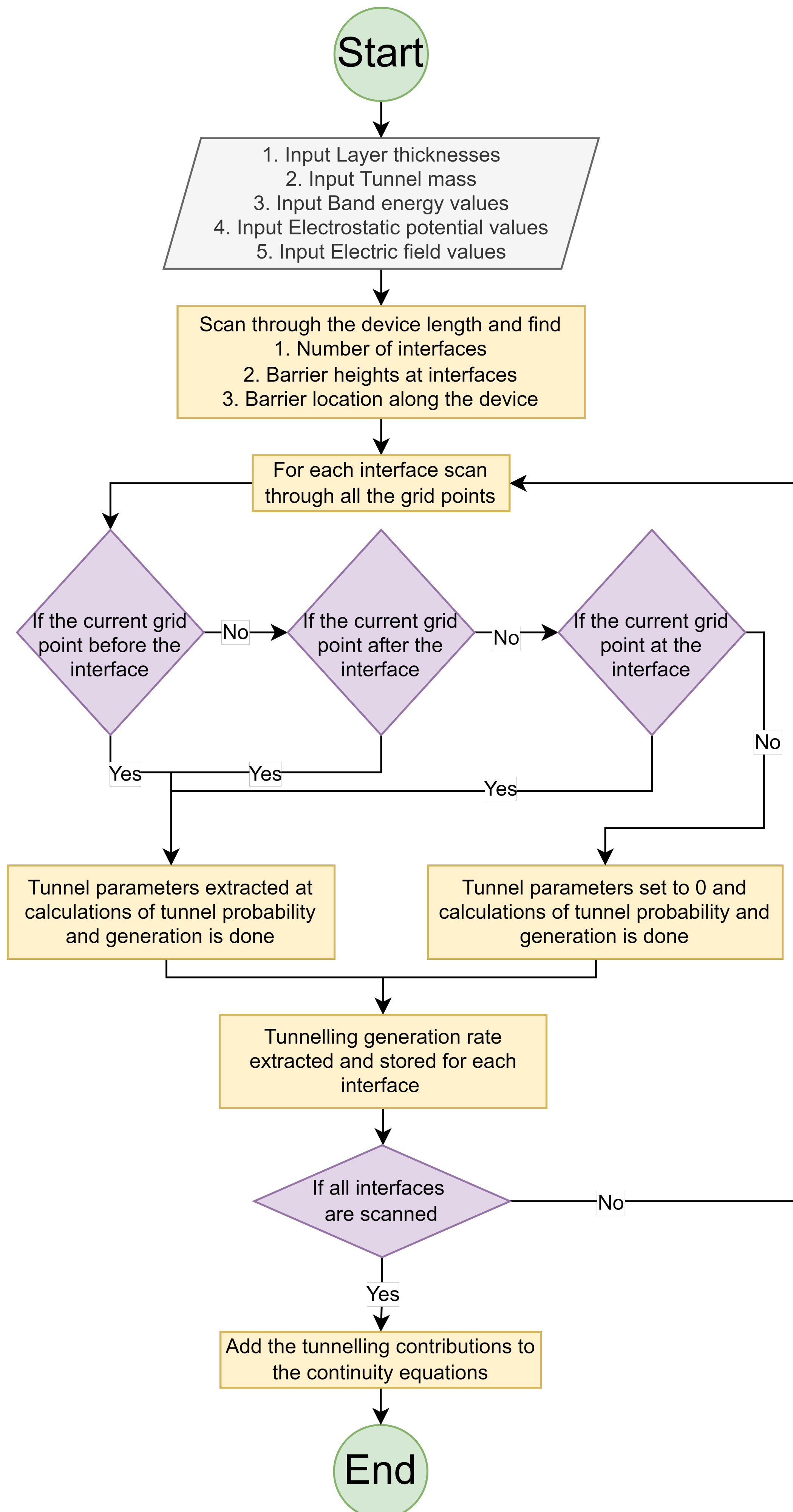
Start
1. Input Layer thicknesses
2. Input Tunnel mass
3. Input Band energy values
4. Input Electrostatic potential values
5. Input Electric field values
Scan through the device length and find
1. Number of interfaces
2. Barrier heights at interfaces
3. Barrier location along the device
For each interface scan through all the grid points
If the current grid point before the interface
No
If the current grid point after the interface
No
If the current grid point at the interface
No
Yes
Yes
Yes
Tunnel parameters extracted at calculations of tunnel probability and generation is done
Tunnel parameters set to 0 and calculations of tunnel probability and generation is done
Tunnelling generation rate extracted and stored for each interface
If all interfaces are scanned
No
Yes
Add the tunnelling contributions to the continuity equations
End

3.2. Newly developed ASA algorithm for band to band tunnelling

For the band to band tunnelling algorithm, the input parameters are the layer thickness (entire device depth and thickness of each layer), band energy values and the electric field values for the simple band to band model. If a non-local band to band model is used, then layer thickness (entire device depth and thickness of each layer), band energy values and the tunnelling mass for electrons and holes for each layer is required. These inputs are again directly related to the equations we have seen in the Section B.2 and are stored in certain variables.

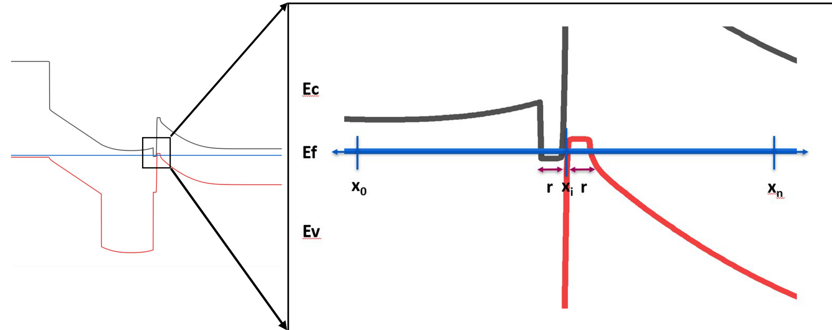

Figure 3.4: Illustration of band diagram vs device depth for the band to band tunnelling process at the interface x_i.

The above figure will be used as a reference for the algorithm development. Please note that this figure is only for illustration purpose and does not represent any real device. The first step is identifying the the interfaces (x_i) along the device length(grid points from x_0 to x_n).

Just like the newly developed algorithm for direct tunnelling, the next step is to run a scan through the entire device for n number of times (ie. for n interfaces) with the help of two for loops as per C++ syntax. So for a sample device with 100 grid-points and 5 interfaces, the two for loops scans through all 100 grid points for 5 times resulting in the total number of simulation steps processed by the algorithm to be 500. At each device (grid-points) scan, certain conditions are checked to ensure smooth operation while checking for the band to band tunnelling contributions in the device with respect to a particular interface x_i. Below are the following conditions:

1. If the current simulation grid point is before the interface grid-point x_i.
2. If the current simulation grid point is after the interface grid-point x_i.
3. If the current simulation grid point is exactly at the interface grid-point x_i.

However unlike the direct tunnelling process (or intra-band tunnelling process), band to band tunnelling process involves charge carrier tunnelling from either valence band on one side of the interface to the conduction band on the other side of the interface and vice versa. Additionally, for the band to band tunnelling to take place, the charge carrier transport should happen at the same energy level. Hence, the additional conditions which are taken into account are:

1. If the CB energy at the current simulation grid point from the interface x_i is less than or equal to the VB energy on the other side of the interface x_i.
2. If the VB energy at the current simulation grid point from the interface x_i is greater than or equal to the CB energy on the other side of the interface x_i.

If the CB energy at the current simulation grid point from the interface x_i is less than or equal to the VB energy on the other side of the interface (twice the tunnelling distance r from the current grid point), tunnelling will happen from the CB to the VB at the same energy level. If simple band to band tunnelling is used (see Section 2.4.3), electron generation rate will be calculated using Eq. 2.47. If non-local band to band tunnelling model is used (see Section 2.4.3), the tunnel probability and the tunnel generation rate from the CB to VB will be calculated using Eq. 2.48 and Eq. 2.50 respectively.

If the VB energy at the current simulation grid point from the interface x_i is greater than or equal to the CB energy on the other side of the interface, tunnelling will happen from the VB to the CB at the

same energy level. If simple band to band tunnelling is used, hole generation rate will be calculated using Eq. 2.47. If non-local band to band tunnelling model is used, the tunnel probability and the tunnel generation rate from the VB to CB will be processed using Eq. 2.49 and Eq. 2.51 respectively. If none of the conditions above are satisfied, the tunnel probability and the tunnel generation values are set to zero.

These above additional conditions is checked after the current simulation grid point conditions are checked. If the current simulation grid point is before the interface grid-point x_i, the necessary parameters for the band to band tunnelling are extracted. For the simple band to band tunnelling model, the electric field E at the current grid point are extracted. For the non-local band to band tunnelling, parameters such as the band energy values, tunnelling distance r (from the current grid point to the interface), tunnel mass m and the electron and hole fermi levels $E_{fn}(u)$ and $E_{fp}(u)$ at the current grid point are found and stored in separate variables. The fermi levels $E_{fn}(l)$ and $E_{fp}(l)$ are the electron and hole fermi level respectively on the other side of the interface (right hand side of the interface grid point x_i in this case) at the distance r. Its grid point will be twice the the tunnelling distance r from the current grid point. In addition, the band energy values from the current grid point to the interface are stored in a vector form since it will be used in the integration term with respect to $E(r)$ of the tunnelling probability Eq. 2.48 and Eq. 2.49. Trapezoidal integration method is used for the integration term in Eq. 2.48 and Eq. 2.49 and the calculation method for the tunnelling probability is done separately in a different function. Please note that a Richardson constant of 120 $A/cm^2/K^2$ was chosen again as default based on the research by C.R. Crowell [9] and it is material dependent. The value can be modified from the code as per the user's device configuration. Another important term to consider is the gradient of the band energies $\frac{\partial E_{CB}(x)}{\partial x}$ and $\frac{\partial E_{VB}(x)}{\partial x}$ from Eq. 2.50 and Eq. 2.51 of the non-local tunnel generation rate where x is either the current grid point or the grid point at twice the tunnelling distance from the current grid point. Its value is calculated based on the following equation.

$$\frac{\partial E(x)}{\partial x} \approx \text{Lim}_{\Delta x \to 0} \frac{E(x_{i+1}) - E(x_{i-1})}{\Delta x} \quad ; \Delta x = x_{i+1} - x_{i-1} \tag{3.1}$$

With all the necessary parameters available, the generation rate due to non-local band to band tunnelling at the current grid point as per Eq. 2.50 and Eq. 2.51 is calculated in a different function and the respective value is stored in a matrix for the particular grid point and interface.

If the current simulation grid point is after the interface grid-point x_i, all the parameters discussed above that are extracted are of the current grid point with respect to the interface x_i except for the electron and hole fermi levels $E_{fn}(l)$ and $E_{fp}(l)$ and the band energy gradient $\frac{\partial E(l)}{\partial x}$ which is used for the non-local band to band tunnelling model. Here, the fermi levels $E_{fn}(l)$ and $E_{fp}(l)$ and the band energy gradient $\frac{\partial E(l)}{\partial x}$ values correspond to the grid point at the other side of the interface (ie. the left hand side) at twice the tunnelling distance r from the current grid point. If the current simulation grid point is exactly at the interface grid point x_i, all the parameters extracted are of the current grid point including the fermi levels and the band energy gradient. In this case, the tunnelling distance r will be zero. Tunnelling probabilities for general device configuration ranges from 0-1 where at the interface, the maximum tunnelling probability of 1 can be achieved. Tunnelling generations on the other hand can vary depending on the strength of electric field (if simple band to band tunnelling model is used) or the band energy gradient of the barrier (if non-local band to band tunnelling model is used). In general, the the shape of the graphs for the tunnelling generation rate will look like as shown in Fig 3.5.

As seen in Fig 3.5, The generation rate of electron increases from the point where the CB is lower than or equal to VB (as per Fig 3.4) towards the interface. On the other side of the interface, recombination rate of electrons (generation rate of holes) increases towards the interface where VB is greater than or equal to CB. In between the two band edges, no generation rate is noticed as this region consists of forbidden states resulting in no charge carrier generation or recombination. Apart from the conditions discussed above, there are other conditions to consider to avoid unexpected errors. These are:

1. If the grid points are continuous or discontinuous.
2. If the parameter extraction goes out of bounds.
3. If the tunnelling distance is too large or unrealistic.

4. If the fermi levels are zero.

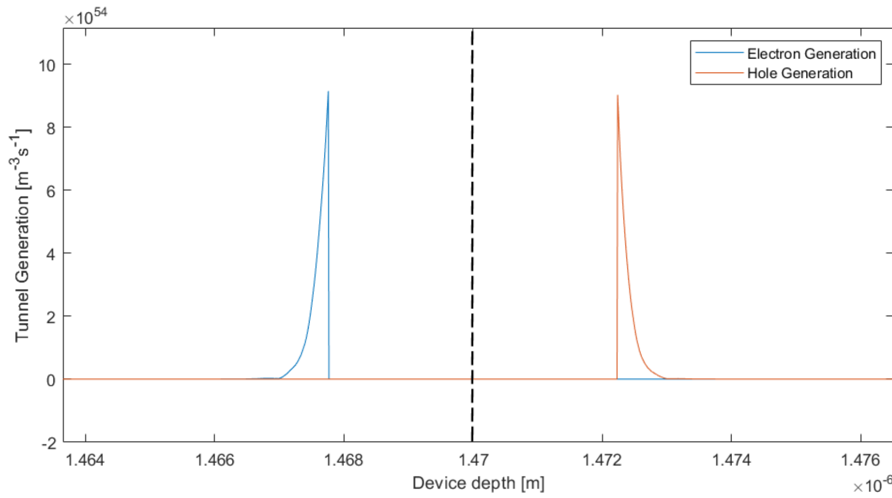

Figure 3.5: Illustration of band to band tunnel generation rate as a function of device depth for a sample perovskite/silicon tandem device with tunnel junction interface x_i at 1.47μm depth of device. Forbidden band states are present in between the band edges of VB and CB resulting in zero tunnel generation rate.

For the first condition, a check on the continuity of the grid points is carried out at the interfaces between two layers. But this will not have any effect on the band to band tunnelling generation since there are forbidden states at the tunnel junction interface as seen in Fig 3.5.

The second condition is applied when the tunnelling parameters are extracted for the calculation of the tunnel generation. If the parameters cannot be found due to grid point going beyond the device depth, those parameters are set to zero and the rest of the calculations are processed.

The third condition is with respect towards the band to band tunnelling distance. There are cases where for a certain interface, the conduction band energy on one end of the device is lower than or equal to the valence band energy on the other end of the device. In reality, these layers can not take part in the band to band tunnelling process but the calculation for the tunnel generation will still be carried out. the tunnelling probability will be low, but it will still result in a finite value. In this condition, the max tunnelling distance from the interface is set to 100 nm, so that if such unexpected conditions occur, the algorithm will set the tunnelling probabilities and the tunnelling generation rates to zero and skip unnecessary calculations, thereby improving simulation speed.

The fourth condition is with respect towards the fermi levels $E_{fn}(x)$ and $E_{fp}(x)$ for the band to band tunnelling generation Eq. 2.50 and Eq. 2.51. There are cases where for certain grid points, both $E_{fn}(x)$ and $E_{fp}(x)$ of the current grid point and the grid point on the other side of the interface is zero. This results in the tunnel generation to be zero which is not true. In reality, its value will be finitely small. If such a condition occurs, the fermi level energies are set by the algorithm to a minimum value of +/-7.3475918173e-16, which is chosen based on the minimum value of the fermi level seen in most simulations in ASA. With these values all the calculations for the tunnel generations are then performed.

The entire parameter extraction and calculations for the tunnel generation is done for every grid point and the process is repeated again for every interface. The reason is that each grid point has different tunnelling contribution and interacts differently for each interface along the device. This is done for the conduction band and valence band together since band to band tunnelling is an inter-band tunnelling process. All the tunnel probabilities and the tunnel generation values are stored in a mxn matrix (m grid points and n interface), one for CB and one for VB.

Finally the generation rates of all the interfaces are added together for every grid-point and stored in a vector list which can be then printed as a final text file result with three columns (Depth x.....Generation

rate CB.....Generation rate VB) and added to its respective continuity equations. A C++ code for this algorithm can be found in Appendix D for reference. A flowchart briefly explaining the algorithm can be shown in figure below:

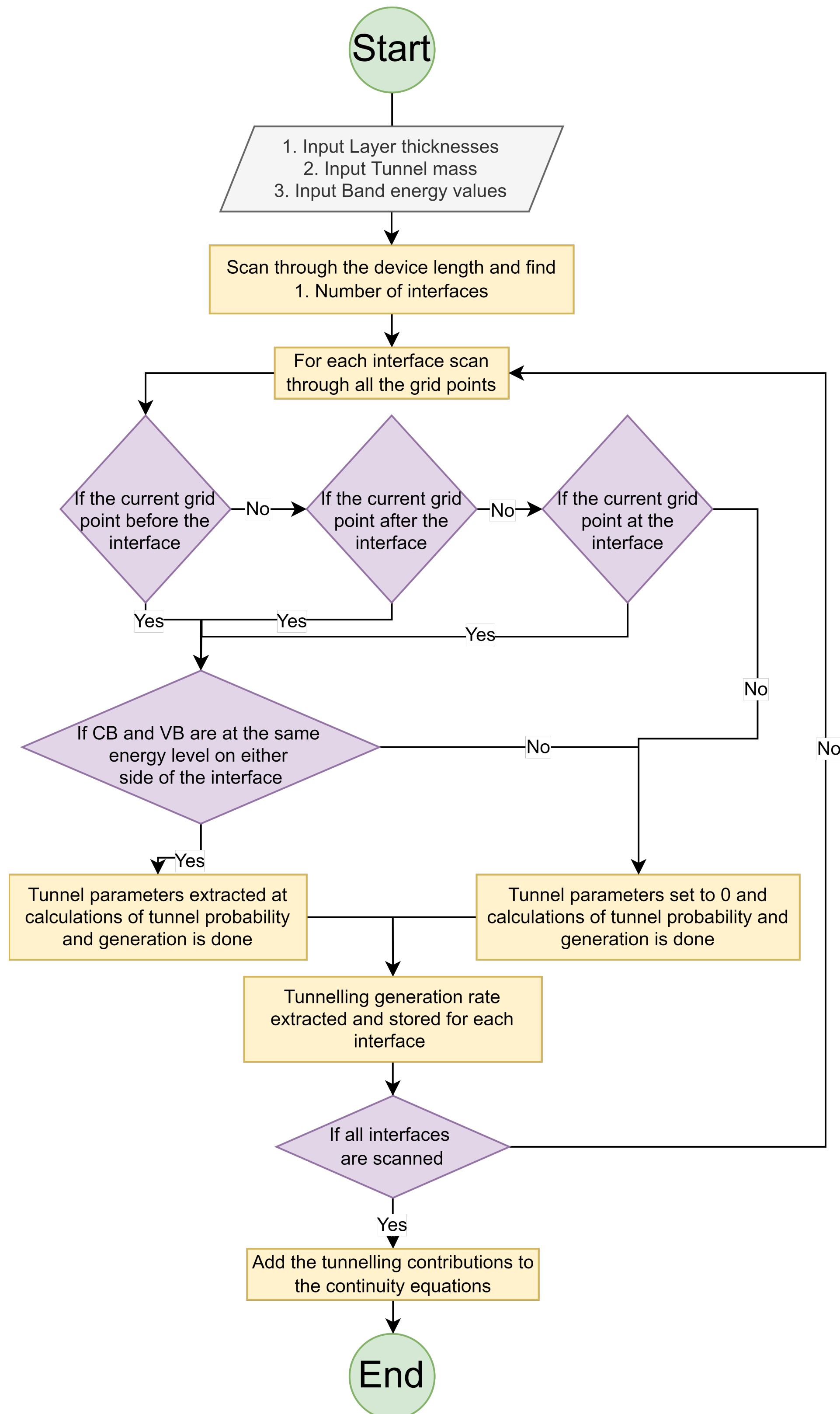

3.3. Conclusion

The objective of this chapter was to develop and automated system for the tunnelling models discussed in the previous chapter. A fully fledged algorithm was designed for the automation of the direct tunnelling and the band to band tunnelling process with limited input from the user while using the models as seen in Section 2.4. In simple terms, the algorithm takes in the required input and scans through the device length for each interface and check for tunnel contributions and performs calculations when necessary. All necessary conditions are included inside the algorithms to ensure that the simulation is accurately solved.

A C++ code for the above algorithm can be found in Appendix C and D. These codes can be run both externally and then incorporated into ASA or can be directly be included in the ASA source code. We shall begin with the validation of the newly developed algorithms in the next chapter.

4 ASA validation of the tunnelling models

With the newly developed algorithms for the tunnelling models in the previous chapter, we shall now focus on the third objective of this thesis project which is to validate the newly developed algorithms for various device architectures and to verify the performance results seen in literature or simulations performed in other software suites. A comparison is made between the JV curve obtained from the newly developed algorithms and the JV curve obtained from other external results in literature or other external simulations.

4.1. Validation of direct tunnelling using a PN junction

The PN junction device that we are going to validate is based on the parameters used by Cleef et.al. [7]. The device consist of the p-doped hydrogenated amorphous silicon as the top layer and n-doped crystalline silicon as the bottom layer sandwiched between tin oxide TCO layer and aluminium back contact. The device diagram is given in the figure below.

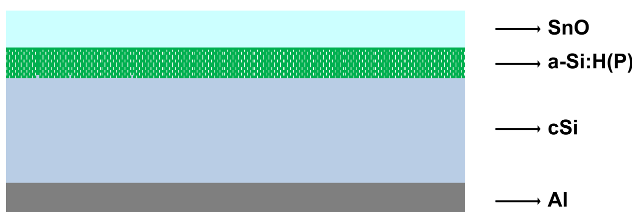

Figure 4.1: Device structure of a simple PN device [7].

The necessary parameters for the device simulation can be given in the table below. The ASA input file for this simulation can be referred to in Appendix E.1.

Table 4.1: PN junction electrical parameters [7].

Parameters	**SnO (TCO)**	**a-Si:H (p type)**	**c-Si (n type)**	**Al (Back contact)**
Thickness (m)	70e-9	30e-9	250e-6	300e-9
Bandgap (eV)	3.5	1.98	1.124	-
Electron affinity (eV)	4	3.62	4.05/3.95	-
N_c ($m^{-3}eV^{-1}$)	2.2e26	2e26	2e26	-
N_v ($m^{-3}eV^{-1}$)	2.2e25	2e26	2e26	-
Dielectric constant (ε_r)	9	11.9	11.8	-
Doping (donor/acceptor) (m^{-3})	1e26/0	0/1.035e25	1.0e22/0	-
Mobility (μ_e/μ_h)(m^2/Vs)	20e-4/10e-4	10e-4/10e-4	0.13/0.04	-
Electron/Hole Lifetime (τ_n/τ_p)(s)	1e-6/1e-5	-	10e-4/10e-4	-

Since all the layers simulated are flat, the device was simulated using GenPro-1 optical model with the front and back contact set as ohmic. It is important to note that the electron affinity values of the n-doped crystalline silicon layer were modified from 4.05 eV (Reference case χ=4.05 eV) to 3.95 eV (1st case χ=3.95 eV). As a result, the barrier height peak at the valence band between the p-type and the n-type layer increases as shown in the band diagram in Fig 4.2. The electron affinity for the reference case was chosen to be 4.05 eV since any value above or below 4.05 eV can significantly reduce the fill factor FF due to poor charge carrier transport.

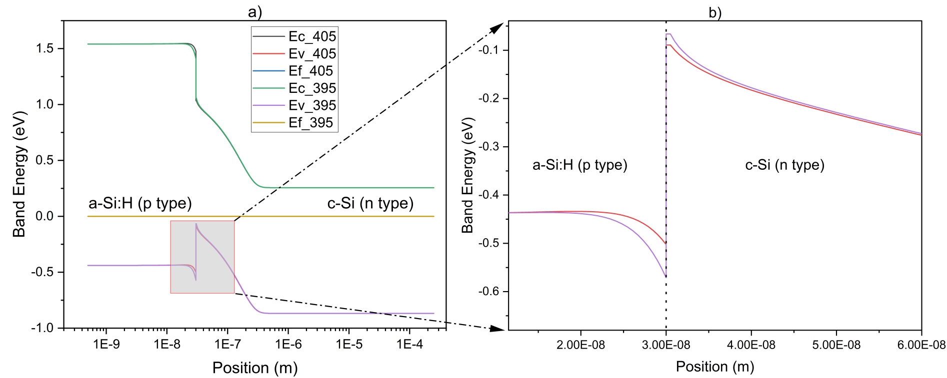

Figure 4.2: a)Band energy diagram with respect to the position of a simple PN device consisting of conduction band Ec, valence band Ev and fermi level Ef for χ=4.05eV and χ=3.95eV b)Enlarged section of the valence band barrier height at the interface of the PN junction (marked with dotted lines) resulting in tunnelling effects.

An increase in barrier height means that the charge accumulates more at the interface with less movement across resulting in a lower JV curve (χ=3.95 w/o DT tunn) as seen in Fig 4.3. However, with sufficient energy, the charge carriers can tunnel through the PN junction and the reference case JV curve can be mostly recovered. The DT algorithm was then processed for this device configuration. The tunnel generations were added to the continuity equations and the JV curve and other performance results were extracted. Please note that all comparison of the JV curves are made with respect to the reference case since this gives the maximum FF. The logic follows that any change in the electron affinity will change the barrier height affecting the charge transport and eventually resulting in a different JV curve. But due to charge carrier tunnelling and thermionic emission, the charge carrier transport is not hindered as compared to the reference case.

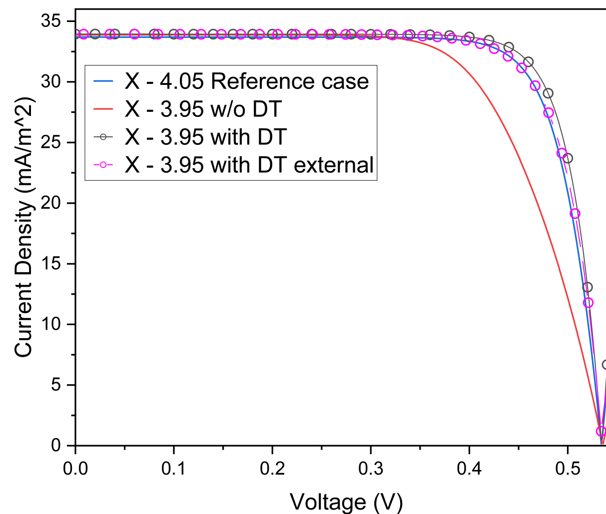

Figure 4.3: JV curve of the PN junction with and without direct tunnelling for the first case of χ=3.95 eV. The newly developed automated DT model shows good agreement with the reference case χ=4.05 eV and the external DT model resulting in similar current voltage characteristics.

As seen in the Fig 4.3, the JV curve including the newly developed DT model for the first case (χ=3.95 eV) follows the reference case scenario (χ=4.05 eV) almost perfectly with the similar short circuit current density J_{SC} and open circuit voltage V_{OC}. There is however a 2% difference between the reference case fill factor FF and the first case with DT fill factor (with slightly higher FF than the former). This is considering the fact that tunnelling for the reference case was not considered initially and in reality, slightly more charges can tunnel through the barrier of the reference case scenario. However, the algorithm is accurate and the result is very close to the realistic values. This is also validated using external result obtained from a direct tunnelling subroutine made by PVMD group member C.M Ruiz in which the tunnelling contributions were fitted to the experimental results as reported by Cleef et al. via a Gaussian function [7]. Its tunnelling contribution was then manually added to the continuity equations. Its respective JV curve was then obtained given under χ - 3.95 with DT external in Fig. 4.3. A good agreement is shown with the algorithm generated tunnel generation and the external subroutine made by the PVMD group member C.M Ruiz. The table below summarizes the performance results for each of the cases presented.

Table 4.2: PN junction performance with and without direct tunnelling.

Parameters	Voc (V)	Isc (mA/cm^2)	FF	Efficiency (%)
Reference case χ=4.05 eV	0.534	33.70	0.789	14.2
First case χ=3.95 eV without DT	0.536	33.88	0.676	12.2
First case χ=3.95 eV with DT	0.534	33.93	0.801	14.5
First case χ=3.95 eV with external DT	0.533	33.92	0.78	14.1

4.2. Validation of direct tunnelling using a Silicon hetero-junction

Another validation for the direct tunnelling was commenced for the silicon heterojunction device (or SHJ device). The device architecture is based on a PIN configuration where the crystalline silicon is sandwiched between p-doped hydrogenated amorphous silicon and n-doped hydrogenated amorphous silicon. Intrinsic hydrogenated amorphous silicon is added in between the doped amorphous and crystalline silicon layer for improved surface passivation. The device also includes silicon nitride as anti-reflective coating, tin oxide and TCO layer and aluminium as back contact. The device architecture is based on the parameters used by Varache et al. [38, 48]. The device diagram is given in the figure below.

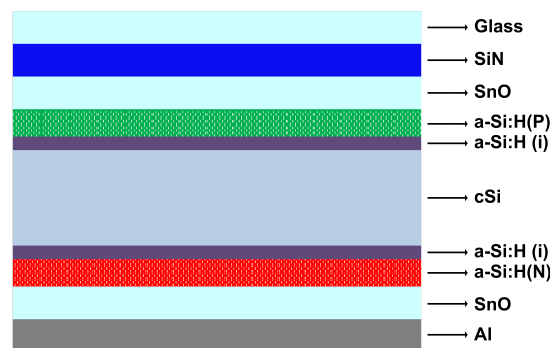

Figure 4.4: Device structure of a simple SHJ device [38].

The necessary parameters for the device simulation can be given in the table 4.3. The ASA input file for this simulation can be referred to in Appendix E.2.

Table 4.3: SHJ junction electrical parameters [48, 38].

Parameters	SnO (TCO)	a-Si:H (p type)	i-a-Si:H	a-Si:H (n type)	c-Si (n type)	Al (Back contact)
Thickness (m)	80e-9	20e-9	5e-9	20e-9	170e-6	300e-9
Bandgap (eV)	3.5	1.7	1.7	1.7	1.124	-
Electron affinity (eV)	4	3.9	4.0	3.0	4.0	-
N_c ($m^{-3}eV^{-1}$)	2.2e26	2e26	2e26	2e26	2.8e25	-
N_v ($m^{-3}eV^{-1}$)	2.2e25	2e26	2e26	2e26	2.8e25	-
Dielectric constant (ε_r)	9	11.9	11.9	11.9	11.8	-
Activation doping energy (eV)	-	0.3	-	0.15	-	-
Doping (m^{-3})	1e26/0	-	-	-	5e21	-
Mobility (μ_e/μ_h)(m^2/Vs)	20e-4/10e-4	1e-3/5e-4	2e-3/1e-3	1e-3/5e-4	0.13/0.04	-
CBT slope (meV)	-	20	20	20	-	-
VBT slope (meV)	-	15	15	15	-	-
Electron/Hole Lifetime (τ_n/τ_p)(s)	1e-6/1e-5	-	-	-	10e-3/10e-3	-
Auger coefficients (electons/holes) (m^6s^{-1})	-	-	-	-	2.2e-43/9.9e-43	-

The device architecture is entirely flat, hence GenPro-1 optical model is used for the simulation of the device with the front and back contact set to ohmic. Glass (0.1 mm) and SiN (70 nm) are purely optical layers so we do not include the electrical parameters in the simulation. The simulation for these parameters is carried out and a band diagram is extracted as shown in Fig 4.5. As seen in Fig 4.5, potential barriers or spikes can be noticed at the interfaces for both CB and VB. These barriers can result in potential direct tunnelling effect of charge carriers across the interfaces.

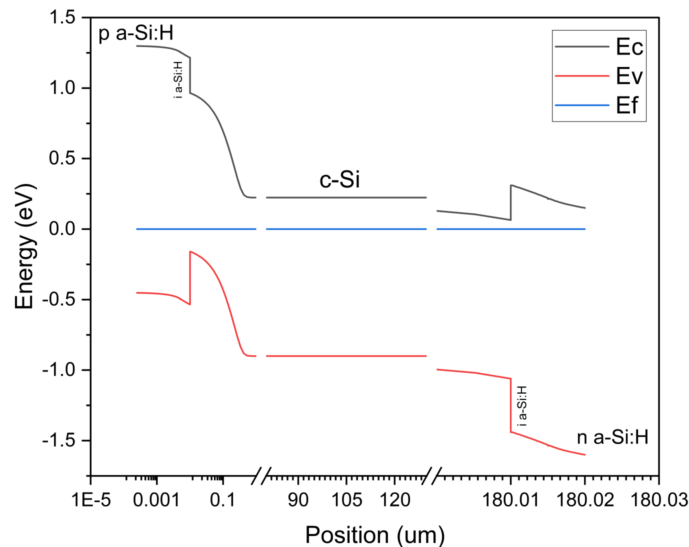

Figure 4.5: Band energy diagram with respect to the position of a simple simple SHJ device consisting of conduction band Ec, valence band Ev and fermi level Ef for each of the layers given in text. Visible barrier heights in the bands leads to tunnelling effects in the device [48, 38].

Presented below are the JV curves for three cases, first being the base case of the simulation of the SHJ without direct tunnelling effect taken into account. In the second case, we present the JV curve where the newly developed direct tunnelling algorithm is applied to the SHJ simulation. To verify the algorithm, an external direct tunnelling subroutine created by PVMD group member C.M Ruiz in which the tunnelling contributions were fitted to the experimental results as reported by Varache et al. [48] via a Gaussian function. Its tunnelling contribution was then manually added to the continuity equations and the JV curve obtained is presented in the third case. Please note that all comparison of the JV curves are made with respect to the third case since the JV curve in the third case directly correlates with the experimental results.

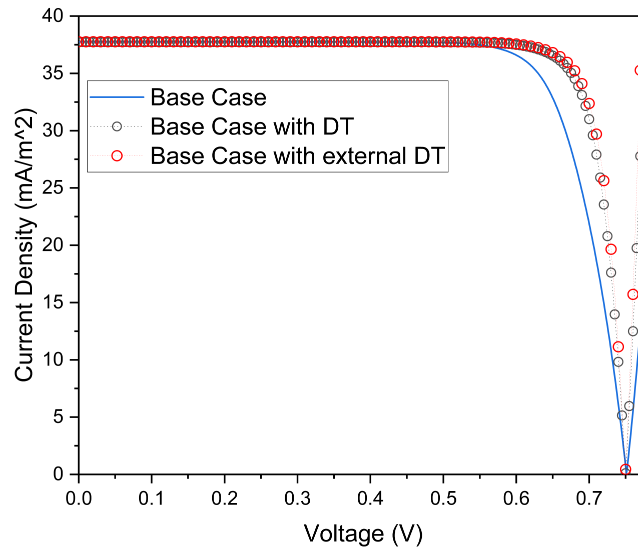

Figure 4.6: JV curve of the Silicon hetero-junction with and without direct tunnelling. The newly developed DT algorithm applied on the base case is in good agreement with the external DT subroutine resulting in similar current voltage characteristics.

As seen in Fig 4.6, the automated direct tunnelling algorithm is in good agreement with the external direct tunnelling subroutines ensuring accuracy of the model and algorithm for the direct tunnelling. The short circuit current density J_{SC} and open circuit voltage V_{OC} is almost the same for the base cases with DT. The difference in the FF noticed is about 1% which is considered acceptable for validation. The table below summarizes the performance results for each of the cases presented.

Table 4.4: Silicon hetero-junction performance with and without direct tunnelling.

Parameters	**Voc** (V)	**Isc** (mA/cm^2)	**FF**	**Efficiency (%)**
Base case without DT	0.7512	37.74	0.7806	22.13
Base case with DT	0.7499	37.74	0.8422	23.83
Base case with external DT	0.7497	37.76	0.8512	24.1

4.3. Validation of band to band tunnelling using a Pvk/cSi tandem

We shall now validate the newly developed band to band tunnelling model. We used the non-local band to band tunnelling model for the validation purpose. The device architecture taken into account for the validation purpose is the perovskite silicon tandem device. It is based on the nip-nip configuration developed at HZB by Al-Ashouri et al. [4]. The perovskite top cell consist of SnO_2 and PTAA as ETL and HTL respectively. In between SnO_2 and the perovskite absorber, C_{60} is used for effective surface passivation and charge carrier transport between the layer.

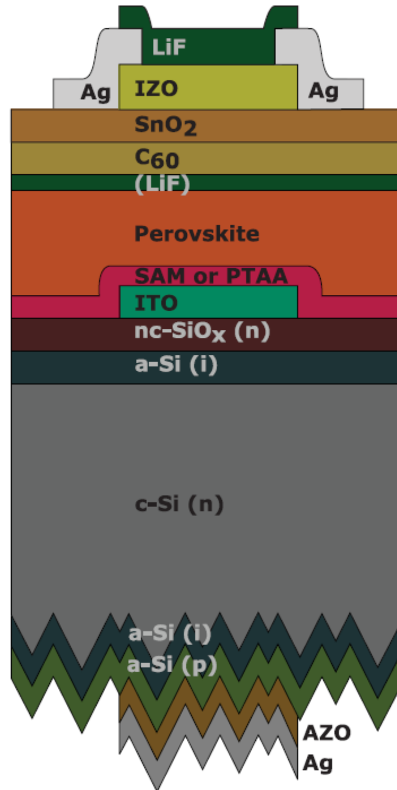

Figure 4.7: Pvk/c-Si architecture developed at HZB, Germany [4].

The device structure uses PTAA instead of SAM as the hole transport layer for simulation purpose due to the availability of the optical data (complex refractive index data) of PTAA. In addition, the device has textured layers below the crystalline silicon layer. The rest of the layers are flat. We shall use the GenPro-4 optical model to commence the optical simulation of the device structure and obtain the generation profile which then is imported into the ASA software to couple optical and electrical simulation. The input parameters for the device structure used by both GenPro-4 and ASA can be tabulated in the table given below. Please note that this paper focuses on the experiment of the tandem device with efficiencies greater than 29% by using the SAM layer having an overall tandem efficiency of 29.15%. However, the paper also reports the tandem efficiency of about 26.79% when PTAA is used. Hence data extraction and comparison is made when the PTAA layer is used.

Table 4.5: Pvk/cSi tandem electrical parameters by Al Ashouri et al. [4]

Parameters	**IZO (TCO)**	**SnO_{2} (ETL)**	**C_{60} (ETL)**	**Perovskite**	**PTAA (HTL)**	**ITO (TRJ)**	**nc-SiO_{x} (n++)**	**i-aSi:H (front/back)**	**c-Si (n type)**	**p-aSi:H (p++)**	**AZO (TCO)**
Thickness (m)	85e-9	5e-9	7e-9	532e-9	23e-9	63e-9	111e-9	9e-9/6e-9	300e-6	12e-9	55e-9
Bandgap (eV)	3.5	3.5	2	1.68	3.0	3.65	1.7	1.75	1.124	1.75	3.5
Electron affinity (eV)	4.65	4	3.9	3.9	2.5	4.8	3.9	3.8	4.05	3.8	4.65
N_c $(m^{-3}eV^{-1})$	2.2e24	2.2e24	8e25	4.42e23	2.2e24	5.8e24	2e26	2e26	2.86e25	2e26	2.2e24
N_v $(m^{-3}eV^{-1})$	1.8e25	1.8e25	8e25	8.47e24	1.8e25	1e24	2e26	2e26	3.1e25	2e26	1.8e25
Dielectric constant (ε_r)	9	9	4.2	6.5	3	8.9	11.9	11.9	11.8	11.9	9
Doping (m^{-3})	0	2e25	2.6e24	2e16	3e24	1e26	2.5e26	0	1e22	2e26	1e26
Mobility $(\mu_e/\mu_h)(m^2/Vs)$	100e-4/ 25e-4	100e-4/ 10e-4	0.08e-4/ 0.0035e-4	1.62e-4/ 1.62e-4	0.002e-4/ 0.00015e-4	10e-4/ 10e-4	10e-4/ 2e-4	20e-4 /5e-4	1300e-4/ 400e-4	10e-4/ 1e-4	100e-4/ 25e-4
Electron/Hole Lifetime $(\tau_n/\tau_p)(s)$	-	1e-5/ 1e-6	1e-9/ 1e-9	2.88e-7/ 2.88e-7	1e-9/ 1e-9	1e-6/ 1e-6	1e-6/ 1e-6	-	10e-3/ 10e-3	1e-6/ 1e-6	-

We shall first look at the condition where all the layers are initially flat to demonstrate the effect of flat and textured interface on the tandem photocurrent. The GenPro-4 simulations are then conducted and the absorptance profile and the tandem photocurrent for the device can be extracted and is depicted

in Fig. 4.8.

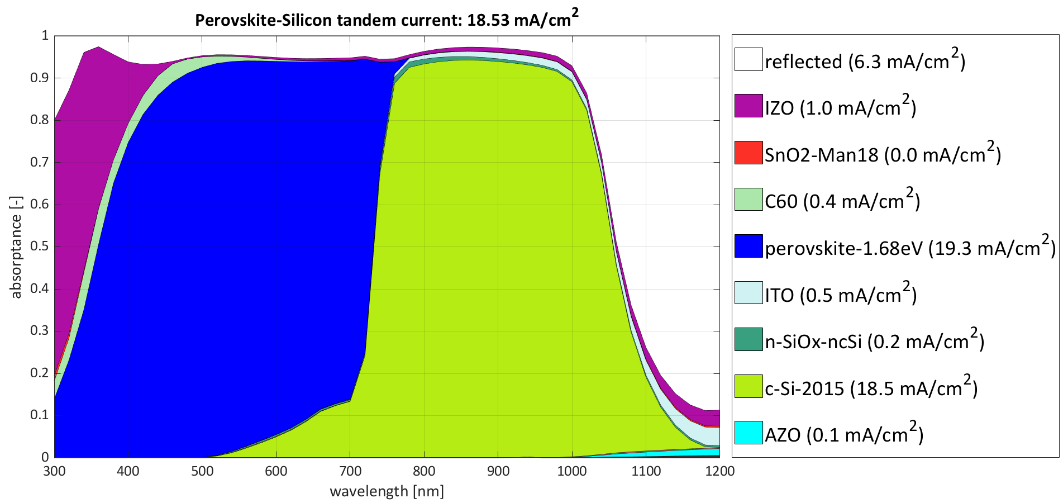

Figure 4.8: Absorptance profile for a entirely flat Pvk/cSi device. [4, 41].

As seen in Fig. 4.8, majority of the light absorption losses are seen in the infrared region where the bottom cell is unable to absorb a percentage of light incident on it. As per Al-Ashouri et.al. [4], the layers below the crystalline silicon is textured to trap light and reflect it back into the silicon sub-cell. With textures, light absorption is improved and can be seen in the increased photo-current in the silicon sub-cell as depicted in Fig. 4.9.

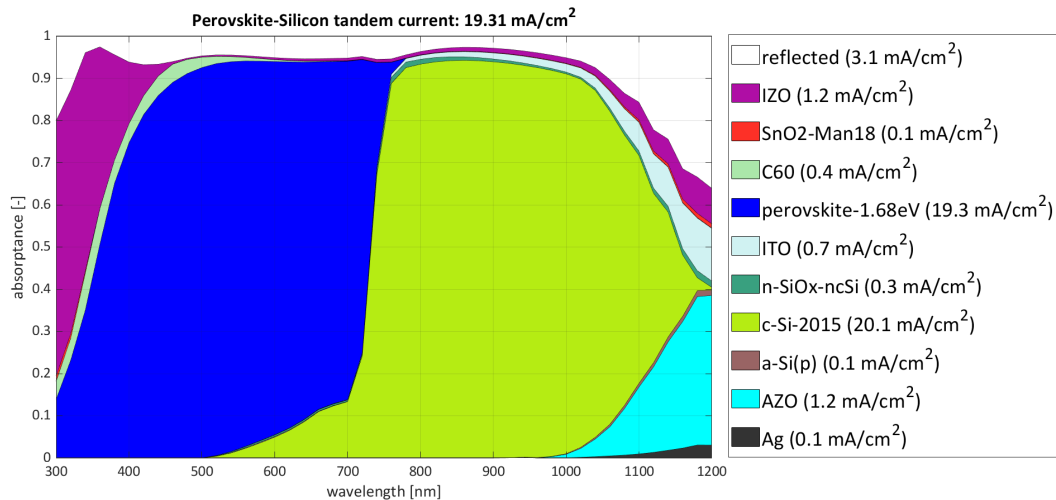

Figure 4.9: Absorptance profile for a bottom textured Pvk/cSi device. As compared to the flat absorptance profile as seen in Fig. 4.8, a higher tandem photocurrent is obtained due to light trapping feature in the bottom cell which can improve the short circuit current density when conducting electrical simulations [4, 41].

The input files for GenPro4 for the above configurations can be found in Appendix E.3.1 and E.3.2. The generation profile for the bottom textured tandem device is extracted from the GenPro-4 simulations and is fed into the ASA input file. The ASA input file for the perovskite/silicon tandem can be found in Appendix E.3.3. After the simulation is carried out, The band energy values can be extracted and the band diagram is plotted as shown in the figure below.

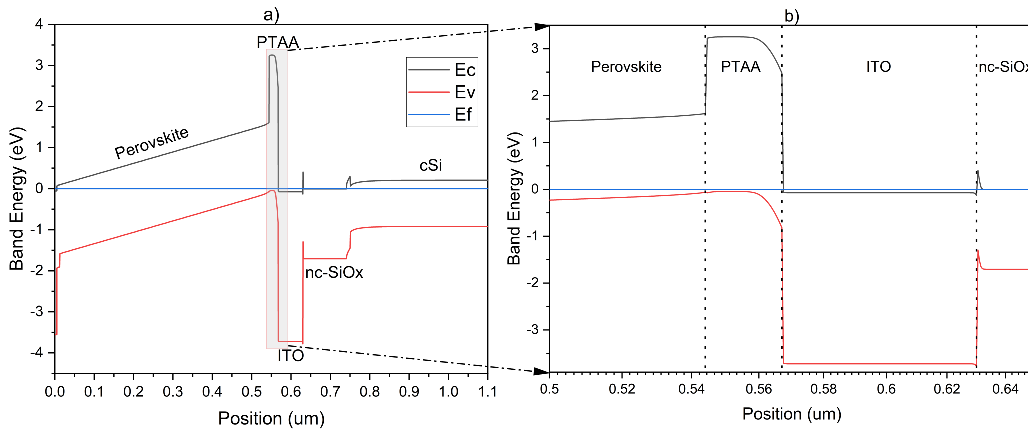

Figure 4.10: a)Band energy diagram with respect to the position of a perovskite-silicon tandem device by Al-Ashouri et al. [4] consisting of conduction band Ec, valence band Ev and fermi level Ef for each of the layers given in text b)Enlarged section of the tunnel recombination junction at the interface of the PTAA and ITO layer (marked with dotted lines) resulting in band to band tunnelling effects.

The band energy values that are extracted is then fed into the newly developed direct and band to band tunnelling algorithm and the tunnelling generation rates were extracted. This was then added to the continuity equations. The JV curve and other performance results can then be be extracted. In the following JV curve, we present three cases for validation purpose, the first two cases being the JV curve from forward and reversed scanned experimental measurement respectively as reported by Al-Ashouri et al. [4]. The third case is the JV curve obtained from the opto-electrical simulation without using any tunnelling contribution. The fourth and fifth case include DT only and BBT only respectively. The sixth and final case is the JV curve obtained from the opto-electrical simulation using the ASA software along with the newly developed DT and BBT algorithm together. All comparisons are made with respect to the experimental JV curves.

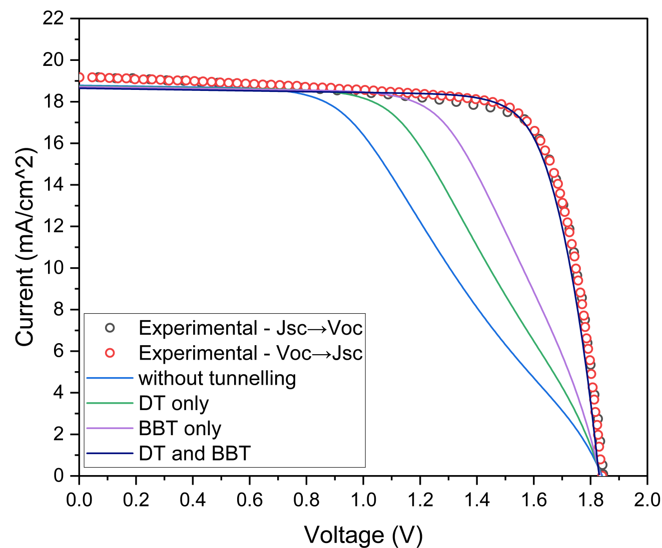

Figure 4.11: JV curves based on the perovskite-silicon tandem device by Al. Ashouri et.al. [4] with and without DT and BBT. The newly developed DT and BBT is in good agreement with the experiments resulting in similar current voltage characteristics.

As seen in Fig. 4.11, the JV curve obtained from the final ASA simulation shows almost good agreement with the forward and reverse scanned experimental JV curve from Al-Ashouri et al. [4]. There is however a slight difference in the JV curve before the maximum power point with sightly different short circuit current density values. One possible reason can be that the texturing used in the experimental setup does not precisely represent the texturing features used in the GenPro4 optical simulations lead-

ing to slight drop in the tandem photocurrent in optical simulation. Other reason can be a fact that the electrical resistive losses were less in the experimental setup leading its higher J_{SC} value. It can also be a fact that the deposition of the layer was very good resulting in minimal defects and voids leading to less charge recombination processes and improving the tandem performance of the experimental results. Nevertheless, after the maximum power point, the JV curves follows perfectly with the experimental JV curve.

When the performance of the experimental and simulation results were studied, the percentage error were calculated for V_{OC}, J_{SC} and FF for the experimental and simulation results. The maximum error percentages recorded were 1%, 2.8% and 3.4% for V_{OC}, J_{SC} and FF respectively. Since higher percentage errors were noticed in the J_{SC} and FF, further improvement of the simulation JV curve can be made with an increase in the perovskite thickness and a slight decrease in crystalline silicon thickness during the GenPro4 optical simulation. The thickness of the perovskite layer and the crystalline silicon layer can be manipulated by -/+10% as suggested from the authors of the Al-Ashouri paper due to the fact that the thickness after deposition sequence may not be precise from the required layer thickness. By this slight change in the thickness, a slightly higher tandem photocurrent value can be obtained. When coupling the GenPro4 optical simulation file to the ASA electrical simulation, this will result in a lower J_{SC} value than the GenPro4 tandem photocurrent but higher than the initial J_{SC} value (18.65 mA/cm^2). It always follows the logic that the photocurrent of the GenPro4 optical simulation (19.31 mA/cm^2 from Fig. 4.9) is always higher than J_{SC} from the combined opto-electrical simulation in ASA (18.65 mA/cm^2 from Fig. 4.11) due to electrical losses incorporated in the simulation. With this logic, the error percentages of the J_{SC} and FF can be further reduced. Other methods of improvement can be seen in the complex refractive index data for all the layers. As reported by Al-Ashouri et al. [4], the complex refractive index data provided are from other literature and not from the experiment itself. For the same material, different electronic properties like doping can have a significant impact on the optical refractive index and can alter the photocurrent significantly. Using the complex refractive index data for the specific experiment is essential in order to have an accurate and improved photocurrent that is close to realistic values. Nevertheless, we can safely conclude that newly developed direct tunnelling and band to band tunnelling algorithm provides the best possible agreement with both simulation and experimental results with a maximum error percentage of about 3%. A good agreement can be seen in the trend of the JV curve of both the experimental and simulation results. In the following table the performance results of the experiment and the simulation are summarised.

Table 4.6: Perovskite-Silicon tandem performance comparison with experimental and simulation results [4].

Parameters	**Voc** (V)	**Jsc** (mA/cm^2)	**FF**	**Efficiency (%)**
First case - Forward voltage scan experimental result	1.85	19.19	0.7561	26.79
Second case - Reverse voltage scan experimental result	1.85	19.17	0.760	26.95
Third case - ASA simulation without any tunnelling	1.83	18.78	0.475	16.32
Fourth case - ASA simulation with DT only	1.83	18.74	0.560	19.2
Fifth case - ASA simulation with BBT only	1.83	18.71	0.635	21.74
Sixth case - ASA simulation with DT and BBT	1.83	18.65	0.783	26.72

4.4. Conclusion

The objective of this chapter was to validate the newly developed tunnel recombination models such as direct tunnelling and band to band tunnelling. The validation was commenced for PN junction, Silicon hetero-junction and finally the Perovskite-Silicon tandem device. The JV curve for the above device simulations with and without incorporated tunnelling models was extracted and a comparison was made with literature results and simulation results from other software suites.

The newly developed tunnelling algorithms was concluded to be accurate. The JV curve obtained from the ASA simulation showed good agreement with literature results and simulation results from other subroutines with error percentages of less than 3%. With proper tuning of the device layer thickness, texturing and other electrical parameters, further improvement can be done on the simulation and reduce the error percentage when compared to other simulation or literature results. Simulations and performance analysis can now be performed for high efficiency perovskite-silicon tandem devices.

5

ASA Simulations of PVK/c-Si tandem devices

With the newly developed algorithms completely validated for the tunnelling models in the previous chapter, we shall now focus on the fourth objective of this thesis project which is to perform further simulation of the Pvk/c-Si tandem device in ASA to optimize its performance. A comparison is also made between the JV curve obtained from the newly developed algorithms and the JV curve obtained from other external results in literature. This can help in finding new ways to further increase the performance for high efficiency perovskite-silicon tandem devices and reach the SQ limit of 35.7% while including general opto-electrical losses [11].

5.1. Simulation of an improved version of Pvk/cSi tandem device by Tockhorn et al.

We shall have a look at the improved version of Pvk/cSi tandem device by Tockhorn et al. It is based on the nip-nip configuration developed at HZB [46]. The perovskite top cell consist of SnO_2 and a Self-assembled monolayer (SAM) as ETL and HTL respectively. The SAM layer used here is Me-4PACz ([4-(3,6-Dimethyl-9H-carbazol-9-yl)butyl]phosphonic Acid) for good hole carrier transport and surface passivation. In between SnO_2 and the perovskite absorber, C_{60} is used for effective surface passivation and charge carrier transport between the layer. The device structure can be depicted in the figure given below.

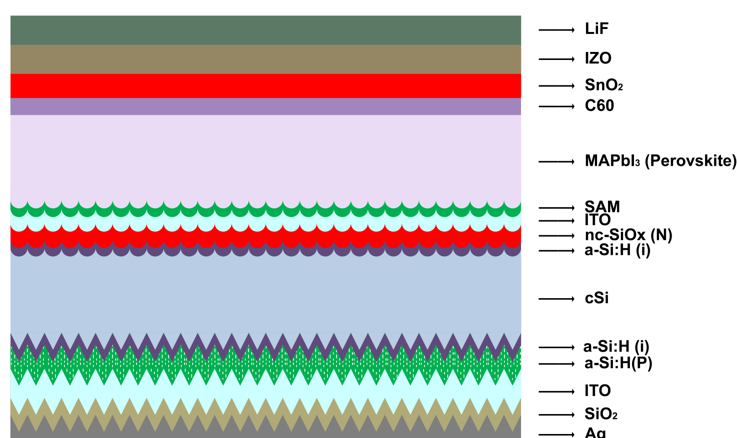

Figure 5.1: Improved Pvk/c-Si architecture developed at HZB, Germany [46].

Since the device structure uses SAM as the hole transport layer, its electrical properties are extracted from the literature of Trinh et al. [47] for the simulation purpose. However there is no literature on the wavelength dependant complex refractive index optical data, hence we shall use the complex refractive data of glass instead. The optical simulation will not give bad result since the SAM layer is very thin (1 nm) and will result in insignificant parasitic light absorption and reflection. We shall use the GenPro-4 optical model to commence the optical simulation of the device structure and obtain the generation profile which then is imported into the ASA software to couple optical and electrical simulation. The input parameters for the device structure used by both GenPro-4 and ASA can be tabulated in the table given below.

Table 5.1: Improved Pvk/cSi tandem electrical parameters by Tockhorn et al. [46]

Parameters	**IZO (TCO)**	**SnO_2 (ETL)**	**C_60 (ETL)**	**Perovskite**	**SAM (HTL)**	**ITO (TRJ)**	**nc-SiO_x (n++)**	**i-aSi:H (front/back)**	**c-Si (n type)**	**p-aSi:H (p++)**	**ITO (TCO)**
Thickness (m)	85e-9	10e-9	10e-9	600e-9	1e-9	20e-9	107e-9	5e-9/5e-9	300e-6	10e-9	10e-9
Bandgap (eV)	3.5	3.5	2	1.68	3.1	3.65	1.7	1.75	1.124	1.75	3.65
Electron affinity (eV)	4.65	4	3.9	3.9	2.06	4.8	3.9	3.8	4.05	3.8	4.8
N_c ($m^{-3}eV^{-1}$)	2.2e24	2.2e24	8e25	4.42e23	1e27	5.8e24	2e26	2e26	2.86e25	2e26	5.8e24
N_v ($m^{-3}eV^{-1}$)	1.8e25	1.8e25	8e25	8.47e24	1e27	1e24	2e26	2e26	3.1e25	2e26	1e24
Dielectric constant (ε_r)	9	9	4.2	6.5	3.5	8.9	11.9	11.9	11.8	11.9	8.9
Doping (m^{-3})	0	2e25	2.6e24	2e16	3e27	3e27	2.5e26	0	1e22	2e26	1e26
Mobility (μ_e/μ_h)(m^2/Vs)	100e-4/ 25e-4	100e-4/ 10e-4	0.08e-4/ 0.0035e-4	1.62e-4/ 1.62e-4	0.001e-4/ 0.001e-4	10e-4/ 10e-4	10e-4/ 2e-4	20e-4 /5e-4	1300e-4/ 400e-4	10e-4/ 1e-4	10e-4/ 10e-4
Electron/Hole Lifetime (τ_n/τ_p)(s)	-	1e-5/ 1e-6	1e-9/ 1e-9	2.88e-7/ 2.88e-7	1e-9/ 1e-9	1e-6/ 1e-6	1e-6/ 1e-6	-	10e-3/ 10e-3	1e-6/ 1e-6	1e-6/ 1e-6

In addition to the device properties, the device has micro-sized texturing below the crystalline silicon layer for the light trapping and scattering of the higher wavelength photons into the silicon layer. The device also incorporates nano-sized sinusoidal-like periodic textures for the layers between perovskite and silicon for light trapping and scattering of lower wavelength photons into the perovskite layer. According to Tockhorn et al. [46], these textures improved the deposition of layers resulting in less voids and recombination losses thereby improving the electrical properties. The end result is an overall higher tandem photocurrent as compared to the simulation on Pvk/cSi conducted previously (See Section 4.3). The absorptance profile for this device architecture is depicted in Fig. 5.2.

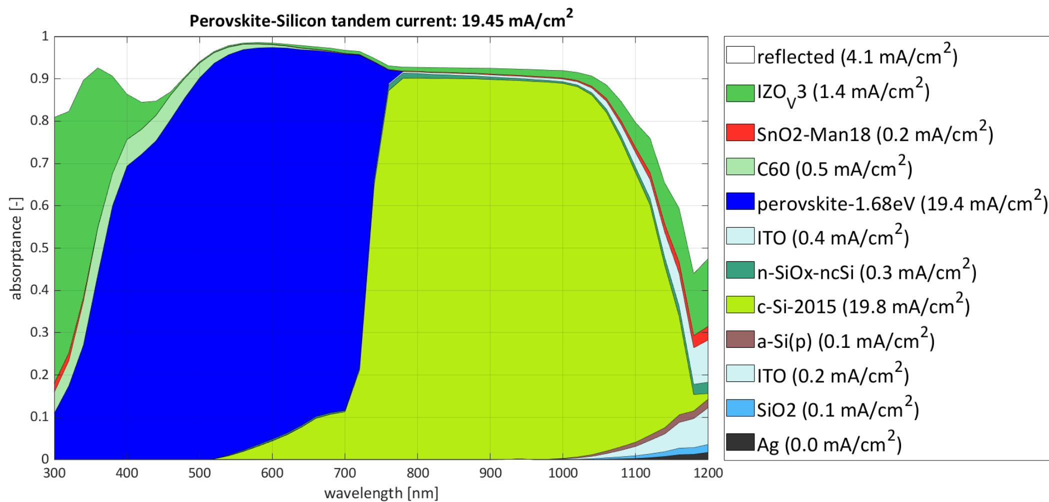

Figure 5.2: Absorptance profile for an improved Pvk/cSi device. A higher tandem photocurrent is obtained due to micro-sized pyramidal textures below the silicon layer and nano-sized sinusoidal-like texture below perovskite layer [41, 46].

The input files for GenPro4 for the above configurations can be found in Appendix F.1. The generation profile for the tandem device is printed from the GenPro-4 simulations and is read into the ASA input file. The ASA input file for the perovskite/silicon tandem can be found in Appendix F.2. After the simulation is carried out, The band energy values can be extracted and the band diagram is plotted as shown in the figure below.

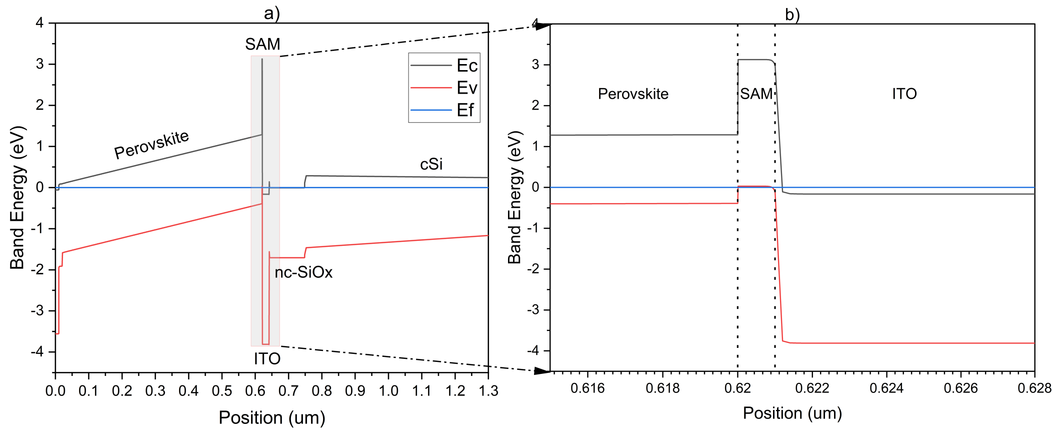

Figure 5.3: a)Band energy diagram with respect to the position of an improved perovskite-silicon tandem device by Tockhorn et al. [4] consisting of conduction band Ec, valence band Ev and fermi level Ef for each of the layers given in text b)Enlarged section of the tunnel recombination junction at the interface of the SAM and ITO layer (marked with dotted lines) resulting in band to band tunnelling effects.

The band energy values that are extracted is then used as input by the newly developed direct and band to band tunnelling algorithm and the tunnelling generation rates were extracted. This was then added to the continuity equations. The JV curve and other performance results can then be be extracted. In the following JV curves, we present two cases, the first case being the JV curve obtained from experimental measurement respectively as reported by Tockhorn et al. [46]. The second case is the JV curve obtained from the opto-electrical simulation in ASA with the tunnelling contributions included.

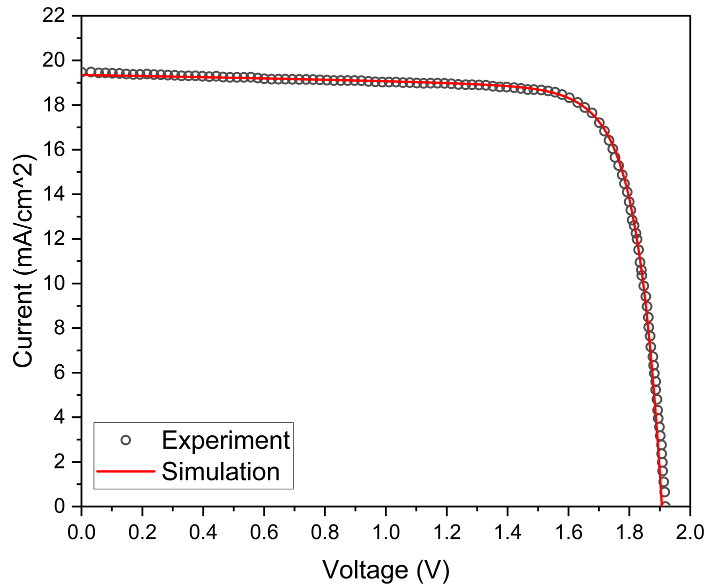

Figure 5.4: JV curves based on the improved perovskite-silicon tandem device by Tockhorn et al. [46] with DT and BBT. The newly developed DT and BBT is in good agreement with the experiments resulting in similar current voltage characteristics.

As seen in Fig. 5.4, the current voltage characteristics of the simulation matches very well with the experimental JV curve. The biggest difference when compared to the simulation of the Pvk/cSi tandem device in Section 4.3 is that the hole transport layer SAM has higher hole mobility than PTAA significantly increasing the FF of the overall JV curve. This combined with nano-sized textures below the perovskite layer with good passivation reduced the recombination losses for the perovskite layer increasing the J_{SC} (V_{OC} increases as well but slightly) for the tandem device thereby increasing the

overall efficiency to 29.6%. It is important to note that the optical data for the layers used here is obtained from other simulations and literatures and is not obtained from the experiment itself. Changing the material doping or the material characteristics slightly can change the complex refractive indices significantly and can change the absorption profile. This is the limiting factor towards improving the photocurrent of the Pvk/cSi tandem or any device in general.

Another improvement that can be considered is for the non-absorber layers for the perovskite top cell. From the Fig. 5.2, parasitic absorption is noticed for the IZO and C60 layer. Reducing the thickness can reduce the parasitic absorption significantly but may hamper the electrical properties due to poor uniform deposition of very thin layers as reported by Tockhorn et al. [46]. Hence there is a trade-off that can be investigated and further optimised. Last but not the least, the type of textures affect the scattering of wavelength dependent photons. For this device, nano-sized sinusoidal like periodic textures for the perovskite cell not only helped with light trapping and scattering, but helped in the deposition of the perovskite layer with less voids which would otherwise deposit poorly over pyramidal like textures. Playing with the shape of the nano-textures and its periodicity for all the layers in the top cell can be investigated further along with the type of deposition techniques (hybrid co-evaporation and solution spin coating). These methods combined can easily help with reaching the SQ limit of 35.7% efficiency mark for the Pvk/cSi tandem solar cells and that is something we can speculate from the current world record holder of the Pvk/cSi tandem device efficiency from EPFL and CSEM [6]. In the following table the performance results of the experiment and the simulation are summarised:

Table 5.2: Perovskite-Silicon tandem performance comparison with experimental and simulation results [46]

Parameters	**Voc (V)**	**Jsc (mA/cm^2)**	**FF**	**Efficiency (%)**
Experiment	1.918	19.48	0.792	29.597
Simulation	1.905	19.35	0.802	29.584

5.2. Conclusion

The objective of this chapter was to perform further simulation of the Pvk/c-Si tandem device in ASA to optimize its performance. The JV curve for the above device simulation with the incorporated tunnelling models was extracted and a comparison was made with the experimental results.

The JV curve obtained from the ASA simulation showed good agreement with the experimental results with an efficiency of 29.6%. Several methods were proposed to help reach the SQ limit of 35.7% efficiency mark. Methods such as proper tuning of the non-absorbing layers of the perovskite top cell thickness, doping and mobilities was suggested. This along with the trial and error of different nano-texturing features and periodicity for the perovskite top cell layers for investigating the light trapping and scattering effect can increase the J_{SC} and FF which can increase the overall efficiency.

6 Conclusion and Recommendation

This chapter finally concludes this thesis project and provides insights and recommendations towards future ASA simulation works on perovskite-silicon tandem devices. The goal of this thesis project was to optimize the simulation of perovskite-silicon tandem device by incorporating advanced optical and electrical models with the newly developed tunnelling algorithm to accurately simulate perovskite-silicon tandem device or any device in general.

6.1. Conclusion

For this thesis project we focused on four main objectives:

1. To understand the solar cell modelling approach in ASA and the tunnel recombination models that can be incorporated in the source code for the simulation of multi-junction devices
2. To develop an algorithm (C++ code) that can automatically detect and process the tunnelling models in ASA for Pvk/c-Si tandem device or any device in general.
3. To validate the algorithm (C++ code) with experimental or other simulation results.
4. To perform further simulation of the Pvk/c-Si tandem device in ASA to optimize its performance.

For the first objective, a typical solar cell modelling approach used in the ASA software was explained. We further explained the electrical modelling approach starting with the fundamental differential transport equations like the Poisson and Continuity equations. These models are necessary for the processing of the band energy diagram, electrostatic potential and electric field for a particular solar cell device. In addition, the generation recombination processes and the DOS models for amorphous silicon was touched upon. Finally the tunnelling models used in the development of an automated tunnelling algorithm was extensively explained. These models includes the DT model by Ieong et al [18], simple BBT model [31] and non-local BBT model [31]. The band energy diagram, electrostatic potential and electric field are then used for the Direct tunnelling model by Ieong et al [18], simple band to band tunnelling model [31] and non-local band to band tunnelling models [18, 31] for which the generation rate due to tunnelling can be extracted and added to the continuity equations of Eq 2.2 and Eq 2.3 for electrons and holes respectively and achieve convergence for the final device performance (JV curve, Fill Factor etc).

For the second objective, we focused on the design of a new algorithm that can run the tunnelling models as effectively as possible. Moreover, we introduced a new implementation method that can automate these algorithms with minimal input requirements from the user with the computer deciding that aspect without any difficulties. These algorithms need to be processed after the poisson's simulation and before the continuity equation simulations for proper convergence to be achieved. A fully fledged algorithm was then designed for the automation of the direct tunnelling (by Ieong et.al. [18]) and the band to band tunnelling process (simple and non-local BBT model [31]) with limited input from the user while using the models as seen in Section 2.4. In simple terms, the algorithm takes in the required input and scans through the device length for each interface and check for tunnel contributions and

performs the tunnelling calculations when necessary. All necessary conditions are included inside the algorithms to ensure that the simulation is accurately solved. Any unexpected errors and situations like grid points going out of bounds, or continuity of gridpoints at the interface or an unrealistic tunnelling length were taken into consideration and rectified within the algorithm. When running the algorithm, the extracted tunnelling generation rate was then fed into the continuity equations the performance results of the device simulation was extracted.

For the third objective, we focused on the validation of the newly developed tunnelling algorithms for various device architectures and verification of the performance results as seen in literature or simulations performed in other software suites was conducted. A comparison was made between the JV curve obtained with the developed algorithms and other external simulation results.The validation was commenced for PN junction, Silicon hetero-junction and finally the Perovskite-Silicon tandem device. The JV curve for the above device simulations with and without incorporated tunnelling models was extracted and a comparison was made with literature results and simulation results from other software suites. The newly developed tunnelling algorithms was concluded to be accurate. The JV curve obtained from the ASA simulation showed good agreement with literature results and simulation results from other software suites with a maximum error percentages of about 3%. With proper tuning of the device layer thickness, texturing and other electrical parameters, further improvement could be done on the simulation and the error percentage when compared to other simulation or literature results could be reduced. A fully functional opto-electrical solar cell simulator for tandem devices, simulations and performance analysis could be performed for high efficiency perovskite-silicon tandem devices.

The objective of fourth and final chapter was to perform further simulation of the Pvk/c-Si tandem device in ASA to optimize its performance. The JV curve for the above device simulation with the incorporated tunnelling models was extracted and a comparison was made with the experimental results. The JV curve obtained from the ASA simulation showed good agreement with the experimental results with a max efficiency of 29.6%. Several methods were proposed to help reach the SQ limit of 35.7% efficiency mark. Methods such as proper tuning of the non-absorbing layers of the perovskite top cell thickness, doping and mobilities was suggested. This along with the trial and error of different nano-texturing features and periodicity for the perovskite top cell layers for investigating the light trapping and scattering effect can increase the J_{SC} and FF which can increase the overall efficiency.

6.2. Recommendation

During the entire thesis project, several ideas emerged that can potentially improve the simulation experience of not just Pvk/cSi tandem device, but for any kind of device architecture on the market. Below are some of the future works that can be conducted to make this happen.

The first recommendation is with respect to the BBT and TAT model. In all the tunnelling models (DT and BBT) that were discussed in Section 2.4, the tunnelling of charge carriers happen at the same band energy level. This is not always true for BBT model. There are cases were with sufficient energy, the charge carriers can get excited to a different energy level and then tunnel through the TRJ even though the tunnelling bands are not aligned at the same energy. In this case, BBT contribution along with TAT contribution will be taken into consideration when simulating tunnelling effects. The newly developed BBT algorithm does not take TAT effects into consideration and will not work if the CB is not aligned with the VB at the TRJ. Integrating BBT and TAT together in the single algorithm is very complex and time consuming since the existing TAT model in ASA has poor convergence and will not work perfectly together with other tunnelling models. A recommendation is to use a different TAT model proposed by Palma et.al. [26] (This is currently under construction by the PVMD member C.M. Ruiz). This model has better convergency without any approximations involved as compared to the TAT model proposed by J.A. Willemen [52] which ASA uses. This is subjected to further research and development.

The second recommendation is with respect to the integration of GenPro4 optical simulation and ASA electrical simulation. For complex texturing features on multiple layers, the simulation time drastically increases depending on the optical model settings used in GenPro4. This is done separately on MATLAB and the generation profile is printed. This generation profile is then read into ASA to couple

optical and electrical simulation. This itself takes a lot of time especially when there is texturing on multiple layers of the device. This two step approach makes the entire simulation extremely time consuming. An idea would be is make the entire GenPro4 model in C++ and directly incorporate the model into the ASA source code. Making this subroutine will definitely make ASA a complete opto-electrical simulation suite for any kind of device without additional steps or approach.

The third recommendation is with respect to the tunnelling algorithm. The algorithm checks for the tunnelling contributions at each interface along the device. In theory, the newly developed DT and BBT algorithm can work for n number of multi-junction devices. In this thesis project, the validation of the tunnelling algorithm was done for Pvk/cSi tandem device. In future, more validations can be performed for triple junction of quadruple junction devices.

The fourth recommendation is with regards to the improvement of the tandem device performance in both simulation and experiment. It is important to note that the optical data for the layers used here is obtained from other simulations and literatures and is not obtained from the experiment itself. Changing the material doping or the material characteristics slightly can change the complex refractive indices significantly and can change the absorption profile. This is the limiting factor towards improving the photocurrent of the Pvk/cSi tandem or any device in general. Another improvement that can be considered is for the non-absorber layers for the perovskite top cell. Reducing the thickness can reduce the parasitic absorption significantly but may hamper the electrical properties due to poor uniform deposition of very thin layers. Hence there is a trade-off that can be investigated and further optimised. Last but not the least, the type of textures affect the scattering of wavelength dependent photons. Playing with the shape of the nano-textures and its periodicity for all the layers in the top cell can be investigated further along with the type of deposition techniques (hybrid co-evaporation and solution spin coating). These methods combined can easily help with reaching the SQ limit of 35.7% efficiency mark for the Pvk/cSi tandem solar cells.

References

[1] Urs Aeberhard et al. "Analysis and optimization of perovskite-silicon tandem solar cells by full opto-electronic simulation". In: (2020), pp. 37–38. DOI: 10.1109/NUSOD49422.2020.9217773.

[2] S. Akhil et al. "Review on perovskite silicon tandem solar cells: Status and prospects 2T, 3T and 4T for real world conditions". In: *Materials Design* 211 (2021), p. 110138. ISSN: 0264-1275. DOI: https://doi.org/10.1016/j.matdes.2021.110138. URL: https://www.sciencedirect.com/science/article/pii/S0264127521006936.

[3] S. Akhil et al. "Review on perovskite silicon tandem solar cells: Status and prospects 2T, 3T and 4T for real world conditions". In: *Materials Design* 211 (2021), p. 110138. ISSN: 0264-1275. DOI: https://doi.org/10.1016/j.matdes.2021.110138. URL: https://www.sciencedirect.com/science/article/pii/S0264127521006936.

[4] Amran Al-Ashouri et al. "Monolithic perovskite/silicon tandem solar cell with >29% efficiency by enhanced hole extraction". In: *Science* 370.6522 (2020), pp. 1300–1309. DOI: 10.1126/science.abd4016. eprint: https://www.science.org/doi/pdf/10.1126/science.abd4016. URL: https://www.science.org/doi/abs/10.1126/science.abd4016.

[5] S. M. Bedair, M. F. Lamorte, and J. R. Hauser. "A two□junction cascade solar□cell structure". In: *Applied Physics Letters* 34.1 (1979), pp. 38–39. DOI: 10.1063/1.90576. eprint: https://doi.org/10.1063/1.90576. URL: https://doi.org/10.1063/1.90576.

[6] Emiliano Bellini. *CSEM, EPFL achieve 31.25% efficiency for tandem perovskite-silicon solar cell*. July 2022. URL: https://www.pv-magazine.com/2022/07/07/csem-epfl-achieve-31-25-efficiency-for-tandem-perovskite-silicon-solar-cell/.

[7] M. W. M. van Cleef, R. E. I. Schropp, and F. A. Rubinelli. "Significance of tunneling in p+ amorphous silicon carbide n crystalline silicon heterojunction solar cells". In: *Applied Physics Letters* 73.18 (1998), pp. 2609–2611. DOI: 10.1063/1.122521. eprint: https://doi.org/10.1063/1.122521. URL: https://doi.org/10.1063/1.122521.

[8] Ludmila Cojocaru et al. "Simulation of IV Curves for Inverted Planar Structure Perovskite Solar Cells using Equivalent Circuit Model with Inductance". In: (2015). DOI: https://doi.org/10.1246/cl.150933.

[9] C.R. Crowell. "The Richardson constant for thermionic emission in Schottky barrier diodes". In: *Solid-State Electronics* 8.4 (1965), pp. 395–399. ISSN: 0038-1101. DOI: https://doi.org/10.1016/0038-1101(65)90116-4. URL: https://www.sciencedirect.com/science/article/pii/0038110165901164.

[10] Michele De Bastiani et al. "All Set for Efficient and Reliable Perovskite/Silicon Tandem Photovoltaic Modules?" In: *Solar RRL* n/a.n/a (), p. 2100493. DOI: https://doi.org/10.1002/solr.202100493. eprint: https://onlinelibrary.wiley.com/doi/pdf/10.1002/solr.202100493. URL: https://onlinelibrary.wiley.com/doi/abs/10.1002/solr.202100493.

[11] Bruno Ehrler et al. "Photovoltaics Reaching for the Shockley–Queisser Limit". In: *ACS Energy Letters* 5.9 (2020), pp. 3029–3033. DOI: 10.1021/acsenergylett.0c01790. eprint: https://doi.org/10.1021/acsenergylett.0c01790. URL: https://doi.org/10.1021/acsenergylett.0c01790.

[12] Gross Jose Godoy. *Simulation of Perovskite absorber materials for the application in flexible thin-film devices following HyET's solar cell structure | TU Delft Repositories*. Nov. 2021. URL: https://repository.tudelft.nl/islandora/object/uuid:e21b57b1-2b15-4654-a212-ade75778d990?collection=education.

[13] Martin A. Green et al. "Solar cell efficiency tables (version 56)". In: *Progress in Photovoltaics: Research and Applications* 28.7 (2020), pp. 629–638. DOI: https://doi.org/10.1002/pip.3303. eprint: https://onlinelibrary.wiley.com/doi/pdf/10.1002/pip.3303. URL: https://onlinelibrary.wiley.com/doi/abs/10.1002/pip.3303.

[14] G.A.M. Hurkx, D.B.M. Klaassen, and M.P.G. Knuvers. “A new recombination model for device simulation including tunneling”. In: *IEEE Transactions on Electron Devices* 39.2 (1992), pp. 331–338. DOI: 10.1109/16.121690.

[15] G.A.M. Hurkx, D.B.M. Klaassen, and M.P.G. Knuvers. “A new recombination model for device simulation including tunneling”. In: *IEEE Transactions on Electron Devices* 39.2 (1992), pp. 331–338. DOI: 10.1109/16.121690.

[16] T. Ibn-Mohammed et al. “Perovskite solar cells: An integrated hybrid lifecycle assessment and review in comparison with other photovoltaic technologies”. In: *Renewable and Sustainable Energy Reviews* 80 (2017), pp. 1321–1344. ISSN: 1364-0321. DOI: https://doi.org/10.1016/j.rser.2017.05.095. URL: https://www.sciencedirect.com/science/article/pii/S1364032117307311.

[17] IEA. *Renewables 2020 – Analysis*. british. 2020. URL: https://www.iea.org/reports/renewables-2020 (visited on 11/08/2021).

[18] MeiKei Ieong et al. “Comparison of raised and Schottky source/drain MOSFETs using a novel tunneling contact model”. In: (1998), pp. 733–736. DOI: 10.1109/IEDM.1998.746461.

[19] International Energy Agency. *World Energy Outlook 2021 – Analysis*. british. Oct. 1, 2021. URL: https://www.iea.org/reports/world-energy-outlook-2021 (visited on 11/08/2021).

[20] Saqib Iqbal et al. “Computational modelling of monolithically stacked perovskite/silicon tandem solar cells using monofacial and bifacial designs”. In: *Optik* 206 (2020), p. 163427. ISSN: 0030-4026. DOI: https://doi.org/10.1016/j.ijleo.2019.163427. URL: https://www.sciencedirect.com/science/article/pii/S0030402619313257.

[21] IRENA. *Patents Evolution*. 2019. URL: https://www.irena.org/Statistics/View-Data-by-Topic/Innovation-and-Technology/Patents-Evolution (visited on 11/08/2021).

[22] IRENA. *World Energy Transitions Outlook: 1.5°C Pathway*. June 1, 2021. URL: https://www.irena.org/publications/2021/Jun/World-Energy-Transitions-Outlook (visited on 11/08/2021).

[23] K. Jäger et al. “A scattering model for nano-textured interfaces and its application in opto-electrical simulations of thin-film silicon solar cells”. In: *Journal of Applied Physics* 111.8 (2012), p. 083108. DOI: 10.1063/1.4704372. eprint: https://doi.org/10.1063/1.4704372. URL: https://doi.org/10.1063/1.4704372.

[24] Klaus Jäger. “On the scalar scattering theory for thin-film solar cells”. In: (2012).

[25] Jaeki Jeong et al. “Pseudo-halide anion engineering for α-FAPbI3 perovskite solar cells”. In: *Nature* 592 (Apr. 2021), pp. 1–5. DOI: 10.1038/s41586-021-03406-5.

[26] F. Jiménez-Molinos et al. “Physical model for trap-assisted inelastic tunneling in metal-oxide-semiconductor structures”. In: *Journal of Applied Physics* 90.7 (2001), pp. 3396–3404. DOI: 10.1063/1.1398603. eprint: https://doi.org/10.1063/1.1398603. URL: https://doi.org/10.1063/1.1398603.

[27] Evan O. Kane. “Theory of Tunneling”. In: *Journal of Applied Physics* 32.1 (1961), pp. 83–91. DOI: 10.1063/1.1735965. eprint: https://doi.org/10.1063/1.1735965. URL: https://doi.org/10.1063/1.1735965.

[28] LV Keldysh. “Dynamic tunneling”. In: *Sov. Phys. JETP* 6 (1958), p. 665.

[29] Akihiro Kojima et al. “Organometal Halide Perovskites as Visible-Light Sensitizers for Photovoltaic Cells”. In: *Journal of the American Chemical Society* 131.17 (2009). PMID: 19366264, pp. 6050–6051. DOI: 10.1021/ja809598r. eprint: https://doi.org/10.1021/ja809598r. URL: https://doi.org/10.1021/ja809598r.

[30] J. J. Liou. “Modeling the tunnelling current in reverse-biased p/ n junctions”. In: *Solid State Electronics* 33.7 (1990), pp. 971–972. DOI: 10.1016/0038-1101(90)90081-O.

[31] Sentaurus User’s Manual and I Version. “Synopsys TCAD Sentaurus”. In: *Inc., Mountain View, CA* 2009 (2015).

[32] Lei Meng et al. "Recent Advances in the Inverted Planar Structure of Perovskite Solar Cells". In: *Accounts of Chemical Research* 49.1 (2016). PMID: 26693663, pp. 155–165. DOI: 10.1021/acs.accounts.5b00404. eprint: https://doi.org/10.1021/acs.accounts.5b00404. URL: https://doi.org/10.1021/acs.accounts.5b00404.

[33] Takashi Minemoto and Masashi Murata. "Device modeling of perovskite solar cells based on structural similarity with thin film inorganic semiconductor solar cells". In: *Journal of Applied Physics* 116.5 (2014), p. 054505. DOI: 10.1063/1.4891982. eprint: https://doi.org/10.1063/1.4891982. URL: https://doi.org/10.1063/1.4891982.

[34] Mehrdad Najafi et al. "Highly Efficient and Stable Flexible Perovskite Solar Cells with Metal Oxides Nanoparticle Charge Extraction Layers". In: *Small* 14.12 (2018), p. 1702775. DOI: https://doi.org/10.1002/smll.201702775. eprint: https://onlinelibrary.wiley.com/doi/pdf/10.1002/smll.201702775. URL: https://onlinelibrary.wiley.com/doi/abs/10.1002/smll.201702775.

[35] NREL. *Best Research-Cell Efficiency Chart*. 2021. URL: https://www.nrel.gov/pv/cell-efficiency.html (visited on 11/09/2021).

[36] *Oxford PV hits new world record for solar cell | Oxford PV*. Dec. 21, 2020. URL: https://www.oxfordpv.com/news/oxford-pv-hits-new-world-record-solar-cell.

[37] M. J. Powell and S. C. Deane. "Improved defect-pool model for charged defects in amorphous silicon". In: *Phys. Rev. B* 48 (15 Oct. 1993), pp. 10815–10827. DOI: 10.1103/PhysRevB.48.10815. URL: https://link.aps.org/doi/10.1103/PhysRevB.48.10815.

[38] Paul Procel et al. "The role of heterointerfaces and subgap energy states on transport mechanisms in silicon heterojunction solar cells". English. In: *Progress in Photovoltaics: research and applications* 28.9 (2020), pp. 935–945. ISSN: 1062-7995. DOI: 10.1002/pip.3300.

[39] Chih-Tang Sah and William Shockley. "Electron-hole recombination statistics in semiconductors through flaws with many charge conditions". In: *Physical Review* 109.4 (1958), p. 1103.

[40] Florent Sahli et al. "Fully textured monolithic perovskite/silicon tandem solar cells with 25.2% power conversion efficiency". In: *Nature Materials* 17.9 (2018), pp. 820–826. DOI: 10.1038/s41563-018-0115-4.

[41] Rudi Santbergen et al. "GenPro4 Optical Model for Solar Cell Simulation and Its Application to Multijunction Solar Cells". In: *IEEE Journal of Photovoltaics* 7.3 (2017), pp. 919–926. DOI: 10.1109/JPHOTOV.2017.2669640.

[42] A. Schenk. "Rigorous theory and simplified model of the band-to-band tunneling in silicon". In: *Solid-State Electronics* 36.1 (1993), pp. 19–34. ISSN: 0038-1101. DOI: https://doi.org/10.1016/0038-1101(93)90065-X. URL: https://www.sciencedirect.com/science/article/pii/003811019390065X.

[43] Ruud E. I. Schropp and Miro Zeman. "Amorphous and Microcrystalline Silicon Solar Cells: Modeling, Materials and Device Technology". In: 1998.

[44] W Shockley and JT Last. "Statistics of the charge distribution for a localized flaw in a semiconductor". In: *Physical Review* 107.2 (1957), p. 392.

[45] Int Silvaco. "Silvaco ATLAS user's manual". In: *Santa Clara, CA, Ver* 5 (2013).

[46] Philipp Tockhorn et al. "Nano-optical designs enhance monolithic perovskite/silicon tandem solar cells toward 29.8% efficiency". In: *Nano-optical designs enhance monolithic perovskite/silicon tandem solar cells toward 29.8% efficiency* (2022). DOI: 10.21203/rs.3.rs-1439562/v1.

[47] Cham Thi Trinh et al. "Electrical and optical simulation of perovskite/silicon tandem solar cells using Tcad-Sentaurus". In: *2021 IEEE 48th Photovoltaic Specialists Conference (PVSC)*. 2021, pp. 2324–2327. DOI: 10.1109/PVSC43889.2021.9519104.

[48] R. Varache et al. "Investigation of selective junctions using a newly developed tunnel current model for solar cell applications". In: *Solar Energy Materials and Solar Cells* 141 (2015), pp. 14–23. ISSN: 0927-0248. DOI: https://doi.org/10.1016/j.solmat.2015.05.014. URL: https://www.sciencedirect.com/science/article/pii/S0927024815002196.

[49] Marta Victoria et al. "Solar photovoltaics is ready to power a sustainable future". In: *Joule* 5.5 (2021), pp. 1041–1056. ISSN: 2542-4351. DOI: https://doi.org/10.1016/j.joule.2021.03.005. URL: https://www.sciencedirect.com/science/article/pii/S2542435121001008.

[50] Kyounghoon Yang, Jack R. East, and George I. Haddad. "Numerical modeling of abrupt heterojunctions using a thermionic-field emission boundary condition". In: *Solid-State Electronics* 36.3 (1993), pp. 321–330. ISSN: 0038-1101. DOI: https://doi.org/10.1016/0038-1101(93)90083-3. URL: https://www.sciencedirect.com/science/article/pii/0038110193900833.

[51] Miro Zeman et al. "Advanced semiconductor analysis". In: *TU Delft* (2003).

[52] Miro Zeman et al. "Computer modelling of current matching in a-Si : H/a-Si : H tandem solar cells on textured TCO substrates". In: *Solar Energy Materials and Solar Cells* 46 (1997), pp. 81–99.

[53] Miaomiao Zhang et al. "Recent progress in inorganic tin perovskite solar cells". In: *Materials Today Energy* (2021), p. 100891. ISSN: 2468-6069. DOI: https://doi.org/10.1016/j.mtener.2021.100891. URL: https://www.sciencedirect.com/science/article/pii/S2468606921002562.

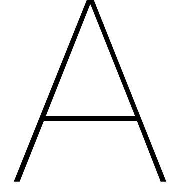

Solar Cell Modelling in ASA - additional models

The fundamental modelling procedure in ASA is briefly explained in Chapter 2. However, all the models were not touched upon due to the scope of this project. Here we explain the additional electrical and optical models that are required for the simulation to achieve good performance results.

A.1. Electrical modelling - additional models

A.1.1. Boundary conditions for ohmic and schottky contacts

The front and back contact of the device are the two boundaries in 1-D device modeling. The boundary conditions are determined by how a device's contacts are modeled. In general, there are two types of contacts: Ohmic contacts and Schottky contacts [51].

The electrostatic potential and electron and hole concentrations at the device's boundaries (x = 0 and x = L) are either fixed or determined by surface recombination in the case of Ohmic contacts. The majority carrier concentration is considered to be independent of the injection level. The device thickness is denoted by the letter L. Infinite recombination and charge neutrality can be assumed for ideal ohmic contacts resulting in the space charge for front and back contact to be zero ($\rho(x=0) = \rho(x=L) = 0$) [51]. The electrostatic potential ψ and quasi-Fermi potentials Ψ_{fn} and Ψ_{fp} at the boundaries are subjected to the following conditions:

$$\psi(x=0) = \psi_0(x=0) + V_{app} \tag{A.1}$$

$$\psi(x=L) = \psi_0(x=L) \tag{A.2}$$

$$\Psi_{fn}(x=0) = \Psi_{fp}(x=0) = V_{app} \tag{A.3}$$

$$\Psi_{fn}(x=L) = \Psi_{fp}(x=L) = 0 \tag{A.4}$$

where $\psi(x=0)$ and $\psi(x=L)$ are the solutions to the Eq. (**??**) and the condition that $\rho(x=0) = \rho(x=L) = 0$. The surface recombination velocities for electrons S_n and holes S_p define the carrier concentrations at the boundaries for generic Ohmic contacts [51]. For this form of contact, the electron and hole current densities are described as follows:

$$\begin{aligned} J_n(x=0) &= qS_{n0}\left[n(x=0) - n_{eq}(x=0)\right] \\ J_n(x=L) &= qS_{nL}\left[n(x=L) - n_{eq}(x=L)\right] \end{aligned} \tag{A.5}$$

$$\begin{aligned} J_p(x=0) &= qS_{p0}\left[p(x=0) - p_{eq}(x=0)\right] \\ J_p(x=L) &= qS_{pL}\left[p(x=L) - p_{eq}(x=L)\right] \end{aligned} \tag{A.6}$$

where n and p are the electron and hole concentrations at the front and back contacts, respectively, and n_{eq} and p_{eq} are the electron and hole concentrations at the front and back contacts in thermodynamic equilibrium. The surface recombination velocities for electrons at the front and back contacts

are S_{n0} and S_{nL}, respectively, and the surface recombination velocities for holes at the front and back contacts are S_{p0} and S_{pL}, respectively [51].

The position of the Fermi level at a Schottky contact is assumed to be dependent on the effective barrier height, φ_B, of the metal semiconductor interface at thermal equilibrium in the case of a Schottky contact. The difference between the metal's work function, φ_m, and the semiconductor's electron affinity, χ_s, determines this barrier. The concentration of electrons and holes at the interface can then be calculated once the position of the Fermi level at the interface is fixed by φ_B [51].

$$\varphi_B = \varphi_m - \chi_s = E_c - E_f \tag{A.7}$$

$$n_{eq} = N_C \exp\left(-\frac{q\varphi_B}{kT}\right) \tag{A.8}$$

$$p_{eq} = n_i^2 / n_{eq} \tag{A.9}$$

where n_i is the intrinsic carrier concentration of the semiconductor material.The majority carriers dominate current transport through the Schottky barrier, which is driven by the thermionic-emission mechanism [51]. The current density is calculated using the thermionic-emission theory as follows:

$$J = A^* T^2 \exp\left(-\frac{q\varphi_B}{kT}\right)\left[\exp\left(\frac{qV_{app}}{kT}\right) - 1\right] \tag{A.10}$$

where A^* is the Richardson constant.

A.1.2. Recombination-Generation (R-G) statistics

For c-Si, the recombination typical takes place in the band-gap consisting of a single level recombination center. As a-Si have multiple states in the forbidden region of the energy band, the recombination rate has to be integrated for all the states. The trapped charges are also distinguished between tails states (donor like states and acceptor like states) and DB states. These parameters are represented by the following equations:

$$R_{net} = \int_{E_v^{\text{mob}}}^{E_c^{\text{mob}}} N(E)\eta_R(E)dE \tag{A.11}$$

$$\rho_D = q\int_{E_c^{mob}}^{E_v^{mob}} N_D(E)[1 - f(E)]dE \tag{A.12}$$

$$\rho_A = -q\int_{E_c^{mob}}^{E_v^{mob}} N_A(E)f(E)dE \tag{A.13}$$

$$\rho_{DB} = q\int_{E_c^{mob}}^{E_v^{mob}} N_{DB}(E)\left[F^+(E) - F^-(E)\right]dE \tag{A.14}$$

where $N(E)$ is the DOS at the energy level in the band-gap E, $\eta_R(E)$ is the recombination rate contribution at the energy level in the band-gap E, $f(E)$ is the occupation function, $F^+(E)$ and $F^-(E)$ are the occupation functions of empty and doubly occupied DB respectively. The assumption that recombination centers are non interacting with each other and can only interact with the VB and CB, the Shockley-Read-Hall (SRH) R-G statistics is used for VBT and CBT (for single level states) [44] while Sah and Shockley multi-state approach is used for amphoteric DB states [39].

The SRH theory is based on four process that occur between the energy level E_T in the band-gap and the VB and CB as shown in Fig A.1 [44]:

1. Electron capture at R-G center
2. Electron emission at R-G center
3. Hole capture at R-G center
4. Hole emission at R-G center

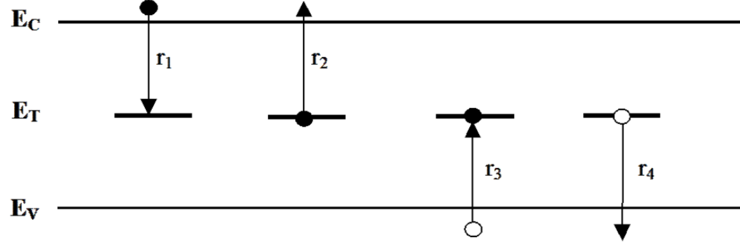

Figure A.1: SRH recombination process between energy level at band-gap and the extended states [44][51]

For the VBT, the recombination rate at energy E_T is given by the Eq (A.15):

$$R_{VB} = N_D \frac{C_p^0 C_n^+ \left(np - n_i^2\right)}{C_p^0 n + e_p^+ + C_n^+ p + e_n^0} \tag{A.15}$$

$$e_n^0 = C_n^+ N_c \exp\left[\left(E_T - E_c\right)/kT\right] \tag{A.16}$$

$$e_p^+ = C_p^0 N_v \exp\left[\left(E_v - E_T\right)/kT\right] \tag{A.17}$$

where N_D is the donor states at E_T, C_p^0 and C_n^+ are the capture coefficient of holes and electrons respectively, e_p^+ and e_n^0 are the emission coefficients of holes and electrons respectively. The occupation function of donor like states is described by a Fermi-Dirac distribution function given by the Eq (A.18):

$$f^0 = \frac{C_n^+ n + e_p^+}{C_n^+ n + e_n^0 + C_p^0 p + e_p^+} \tag{A.18}$$

With the above equations, The recombination and trapped hole concentration is then integrated over all the m energy levels of the continuous density of VBT states using Eq (A.11) and Eq (A.12) to get the total R-G statistics of the VBT as shown in the following equations:

$$R_{VB}^{tot} = \sum_m R_{VB} \tag{A.19}$$

$$p_{VB}^{tot} = \sum_m N_D \left(1 - f^0\right) \tag{A.20}$$

Analogous to the VBT, the acceptor like states is considered for CBT resulting in the following equations for the R-G statistics:

$$R_{CB} = N_D \frac{C_p^- C_n^0 \left(np - n_i^2\right)}{C_p^- n + e_p^0 + C_n^0 p + e_n^-} \tag{A.21}$$

$$e_n^- = C_n^0 N_c \exp\left[\left(E_T - E_c\right)/kT\right] \tag{A.22}$$

$$e_p^0 = C_p^- N_v \exp\left[\left(E_v - E_T\right)/kT\right] \tag{A.23}$$

$$f^- = \frac{C_n^0 n + e_p^0}{C_n^0 n + e_n^- + C_p^- p + e_p^0} \tag{A.24}$$

With the above equations, The recombination and trapped electron concentration is then integrated over all the m energy levels of the continuous density of CBT states using Eq (A.11) and Eq (A.13) to get the total R-G statistics of the VBT as shown in the following equations:

$$R_{CB}^{tot} = \sum_m R_{CB} \tag{A.25}$$

$$n_{CB}^{tot} = \sum_m N_A f^- \tag{A.26}$$

For the DB states on the other hand, Sah and Shockley multi-state approach is used [39]. This theory is based on the fact that DB states can exist as positive (D^+), neutral (D^0) and negative (D^-). Its band diagram is represented by two energy levels $E^{+/0}$ and $E^{0/-}$. The transitions of the amphoteric DB states and the extended states (VB and CB) is similar to SRH process but takes multi-level approach of donor-like and acceptor-like energy level in the band diagrams. Its transitions can be illustrated in Fig A.2.

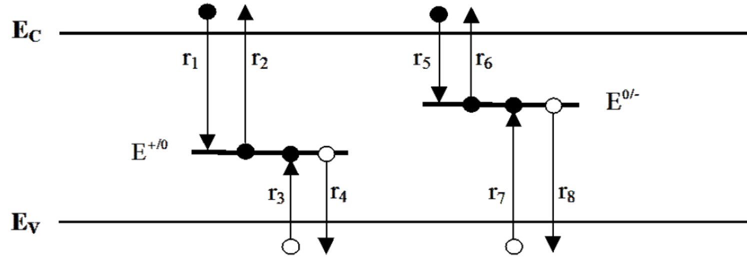

Figure A.2: Sah and Shockley recombination process between energy levels at band-gap and the extended states [39][51]

The emission coefficients is determined from the principle of detailed balance and is given by the equations:

$$e_n^0 = C_n^+ N_c \exp\left[\frac{(E - kT\ln 2) - E_c}{kT}\right] \tag{A.27}$$

$$e_p^+ = C_p^0 N_v \exp\left[\frac{E_v - (E - kT\ln 2)}{kT}\right] \tag{A.28}$$

$$e_n^- = C_n^0 N_c \exp\left[\frac{(E + U + kT\ln 2) - E_c}{kT}\right] \tag{A.29}$$

$$e_p^0 = C_p^- N_v \exp\left[\frac{E_v - (E + U + kT\ln 2)}{kT}\right] \tag{A.30}$$

The probability of the DB state being positive, neutral and negative is given by its occupation function F^+, F^0 and F^- respectively and its sum is supposed to be unity. The occupation functions are given by the following equations:

$$F^+ = \frac{P^- P^0}{N^+ P^- + P^0 P^- + N^+ N^0} \tag{A.31}$$

$$F^0 = \frac{P^- N^+}{N^+ P^- + P^0 P^- + N^+ N^0} \tag{A.32}$$

$$F^- = \frac{N^0 N^+}{N^+ P^- + P^0 P^- + N^+ N^0} \tag{A.33}$$

where:

$$N^+ = C_n^+ n + e_p^+ \tag{A.34}$$

$$P^0 = C_p^0 p + e_n^0 \tag{A.35}$$

$$N^0 = C_n^0 n + e_p^0 \tag{A.36}$$

$$P^- = C_p^- p + e_n^- \tag{A.37}$$

The R-G statistics for the DB states for energy levels $E^{+/0}$ and $E^{0/-}$ in the band-gap is given by Eq (A.38):

$$R_{DB} = N_{DB}\left(np - n_i^2\right)\frac{C_n^+ C_p^0 P^- + C_n^0 C_p^- N^+}{N^+ P^- + P^0 P^- + N^+ N^0} \tag{A.38}$$

Just like VBT and CBT, the total R-G statistics for the DB states and the total concentration of holes and electrons in the DB states is given by the following equations:

$$R_{DB}^{tot} = \sum_m R_{DB} \quad \text{(A.39)}$$

$$p_{DB}^{tot} = \sum_m N_{DB} F^+ \quad \text{(A.40)}$$

$$n_{DB}^{tot} = \sum_m N_{DB} F^- \quad \text{(A.41)}$$

Finally, the total R-G statistics and the total space charge for all the localized states in the band-gap is given by the following equations:

$$R_{net} = R_{VB}^{tot} + R_{CB}^{tot} + R_{DB}^{tot} \quad \text{(A.42)}$$

$$\rho_{loc}^{tot} = q\left(p_{VB}^{\text{tot}} - n_{CB}^{\text{tot}} + p_{DB}^{\text{tot}} - n_{DB}^{\text{tot}}\right) \quad \text{(A.43)}$$

It is important to not that these models do not take into account the strong dependence of carrier mobility, minority carrier lifetime and bang-gap as a function of electric field, doping and temperature for crystalline semiconductors and has to be included in the modelling [51].

A.1.3. Recombination-Generation (R-G) statistics for crystalline semiconductors

For crystalline materials, the SRH lifetime is included to show the strong dependence on the doping and the temperature of the material. The following relation is used to describe the increase in the recombination process due to the temperature and doping effects [51]:

$$\tau(T) = \tau_0 \left(\frac{T}{T_0}\right)^{\alpha} \quad \text{(A.44)}$$

$$\tau(N) = \tau_0 \left(\frac{N}{N_{\text{onset}}}\right)^{\beta} \quad \text{for } N > N_{\text{onset}} \quad \text{(A.45)}$$

here τ_0 is the lifetime of holes or electrons at temperature T_0 (the default value is 300K), with N and N_{onset}, the impurity concentration and the impurity concentration at onset respectively.

Apart from SRH recombination, Auger recombination (also known as a three particle recombination process) which is dominant with heavy doping and Direct recombination (also known as radiative recombination) are also other recombination processes that can occur in crystalline semiconductors [51]. For the Auger recombination, the recombination rate is given by Eq (A.46):

$$R = \left(C_n n + C_p p\right)\left(pn - n_i^2\right) \quad \text{(A.46)}$$

$$C_n = C_{nLI}\left(\frac{N_D}{N_D + p}\right) + \frac{C_{HI}}{2}\left(\frac{p}{N_D + p}\right) \quad \text{(A.47)}$$

$$C_p = C_{pLI}\left(\frac{N_A}{N_A + n}\right) + \frac{C_{HI}}{2}\left(\frac{n}{N_A + n}\right) \quad \text{(A.48)}$$

where C_{nLI} and C_{pLI} are the Auger capture rates for electrons and holes respectively and C_{HI} is the capture rate at high level injection. Direct recombination is given by Eq (A.49) where B is a constant:

$$R = B\left(pn - {n_i}^2\right) \quad \text{(A.49)}$$

A.2. Optical modelling - In depth Analysis

One of the main goals of any semiconductor device is to maximize the light absorption when light is introduced to the semiconductor material. A knowledge optical generation rate parameter G_{opt} is an important to achieve accurate generation rate profile. A typical semiconductor device can have multiple layers (both thin and thick layers) with or without texturing. Use of simple absorption formulas like the Lambert-Beer law may need to be replaced by more complex optical models. Starting with the Lambert-Beer approach, other optical models like the GenPro models will also be discussed.

A.2.1. Lambert-Beer law

This law is based on the fact that photon flux density reduces after passing a certain distance into the semiconductor device due to light absorption [51]. The photon flux density at a certain thickness into the material for a certain wavelength (λ) of light is given by the Eq. (A.50):

$$\Phi(x,\lambda) = \Phi^0(\lambda)\exp(-\alpha(\lambda)x) \tag{A.50}$$

$$\Phi^0(\lambda) = P(\lambda)\frac{\lambda}{hc} \tag{A.51}$$

where Φ^0 is the photon flux density for an incident light of a certain wavelength, $\alpha(\lambda)$ is the absorption coefficient of the material for a certain wavelength of light and x is the distance into the material. As seen in Eq. (A.51), the photon flux density can be related to irradiance. The spectral generation rate $g_{sp}(x,\lambda)$ relates to the number of electron-hole pair generated at a certain thickness into the device at a certain wavelength of light [51]. This is then integrated over the wavelengths of light to get the optical generation rate G_{opt}. These two parameters are calculated in the following equation:

$$g_{sp}(x,\lambda) = \eta_g \Phi^0(\lambda)\alpha(\lambda)e^{-\alpha(\lambda)x} \tag{A.52}$$

$$G_{opt}(x) = \int_{\lambda_1}^{\lambda_2} g_{sp}(x,\lambda)d\lambda \tag{A.53}$$

where η_g is the generation quantum efficiency. This value is unity if one electron-hole pair generated by one photon is assumed. The $G_{opt}(x)$ can also be related to the absorption profile $A(x)$ by Eq. (A.54):

$$G_{opt}(x) = \eta_g A(x) \tag{A.54}$$

The above equations can be tuned further to include reflection losses for different layers like the front and back layers to get a more accurate generation profile.

A.2.2. GenPro1: Optical modelling for flat interface

This is based on the coherent light analysis for flat interfaces. It is used for a multi-layer semiconductor device and estimates the optical parameters like reflectance, transmittance and absorptance. A typical semiconductor material is characterized by its complex refractive $\tilde{n} = n - i\kappa$, with n the refractive index of the material and k the extinction coefficient [51]. Reflectance and Transmittance is then calculated that describe the ratio of reflected or transmitted light to the incident light at a particular interface. This is given by the following Fresnel amplitude coefficients for reflection and transmission for an interface between two mediums:

$$\tilde{r} = \frac{\tilde{n}_0 - \tilde{n}_1}{\tilde{n}_0 + \tilde{n}_1} \tag{A.55}$$

$$\tilde{t} = \frac{2\tilde{n}_0}{\tilde{n}_0 + \tilde{n}_1} \quad (\tilde{t} = 1 + \tilde{r}) \tag{A.56}$$

where $\tilde{n}_0$ and $\tilde{n}_1$ are the complex refractive index of medium 0 and 1. $\tilde{r}$ and $\tilde{t}$ are complex numbers for the reflection and transmission. The Reflectance and Transmittance can be found by the following equations:

$$R = |\tilde{r}|^2 \tag{A.57}$$

$$T = 1 - R \tag{A.58}$$

When the light is incident at an angle to the surface, the reflectance and transmittance will also change as shown in Fig A.3. Snell's law is used is indicate the ratio between incident angle (given by θ_0) and reflected angle (given by θ_1) at the interface for a non-absorbing medium as given in Eq. (A.59) [51]. If an absorbing medium is used, then complex refractive indices and angles need to be used in Eq. (A.59) instead:

$$\frac{n_0}{n_1} = \frac{\sin(\theta_1)}{\sin(\theta_0)} \tag{A.59}$$

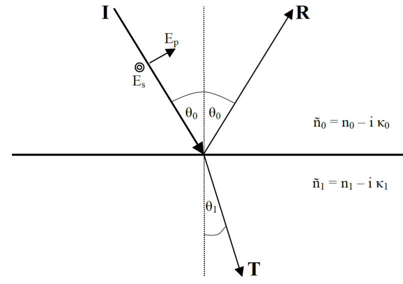

Figure A.3: Reflection and Transmission of incident light on a flat interface [51].

If the polarised light is taken into consideration, the complex refractive indices will differ for s-polarised (electric field is perpendicular to the plane of incidence given by Es in Fig A.3) and p-polarised light (electric field is parallel to the plane of incidence given by Ep in Fig A.3) [51]. The effective complex refractive index for s and p polarise light is given by:

$$\tilde{n}_{is,eff} = \tilde{n}_i \cos\tilde{\theta}_i \tag{A.60}$$

$$\tilde{n}_{ip,eff} = \frac{\tilde{n}_i}{\cos\tilde{\theta}_i} \tag{A.61}$$

Equations from (A.55) to (A.58) can then be used to find its respective reflectance and and transmittance. The final reflectance and transmittance is the mean of the polarised reflectance and transmittance respectively [51].

When we take a layer with two flat surfaces into consideration, light absorption and phase shift of light can take place for a medium with a certain thickness. Multiple reflections has to be taken into account making calculation of reflectance and transmittance complex. We will take two cases of optical behavior with respect to a beam of light [51].

For the first case, If the thickness of a layer is substantially smaller than the coherence length of the light incident on the system, it is said to be coherent. For a normally incident light, the reflectance R, transmittance T and total absorption A can be calculated using the following equations from Fresnel coefficients of reflection and transmission of interfaces 1 and 2 as shown in Fig A.4 [51]:

$$\tilde{r} = \tilde{r}_1 + \frac{\tilde{t}_1\tilde{t}'_1\tilde{r}_2 e^{-2i\tilde{\delta}_1}}{1-\tilde{r}_2\tilde{r}'_1 e^{-2i\tilde{\delta}_1}} \tag{A.62}$$

$$\tilde{t} = \frac{\tilde{t}_1\tilde{t}_2 e^{-i\tilde{\delta}_1}}{1-\tilde{r}_2\tilde{r}'_1 e^{-2i\tilde{\delta}_1}} \tag{A.63}$$

$$\tilde{\delta}_1 = \frac{2\pi}{\lambda} d_1\tilde{n}_1 = \frac{2\pi}{\lambda} d_1\left(n_1 - i\kappa_1\right) \tag{A.64}$$

$$R = |\tilde{r}|^2 \tag{A.65}$$

$$T = \left|\frac{\tilde{n}_2}{\tilde{n}_0}\right| |\tilde{t}|^2 \tag{A.66}$$

$$A = 1 - R - T \tag{A.67}$$

Where $\tilde{\delta}_1$ is the complex phase shift of light with the real part the phase shift of light and the imaginary part the light absorption thoughout the layer thickness d_1. Finally, the normalized absorption in the layer is given by Eq. (A.68):

$$A'(x) = \alpha_1 \left|\frac{\tilde{n}_1}{\tilde{n}_0}\right| \left|\tilde{t}_1\right|^2 \left|\frac{e^{-i\tilde{\delta}_1 x/d_1} + \tilde{r}_2 e^{-i\tilde{\delta}_1} e^{-i\tilde{\delta}_1 (d_1 - x)/d_1}}{1-\tilde{r}_2\tilde{r}'_1 e^{-2i\tilde{\delta}_1}}\right|^2 \tag{A.68}$$

where α_1 is the absorption coefficient of the layer

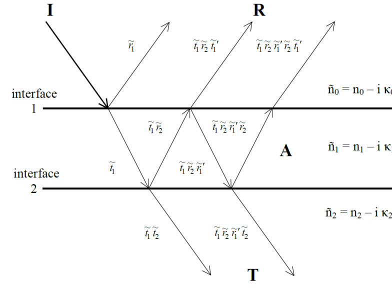

Figure A.4: Reflection and Transmission of incident light on a layer with two interfaces [51].

There is no interference effect in the second case of an incoherent layer where light frequency and wavelengths are not in phase, hence the reflectance and transmittance are computed by adding the the square of the amplitudes together rather than the amplitudes itself [51]. The reflectance, transmittance, absorption, and normalized absorption profile are then calculated using the following equations:

$$R = R_1 + \frac{T_1 R_2 T_1' e^{-2\alpha_1 d_1}}{1 - R_2 R_1' e^{-2\alpha_1 d_1}} = |\tilde{r}_1|^2 + \frac{\left|\tilde{t}_1\right|^2 |\tilde{r}_2|^2 \left|\tilde{t}_1'\right|^2 e^{-2\alpha_1 d_1}}{1 - |\tilde{r}_2|^2 |\tilde{r}_1'|^2 e^{-2\alpha_1 d_1}} \tag{A.69}$$

$$T = \frac{T_1 T_2 e^{-\alpha_1 d_1}}{1 - R_2 R_1' e^{-2\alpha_1 d_1}} = \left|\frac{\tilde{n}_2}{\tilde{n}_0}\right| \frac{\left|\tilde{t}_1\right|^2 \left|\tilde{t}_2\right|^2 e^{-\alpha_1 d_1}}{1 - |\tilde{r}_2|^2 |\tilde{r}_1'|^2 e^{-2\alpha_1 d_1}} \tag{A.70}$$

$$A = 1 - R - T \tag{A.71}$$

$$A'(x) = \alpha_1 \left|\frac{\tilde{n}_1}{\tilde{n}_0}\right| \left|\tilde{t}_1\right|^2 \frac{e^{-\alpha_1 x} + |\tilde{r}_2|^2 e^{-\alpha_1 (2d_1 - x)}}{1 - |\tilde{r}_2|^2 |\tilde{r}_1'|^2 e^{-2\alpha_1 d_1}} \tag{A.72}$$

Using the Fresnel coefficients for the interfaces of a coherent or incoherent single layer, we iteratively use this approach of characterizing a layer as an effective interface to all subsequent layers of the system in the case of a multi-layer structure. The entire multi-layer structure is characterized as one effective interface at the end, and the layer's reflectance, transmittance, and absorption can be estimated using the equations above equations for coherent or incoherent layers [51].

A.2.3. GenPro2: Optical modelling for rough interfaces by incoherent analysis

GenPro2 model uses incoherent analysis for all multi-layer semiconductors with both flat and rough interfaces. This model is used for devices that employ light trapping techniques with the use of texturing that scatter light (diffuse light) in different angles [51]. By the concept of conservation of energy:

$$R_s + T_s + \sum R_d + \sum T_d = 1 \tag{A.73}$$

where R_s is the specular reflectance, T_s is the specular transmittance, R_d is the diffuse reflectance and T_d is the diffuse transmittance. A rough interface is defined as a flat interface with minor perturbations that induce dispersion in this model. In general, the reflectance and transmittance for a rough surface is a function of incoming and outgoing light (Ω_{in}, Ω_{out}), the root mean square roughness (σ_r) and the root mean square slope m [51]. In a real device, the incident light on a rough surface can scatter in all directions into the surface and can be described as a half sphere distribution of outgoing light. This half sphere as shown in Fig A.5 is described by a solid angle $\Omega = (\theta, \phi)$ with $0 \leq \theta < \pi/2, -\pi \leq \varphi \leq \pi$. Assumption is made that light is distributed uniformly along ϕ and therefore independent. The light intensity F is then given in terms of solid angle in Eq. (A.74) [51].

$$F(\Omega) = F(2\pi \sin\theta) \tag{A.74}$$

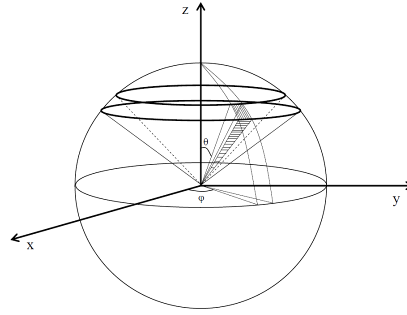

Figure A.5: Solid angle distribution of light for a rough surface [51]

Using the solid angle distribution of intensity F, an array of NxN elements can be made for reflectance and transmittance of light between multiple layers for specular and diffuse light. Let us take an example of an interface with incident lights from above and below the interface as shown in Fig A.6 [51].

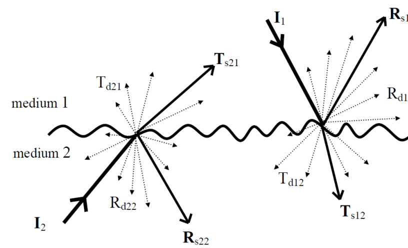

Figure A.6: Reflection and transmission processes for a rough interface [51]

Let the light intensities (up/down direction) in the first and second medium be F_1^-/F_1^+ and F_2^-/F_2^+ respectively. They are given by the following equations:

$$F_1^- = R_{11}F_1^+ + T_{21}F_2^- \tag{A.75}$$

$$F_2^+ = T_{12}F_1^+ + R_{22}F_2^- \tag{A.76}$$

For the multi-rough surfaces with light scattering, we use assumptions that a rough surfaces reflects the same intensity of light as a flat surface and can be represented by total reflection of the interface including specular and diffuse light as given in Eq. (A.77) [51]:

$$R_s + \sum_{\theta_{\text{out}}} R_d = R_{\text{tot}} = R_{\text{flat}} \tag{A.77}$$

Also the relation between the diffused reflected light and the total reflected light is given by Eq. (A.78):

$$R_d\left(\lambda, \theta_{\text{in}}, \theta_{\text{out}}\right) = H_R\left(\lambda, \theta_{in}\right) f_R\left(\lambda, \theta_{\text{out}}\right) R_{\text{flat}}\left(\lambda, \theta_{\text{in}}, \theta_{\text{out}}\right) \tag{A.78}$$

$$H_R\left(\lambda, \theta_{in}\right) = C_R(\lambda) f_R\left(\lambda, \theta_{in}\right) \tag{A.79}$$

where $H_R\left(\lambda, \theta_{in}\right)$ is the haze parameter for reflected light which defines the scattering level, C_R is the scattering coefficient which is the ratio of diffuse and total reflected light and $f_R\left(\lambda, \theta_{\text{out}}\right)$ is the angular distribution function of reflected light. The similar concept can be applied for specular and diffuse transmitted light as given by the following equations:

$$T_s + \sum_{\theta_{\text{out}}} T_d = T_{\text{flat}} \tag{A.80}$$

$$T_d\left(\lambda, \theta_{\text{in}}, \theta_{\text{out}}\right) = H_T\left(\lambda, \theta_{in}\right) f_T\left(\lambda, \theta_{\text{out}}\right) T_{\text{flat}}\left(\lambda, \theta_{\text{in}}, \theta_{\text{out}}\right) \tag{A.81}$$

$$H_T(\lambda, \theta_{in}) = C_T(\lambda) f_T(\lambda, \theta_{in}) \quad \text{(A.82)}$$

Finally, similar to GenPro1 model, We iteratively apply this approach of characterizing a layer as an effective interface to all subsequent layers of the system in the case of a multi-layer structure. Assuming that the incoming light intensities F_1^+ and F_m^-, optical properties of all media, and the scattering qualities of all interfaces are all known, the light intensity F may be computed at every interface of a multilayer structure (with m media) [51]. The wavelength absorption profile in the j-th medium is given by Eq. (A.82):

$$A_j(\lambda, x_j) = \int \frac{\alpha_j}{\cos(\theta)} F_{j,x_j}^-(\Omega) d\Omega + \int \frac{\alpha_j}{\cos(\theta)} F_{j,x_j}^+(\Omega) d\Omega \quad \text{(A.83)}$$

where F_{j,x_j}^+ and F_{j,x_j}^- are the downwards and upwards light intensities at a device depth of x_j of the j-th medium [51]. The normalised absorption profile is found using Eq. (A.83) and the generation rate profile is calculated by integrating the absorption profile over the wavelength spectrum as given in (A.84):

$$A_j'(\lambda, x_j) = \frac{A_j(\lambda, x_j)}{\sum_\Omega F_1^+(\lambda, \Omega)} \quad \text{(A.84)}$$

$$G_j(x) = \int A_j'(\lambda, x_j) \eta_g(\lambda) \Phi^0(\lambda) d\lambda \quad \text{(A.85)}$$

where $\Phi^0(\lambda)$ is the photon flux density.

A.2.4. GenPro3: Optical modelling for rough interfaces by semi-coherent analysis

In GenPro2 model, interference effect is not included since specular light is assumed to be incoherent which is not true for realistic solar cells. GenPro3 model uses the combination of GenPro1 model for coherent analysis for specular light and GenPro2 model for incoherent analysis for diffused light [51].

The coherent analysis of specular light is conducted first where modified Fresnel coefficients $\tilde{r}_{\text{spec}}$ and $\tilde{t}_{\text{spec}}$ for reflectance and transmittance respectively, is used for textured interface as given in the following equations:

$$\tilde{r}_{\text{spec}} = \tilde{r} \cdot \sqrt{1 - H_R} = \frac{\tilde{n}_0 - \tilde{n}_1}{\tilde{n}_0 + \tilde{n}_1} \cdot \sqrt{1 - H_R} \quad \text{(A.86)}$$

$$\tilde{t}_{\text{spec}} = \tilde{t} \cdot \sqrt{1 - H_T} = \frac{2\tilde{n}_0}{\tilde{n}_0 + \tilde{n}_1} \cdot \sqrt{1 - H_T} \quad \text{(A.87)}$$

where H_R and H_T are the haze parameters for reflected and transmitted light as seen in Eq. (A.79) and Eq. (A.82) respectively. For flat surface, $H_R = H_T = 0$ whereas for rough surface, H_R and H_T is between 0 and 1. After this, normal GenPro1 calculations as seen in Section A.2.2 is conducted to determine coherent specular light intensities for textured surfaces for incoming light intensities $I_{inc1(coh)}$ and $I_{inc2(coh)}$ for example as shown in Fig A.7 [51].

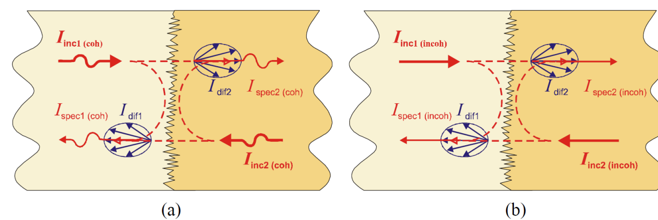

Figure A.7: Simulation of incident light for textured surface by a)coherent analysis b)incoherent analysis [51]

$I_{inc1(coh)}$ and $I_{inc2(coh)}$ after reflection and transmission, a part of this light is specular while the other other art is diffused. Calculation of diffused light requires values of I_{inc1} and I_{inc2} but these values

are different for coherent and incoherent analysis. The next step is to conduct incoherent analysis using GenPro2 model as seen in Section A.2.3 for I_{inc1} and I_{inc2} to get $I_{inc1(incoh)}$ $I_{inc2(incoh)}$ and are multiplied with a certain correction factor c_1 and c_2 to achieve the same value of light intensities calculated from coherent analysis [51]. These factors are given in the following equations:

$$c_1 = \frac{I_{inc1(coh)}}{I_{inc1(incoh)}} \tag{A.88}$$

$$c_2 = \frac{I_{inc2(coh)}}{I_{inc2(incoh)}} \tag{A.89}$$

These factors are correctly applied to reflectances and transmittances of the interfaces in GenPro2 model, rather than intensities, resulting in the same effect. Specular light can still be classified as incoherent during the calculation of dispersed light if this correction is only applied to specular intensities. The incoherent specular part is replaced with the one estimated in the coherent analysis in the first step at the end of incoherent analysis. The ultimate outcome of semi-coherent analysis with the GenPro3 optical model is essentially the consequence of this substitution [51].

A.2.5. GenPro4: Optical modelling using ray and wave optics

A new generation of optical simulations in 1D can be performed using a MATLAB-based program called GenPro4, developed by Santbergen et al. [41] at the Delft University of Technology. Reflectance (R), transmittance (T), and absorptance (A) spectra of each layer of a solar cell, as well as their implied photocurrent densities (J_ph), can be generated with this optical model very accurately. Here wave and ray optics are combined in this optical model [41]. This model is based on the net-radiation flux method with an addition of light scattering effects on textured interfaces. It accounts for interference effects in thin layers and small textures with sizes close to the wavelength of light, as well as basic ray optics in thick layers or large textured layers [41].

Let us take a flat multi-layer device as shown in Fig A.8 to illustrate the net radiation method. At each interface, incoming and outgoing fluxes are defined at both sides of the interface [41]. The net radiation (in W/m^2) due to all possible photon pathways is represented by each flux by a set a of linear equations:

$$\begin{cases} q_i^a = \tau_i \cdot q_{i-1}^d \\ q_i^b = r_i \cdot q_i^a + t_i \cdot q_i^c \\ q_i^c = \tau_{i+1} \cdot q_{i+1}^b \\ q_i^d = t_i \cdot q_i^a + r_i \cdot q_i^c \end{cases} \tag{A.90}$$

where q_i^x is the flux at interface i approaching from above or below the interface (x=a,b,c,d), r_i and t_i are the interface reflectance and transmittance respectively found using Fresnel equations and τ_i is the layer transmittance calculated from Lambert-Beer law. All fluxes can be normalized to incident power so that they can be written in non-dimensional form. Assuming that all light is incident from the top and none from the bottom, $q_1^a = 1$ and $q_I^c = 0$ are obtained, where I is the total number of interfaces [41]. R, T and A_i (which is the sum of flux entering minus the flux leaving the interface) can then be extracted by the following equations:

$$R = q_1^b \tag{A.91}$$

$$T = q_I^d \tag{A.92}$$

$$A_i = q_{i-1}^d - q_{i-1}^c + q_i^b - q_i^a \tag{A.93}$$

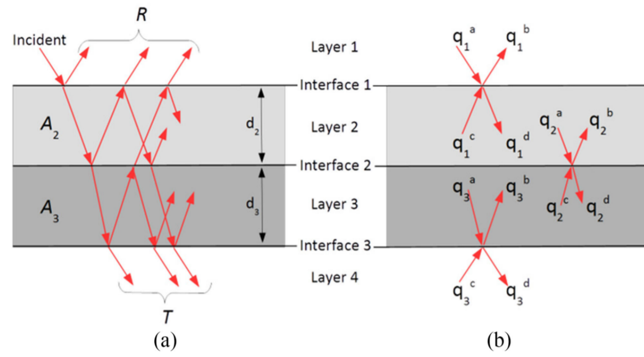

Figure A.8: A multi-layer structure with the numbering convention for layers and interfaces. a)Optical paths contributing to R, T and A_i b)Net-radiation fluxes.

However, this approach can only be used for thick incoherent "layers" (thick compared to the length of coherence of light which is approximately 1 micrometer). To simulate for thin coherent "coatings" (thin layers are considered to be coatings for GenPro4 simulation) and take interference into account, wave equations (that contain complex electromagnetic wave information) is used to represent fluxes [41].

Similar to the net radiation method for flat interfaces, textured interfaces can also simulated the same way except that the light can be propagated towards multiple directions due to light scattering. These directions can be represented in the form of a hemisphere subdivided with angular intervals (representing a sub flux in the form of a cone with 30 sub fluxes in one flux) as shown in Fig A.9 [41]. Every point in the propagation can be expressed in the form of azimuth (ϕ) and zenith (θ) angle. Sub flux equations can then be expressed in terms of angular interval in the hemisphere as shown below:

$$\begin{cases} \boldsymbol{q}_i^a = \boldsymbol{\tau}_i \cdot \boldsymbol{q}_{i-1}^d \\ \boldsymbol{q}_i^b = \boldsymbol{r}_i^+ \cdot \boldsymbol{q}_i^a + \boldsymbol{t}_i^- \cdot \boldsymbol{q}_i^c \\ \boldsymbol{q}_i^c = \boldsymbol{\tau}_{i+1} \cdot \boldsymbol{q}_{i+1}^b \\ \boldsymbol{q}_i^d = \boldsymbol{t}_i^+ \cdot \boldsymbol{q}_i^a + \boldsymbol{r}_i^- \cdot \boldsymbol{q}_i^c \end{cases} \tag{A.94}$$

Here these sub fluxes are found for all the angular intervals V (usually 30 for good accuracy) and stored in a form of a matrix ($q_i^x(1)....q_i^x(V)$). Similarly $\boldsymbol{r}_i$, $\boldsymbol{t}_i$ and $\boldsymbol{\tau}_i$ are also in the form of a VxV matrix (here $\boldsymbol{r}_i$, $\boldsymbol{t}_i$ are also referred to as scattering matrices). The superscripts "+" and "–" are used to differentiate the $\boldsymbol{r}_i$ and $\boldsymbol{t}_i$ matrices for light incident on interface i from the top and bottom, respectively.

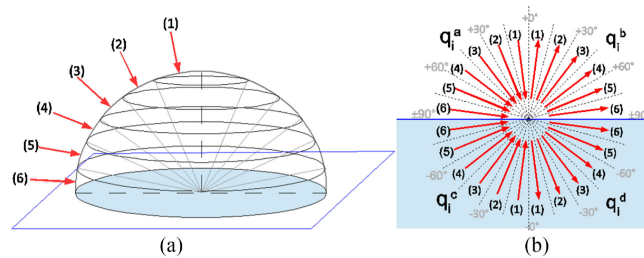

Figure A.9: a) Propagation of light with different angular intervals in a hemispherical form at an interface b) Sub fluxes at interface 1 [41].

Similar to the net radiation flux for flat interfaces, R, T and A_i (which is the sum of flux entering minus the flux leaving the interface) can then be extracted for textured interfaces by summing up all the sub fluxes for different angular interval at a particular interface and the propagation direction [41]. This is given by the following equations:

$$R = \sum \boldsymbol{q}_1^b \tag{A.95}$$

$$T = \sum \boldsymbol{q}_I^d \tag{A.96}$$

$$A_i = \sum \boldsymbol{q}_{i-1}^d - \sum \boldsymbol{q}_{i-1}^c + \sum \boldsymbol{q}_i^b - \sum \boldsymbol{q}_i^a \tag{A.97}$$

To summarise, each interface i is defined by four scattering matrices ($\boldsymbol{r}_i^+$, $\boldsymbol{t}_i^+$, $\boldsymbol{r}_i^-$, $\boldsymbol{t}_i^-$). The matrix element (u,v) is used to represent the likelihood that a photon incident from angular interval v will end up at interval u following reflection or transmission. For flat interfaces, a simple ray-optics model based on the Fresnel equations for reflectance and transmittance and Snell's law for refraction angles is utilized. Wave phenomena such as interference and diffraction must be considered for surface textures with features smaller than the wavelength. GenPro4 was used to implement the scalar scattering model described by Jäger et al. [23, 24]. A height map of the surface morphology is used as input for this model. Wave effects can be neglected for surface textures with large feature sizes compared to wavelengths, and ray optics can be used instead. GenPro4 does this with the help of a built-in ray tracing model. Incident rays from interval u are emitted onto the textured interface to calculate column u of the interface matrix, and the angular intensity distribution of rays reflected and transmitted by the interface is recorded. This process is repeated for every incident angular interval. More information on the calculations that are done can be referred from [41].

B

Tunnel Recombination Models - additional models

B.1. Direct Tunneling

In DT method (also called quantum tunneling method or intra-band tunnelling), the electrons/holes from one semiconductor material band-edge can tunnel through the forbidden states of the insulating layer and cross the other side of the insulating layer to the same band edge (CB-CB/VB-VB) of similar energy states of another semiconductor material. There are different models related to direct tunneling given in literature, but we shall focus on few models that are have simple and accurate expression for the tunneling parameters.

B.1.1. Direct tunneling model proposed by Varache et al.

The model proposed by Varache et al. [48] is based on the Yang's direct tunneling model [50] where tunneling through a insulating layer in either VB or CB with band discontinuities at the hetero-junction of two semiconductors were taken into account as shown in Fig B.1.

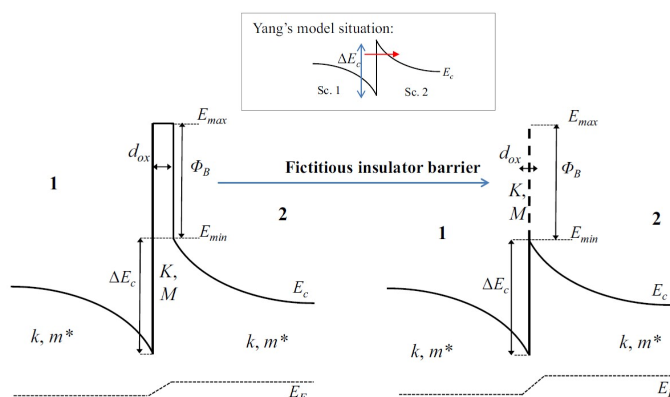

Figure B.1: Energy band diagram for a semiconductor/insulator/semiconductor layers [50]

However Varache et al. [48] proposed a similar model that was implemented in AFORS-HET (1D solar simulator). This model assumes a fictitious insulating layer in between two semiconductors. The insulator layer is addressed analytically instead of directly modeling it, i.e. solving the semiconductor equations in it. The input parameters for the analytic computation are taken from the semiconductor/semiconductor interface grid-points. To arrive at the tunnelling model, following assumptions were made. (i) No energy was lost during the tunnelling process, (ii) the tunnelling mass was same on either side of the barrier and (iii) a rectangular tunnel barrier was considered. The foundation of all the tunneling models used by Verache et al. [48] was based on the Tsu-Esaki formula that was also used for

the direct tunneling model proposed by Ieong et al. [18]. This is given below in Eq. (B.1) as a function of energy E:

$$J_{e,tun} = \frac{4\pi \text{qm}^*}{h^3} \int_{E_{\text{min}}}^{+\infty} T(E)N(E)dE \tag{B.1}$$

where $N(E)$ is the number of particles likely to tunnel, $T(E)$ is the tunnelling probability of an electron through the barrier, E_{min} is the minimum CB band edge energy. $T(E)$ can be analytically derived and can be given in the below expressions for two cases, one if the tunneling energy of the electron is greater than the maximum barrier energy for tunnelling of the insulator E_{max} and two, if the tunneling energy of the electron is less than the maximum barrier energy for tunnelling of the insulator E_{max}:

$$T_{\text{tun}}(E) = \frac{4K^2 k_1 k_2}{K^2 (k_1 + k_2)^2 + (K^2 + k_1^2)(K^2 + k_2^2) \sinh^2 (K d_{ox})} \text{ for } E \leq E_{\text{max}} \tag{B.2}$$

$$T_{\text{res}}(E) = \frac{4K^2 k_1 k_2}{K^2 (k_1 + k_2)^2 + (K^2 - k_1^2)(K^2 - k_2^2) \sin^2 (K d_{0x})} \text{ for } E \geq E_{\text{max}} \tag{B.3}$$

where wave vectors (k_1, k_2, K) are given by:

$$\begin{aligned} k_1 &= \sqrt{\tfrac{2m^*}{\hbar^2} (E - E_{\text{min}})}, \quad k_2 = \sqrt{\tfrac{2m^*}{\hbar^2} (E - E_{\text{min}} + \Delta E_C)} \\ K &= \sqrt{\tfrac{2M}{\hbar^2} (E - E_{\text{max}})} \text{ for } E \geq E_{\text{max}}, \quad K = \sqrt{\tfrac{2M}{\hbar^2} (E_{\text{max}} - E)} \text{ for } E \leq E_{\text{max}} \end{aligned} \tag{B.4}$$

where m^* is the effective tunnelling mass of electron in the semiconductor, M is effective tunnelling mass of electron in the insulator, $E_{max} - E_{min}$ represents the barrier height ϕ_B, d_{ox} is the layer thickness of the insulator. The tunnelling and the resonant modes are represented by T_{tun} and T_{res} respectively. $N(E)$ can be represented by the below Eq. (B.5):

$$N(E) = k_B T \left(\text{exp} \left(-\frac{E - E_{F,1}}{k_B T} \right) - \text{exp} \left(-\frac{E - E_{F,2}}{k_B T} \right) \right) \tag{B.5}$$

where $E_{F,i}$ is the quasi-Fermi level for material i. Using Maxwell-Boltzmann approximation on the expression for carrier density, electron tunnelling current $J_{e,tun}$ can be expressed in the following equation:

$$J_{e,tun} = \frac{4\pi \text{qm}^*}{h^3} k_B T \int_{E_{min}}^{+\infty} \left[\frac{n_1}{N_{c,1}} e^{-\frac{E - E_{c,1}}{k_B T}} T(E) - \frac{n_2}{N_{c,2}} e^{-\frac{E - E_{c,2}}{k_B T}} T(E) \right] dE \tag{B.6}$$

When $E_{min} = E_{c,2}$ as shown in Fig B.1 is used and Eq. (B.6) is further simplified, the expression becomes as follows:

$$J_{e,tun} = A^* T^2 \delta \left(\frac{n_2}{N_{c,2}} - \frac{n_1}{N_{c,1}} e^{-\frac{\Delta E_c}{k_B T}} \right) \tag{B.7}$$

where δ is the tunnelling factor and is given by:

$$\delta = \int_0^{\frac{\phi_B}{k_B T}} e^{-u} T_{\text{Tun}} (k_B T u + E_{\text{min}}) \, du + \int_{\frac{\phi_B}{k_B T}}^{+\infty} e^{-u} T_{\text{Tres}} (k_B T u + E_{\text{min}}) \, du \tag{B.8}$$

When electrostatic potential drop is accounted, with large inter-facial electric fields, the band diagram can be slightly changed in comparison to the scenario when there is no tunnel barrier or when the barrier is rectangular, as shown schematically in Fig B.2. The barrier height is increased or decreased by half the amount of the electrostatic potential drop Δ_V in the insulator in this approximation. The inter-facial electric field E_{int}, which is believed to be constant in the insulator layer, is used to determine Δ_V. Also the effective barrier height $\phi_{B,eff}$ can be determined in the following equations:

$$\Delta V = -d_{0x} \frac{\epsilon}{\epsilon_{0x}} E_{int} \tag{B.9}$$

$$\Phi_{B,eff} = \Phi_B - \frac{\Delta V}{2} \tag{B.10}$$

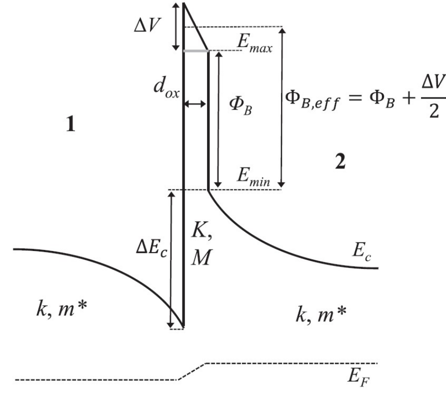

Figure B.2: Energy band diagram taking into account the electrostatic potential drop [48]

B.2. Band to Band Tunneling

In BBT method (also called inter-band tunnelling or zener tunnelling), the electrons/holes from one semiconductor material band-edge can tunnel through the forbidden states of the insulating layer and cross the other side of the insulating layer to a different band edge (CB-VB/VB-CB) of similar energy states of another semiconductor material. There are different models related to band to band tunneling given in literature, but we shall focus on few models that are have simple and accurate expression for the tunneling parameters [31, 45].

B.2.1. Band to band tunnelling model proposed by Hurkx et al.

The BBT model by Hurkx et al. [15] is very similar to the simple BBT models by Kane and Keldyshs as seen above. Like any other BBT method, Local band bending may be sufficient to allow electrons to tunnel from the VB into the CB if a sufficiently strong electric field exists within the device. The right-hand side of the continuity equations includes this additional generation/recombination process. According to Hurkx et al. [15], this additional generation/recombination process due to BBT tunnelling is given below in Eq. (B.11):

$$R_{BBT-Hurkx} = ADE^P \,\text{exp}\left(-\frac{BE_{\text{g}}(T)^{3/2}}{E_{\text{g}}(300\ \text{K})^{3/2}E}\right) \tag{B.11}$$

This equation is similar to Eq. (**??**). The additional terms include the statistical factor D and the temperature dependence on the energy band-gap of the layer $E_g(T)$. The Statistical factor D is given by Eq. (B.12):

$$D = \frac{np - n_{\text{i,eff}}^2}{(n + n_{\text{i,eff}})\,(p + n_{\text{i,eff}})}(1 - |\alpha|) + \alpha \tag{B.12}$$

here the original equation of Hurkx is obtained if $\alpha = 0$. If $\alpha = 1$ results in the recombination process as seen in Eq. (B.11) while $\alpha = -1$ results in the generation process. $n_{i,eff}$ is the effective intrinsic concentration of charge carriers. In many simulation softwares like TCAD Sentaurus and Silvaco Atlas, $\alpha = 0$ by default and the original Hurkx equation is used but can be changed by the user [15, 31]. The different values of the coefficients A, B and P can be represented in the Table B.1:

Table B.1: Coefficients for the Hurkx BBT model [15, 31, 45]

P	A	B
2	3.4e21 $cm^{-1}s^{-1}V^{-2}$	2.26e7 Vcm^{-1}
2	9.66e18 $cm^{-1}s^{-1}V^{-2}$	3e7 Vcm^{-1}
2.5	4e14 $cm^{-1/2}s^{-1}V^{-5/2}$	1.9e7 Vcm^{-1}

B.2.2. Band to band tunnelling model proposed by A.Schenk

A. Schenk conducted a thorough investigation on BBT model [42]. After developing a rigorous theory, an approximation solution acceptable for device simulations was produced. He demonstrates that phonon aided BBT is typically dominant compared to any other BBT processes (for example direct BBT). As a result, direct band-to-band tunneling is ignored. The electric field is also assumed to be constant throughout the tunneling length in the model. As a result, it is a local tunnelling model [42]. The generation/recombination process due to Schenk's BBT is given by the following equations:

$$R_{BBT-Schenk} = AE^{7/2}\tilde{D}\left[\frac{\left(E_{\mathrm{C}}^{\mp}\right)^{-3/2}\exp\left(-\frac{E_{\mathrm{C}}^{\mp}}{E}\right)}{\exp\left(\frac{\hbar\omega}{kT}\right)-1}+\frac{\left(E_{\mathrm{C}}^{\pm}\right)^{-3/2}\exp\left(-\frac{E_{\mathrm{C}}^{\pm}}{E}\right)}{1-\exp\left(-\frac{\hbar\omega}{kT}\right)}\right] \tag{B.13}$$

$$\tilde{D} = \frac{\tilde{n}\tilde{p}-n_{\mathrm{i,\,eff}}^2}{\left(\tilde{n}+n_{\mathrm{i,\,eff}}\right)\left(\tilde{p}+n_{\mathrm{i,\,eff}}\right)} \tag{B.14}$$

$$E_{\mathrm{C}}^{\pm} = B\left(E_{\mathrm{g,eff}} \pm \hbar\omega\right)^{3/2} \tag{B.15}$$

In Eq. (B.15), the upper (positive sign) symbol refers to tunnelling recombination ($np < n_{i,eff}^2$) and the lower (negative sign) symbol refers to tunnelling generation ($np > n_{i,eff}^2$), $\hbar\omega = 18.6meV$ refers to the energy of transverse acoustic phonon. $\tilde{n}$ and $\tilde{p}$ in Eq. (B.14) are the modified electron and hole densities respectively and are given by the following equation:

$$\tilde{n} = n\left(\frac{n_{\mathrm{i,eff}}}{N_{\mathrm{C}}}\right)^{\frac{\gamma_n\left|\nabla E_{\mathrm{f},n}\right|}{E}} \quad \tilde{p} = p\left(\frac{n_{\mathrm{i,eff}}}{N_{\mathrm{V}}}\right)^{\frac{\gamma_p\left|\nabla E_{\mathrm{f},p}\right|}{E}} \tag{B.16}$$

$$\gamma_n = n/\left(n+n_{\mathrm{ref}}\right) \quad \gamma_p = p/\left(p+p_{\mathrm{ref}}\right) \tag{B.17}$$

The density correction factors for electrons and holes are given in Eq. (B.17) where n_{ref} and p_{ref} are the reference densities of electrons and holes respectively and is $10^3 cm^{-3}$ by default in most of the simulation softwares [42]. The parameters A and B is given in Table B.2 [31, 45].

Table B.2: Coefficients for the Schenk's BBT model [31, 45]

A	B
8.977e20 $cm^2 s^{-1} V^{-2}$	2.14667e7 $eV^{(-3/2)} V cm^{-1}$

B.2.3. Non-local band to band tunneling model - version 2

The band-to-band tunneling models presented so far in this section determine a recombination-generation rate at each point purely based on the local electric field value. As a result, they are referred to as local tunnelling models. One must account for the spatial variation of the energy bands in order to represent the tunneling process more precisely [27, 45]. One must also consider the fact that the generation and recombination of opposing carrier types do not occur in the same spatial location and can depicted in Fig B.3 for a reverse biased pn junction where the tunneling mechanism is believed to be elastic [27, 45]. Tunneling current may be obtained at forward bias for degenerately doped p-n junctions, resulting in negative differential resistance in the forward I-V curve. Non-local BBT model can allow for modelling of this forward and reverse tunnelling currents [27, 45].

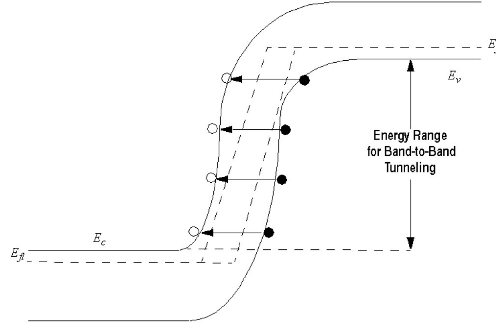

Figure B.3: Non-local BBT method [27, 45]

We now that energy band profile dynamically determines the tunnelling path. This model also does not require the user to specify the non-local mesh. The tunnelling path is therefore determined with the following assumptions. The tunnelling path starts from the VB in the non-local active region. The path is then a straight line in the direction opposite to the VB gradient at the start point. The energy for tunnelling is equal to the VB energy at start point and is also equal to the CB energy plus band offset at the end point where the path ends at CB [31].

Let us consider a path of length l starting from $x = 0$ and ending at $x = l$ with holes generated at the start point and electron generated at the end point. BBT processes include direct BBT or phonon-assisted BBT. For the direct BBT, the recombination rate due to direct BBT process can be given by the following equation followed by its parameter equations:

$$R^{\mathrm{d}}_{\mathrm{BBT-NL}} = |\nabla E_{\mathrm{V}}(0)|\, C_{\mathrm{d}} \exp\left(-2\int_0^l \kappa dx\right)\left[\left(\exp\left[\frac{\varepsilon - E_{\mathrm{f},n}(l)}{kT(l)}\right]+1\right)^{-1} - \left(\exp\left[\frac{\varepsilon - E_{\mathrm{f},p}(0)}{kT(0)}\right]+1\right)^{-1}\right] \tag{B.18}$$

$$C_{\mathrm{d}} = \frac{g\pi}{36h}\left(\int_0^l \frac{dx}{\kappa}\right)^{-1}\left[1-\exp\left(-k_{\mathrm{m}}^2\int_0^l \frac{dx}{\kappa}\right)\right] \tag{B.19}$$

$$\kappa = \frac{1}{\hbar}\sqrt{m_{\mathrm{r}} E_{\mathrm{g,tun}}\left(1-\alpha^2\right)} \tag{B.20}$$

$$\alpha = -\frac{m_0}{2m_{\mathrm{r}}} + 2\sqrt{\frac{m_0}{2m_{\mathrm{r}}}\left(\frac{\varepsilon - E_{\mathrm{V}}}{E_{\mathrm{g,tun}}} - \frac{1}{2}\right) + \frac{m_0^2}{16m_{\mathrm{r}}^2} + \frac{1}{4}} \tag{B.21}$$

$$\frac{1}{m_{\mathrm{r}}} = \frac{1}{m_{\mathrm{V}}} + \frac{1}{m_{\mathrm{C}}} \tag{B.22}$$

where g is the degeneracy factor, $\epsilon = E_V(0) = E_C(l) + \Delta E_C(l)$ is the tunnelling energy. $\Delta_C(l)$ can be positive for a CB valley where minimum energy is greater than CB energy. κ is the magnitude of the wave-vector, $E_{g,tun} = E_{g,eff} + \Delta E_C$ is the effective bandgap for tunnelling, The maximum valence-band energy ϵ_{max} and the minimum conduction-band energy ϵ_{min} are used to calculate k_m, which is the maximum transverse momentum. This and the effective mass in the CB m_C and VB m_V are given below in the following equations:

$$k_{\mathrm{m}}^2 = \min\left(k_{\mathrm{cm}}^2 = \frac{2m_{\mathrm{C}}\left(\varepsilon - \varepsilon_{\mathrm{min}}\right)}{\hbar^2}, k_{\mathrm{vm}}^2 = \frac{2m_{\mathrm{V}}\left(\varepsilon_{\mathrm{max}} - \varepsilon\right)}{\hbar^2}\right) \tag{B.23}$$

$$\frac{1}{m_{\mathrm{C}}} = \frac{1}{2m_{\mathrm{r}}} + \frac{1}{m_0} \quad \frac{1}{m_{\mathrm{V}}} = \frac{1}{2m_{\mathrm{r}}} - \frac{1}{m_0} \tag{B.24}$$

The recombination rate due to phonon-assisted BBT process can be given by the following equation followed by its parameter equations:

$$
\begin{aligned}
R^{\mathrm{p}}_{\text{BBT-NL}} = |\nabla E_{\mathrm{V}}(0)|\, C_{\mathrm{p}} \exp\left(-2\int_0^{x_0} \kappa_{\mathrm{V}} dx - 2\int_{x_0}^{l} \kappa_{\mathrm{C}} dx\right) \\
\left[\left(\exp\left[\frac{\varepsilon - E_{\mathrm{F},n}(l)}{kT(l)}\right]+1\right)^{-1} - \left(\exp\left[\frac{\varepsilon - E_{\mathrm{F},p}(0)}{kT(0)}\right]+1\right)^{-1}\right]
\end{aligned}
\tag{B.25}
$$

$$
\begin{aligned}
C_{\mathrm{p}} = \int_0^{l} \frac{g\left(1+2N_{\mathrm{op}}\right) D_{\mathrm{op}}^2}{2^6\pi^2\rho\varepsilon_{\mathrm{op}}E_{\mathrm{g,tun}}} \sqrt{\frac{m_{\mathrm{V}} m_{\mathrm{C}}}{hl\sqrt{2m_{\mathrm{r}}E_{\mathrm{g,tun}}}}} dx \left(\int_0^{x_0} \frac{dx}{\kappa_{\mathrm{V}}}\right)^{-1} \left(\int_{x_0}^{l} \frac{dx}{\kappa_{\mathrm{C}}}\right)^{-1} \\
\left[1-\exp\left(-k_{\mathrm{vm}}^2\int_0^{x_0}\frac{dx}{\kappa_{\mathrm{V}}}\right)\right]\left[1-\exp\left(-k_{\mathrm{cm}}^2\int_{x_0}^{l}\frac{dx}{\kappa_{\mathrm{C}}}\right)\right]
\end{aligned}
\tag{B.26}
$$

where $N_{op} = [exp(\epsilon_{op}/kT) - 1]^{-1}$ is the number of optical phonons, ϵ_{op} is the energy of the optical phonons and D_{op} is the deformation potential of the optical phonon, ρ is the mass density. The magnitude of imaginary wavevectors κ_V and κ_C can be given in the following equations:

$$
\kappa_{\mathrm{V}} = \frac{1}{\hbar}\sqrt{2m_{\mathrm{V}}\left|\varepsilon - E_{\mathrm{V}}\right|}\,\Theta\left(\varepsilon - E_{\mathrm{V}}\right) \tag{B.27}
$$

$$
\kappa_{\mathrm{C}} = \frac{1}{\hbar}\sqrt{2m_{\mathrm{C}}\left|E_{\mathrm{C}} + \Delta E_{\mathrm{C}} - \varepsilon\right|}\,\Theta\left(E_{\mathrm{C}} + \Delta E_{\mathrm{C}} - \varepsilon\right) \tag{B.28}
$$

and x_0 is the location where $\kappa_V = \kappa_C$. The above expressions can be simplified and reduced to simple Kane [27] and Keldysh [28] models in the presence of uniform electric field and can be given in the equation below:

$$
R_{\text{BBT-NL}} = A\left(\frac{E}{E_0}\right)^{P} \exp\left(-\frac{B}{E}\right) \tag{B.29}
$$

where $E_0 = 1V/cm$, $P = 2$ for direct BBT process and $P = 2.5$ for phonon-assisted BBT. With no bandgap narrowing effect at a temperature of 300K, the coefficients A and B for direct BBT process is given in the following equations:

$$
A = \frac{g\pi m_{\mathrm{r}}^{1/2}\left(qE_0\right)^2}{9h^2\left[E_g(300\ \mathrm{K}) + \Delta E_{\mathrm{C}}\right]^{1/2}} \tag{B.30}
$$

$$
B = \frac{\pi^2 m_{\mathrm{r}}^{1/2}\left[E_{\mathrm{g}}(300\ \mathrm{K}) + \Delta E_{\mathrm{C}}\right]^{3/2}}{qh} \tag{B.31}
$$

Likewise, the coefficients A and B for phonon-assisted BBT process is given in the following equations:

$$
A = \frac{g\left(m_{\mathrm{V}} m_{\mathrm{C}}\right)^{3/2}\left(1+2N_{\mathrm{op}}\right) D_{\mathrm{op}}^2 \left(qE_0\right)^{5/2}}{2^{21/4}h^{5/2}m_{\mathrm{r}}^{5/4}\rho\varepsilon_{\mathrm{op}}\left[E_{\mathrm{g}}(300\ \mathrm{K}) + \Delta E_{\mathrm{C}}\right]^{7/4}} \tag{B.32}
$$

$$
B = \frac{2^{7/2}\pi m_{\mathrm{r}}^{1/2}\left[E_{\mathrm{g}}(300\ \mathrm{K}) + \Delta E_{\mathrm{C}}\right]^{3/2}}{3qh} \tag{B.33}
$$

The default values of the parameters A, B and ϵ_{op} used in TCAD Sentaurus is given in Table B.3 [31].

Table B.3: Coefficients for the Non-local BBT model [31]

A	B	ϵ_{op}
4e14 $cm^{-3}s^{-1}$	1.9e7 $eV^{(-3/2)}Vcm^{-1}$	0.037 eV

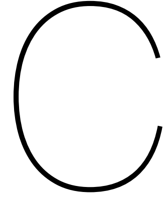

C++ code for the direct tunnelling algorithm

We present the C++ code that in included into the ASA source code to perform the direct tunnelling process for any kind of solar cell device.

```
1 #include <conio.h>
2 #include <iostream>
3 #include <stdio.h>
4 #include <cmath>
5 #include <math.h>
6 #include <algorithm>
7 #include <vector>
8 #include <fstream>
9 #include <sstream>
10 #include <iterator>
11 #include <iomanip>
12 #include <string>
13
14 using namespace std;
15 // Use "reverse(matrix.begin(), matrix.end());" To flip a 1D vector
16 void print_1D_vector(vector<double> matrix); // Function to
print the 1D array
17 void print_2D_vector(vector<vector<double>> matrix); // Function to
print the 2D array
18 void transpose_matrix(vector<vector<double>> &matrix); // Transposing a 2D
array
19 vector<double> find_index(vector<double> &matrix,double value); // Finding index
position in a 1D array
20 vector<double> slice(vector<double> const &v, double m, double n); // Extract a
range
of elements from an array
21 void extract_rows_from_matrix(vector<vector<double>> matrix_1, int row,
vector<double>
&matrix_2); // Extracting a row from 2D array
22 void extract_columns_from_matrix(vector<vector<double>> matrix_1, int column,
vector<double>
&matrix_2); // Extracting a column from 2D array
23 void get_matrix_from_file(string filename,vector<vector<double>>
&matrix); // Extract the data file into a 2D array
24 void print_file_from_2D_matrix(vector<vector<double>> matrix,string
filename); // Print .txt or .dat file of the array data
25 void print_file_from_1D_matrix(vector<double> matrix,string
filename); // Print .txt or .dat file of the array data
26 double Gamma_DT_r(double r,double m,double phi_b,double phi_m,vector<double>
psi_x); // Ieong's Direct tunneling probability function
27 double Gen_DT_r(double phi_m,double phi_n,double psi_x,double T,double E,double
A,double
gamma_r); // Ieong's Direct tunneling generation rate function
28
29 int main()
30 {
31 vector<double> layer_thickness={850e-9, 300e-9, 300e-9, 20e-9, 20e-9, 250e-6,
100e-9}; //
Array for storing the thickness of each layer
32 vector<double> m_e_trial={0.2, 0.2, 0.2, 0.2, 0.2, 0.2, 0.2}; // electron
tunnelling mass
for each layer
33 vector<double> m_h_trial={0.2, 0.2, 0.2, 0.2, 0.2, 0.2, 0.2}; // hole tunnelling
mass for
each layer
34
35 vector<double> m_e;
36 vector<double> m_h;
37
38 for (int i=0; i<(m_e_trial.size()); i++){
39 double m_1=m_e_trial[i]*9.1093837015*(10.0e-31);
40 double m_2=m_h_trial[i]*9.1093837015*(10.0e-31);
41 m_e.push_back(m_1);
42 m_h.push_back(m_2);
43 }
44
45 double m; // 0.2*9.1093837015*(10.0e-31) Tunnel mass in Kg
46 double A=1.2e5; // Richardson constant in A/(m2*K2)
47 double T=300.0; // Temperature in K
48
49 vector<vector<double>> band_values; // Matrix with all the band energies
50 get_matrix_from_file("bands_pvk_cSi_tandem_dark.dat",band_values);
51 vector<vector<double>> psi_x_data;
52 get_matrix_from_file("Potential_pvk_cSi_tandem.dat",psi_x_data);
53 vector<vector<double>> Electric_field_data;
54 get_matrix_from_file("Electric_field_pvk_cSi_tandem.dat",Electric_field_data);
55
56 vector<double> depth_x; // Vector with device mesh depth
57 extract_columns_from_matrix(band_values, 0, depth_x);
58
59 vector<double> psi_x_values; // Vector with Electrostatic potential values along
depth of device
60 extract_columns_from_matrix(psi_x_data, 1, psi_x_values);
61 vector<double> Electric_field_values; // Vector with Electric field values along
depth of
device
62 extract_columns_from_matrix(Electric_field_data, 1, Electric_field_values);
63
64 vector<vector<double>> gamma_r_VB; // Matrix with Tunnel probability values
along depth
of device for every interface in Valence band
65 vector<vector<double>> gamma_r_CB; // Matrix with Tunnel probability values
along depth
of device for every interface in Conduction band
66 vector<vector<double>> gen_r_VB; // Matrix with Tunnel generation values along
depth
of device for every interface in Valence band
67 vector<vector<double>> gen_r_CB; // Matrix with Tunnel generation values along
depth
of device for every interface in Conduction band
68
69 vector<double> phi_b_VB_range; // Vector with barrier height differences along
device depth in the Valence band
70 vector<double> phi_b_CB_range; // Vector with barrier height differences along
device depth in the Conduction band
71
72 for (int i = 0; i < depth_x.size(); i++){ // for ith index of the device depth
73 if (i<(depth_x.size()-1)){
74 phi_b_VB_range.push_back(abs(band_values[i][3]-band_values[i+1][3])); // Storing
the value of band energy difference Ev(i)-Ev(i+1)
75 phi_b_CB_range.push_back(abs(band_values[i][2]-band_values[i+1][2])); // Storing
the value of band energy difference Ec(i)-Ec(i+1)
76 }
77 else {
78 phi_b_VB_range.push_back(abs(band_values[i][3]-band_values[i][3])); // Storing
the value of band energy difference Ev(i)-Ev(i)
79 phi_b_CB_range.push_back(abs(band_values[i][2]-band_values[i][2])); // Storing
the value of band energy difference Ec(i)-Ec(i)
```

```
80 }
81 }
82 // Finding barrier height and its location for n device layers and n-1
interfaces
83 vector<double> barrier_location_VB; // Vector initialization for barrier
locations
along Valence band
84 vector<double> barrier_location_CB; // Vector initialization for barrier
locations
along Conduction band
85 vector<double> int_face_VB_trial; // Vector initialization for the index number
of
the interfaces along Valence band
86 vector<double> int_face_CB_trial; // Vector initialization for the index number
of
the interfaces along Conduction band
87 vector<double> phi_b_VB; // Vector initialization for barrier heights of
all interfaces along Valence band
88 vector<double> phi_b_CB; // Vector initialization for barrier heights of
all interfaces along Conduction band
89
90 if (layer_thickness.size()<=2){ // if only two layers present or only one
interface in the
entire device
91 barrier_location_VB.push_back(layer_thickness[0]); // barrier location with
respect to
the device depth
92 barrier_location_CB.push_back(layer_thickness[0]);
93 int_face_VB_trial=find_index(depth_x,barrier_location_VB[0]); // index number of
the
interface in the depth_x array for Valence band VB
94 int_face_CB_trial=find_index(depth_x,barrier_location_CB[0]); // index number of
the
interface in the depth_x array for Conduction band CB
95 phi_b_VB.push_back(phi_b_VB_range[int_face_VB_trial[0]]);
96 phi_b_CB.push_back(phi_b_CB_range[int_face_CB_trial[0]]);
97 } else{ // if more than two layers present or multiple interfaces in
the entire device
98 double layer_trial=0.0;
99 for (int i=0; i<(layer_thickness.size()-1); i++){
100 barrier_location_VB.push_back(layer_thickness[i]+layer_trial);
101 barrier_location_CB.push_back(layer_thickness[i]+layer_trial);
102 layer_trial=layer_trial+layer_thickness[i];
103 int_face_VB_trial=find_index(depth_x,barrier_location_VB[i]);
104 int_face_CB_trial=find_index(depth_x,barrier_location_CB[i]);
105 phi_b_VB.push_back(phi_b_VB_range[int_face_VB_trial[0]]);
106 phi_b_CB.push_back(phi_b_CB_range[int_face_CB_trial[0]]);
107 }
108 }
109
110 // Calculating Tunnelling Probability and Tunnel Generation rate for each
interface
111 double phi_n_VB;
112 double phi_n_CB;
113 double r_VB;
114 double r_CB;
115 vector<double> psi_x_VB;
116 vector<double> psi_x_CB;
117 double phi_m_VB;
118 double phi_m_CB;
119
120 for (int i=0; i<(layer_thickness.size()-1); i++){ // for i interfaces
121 // Calculation for Valence band
122 vector<double> gamma_r_col_VB;
123 vector<double> gen_r_col_VB;
124 vector<double> int_face_VB=find_index(depth_x,barrier_location_VB[i]);
125 for (int j=0; j<depth_x.size(); j++){ // for ith device depth
126 if (depth_x[j]<barrier_location_VB[i] && (int_face_VB.size()==1)){ // if the
device
depth i is on left side of the barrier and the barrier has no continuity
127 if (((2*int_face_VB[0])-j)<0){
128 phi_n_VB=0.0;
129 }else if (((2*int_face_VB[0])-j)>(depth_x.size()-1)){
130 phi_n_VB=0.0;
131 }else{
132
phi_n_VB=abs(band_values[(2*int_face_VB[0])-j][5]-band_values[(2*int_face_VB[0])-j]
[3]);
133 }
134 r_VB=barrier_location_VB[i]-depth_x[j];
135 psi_x_VB=slice(psi_x_values,j,int_face_VB[0]);
136 reverse(psi_x_VB.begin(),psi_x_VB.end());
137 m=m_e[i];
138 }else if (depth_x[j]<barrier_location_VB[i] && (int_face_VB.size()==2)){ // if
the
device depth i is on left side of the barrier and the barrier has continuity
139 if (((2*int_face_VB[0])-j+1)<0){
140 phi_n_VB=0.0;
141 }else if (((2*int_face_VB[0])-j+1)>(depth_x.size()-1)){
142 phi_n_VB=0.0;
143 }else{
144
phi_n_VB=abs(band_values[(2*int_face_VB[0])-j+1][5]-band_values[(2*int_face_VB[0])-
j+1][3]);
145 }
146 r_VB=barrier_location_VB[i]-depth_x[j];
147 psi_x_VB=slice(psi_x_values,j,int_face_VB[0]);
148 reverse(psi_x_VB.begin(),psi_x_VB.end());
149 m=m_e[i];
150 }else if (depth_x[j]==barrier_location_VB[i] && (int_face_VB.size()==1)){ // if
the
device depth i is on the barrier and the barrier has no continuity
151 phi_n_VB=abs(band_values[j][5]-band_values[j][3]);
152 r_VB=barrier_location_VB[i]-depth_x[j];
153 psi_x_VB=slice(psi_x_values,j,int_face_VB[0]);
154 reverse(psi_x_VB.begin(),psi_x_VB.end());
155 m=m_e[i];
156 }else if (depth_x[j]==barrier_location_VB[i] && (int_face_VB.size()==2)){ // if
the
device depth i is on the barrier and the barrier has continuity
157 if (j==int_face_VB[0]){
158 phi_n_VB=abs(band_values[j+1][5]-band_values[j+1][3]);
159 psi_x_VB=slice(psi_x_values,j,int_face_VB[0]);
160 m=m_e[i];
161 }else{
162 phi_n_VB=abs(band_values[j-1][5]-band_values[j-1][3]);
163 psi_x_VB=slice(psi_x_values,int_face_VB[1],j);
164 m=m_e[i+1];
165 }
166 r_VB=barrier_location_VB[i]-depth_x[j];
167 reverse(psi_x_VB.begin(),psi_x_VB.end());
168 }else if (depth_x[j]>barrier_location_VB[i] && (int_face_VB.size()==2)){ // if
the
device depth i is on the right side of the barrier and the barrier has continuity
169 if (((2*int_face_VB[1])-j-1)<0){
170 phi_n_VB=0.0;
171 }else if (((2*int_face_VB[1])-j-1)>(depth_x.size()-1)){
172 phi_n_VB=0.0;
173 }else{
174
phi_n_VB=abs(band_values[(2*int_face_VB[1])-j-1][5]-band_values[(2*int_face_VB[1])-
j-1][3]);
175 }
176 r_VB=depth_x[j]-barrier_location_VB[i];
177 psi_x_VB=slice(psi_x_values,int_face_VB[1],j);
178 m=m_e[i+1];
179 }else{ // if the
device depth i is on the right side of the barrier and the barrier has no
continuity
180 if (((2*int_face_VB[0])-j)<0){
181 phi_n_VB=0.0;
182 }else if (((2*int_face_VB[0])-j)>(depth_x.size()-1)){
183 phi_n_VB=0.0;
184 }else{
185
phi_n_VB=abs(band_values[(2*int_face_VB[0])-j][5]-band_values[(2*int_face_VB[0])-j]
[3]);
186 }
187 r_VB=depth_x[j]-barrier_location_VB[i];
188 psi_x_VB=slice(psi_x_values,int_face_VB[0],j);
189 m=m_e[i+1];
190 }
191 phi_m_VB=abs(band_values[j][5]-band_values[j][3]);
192 double gamma_r_trial_VB=Gamma_DT_r(r_VB,m,phi_b_VB[i],phi_n_VB,psi_x_VB); //
Tunnelling probability
193 gamma_r_col_VB.push_back(gamma_r_trial_VB);
194
gen_r_col_VB.push_back(Gen_DT_r(phi_m_VB,phi_n_VB,psi_x_values[j],T,Electric_field_
values[j],A,ga
mma_r_trial_VB)); // Tunnelling generation
195 }
196 gamma_r_VB.push_back(gamma_r_col_VB);
197 gen_r_VB.push_back(gen_r_col_VB);
198
199 // Calculation for Conduction band
200 vector<double> gamma_r_col_CB;
201 vector<double> gen_r_col_CB;
202 vector<double> int_face_CB=find_index(depth_x,barrier_location_CB[i]);
203 for (int j=0; j<depth_x.size(); j++){ // for ith device depth
204 if (depth_x[j]<barrier_location_CB[i] && (int_face_CB.size()==1)){
205 if (((2*int_face_CB[0])-j)<0){
206 phi_n_CB=0.0;
207 }else if (((2*int_face_CB[0])-j)>(depth_x.size()-1)){
208 phi_n_VB=0.0;
209 }else{
210
phi_n_CB=abs(band_values[(2*int_face_CB[0])-j][4]-band_values[(2*int_face_CB[0])-j]
[2]);
211 }
212 r_CB=barrier_location_CB[i]-depth_x[j];
213 psi_x_CB=slice(psi_x_values,j,int_face_CB[0]);
214 reverse(psi_x_CB.begin(),psi_x_CB.end());
215 m=m_h[i];
216 }else if (depth_x[j]<barrier_location_CB[i] && (int_face_CB.size()==2)){
217 if (((2*int_face_CB[0])-j+1)<0){
218 phi_n_CB=0.0;
219 }else if (((2*int_face_CB[0])-j+1)>(depth_x.size()-1)){
220 phi_n_VB=0.0;
221 }else{
222
phi_n_CB=abs(band_values[(2*int_face_CB[0])-j+1][4]-band_values[(2*int_face_CB[0])-
j+1][2]);
223 }
224 r_CB=barrier_location_CB[i]-depth_x[j];
225 psi_x_CB=slice(psi_x_values,j,int_face_CB[0]);
226 reverse(psi_x_CB.begin(),psi_x_CB.end());
227 m=m_h[i];
228 }else if (depth_x[j]==barrier_location_CB[i] && (int_face_CB.size()==1)){
229 phi_n_CB=abs(band_values[j][4]-band_values[j][2]);
230 r_CB=barrier_location_CB[i]-depth_x[j];
231 psi_x_CB=slice(psi_x_values,j,int_face_CB[0]);
232 reverse(psi_x_CB.begin(),psi_x_CB.end());
233 m=m_h[i];
234 }else if (depth_x[j]==barrier_location_CB[i] && (int_face_CB.size()==2)){
235 if (j==int_face_CB[0]){
236 phi_n_CB=abs(band_values[j+1][4]-band_values[j+1][2]);
237 psi_x_CB=slice(psi_x_values,j,int_face_CB[0]);
238 m=m_h[i];
239 }else{
240 phi_n_CB=abs(band_values[j-1][4]-band_values[j-1][2]);
241 psi_x_CB=slice(psi_x_values,int_face_CB[1],j);
242 m=m_h[i+1];
243 }
244 r_CB=barrier_location_CB[i]-depth_x[j];
245 reverse(psi_x_CB.begin(),psi_x_CB.end());
246 }else if (depth_x[j]>barrier_location_CB[i] && (int_face_CB.size()==2)){
247 if (((2*int_face_CB[1])-j-1)<0){
248 phi_n_CB=0.0;
249 }else if (((2*int_face_CB[1])-j-1)>(depth_x.size()-1)){
250 phi_n_VB=0.0;
251 }else{
252
phi_n_CB=abs(band_values[(2*int_face_CB[1])-j-1][4]-band_values[(2*int_face_CB[1])-
j-1][2]);
253 }
254 r_CB=depth_x[j]-barrier_location_CB[i];
255 psi_x_CB=slice(psi_x_values,int_face_CB[1],j);
256 m=m_h[i+1];
257 }else{
258 if (((2*int_face_CB[0])-j)<0){
259 phi_n_CB=0.0;
260 }else if (((2*int_face_CB[0])-j)>(depth_x.size()-1)){
261 phi_n_VB=0.0;
262 }else{
263
phi_n_CB=abs(band_values[(2*int_face_CB[0])-j][4]-band_values[(2*int_face_CB[0])-j]
```

```
[2]);
264 }
265 r_CB=depth_x[j]-barrier_location_CB[i];
266 psi_x_CB=slice(psi_x_values,int_face_CB[0],j);
267 m=m_h[i+1];
268 }
269 phi_m_CB=abs(band_values[j][4]-band_values[j][2]);
270 double gamma_r_trial_CB=Gamma_DT_r(r_CB,m,phi_b_CB[i],phi_n_CB,psi_x_CB);
271 gamma_r_col_CB.push_back(gamma_r_trial_CB);
272
gen_r_col_CB.push_back(Gen_DT_r(phi_m_CB,phi_n_CB,psi_x_values[j],T,Electric_field_
values[j],A,ga
mma_r_trial_CB));
273 }
274 gamma_r_CB.push_back(gamma_r_col_CB);
275 gen_r_CB.push_back(gen_r_col_CB);
276 }
277
278 // combining depth_x array and tunnelling values into one single 2d array of
the order of
[depth(x)....DT_Tun_CB_interface(n)....DT_Tun_VB_interface(n)]
279 vector<vector<double>> gamma_final;
280 vector<vector<double>> gen_final;
281 if (gen_r_CB.size()>1){
282 cout << gen_r_CB.size() <<" interfaces detected for the Direct Tunnelling
process \n";
283 vector<double> gamma_sum_CB;
284 vector<double> gamma_sum_VB;
285 vector<double> gen_sum_CB;
286 vector<double> gen_sum_VB;
287 for(int x = 0; x < gamma_r_CB[0].size(); x++){
288 double sum_CB=0;
289 double sum_VB=0;
290 double sum_one_CB=0;
291 double sum_one_VB=0;
292 for(int y = 0; y < gamma_r_CB.size(); y++){
293 sum_CB=sum_CB+gamma_r_CB[y][x];
294 sum_VB=sum_VB+gamma_r_VB[y][x];
295 sum_one_CB=sum_one_CB+gen_r_CB[y][x];
296 sum_one_VB=sum_one_VB+gen_r_VB[y][x];
297 }
298 gamma_sum_CB.push_back(sum_CB);
299 gamma_sum_VB.push_back(sum_VB);
300 gen_sum_CB.push_back(sum_one_CB);
301 gen_sum_VB.push_back(sum_one_VB);
302 }
303
304 gamma_final.push_back(depth_x);
305 gamma_final.push_back(gamma_sum_CB);
306 gamma_final.push_back(gamma_sum_VB);
307 transpose_matrix(gamma_final);
308
309 gen_final.push_back(depth_x);
310 gen_final.push_back(gen_sum_CB);
311 gen_final.push_back(gen_sum_VB);
312 transpose_matrix(gen_final);
313
314 }else{
315 cout << "Only one interface detected for the Direct Tunnelling proces \n";
316 gamma_final.push_back(depth_x);
317 for (int i=0 ; i<gamma_r_CB.size() ; i++){
318 vector<double> copyRow( gamma_r_CB[i].begin(), gamma_r_CB[i].end());
319 vector<double> copyRow_2( gamma_r_VB[i].begin(), gamma_r_VB[i].end());
320 gamma_final.push_back(copyRow);
321 gamma_final.push_back(copyRow_2);
322 }
323 transpose_matrix(gamma_final);
324
325 gen_final.push_back(depth_x);
326 for (int i=0 ; i<gen_r_CB.size() ; i++){
327 vector<double> copyRow( gen_r_CB[i].begin(), gen_r_CB[i].end());
328 vector<double> copyRow_2( gen_r_VB[i].begin(), gen_r_VB[i].end());
329 gen_final.push_back(copyRow);
330 gen_final.push_back(copyRow_2);
331 }
332 transpose_matrix(gen_final);
333
334 }
335
336 // Creating text files for the results
337 print_file_from_2D_matrix(gamma_final,"gamma_r.txt");
338 print_file_from_2D_matrix(gen_final,"Gen_DT.txt");
339 cout << "The Direct Tunnelling process is finished and the Generation result is
printed in
your current directory folder";
340 return 0;
341 }
342
343 double Gamma_DT_r(double r,double m,double phi_b,double phi_n,vector<double>
psi_x)
344 {
345 double q=1.602*pow(10.0,-19.0); // Charge constant
346 double h=6.582*pow(10.0,-16.0); // Dirac constant in eV
347 double integral_ans=0.0;
348 int n_intervals=psi_x.size();
349 double dx=(r-0.0)/(n_intervals*2.0);
350 for (int i = 0; i < n_intervals; i++) {
351 if (i==0){
352 double area_under_integration=sqrt(2.0*m*((phi_b/q)+phi_n-psi_x[i]))*dx;
353 integral_ans=integral_ans+area_under_integration;
354 }else if (i==(n_intervals-1)){
355 double area_under_integration=sqrt(2.0*m*((phi_b/q)+phi_n-psi_x[i]))*dx;
356 integral_ans=integral_ans+area_under_integration;
357 }else{
358 double area_under_integration=sqrt(2.0*m*((phi_b/q)+phi_n-psi_x[i]))*dx;
359 integral_ans=integral_ans+(2*area_under_integration);
360 }
361 }
362 double gamma_r=exp(((-2.0)/(h))*integral_ans);
363 return gamma_r;
364 }
365
366 double Gen_DT_r(double phi_m,double phi_n,double psi_x,double T,double E,double
A,double gamma_r)
367 {
368 double q = 1.602*pow(10.0,-19.0);
369 double kb = 1.381*pow(10.0,-23.0);
370 double gen_r =
((A*T*E*gamma_r)/kb)*log((1+exp((-q*(psi_x-phi_m))/(kb*T)))/(1+exp((-q*(psi_x-
phi_n))/(kb*T))));
371 return gen_r;
372 }
373
374 void print_1D_vector(vector<double> matrix){
375 for (int i=0;i<matrix.size();i++){
376 cout << matrix[i] << " ";
377 }
378 cout << endl;
379 }
380
381 void print_2D_vector(vector<vector<double>> matrix){
382 for (int i = 0; i < matrix.size(); i++)
383 {
384 for (int j = 0; j < matrix[i].size(); j++)
385 {
386 cout << matrix[i][j] << " ";
387 }
388 cout << endl;
389 }
390 }
391
392 void transpose_matrix(vector<vector<double>> &matrix)
393 {
394 if (matrix.size() == 0)
395 return;
396
397 vector<vector<double>> trans_vec(matrix[0].size(), vector<double>());
398 for (int i = 0; i < matrix.size(); i++)
399 {
400 for (int j = 0; j < matrix[i].size(); j++)
401 {
402 trans_vec[j].push_back(matrix[i][j]);
403 }
404 }
405 matrix = trans_vec; // <--- reassign here
406 }
407
408 vector<double> find_index(vector<double> &matrix,double value){
409 vector<double> index_values;
410 for (int i = 0; i < matrix.size(); i++) {
411 if(abs(matrix[i]-value)<(0.001e-9)){
412 index_values.push_back(i);
413 }
414 }
415 return index_values;
416 }
417
418 vector<double> slice(vector<double> const &v, double m, double n)
419 {
420 auto first = v.cbegin() + m;
421 auto last = v.cbegin() + n + 1;
422 vector<double> vec(first, last);
423 return vec;
424 }
425
426 void extract_rows_from_matrix(vector<vector<double>> matrix_1, int row,
vector<double> &matrix_2)
427 {
428 vector<double> data;
429 for (int i=0; i<matrix_1.size(); i++){
430 for (int j=0; j<matrix_1[i].size(); j++){
431 if(i==row){
432 data.push_back(matrix_1[i][j]);
433 }
434 }
435 }
436 matrix_2 = data;
437 }
438
439 void extract_columns_from_matrix(vector<vector<double>> matrix_1, int column,
vector<double>
&matrix_2)
440 {
441 vector<double> data;
442 for (int i=0; i<matrix_1.size(); i++){
443 for (int j=0; j<matrix_1[i].size(); j++){
444 if(j==column){
445 data.push_back(matrix_1[i][j]);
446 }
447 }
448 }
449 matrix_2 = data;
450 }
451
452 void get_matrix_from_file(string filename,vector<vector<double>> &matrix)
453 {
454 vector< vector<double> > data;
455
456 ifstream in( filename );
457 for ( string line; getline( in, line ); )
458 {
459 stringstream ss( line );
460 vector<double> row;
461 for ( double d; ss >> d; ) row.push_back( d );
462 data.push_back( row );
463 }
464 matrix = data;
465 }
466
467 void print_file_from_2D_matrix(vector<vector<double>> matrix,string filename)
468 {
469 FILE * output;
470 output = fopen (filename.c_str(),"w");
471 for (int i=0; i<matrix.size(); i++){
472 for (int j=0; j<matrix[i].size(); j++){
473 if(j==(matrix[i].size()-1)){
474 fprintf (output, "%.6e",matrix[i][j]);
475 }else{
476 fprintf (output, "%.6e ",matrix[i][j]);
477 }
478 }
479 if(i!=(matrix.size()-1)){
480 fprintf (output, "\n");
481 }
482 }
483 fclose (output);
```

```
484 }
485
486 void print_file_from_1D_matrix(vector<double> matrix,string filename)
487 {
488 FILE * output;
489 output = fopen (filename.c_str(),"w");
490 for (int i=0; i<matrix.size(); i++){
491 if(i==(matrix.size()-1)){
492 fprintf (output, "%.6e",matrix[i]);
493 }else{
494 fprintf (output, "%.6e\n",matrix[i]);
495 }
496 }
497 fclose (output);
498 }
499
```

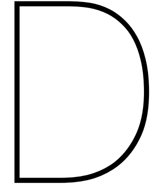

C++ code for the band to band tunnelling algorithm

Similarly, we present the C++ code that in included into the ASA source code to perform the band to band tunnelling process for any kind of solar cell device.

```
1 #include <conio.h>
2 #include <iostream>
3 #include <stdio.h>
4 #include <cmath>
5 #include <math.h>
6 #include <algorithm>
7 #include <vector>
8 #include <fstream>
9 #include <sstream>
10 #include <iterator>
11 #include <iomanip>
12 #include <string>
13
14 using namespace std;
15 // Use "reverse(matrix.begin(), matrix.end());" To flip a 1D vector
16 void print_1D_vector(vector<double> matrix); // Function to
print the 1D array
17 void print_2D_vector(vector<vector<double>> matrix); // Function to
print the 2D array
18 void transpose_matrix(vector<vector<double>> &matrix); // Transposing
a 2D
array
19 vector<double> find_index(vector<double> &matrix,double value); //
Finding index
position in a 1D array
20 vector<double> slice(vector<double> const &v, double m, double n); //
Extract a range
of elements from an array
21 void extract_rows_from_matrix(vector<vector<double>> matrix_1, int
row, vector<double>
&matrix_2); // Extracting a row from 2D array
22 void extract_columns_from_matrix(vector<vector<double>> matrix_1, int
column, vector<double>
&matrix_2); // Extracting a column from 2D array
23 void get_matrix_from_file(string filename,vector<vector<double>>
&matrix); // Extract the data file into a 2D array
24 void print_file_from_2D_matrix(vector<vector<double>> matrix,string
filename); // Print .txt or .dat file of the array data
25 void print_file_from_1D_matrix(vector<double> matrix,string
filename); // Print .txt or .dat file of the array data
26 double Gamma_BBT_r(double r,double m,double Epsilon,vector<double>
E_x,double Tcv_u,double
Tcv_l); // Non-Local Band to Band tunneling probability function
27 double Gen_BBT_r(double number,double A,double gamma_r,double
Vu,double Vl,double E,double
Efu,double Efl,double Tu,double Tl); // Non-Local Band to Band tunneling
generation rate
function
28 double V_BBT(double dy);
29
30 int main()
31 {
32 vector<double> layer_thickness={850e-9, 300e-9, 300e-9, 20e-9, 20e-9,
250e-6, 100e-9}; //
Array for storing the thickness of each layer
33 vector<double> m_e_trial={0.2, 0.2, 0.2, 0.2, 0.2, 0.2, 0.2}; //
electron tunnelling mass
for each layer
34 vector<double> m_h_trial={0.2, 0.2, 0.2, 0.2, 0.2, 0.2, 0.2}; // hole
tunnelling mass for
each layer
35
36 vector<double> m_e;
37 vector<double> m_h;
38
39 for (int i=0; i<(m_e_trial.size()); i++){
40 double m_1=m_e_trial[i]*9.1093837015*(10.0e-31);
41 double m_2=m_h_trial[i]*9.1093837015*(10.0e-31);
42 m_e.push_back(m_1);
43 m_h.push_back(m_2);
44 }
45
46 double A=1.2e5; // Effective Richardson constant A/(m2*K2)
47 double Tu=300.0; // temperature on current point
48 double Tl=300.0; // temperature on point l on other side of barrier
49 double Tcv_u=1.0; // transmission coefficient on current point
50 double Tcv_l=1.0; // transmission coefficient on point l on other side
of barrier
51
52 vector<vector<double>> band_values; // Matrix with all the band
energies
53 get_matrix_from_file("bands_pvk_cSi_tandem_dark.dat",band_values);
54
55 vector<double> depth_x; // Vector with device mesh depth
56 extract_columns_from_matrix(band_values, 0, depth_x);
57 vector<double> Ec; // Vector with Valence band energies
58 extract_columns_from_matrix(band_values, 2, Ec);
59 vector<double> Ev; // Vector with Conduction band energies
60 extract_columns_from_matrix(band_values, 3, Ev);
61
62 vector<vector<double>> Gamma_BBT_CB; // Matrix with Tunnel probability
values along
depth of device for every int_face in Conduction band
63 vector<vector<double>> Gamma_BBT_VB; // Matrix with Tunnel probability
values along
depth of device for every int_face in Valence band
64 vector<vector<double>> Gen_BBT_CB; // Matrix with Tunnel generation
values along depth
of device for every int_face in Conduction band
65 vector<vector<double>> Gen_BBT_VB; // Matrix with Tunnel generation
values along depth
of device for every int_face in Valence band
66
67 // Finding barrier height and its location for n device layers and n-1
int_faces
68 vector<double> barrier_location; // Vector initialization for barrier
locations
along the device
```

```
69
70 if (layer_thickness.size()<=2){ // if only two layers present or only
one int_face in the
entire device
71 barrier_location.push_back(layer_thickness[0]); // barrier location
with respect to the
device depth
72 } else{ // if more than two layers present or multiple int_faces in
the entire device
73 double layer_trial=0.0;
74 for (int i=0; i<(layer_thickness.size()-1); i++){
75 barrier_location.push_back(layer_thickness[i]+layer_trial);
76 layer_trial=layer_trial+layer_thickness[i];
77 }
78 }
79
80 // Calculating Tunnelling Probability and Tunnel Generation rate for
each int_face
81 double r;
82 vector<double> E_x;
83 vector<double> E_x_1;
84 vector<double> E_x_2;
85 double Epsilon;
86 double Epsilon_1;
87 double Epsilon_2;
88
89 for (int i=0; i<(layer_thickness.size()-1); i++){ // for i int_faces
90 // Calculation for Valence band
91 vector<double> gamma_r_col_VB;
92 vector<double> gen_r_col_VB;
93 vector<double> gamma_r_col_CB;
94 vector<double> gen_r_col_CB;
95 vector<double> int_face=find_index(depth_x,barrier_location[i]);
96 for (int j=0; j<depth_x.size(); j++){ // for ith device depth
97 if (depth_x[j]<barrier_location[i] && (int_face.size()==1)){ // if the
device depth
i is on left side of the barrier and the barrier has no continuity
98 r=barrier_location[i]-depth_x[j];
99 if (((2*int_face[0])-j)<0){
100 gamma_r_col_VB.push_back(0.0);
101 gamma_r_col_CB.push_back(0.0);
102 gen_r_col_VB.push_back(0.0);
103 gen_r_col_CB.push_back(0.0);
104 }else if (((2*int_face[0])-j)>(depth_x.size()-1)){
105 gamma_r_col_VB.push_back(0.0);
106 gamma_r_col_CB.push_back(0.0);
107 gen_r_col_VB.push_back(0.0);
108 gen_r_col_CB.push_back(0.0);
109 }else{
110 if (band_values[j][2]<=band_values[(2*int_face[0])-j][3]){
111 E_x=slice(Ec,j,int_face[0]);
112 reverse(E_x.begin(),E_x.end());
113 Epsilon=band_values[(2*int_face[0])-j][3];
114 double gamma_r_trial_CB;
115 if(r>(100.0e-9)){
116 gamma_r_trial_CB=0.0;
117 }else{
118 gamma_r_trial_CB=Gamma_BBT_r(r,m_e[i],Epsilon,E_x,Tcv_u,Tcv_l);
119 }
120 double gamma_r_trial_VB=0.0;
121 gamma_r_col_CB.push_back(gamma_r_trial_CB);
122 gamma_r_col_VB.push_back(gamma_r_trial_VB);
123 double d_Eu;
124 double d_El;
125 if (j==0 && ((2*int_face[0]-j)==(depth_x.size()-1))){
126
d_Eu=(band_values[j+1][2]-band_values[j][2])/(depth_x[j+1]-depth_x[j]);
127
d_El=(band_values[(2*int_face[0])-j][3]-band_values[(2*int_face[0])-j-
1][3])/(depth_x[(2*int_face
[0])-j]-depth_x[(2*int_face[0])-j-1]);
128 }else if (j==(depth_x.size()-1) && ((2*int_face[0]-j)==0)){
129
d_Eu=(band_values[j][2]-band_values[j-1][2])/(depth_x[j]-depth_x[j-1]);
130
d_El=(band_values[(2*int_face[0])-j+1][3]-band_values[(2*int_face[0])-
j][3])/(depth_x[(2*int_face
[0])-j+1]-depth_x[(2*int_face[0])-j]);
131 }else if(j==0){
132
d_Eu=(band_values[j+1][2]-band_values[j][2])/(depth_x[j+1]-depth_x[j]);
133
d_El=(band_values[(2*int_face[0])-j+1][3]-band_values[(2*int_face[0])-j-
1][3])/(depth_x[(2*int_fa
ce[0])-j+1]-depth_x[(2*int_face[0])-j-1]);
134 }else if(j==(depth_x.size()-1)){
135
d_Eu=(band_values[j][2]-band_values[j-1][2])/(depth_x[j]-depth_x[j-1]);
136
d_El=(band_values[(2*int_face[0])-j+1][3]-band_values[(2*int_face[0])-j-
1][3])/(depth_x[(2*int_fa
ce[0])-j+1]-depth_x[(2*int_face[0])-j-1]);
137 }else if((2*int_face[0]-j)==(depth_x.size()-1)){
138
d_Eu=(band_values[j+1][2]-band_values[j-1][2])/(depth_x[j+1]-depth_x[j-
1]);
139
d_El=(band_values[(2*int_face[0])-j][3]-band_values[(2*int_face[0])-j-
1][3])/(depth_x[(2*int_face
[0])-j]-depth_x[(2*int_face[0])-j-1]);
140 }else if((2*int_face[0]-j)==0){
141
d_Eu=(band_values[j+1][2]-band_values[j-1][2])/(depth_x[j+1]-depth_x[j-
1]);
142
d_El=(band_values[(2*int_face[0])-j+1][3]-band_values[(2*int_face[0])-
j][3])/(depth_x[(2*int_face
[0])-j+1]-depth_x[(2*int_face[0])-j]);
```

```
143 }else {
144
d_Eu=(band_values[j+1][2]-band_values[j-1][2])/(depth_x[j+1]-depth_x[j-
1]);
145
d_El=(band_values[(2*int_face[0])-j+1][3]-band_values[(2*int_face[0])-j-
1][3])/(depth_x[(2*int_fa
ce[0])-j+1]-depth_x[(2*int_face[0])-j-1]);
146 }
147 double Vu=V_BBT(d_Eu);
148 double Vl=V_BBT(d_El);
149 double Efu;
150 double Efl;
151 if (abs(band_values[j][4])<=(7.3475918173e-16)){
152 Efu=7.3475918173e-16;
153 }else{
154 Efu=abs(band_values[j][4]);
155 }
156 if (abs(band_values[(2*int_face[0])-j][5])<=(7.3475918173e-16)){
157 Efl=-7.3475918173e-16;
158 }else{
159 Efl=(-1.0)*abs(band_values[(2*int_face[0])-j][5]);
160 }
161
gen_r_col_CB.push_back(Gen_BBT_r(1.0,A,gamma_r_trial_CB,Vu,Vl,band_values
[j][2],Efu,Efl,Tu,Tl));
162 gen_r_col_VB.push_back(0.0);
163 }else if (band_values[j][3]>=band_values[(2*int_face[0])-j][2]){
164 E_x=slice(Ev,j,int_face[0]);
165 reverse(E_x.begin(),E_x.end());
166 Epsilon=band_values[(2*int_face[0])-j][2];
167 double gamma_r_trial_VB;
168 if(r>(100.0e-9)){
169 gamma_r_trial_VB=0.0;
170 }else{
171 gamma_r_trial_VB=Gamma_BBT_r(r,m_h[i],Epsilon,E_x,Tcv_u,Tcv_l);
172 }
173 double gamma_r_trial_CB=0.0;
174 gamma_r_col_CB.push_back(gamma_r_trial_CB);
175 gamma_r_col_VB.push_back(gamma_r_trial_VB);
176 double d_Eu;
177 double d_El;
178 if (j==0 && ((2*int_face[0]-j)==(depth_x.size()-1))){
179
d_Eu=(band_values[j+1][3]-band_values[j][3])/(depth_x[j+1]-depth_x[j]);
180
d_El=(band_values[(2*int_face[0])-j][2]-band_values[(2*int_face[0])-j-
1][2])/(depth_x[(2*int_face
[0])-j]-depth_x[(2*int_face[0])-j-1]);
181 }else if (j==(depth_x.size()-1) && ((2*int_face[0]-j)==0)){
182
d_Eu=(band_values[j][3]-band_values[j-1][3])/(depth_x[j]-depth_x[j-1]);
183
d_El=(band_values[(2*int_face[0])-j+1][2]-band_values[(2*int_face[0])-
j][2])/(depth_x[(2*int_face
[0])-j+1]-depth_x[(2*int_face[0])-j]);
184 }else if(j==0){
185
d_Eu=(band_values[j+1][3]-band_values[j][3])/(depth_x[j+1]-depth_x[j]);
186
d_El=(band_values[(2*int_face[0])-j+1][2]-band_values[(2*int_face[0])-j-
1][2])/(depth_x[(2*int_fa
ce[0])-j+1]-depth_x[(2*int_face[0])-j-1]);
187 }else if(j==(depth_x.size()-1)){
188
d_Eu=(band_values[j][3]-band_values[j-1][3])/(depth_x[j]-depth_x[j-1]);
189
d_El=(band_values[(2*int_face[0])-j+1][2]-band_values[(2*int_face[0])-j-
1][2])/(depth_x[(2*int_fa
ce[0])-j+1]-depth_x[(2*int_face[0])-j-1]);
190 }else if((2*int_face[0]-j)==(depth_x.size()-1)){
191
d_Eu=(band_values[j+1][3]-band_values[j-1][2])/(depth_x[j+1]-depth_x[j-
1]);
192
d_El=(band_values[(2*int_face[0])-j][2]-band_values[(2*int_face[0])-j-
1][2])/(depth_x[(2*int_face
[0])-j]-depth_x[(2*int_face[0])-j-1]);
193 }else if((2*int_face[0]-j)==0){
194
d_Eu=(band_values[j+1][3]-band_values[j-1][2])/(depth_x[j+1]-depth_x[j-
1]);
195
d_El=(band_values[(2*int_face[0])-j+1][2]-band_values[(2*int_face[0])-
j][2])/(depth_x[(2*int_face
[0])-j+1]-depth_x[(2*int_face[0])-j]);
196 }else {
197
d_Eu=(band_values[j+1][3]-band_values[j-1][2])/(depth_x[j+1]-depth_x[j-
1]);
198
d_El=(band_values[(2*int_face[0])-j+1][2]-band_values[(2*int_face[0])-j-
1][2])/(depth_x[(2*int_fa
ce[0])-j+1]-depth_x[(2*int_face[0])-j-1]);
199 }
200 double Vu=V_BBT(d_Eu);
201 double Vl=V_BBT(d_El);
202 double Efu;
203 double Efl;
204 if (abs(band_values[j][5])<=(7.3475918173e-16)){
205 Efu=-7.3475918173e-16;
206 }else{
207 Efu=(-1.0)*abs(band_values[j][5]);
208 }
209 if (abs(band_values[(2*int_face[0])-j][4])<=(7.3475918173e-16)){
210 Efl=7.3475918173e-16;
211 }else{
```

```
212 Efl=abs(band_values[(2*int_face[0])-j][4]);
213 }
214 gen_r_col_CB.push_back(0.0);
215
gen_r_col_VB.push_back(Gen_BBT_r(2.0,A,gamma_r_trial_VB,Vu,Vl,band_values
[j][3],Efu,Efl,Tu,Tl));
216 }else {
217 gamma_r_col_VB.push_back(0.0);
218 gamma_r_col_CB.push_back(0.0);
219 gen_r_col_VB.push_back(0.0);
220 gen_r_col_CB.push_back(0.0);
221 }
222 }
223 }else if (depth_x[j]<barrier_location[i] && (int_face.size()==2)){ //
if the device
depth i is on left side of the barrier and the barrier has continuity
224 r=barrier_location[i]-depth_x[j];
225 if (((2*int_face[0])-j+1)<0){
226 gamma_r_col_VB.push_back(0.0);
227 gamma_r_col_CB.push_back(0.0);
228 gen_r_col_VB.push_back(0.0);
229 gen_r_col_CB.push_back(0.0);
230 }else if (((2*int_face[0])-j+1)>(depth_x.size()-1)){
231 gamma_r_col_VB.push_back(0.0);
232 gamma_r_col_CB.push_back(0.0);
233 gen_r_col_VB.push_back(0.0);
234 gen_r_col_CB.push_back(0.0);
235 }else{
236 if (band_values[j][2]<=band_values[(2*int_face[0])-j+1][3]){
237 E_x=slice(Ec,j,int_face[0]);
238 reverse(E_x.begin(),E_x.end());
239 Epsilon=band_values[(2*int_face[0])-j+1][3];
240 double gamma_r_trial_CB;
241 if(r>(100.0e-9)){
242 gamma_r_trial_CB=0.0;
243 }else{
244 gamma_r_trial_CB=Gamma_BBT_r(r,m_e[i],Epsilon,E_x,Tcv_u,Tcv_l);
245 }
246 double gamma_r_trial_VB=0.0;
247 gamma_r_col_CB.push_back(gamma_r_trial_CB);
248 gamma_r_col_VB.push_back(gamma_r_trial_VB);
249 double d_Eu;
250 double d_El;
251 if (j==0 && ((2*int_face[0]-j+1)==(depth_x.size()-1))){
252
d_Eu=(band_values[j+1][2]-band_values[j][2])/(depth_x[j+1]-depth_x[j]);
253
d_El=(band_values[(2*int_face[0])-j+1][3]-band_values[(2*int_face[0])-
j][3])/(depth_x[(2*int_face
[0])-j+1]-depth_x[(2*int_face[0])-j]);
254 }else if (j==(depth_x.size()-1) && ((2*int_face[0]-j+1)==0)){
255
d_Eu=(band_values[j][2]-band_values[j-1][2])/(depth_x[j]-depth_x[j-1]);
256
d_El=(band_values[(2*int_face[0])-j+2][3]-band_values[(2*int_face[0])-
j+1][3])/(depth_x[(2*int_fa
ce[0])-j+2]-depth_x[(2*int_face[0])-j+1]);
257 }else if(j==0){
258
d_Eu=(band_values[j+1][2]-band_values[j][2])/(depth_x[j+1]-depth_x[j]);
259
d_El=(band_values[(2*int_face[0])-j+2][3]-band_values[(2*int_face[0])-
j][3])/(depth_x[(2*int_face
[0])-j+2]-depth_x[(2*int_face[0])-j]);
260 }else if(j==(depth_x.size()-1)){
261
d_Eu=(band_values[j][2]-band_values[j-1][2])/(depth_x[j]-depth_x[j-1]);
262
d_El=(band_values[(2*int_face[0])-j+2][3]-band_values[(2*int_face[0])-
j][3])/(depth_x[(2*int_face
[0])-j+2]-depth_x[(2*int_face[0])-j]);
263 }else if((2*int_face[0]-j+1)==(depth_x.size()-1)){
264
d_Eu=(band_values[j+1][2]-band_values[j-1][2])/(depth_x[j+1]-depth_x[j-
1]);
265
d_El=(band_values[(2*int_face[0])-j+1][3]-band_values[(2*int_face[0])-
j][3])/(depth_x[(2*int_face
[0])-j+1]-depth_x[(2*int_face[0])-j]);
266 }else if((2*int_face[0]-j+1)==0){
267
d_Eu=(band_values[j+1][2]-band_values[j-1][2])/(depth_x[j+1]-depth_x[j-
1]);
268
d_El=(band_values[(2*int_face[0])-j+2][3]-band_values[(2*int_face[0])-
j+1][3])/(depth_x[(2*int_fa
ce[0])-j+2]-depth_x[(2*int_face[0])-j+1]);
269 }else {
270
d_Eu=(band_values[j+1][2]-band_values[j-1][2])/(depth_x[j+1]-depth_x[j-
1]);
271
d_El=(band_values[(2*int_face[0])-j+2][3]-band_values[(2*int_face[0])-
j][3])/(depth_x[(2*int_face
[0])-j+2]-depth_x[(2*int_face[0])-j]);
272 }
273 double Vu=V_BBT(d_Eu);
274 double Vl=V_BBT(d_El);
275 double Efu;
276 double Efl;
277 if (abs(band_values[j][4])<=(7.3475918173e-16)){
278 Efu=7.3475918173e-16;
279 }else{
280 Efu=abs(band_values[j][4]);
281 }
282 if (abs(band_values[(2*int_face[0])-j+1][5])<=(7.3475918173e-16)){
283 Efl=-7.3475918173e-16;
284 }else{
285 Efl=(-1.0)*abs(band_values[(2*int_face[0])-j+1][5]);
286 }
287
gen_r_col_CB.push_back(Gen_BBT_r(1.0,A,gamma_r_trial_CB,Vu,Vl,band_values
[j][2],Efu,Efl,Tu,Tl));
288 gen_r_col_VB.push_back(0.0);
289 }else if (band_values[j][3]>=band_values[(2*int_face[0])-j+1][2]){
290 E_x=slice(Ev,j,int_face[0]);
291 reverse(E_x.begin(),E_x.end());
292 Epsilon=band_values[(2*int_face[0])-j+1][2];
293 double gamma_r_trial_VB;
294 if(r>(100.0e-9)){
295 gamma_r_trial_VB=0.0;
296 }else{
297 gamma_r_trial_VB=Gamma_BBT_r(r,m_h[i],Epsilon,E_x,Tcv_u,Tcv_l);
298 }
299 double gamma_r_trial_CB=0.0;
300 gamma_r_col_CB.push_back(gamma_r_trial_CB);
301 gamma_r_col_VB.push_back(gamma_r_trial_VB);
302 double d_Eu;
303 double d_El;
304 if (j==0 && ((2*int_face[0]-j+1)==(depth_x.size()-1))){
305
d_Eu=(band_values[j+1][3]-band_values[j][3])/(depth_x[j+1]-depth_x[j]);
306
d_El=(band_values[(2*int_face[0])-j+1][2]-band_values[(2*int_face[0])-
j][2])/(depth_x[(2*int_face
[0])-j+1]-depth_x[(2*int_face[0])-j]);
307 }else if (j==(depth_x.size()-1) && ((2*int_face[0]-j+1)==0)){
308
d_Eu=(band_values[j][3]-band_values[j-1][3])/(depth_x[j]-depth_x[j-1]);
309
d_El=(band_values[(2*int_face[0])-j+2][2]-band_values[(2*int_face[0])-
j+1][2])/(depth_x[(2*int_fa
ce[0])-j+2]-depth_x[(2*int_face[0])-j+1]);
310 }else if(j==0){
311
d_Eu=(band_values[j+1][3]-band_values[j][3])/(depth_x[j+1]-depth_x[j]);
312
d_El=(band_values[(2*int_face[0])-j+2][2]-band_values[(2*int_face[0])-
j][2])/(depth_x[(2*int_face
[0])-j+2]-depth_x[(2*int_face[0])-j]);
313 }else if(j==(depth_x.size()-1)){
314
d_Eu=(band_values[j][3]-band_values[j-1][3])/(depth_x[j]-depth_x[j-1]);
315
d_El=(band_values[(2*int_face[0])-j+2][2]-band_values[(2*int_face[0])-
j][2])/(depth_x[(2*int_face
[0])-j+2]-depth_x[(2*int_face[0])-j]);
316 }else if((2*int_face[0]-j+1)==(depth_x.size()-1)){
317
d_Eu=(band_values[j+1][3]-band_values[j-1][3])/(depth_x[j+1]-depth_x[j-
1]);
318
d_El=(band_values[(2*int_face[0])-j+1][2]-band_values[(2*int_face[0])-
j][2])/(depth_x[(2*int_face
[0])-j+1]-depth_x[(2*int_face[0])-j]);
319 }else if((2*int_face[0]-j+1)==0){
320
d_Eu=(band_values[j+1][3]-band_values[j-1][3])/(depth_x[j+1]-depth_x[j-
1]);
321
d_El=(band_values[(2*int_face[0])-j+2][2]-band_values[(2*int_face[0])-
j+1][2])/(depth_x[(2*int_fa
ce[0])-j+2]-depth_x[(2*int_face[0])-j+1]);
322 }else {
323
d_Eu=(band_values[j+1][3]-band_values[j-1][3])/(depth_x[j+1]-depth_x[j-
1]);
324
d_El=(band_values[(2*int_face[0])-j+2][2]-band_values[(2*int_face[0])-
j][2])/(depth_x[(2*int_face
[0])-j+2]-depth_x[(2*int_face[0])-j]);
325 }
326 double Vu=V_BBT(d_Eu);
327 double Vl=V_BBT(d_El);
328 double Efu;
329 double Efl;
330 if (abs(band_values[j][5])<=(7.3475918173e-16)){
331 Efu=-7.3475918173e-16;
332 }else{
333 Efu=(-1.0)*abs(band_values[j][5]);
334 }
335 if (abs(band_values[(2*int_face[0])-j+1][4])<=(7.3475918173e-16)){
336 Efl=7.3475918173e-16;
337 }else{
338 Efl=abs(band_values[(2*int_face[0])-j+1][4]);
339 }
340 gen_r_col_CB.push_back(0.0);
341
gen_r_col_VB.push_back(Gen_BBT_r(2.0,A,gamma_r_trial_VB,Vu,Vl,band_values
[j][3],Efu,Efl,Tu,Tl));
342 }else {
343 gamma_r_col_VB.push_back(0.0);
344 gamma_r_col_CB.push_back(0.0);
345 gen_r_col_VB.push_back(0.0);
346 gen_r_col_CB.push_back(0.0);
347 }
348 }
349 }else if (depth_x[j]==barrier_location[i] && (int_face.size()==1)){
// if the
device depth i is on the barrier and the barrier has no continuity
350 r=barrier_location[i]-depth_x[j];
351 if (band_values[j][2]<=band_values[j][3]){
352 E_x_1=slice(Ec,j,int_face[0]);
353 Epsilon_1=band_values[j][3];
354 E_x_2=slice(Ev,j,int_face[0]);
355 Epsilon_2=band_values[j][2];
```

```
356 double
gamma_r_trial_CB=Gamma_BBT_r(r,m_e[i],Epsilon_1,E_x_1,Tcv_u,Tcv_l);
357 double
gamma_r_trial_VB=Gamma_BBT_r(r,m_h[i],Epsilon_2,E_x_2,Tcv_u,Tcv_l);
358 gamma_r_col_CB.push_back(gamma_r_trial_CB);
359 gamma_r_col_VB.push_back(gamma_r_trial_VB);
360 double d_Eu;
361 double d_El;
362 double d_Eu_1;
363 double d_El_1;
364 d_Eu=(band_values[j+1][2]-band_values[j-1][2])/(depth_x[j+1]-
depth_x[j-1]);
365 d_El=(band_values[j+1][3]-band_values[j-1][3])/(depth_x[j+1]-
depth_x[j-1]);
366 double Vu=V_BBT(d_Eu);
367 double Vl=V_BBT(d_El);
368 d_Eu_1=(band_values[j+1][3]-band_values[j-1][3])/(depth_x[j+1]-
depth_x[j-1]);
369 d_El_1=(band_values[j+1][2]-band_values[j-1][2])/(depth_x[j+1]-
depth_x[j-1]);
370 double Vu_1=V_BBT(d_Eu_1);
371 double Vl_1=V_BBT(d_El_1);
372
gen_r_col_CB.push_back(Gen_BBT_r(1.0,A,gamma_r_trial_CB,Vu,Vl,band_values
[j][2],band_values[j][4]
,band_values[j][5],Tu,Tl));
373
gen_r_col_VB.push_back(Gen_BBT_r(2.0,A,gamma_r_trial_VB,Vu_1,Vl_1,band_va
lues[j][3],band_values[j
][5],band_values[j][4],Tu,Tl));
374 }else {
375 gamma_r_col_VB.push_back(0.0);
376 gamma_r_col_CB.push_back(0.0);
377 gen_r_col_VB.push_back(0.0);
378 gen_r_col_CB.push_back(0.0);
379 }
380 }else if (depth_x[j]==barrier_location[i] && (int_face.size()==2)){
// if the
device depth i is on the barrier and the barrier has continuity
381 r=barrier_location[i]-depth_x[j];
382 if (j==int_face[0]){
383 if(band_values[j][2]<=band_values[j+1][3]){
384 E_x=slice(Ec,j,int_face[0]);
385 Epsilon=band_values[j+1][3];
386 double
gamma_r_trial_CB=Gamma_BBT_r(r,m_e[i],Epsilon,E_x,Tcv_u,Tcv_l);
387 double gamma_r_trial_VB=0.0;
388 gamma_r_col_CB.push_back(gamma_r_trial_CB);
389 gamma_r_col_VB.push_back(gamma_r_trial_VB);
390 double d_Eu;
391 double d_El;
392
d_Eu=(band_values[j+1][2]-band_values[j-1][2])/(depth_x[j+1]-depth_x[j-
1]);
393 d_El=(band_values[j+2][3]-band_values[j][3])/(depth_x[j+2]-
depth_x[j]);
394 double Vu=V_BBT(d_Eu);
395 double Vl=V_BBT(d_El);
396
gen_r_col_CB.push_back(Gen_BBT_r(1.0,A,gamma_r_trial_CB,Vu,Vl,band_values
[j][2],band_values[j][4]
,band_values[j+1][5],Tu,Tl));
397 gen_r_col_VB.push_back(0.0);
398 }else if (band_values[j][3]>=band_values[j+1][2]){
399 E_x=slice(Ev,j,int_face[0]);
400 Epsilon=band_values[j+1][2];
401 double gamma_r_trial_CB=0.0;
402 double
gamma_r_trial_VB=Gamma_BBT_r(r,m_h[i],Epsilon,E_x,Tcv_u,Tcv_l);
403 gamma_r_col_CB.push_back(gamma_r_trial_CB);
404 gamma_r_col_VB.push_back(gamma_r_trial_VB);
405 double d_Eu;
406 double d_El;
407
d_Eu=(band_values[j+1][3]-band_values[j-1][3])/(depth_x[j+1]-depth_x[j-
1]);
408 d_El=(band_values[j+2][2]-band_values[j][2])/(depth_x[j+2]-
depth_x[j]);
409 double Vu=V_BBT(d_Eu);
410 double Vl=V_BBT(d_El);
411 gen_r_col_CB.push_back(0.0);
412
gen_r_col_VB.push_back(Gen_BBT_r(2.0,A,gamma_r_trial_VB,Vu,Vl,band_values
[j][3],band_values[j][5]
,band_values[j+1][4],Tu,Tl));
413 }else {
414 gamma_r_col_VB.push_back(0.0);
415 gamma_r_col_CB.push_back(0.0);
416 gen_r_col_VB.push_back(0.0);
417 gen_r_col_CB.push_back(0.0);
418 }
419 }else{
420 if(band_values[j][2]<=band_values[j-1][3]){
421 E_x=slice(Ec,int_face[1],j);
422 Epsilon=band_values[j-1][3];
423 double
gamma_r_trial_CB=Gamma_BBT_r(r,m_e[i+1],Epsilon,E_x,Tcv_u,Tcv_l);
424 double gamma_r_trial_VB=0.0;
425 gamma_r_col_CB.push_back(gamma_r_trial_CB);
426 gamma_r_col_VB.push_back(gamma_r_trial_VB);
427 double d_Eu;
428 double d_El;
429
d_Eu=(band_values[j+1][2]-band_values[j-1][2])/(depth_x[j+1]-depth_x[j-
1]);
430 d_El=(band_values[j][3]-band_values[j-2][3])/(depth_x[j]-depth_x[j-
2]);
431 double Vu=V_BBT(d_Eu);
```

```
432 double Vl=V_BBT(d_El);
433
gen_r_col_CB.push_back(Gen_BBT_r(1.0,A,gamma_r_trial_CB,Vu,Vl,band_values
[j][2],band_values[j][4]
,band_values[j-1][5],Tu,Tl));
434 gen_r_col_VB.push_back(0.0);
435 }else if (band_values[j][3]>=band_values[j-1][2]){
436 E_x=slice(Ev,int_face[1],j);
437 Epsilon=band_values[j-1][2];
438 double gamma_r_trial_CB=0.0;
439 double
gamma_r_trial_VB=Gamma_BBT_r(r,m_h[i+1],Epsilon,E_x,Tcv_u,Tcv_l);
440 gamma_r_col_CB.push_back(gamma_r_trial_CB);
441 gamma_r_col_VB.push_back(gamma_r_trial_VB);
442 double d_Eu;
443 double d_El;
444
d_Eu=(band_values[j+1][3]-band_values[j-1][3])/(depth_x[j+1]-depth_x[j-
1]);
445 d_El=(band_values[j][2]-band_values[j-2][2])/(depth_x[j]-depth_x[j-
2]);
446 double Vu=V_BBT(d_Eu);
447 double Vl=V_BBT(d_El);
448 gen_r_col_CB.push_back(0.0);
449
gen_r_col_VB.push_back(Gen_BBT_r(2.0,A,gamma_r_trial_VB,Vu,Vl,band_values
[j][3],band_values[j][5]
,band_values[j-1][4],Tu,Tl));
450 }else {
451 gamma_r_col_VB.push_back(0.0);
452 gamma_r_col_CB.push_back(0.0);
453 gen_r_col_VB.push_back(0.0);
454 gen_r_col_CB.push_back(0.0);
455 }
456 }
457 }else if (depth_x[j]>barrier_location[i] && (int_face.size()==2)){ //
if the device
depth i is on the right side of the barrier and the barrier has
continuity
458 r=depth_x[j]-barrier_location[i];
459 if (((2*int_face[1])-j-1)<0){
460 gamma_r_col_VB.push_back(0.0);
461 gamma_r_col_CB.push_back(0.0);
462 gen_r_col_VB.push_back(0.0);
463 gen_r_col_CB.push_back(0.0);
464 }else if (((2*int_face[1])-j-1)>(depth_x.size()-1)){
465 gamma_r_col_VB.push_back(0.0);
466 gamma_r_col_CB.push_back(0.0);
467 gen_r_col_VB.push_back(0.0);
468 gen_r_col_CB.push_back(0.0);
469 }else{
470 if (band_values[j][2]<=band_values[(2*int_face[1])-j-1][3]){
471 E_x=slice(Ec,int_face[1],j);
472 Epsilon=band_values[(2*int_face[1])-j-1][3];
473 double gamma_r_trial_CB;
474 if(r>(100.0e-9)){
475 gamma_r_trial_CB=0.0;
476 }else{
477 gamma_r_trial_CB=Gamma_BBT_r(r,m_e[i+1],Epsilon,E_x,Tcv_u,Tcv_l);
478 }
479 double gamma_r_trial_VB=0.0;
480 gamma_r_col_CB.push_back(gamma_r_trial_CB);
481 gamma_r_col_VB.push_back(gamma_r_trial_VB);
482 double d_Eu;
483 double d_El;
484 if (j==0 && ((2*int_face[1]-j-1)==(depth_x.size()-1))){
485
d_Eu=(band_values[j+1][2]-band_values[j][2])/(depth_x[j+1]-depth_x[j]);
486
d_El=(band_values[(2*int_face[1])-j-1][3]-band_values[(2*int_face[1])-j-
2][3])/(depth_x[(2*int_fa
ce[1])-j-1]-depth_x[(2*int_face[1])-j-2]);
487 }else if (j==(depth_x.size()-1) && ((2*int_face[1]-j-1)==0)){
488
d_Eu=(band_values[j][2]-band_values[j-1][2])/(depth_x[j]-depth_x[j-1]);
489
d_El=(band_values[(2*int_face[1])-j][3]-band_values[(2*int_face[1])-j-
1][3])/(depth_x[(2*int_face
[1])-j]-depth_x[(2*int_face[1])-j-1]);
490 }else if(j==0){
491
d_Eu=(band_values[j+1][2]-band_values[j][2])/(depth_x[j+1]-depth_x[j]);
492
d_El=(band_values[(2*int_face[1])-j][3]-band_values[(2*int_face[1])-j-
2][3])/(depth_x[(2*int_face
[1])-j]-depth_x[(2*int_face[1])-j-2]);
493 }else if(j==(depth_x.size()-1)){
494
d_Eu=(band_values[j][2]-band_values[j-1][2])/(depth_x[j]-depth_x[j-1]);
495
d_El=(band_values[(2*int_face[1])-j][3]-band_values[(2*int_face[1])-j-
2][3])/(depth_x[(2*int_face
[1])-j]-depth_x[(2*int_face[1])-j-2]);
496 }else if((2*int_face[1]-j-1)==(depth_x.size()-1)){
497
d_Eu=(band_values[j+1][2]-band_values[j-1][2])/(depth_x[j+1]-depth_x[j-
1]);
498
d_El=(band_values[(2*int_face[1])-j-1][3]-band_values[(2*int_face[1])-j-
2][3])/(depth_x[(2*int_fa
ce[1])-j-1]-depth_x[(2*int_face[1])-j-2]);
499 }else if((2*int_face[1]-j-1)==0){
500
d_Eu=(band_values[j+1][2]-band_values[j-1][2])/(depth_x[j+1]-depth_x[j-
1]);
501
d_El=(band_values[(2*int_face[1])-j][3]-band_values[(2*int_face[1])-j-
1][3])/(depth_x[(2*int_face
```

```
[1])-j]-depth_x[(2*int_face[1])-j-1]);
502 }else {
503
d_Eu=(band_values[j+1][2]-band_values[j-1][2])/(depth_x[j+1]-depth_x[j-
1]);
504
d_El=(band_values[(2*int_face[1])-j][3]-band_values[(2*int_face[1])-j-
2][3])/(depth_x[(2*int_face
[1])-j]-depth_x[(2*int_face[1])-j-2]);
505 }
506 double Vu=V_BBT(d_Eu);
507 double Vl=V_BBT(d_El);
508 double Efu;
509 double Efl;
510 if (abs(band_values[j][4])<=(7.3475918173e-16)){
511 Efu=7.3475918173e-16;
512 }else{
513 Efu=abs(band_values[j][4]);
514 }
515 if (abs(band_values[(2*int_face[1])-j-1][5])<=(7.3475918173e-16)){
516 Efl=-7.3475918173e-16;
517 }else{
518 Efl=(-1.0)*abs(band_values[(2*int_face[1])-j-1][5]);
519 }
520
gen_r_col_CB.push_back(Gen_BBT_r(1.0,A,gamma_r_trial_CB,Vu,Vl,band_values
[j][2],Efu,Efl,Tu,Tl));
521 gen_r_col_VB.push_back(0.0);
522 }else if (band_values[j][3]>=band_values[(2*int_face[1])-j-1][2]){
523 E_x=slice(Ev,int_face[1],j);
524 Epsilon=band_values[(2*int_face[1])-j-1][2];
525 double gamma_r_trial_VB;
526 if(r>(100.0e-9)){
527 gamma_r_trial_VB=0.0;
528 }else{
529 gamma_r_trial_VB=Gamma_BBT_r(r,m_h[i+1],Epsilon,E_x,Tcv_u,Tcv_l);
530 }
531 double gamma_r_trial_CB=0.0;
532 gamma_r_col_CB.push_back(gamma_r_trial_CB);
533 gamma_r_col_VB.push_back(gamma_r_trial_VB);
534 double d_Eu;
535 double d_El;
536 if (j==0 && ((2*int_face[1]-j-1)==(depth_x.size()-1))){
537
d_Eu=(band_values[j+1][3]-band_values[j][3])/(depth_x[j+1]-depth_x[j]);
538
d_El=(band_values[(2*int_face[1])-j-1][2]-band_values[(2*int_face[1])-j-
2][2])/(depth_x[(2*int_fa
ce[1])-j-1]-depth_x[(2*int_face[1])-j-2]);
539 }else if (j==(depth_x.size()-1) && ((2*int_face[1]-j-1)==0)){
540
d_Eu=(band_values[j][3]-band_values[j-1][3])/(depth_x[j]-depth_x[j-1]);
541
```

```
d_El=(band_values[(2*int_face[1])-j][2]-band_values[(2*int_face[1])-j-
1][2])/(depth_x[(2*int_face
[1])-j]-depth_x[(2*int_face[1])-j-1]);
542 }else if(j==0){
543
d_Eu=(band_values[j+1][3]-band_values[j][3])/(depth_x[j+1]-depth_x[j]);
544
d_El=(band_values[(2*int_face[1])-j][2]-band_values[(2*int_face[1])-j-
2][2])/(depth_x[(2*int_face
[1])-j]-depth_x[(2*int_face[1])-j-2]);
545 }else if(j==(depth_x.size()-1)){
546
d_Eu=(band_values[j][3]-band_values[j-1][3])/(depth_x[j]-depth_x[j-1]);
547
d_El=(band_values[(2*int_face[1])-j][2]-band_values[(2*int_face[1])-j-
2][2])/(depth_x[(2*int_face
[1])-j]-depth_x[(2*int_face[1])-j-2]);
548 }else if((2*int_face[1]-j-1)==(depth_x.size()-1)){
549
d_Eu=(band_values[j+1][3]-band_values[j-1][3])/(depth_x[j+1]-depth_x[j-
1]);
550
d_El=(band_values[(2*int_face[1])-j-1][2]-band_values[(2*int_face[1])-j-
2][2])/(depth_x[(2*int_fa
ce[1])-j-1]-depth_x[(2*int_face[1])-j-2]);
551 }else if((2*int_face[1]-j-1)==0){
552
d_Eu=(band_values[j+1][3]-band_values[j-1][3])/(depth_x[j+1]-depth_x[j-
1]);
553
d_El=(band_values[(2*int_face[1])-j][2]-band_values[(2*int_face[1])-j-
1][2])/(depth_x[(2*int_face
[1])-j]-depth_x[(2*int_face[1])-j-1]);
554 }else {
555
d_Eu=(band_values[j+1][3]-band_values[j-1][3])/(depth_x[j+1]-depth_x[j-
1]);
556
d_El=(band_values[(2*int_face[1])-j][2]-band_values[(2*int_face[1])-j-
2][2])/(depth_x[(2*int_face
[1])-j]-depth_x[(2*int_face[1])-j-2]);
557 }
558 double Vu=V_BBT(d_Eu);
559 double Vl=V_BBT(d_El);
560 double Efu;
561 double Efl;
562 if (abs(band_values[j][5])<=(7.3475918173e-16)){
563 Efu=-7.3475918173e-16;
564 }else{
565 Efu=(-1.0)*abs(band_values[j][5]);
566 }
567 if (abs(band_values[(2*int_face[1])-j-1][4])<=(7.3475918173e-16)){
568 Efl=7.3475918173e-16;
569 }else{
```

```
570 Efl=abs(band_values[(2*int_face[1])-j-1][4]);
571 }
572 gen_r_col_CB.push_back(0.0);
573
gen_r_col_VB.push_back(Gen_BBT_r(2.0,A,gamma_r_trial_VB,Vu,Vl,band_values
[j][3],Efu,Efl,Tu,Tl));
574 }else {
575 gamma_r_col_VB.push_back(0.0);
576 gamma_r_col_CB.push_back(0.0);
577 gen_r_col_VB.push_back(0.0);
578 gen_r_col_CB.push_back(0.0);
579 }
580 }
581 }else{
582
r=depth_x[j]-barrier_location[i];
// if the device depth i is on the right side of the barrier and the
barrier has no continuity
583 if (((2*int_face[0])-j)<0){
584 gamma_r_col_VB.push_back(0.0);
585 gamma_r_col_CB.push_back(0.0);
586 gen_r_col_VB.push_back(0.0);
587 gen_r_col_CB.push_back(0.0);
588 }else if (((2*int_face[0])-j)>(depth_x.size()-1)){
589 gamma_r_col_VB.push_back(0.0);
590 gamma_r_col_CB.push_back(0.0);
591 gen_r_col_VB.push_back(0.0);
592 gen_r_col_CB.push_back(0.0);
593 }else{
594 if (band_values[j][2]<=band_values[(2*int_face[0])-j][3]){
595 E_x=slice(Ec,int_face[0],j);
596 Epsilon=band_values[(2*int_face[0])-j][3];
597 double gamma_r_trial_CB;
598 if(r>(100.0e-9)){
599 gamma_r_trial_CB=0.0;
600 }else{
601 gamma_r_trial_CB=Gamma_BBT_r(r,m_e[i+1],Epsilon,E_x,Tcv_u,Tcv_l);
602 }
603 double gamma_r_trial_VB=0.0;
604 gamma_r_col_CB.push_back(gamma_r_trial_CB);
605 gamma_r_col_VB.push_back(gamma_r_trial_VB);
606 double d_Eu;
607 double d_El;
608 if (j==0 && ((2*int_face[0]-j)==(depth_x.size()-1))){
609
d_Eu=(band_values[j+1][2]-band_values[j][2])/(depth_x[j+1]-depth_x[j]);
610
d_El=(band_values[(2*int_face[0])-j][3]-band_values[(2*int_face[0])-j-
1][3])/(depth_x[(2*int_face
[0])-j]-depth_x[(2*int_face[0])-j-1]);
611 }else if (j==(depth_x.size()-1) && ((2*int_face[0]-j)==0)){
612
d_Eu=(band_values[j][2]-band_values[j-1][2])/(depth_x[j]-depth_x[j-1]);
613
```

```
d_El=(band_values[(2*int_face[0])-j+1][3]-band_values[(2*int_face[0])-
j][3])/(depth_x[(2*int_face
[0])-j+1]-depth_x[(2*int_face[0])-j]);
614 }else if(j==0){
615
d_Eu=(band_values[j+1][2]-band_values[j][2])/(depth_x[j+1]-depth_x[j]);
616
d_El=(band_values[(2*int_face[0])-j+1][3]-band_values[(2*int_face[0])-j-
1][3])/(depth_x[(2*int_fa
ce[0])-j+1]-depth_x[(2*int_face[0])-j-1]);
617 }else if(j==(depth_x.size()-1)){
618
d_Eu=(band_values[j][2]-band_values[j-1][2])/(depth_x[j]-depth_x[j-1]);
619
d_El=(band_values[(2*int_face[0])-j+1][3]-band_values[(2*int_face[0])-j-
1][3])/(depth_x[(2*int_fa
ce[0])-j+1]-depth_x[(2*int_face[0])-j-1]);
620 }else if((2*int_face[0]-j)==(depth_x.size()-1)){
621
d_Eu=(band_values[j+1][2]-band_values[j-1][2])/(depth_x[j+1]-depth_x[j-
1]);
622
d_El=(band_values[(2*int_face[0])-j][3]-band_values[(2*int_face[0])-j-
1][3])/(depth_x[(2*int_face
[0])-j]-depth_x[(2*int_face[0])-j-1]);
623 }else if((2*int_face[0]-j)==0){
624
d_Eu=(band_values[j+1][2]-band_values[j-1][2])/(depth_x[j+1]-depth_x[j-
1]);
625
d_El=(band_values[(2*int_face[0])-j+1][3]-band_values[(2*int_face[0])-
j][3])/(depth_x[(2*int_face
[0])-j+1]-depth_x[(2*int_face[0])-j]);
626 }else {
627
d_Eu=(band_values[j+1][2]-band_values[j-1][2])/(depth_x[j+1]-depth_x[j-
1]);
628
d_El=(band_values[(2*int_face[0])-j+1][3]-band_values[(2*int_face[0])-j-
1][3])/(depth_x[(2*int_fa
ce[0])-j+1]-depth_x[(2*int_face[0])-j-1]);
629 }
630 double Vu=V_BBT(d_Eu);
631 double Vl=V_BBT(d_El);
632 double Efu;
633 double Efl;
634 if (abs(band_values[j][4])<=(7.3475918173e-16)){
635 Efu=7.3475918173e-16;
636 }else{
637 Efu=abs(band_values[j][4]);
638 }
639 if (abs(band_values[(2*int_face[0])-j][5])<=(7.3475918173e-16)){
640 Efl=-7.3475918173e-16;
641 }else{
```

```
642 Efl=(-1.0)*abs(band_values[(2*int_face[0])-j][5]);
643 }
644
gen_r_col_CB.push_back(Gen_BBT_r(1.0,A,gamma_r_trial_CB,Vu,Vl,band_values
[j][2],Efu,Efl,Tu,Tl));
645 gen_r_col_VB.push_back(0.0);
646 }else if (band_values[j][3]>=band_values[(2*int_face[0])-j][2]){
647 E_x=slice(Ev,int_face[0],j);
648 Epsilon=band_values[(2*int_face[0])-j][2];
649 double gamma_r_trial_VB;
650 if(r>(100.0e-9)){
651 gamma_r_trial_VB=0.0;
652 }else{
653 gamma_r_trial_VB=Gamma_BBT_r(r,m_h[i+1],Epsilon,E_x,Tcv_u,Tcv_l);
654 }
655 double gamma_r_trial_CB=0.0;
656 gamma_r_col_CB.push_back(gamma_r_trial_CB);
657 gamma_r_col_VB.push_back(gamma_r_trial_VB);
658 double d_Eu;
659 double d_El;
660 if (j==0 && ((2*int_face[0]-j)==(depth_x.size()-1))){
661
d_Eu=(band_values[j+1][3]-band_values[j][3])/(depth_x[j+1]-depth_x[j]);
662
d_El=(band_values[(2*int_face[0])-j][2]-band_values[(2*int_face[0])-j-
1][2])/(depth_x[(2*int_face
[0])-j]-depth_x[(2*int_face[0])-j-1]);
663 }else if (j==(depth_x.size()-1) && ((2*int_face[0]-j)==0)){
664
d_Eu=(band_values[j][3]-band_values[j-1][3])/(depth_x[j]-depth_x[j-1]);
665
d_El=(band_values[(2*int_face[0])-j+1][2]-band_values[(2*int_face[0])-
j][2])/(depth_x[(2*int_face
[0])-j+1]-depth_x[(2*int_face[0])-j]);
666 }else if(j==0){
667
d_Eu=(band_values[j+1][3]-band_values[j][3])/(depth_x[j+1]-depth_x[j]);
668
d_El=(band_values[(2*int_face[0])-j+1][2]-band_values[(2*int_face[0])-j-
1][2])/(depth_x[(2*int_fa
ce[0])-j+1]-depth_x[(2*int_face[0])-j-1]);
669 }else if(j==(depth_x.size()-1)){
670
d_Eu=(band_values[j][3]-band_values[j-1][3])/(depth_x[j]-depth_x[j-1]);
671
d_El=(band_values[(2*int_face[0])-j+1][2]-band_values[(2*int_face[0])-j-
1][2])/(depth_x[(2*int_fa
ce[0])-j+1]-depth_x[(2*int_face[0])-j-1]);
672 }else if((2*int_face[0]-j)==(depth_x.size()-1)){
673
d_Eu=(band_values[j+1][3]-band_values[j-1][3])/(depth_x[j+1]-depth_x[j-
1]);
674
d_El=(band_values[(2*int_face[0])-j][2]-band_values[(2*int_face[0])-j-
1][2])/(depth_x[(2*int_face
[0])-j]-depth_x[(2*int_face[0])-j-1]);
675 }else if((2*int_face[0]-j)==0){
676
d_Eu=(band_values[j+1][3]-band_values[j-1][3])/(depth_x[j+1]-depth_x[j-
1]);
677
d_El=(band_values[(2*int_face[0])-j+1][2]-band_values[(2*int_face[0])-
j][2])/(depth_x[(2*int_face
[0])-j+1]-depth_x[(2*int_face[0])-j]);
678 }else {
679
d_Eu=(band_values[j+1][3]-band_values[j-1][3])/(depth_x[j+1]-depth_x[j-
1]);
680
d_El=(band_values[(2*int_face[0])-j+1][2]-band_values[(2*int_face[0])-j-
1][2])/(depth_x[(2*int_fa
ce[0])-j+1]-depth_x[(2*int_face[0])-j-1]);
681 }
682 double Vu=V_BBT(d_Eu);
683 double Vl=V_BBT(d_El);
684 double Efu;
685 double Efl;
686 if (abs(band_values[j][5])<=(7.3475918173e-16)){
687 Efu=-7.3475918173e-16;
688 }else{
689 Efu=(-1.0)*abs(band_values[j][5]);
690 }
691 if (abs(band_values[(2*int_face[0])-j][4])<=(7.3475918173e-16)){
692 Efl=7.3475918173e-16;
693 }else{
694 Efl=abs(band_values[(2*int_face[0])-j][4]);
695 }
696 gen_r_col_CB.push_back(0.0);
697
gen_r_col_VB.push_back(Gen_BBT_r(2.0,A,gamma_r_trial_VB,Vu,Vl,band_values
[j][3],Efu,Efl,Tu,Tl));
698 }else {
699 gamma_r_col_VB.push_back(0.0);
700 gamma_r_col_CB.push_back(0.0);
701 gen_r_col_VB.push_back(0.0);
702 gen_r_col_CB.push_back(0.0);
703 }
704 }
705 }
706 }
707 Gamma_BBT_VB.push_back(gamma_r_col_VB);
708 Gen_BBT_VB.push_back(gen_r_col_VB);
709 Gamma_BBT_CB.push_back(gamma_r_col_CB);
710 Gen_BBT_CB.push_back(gen_r_col_CB);
711 }
712
713 // combining depth_x array and tunnelling values into one single 2d
array of the order of
[depth(x)....DT_Tun_CB_int_face(n)....DT_Tun_VB_int_face(n)]
714 vector<vector<double>> gamma_final;
715 vector<vector<double>> gen_final;
716 if (Gen_BBT_CB.size()>1){
717 vector<double> gamma_sum_CB;
718 vector<double> gamma_sum_VB;
719 vector<double> gen_sum_CB;
720 vector<double> gen_sum_VB;
721 for(int x = 0; x < Gamma_BBT_CB[0].size(); x++){
722 double sum_CB=0;
723 double sum_VB=0;
724 double sum_one_CB=0;
725 double sum_one_VB=0;
726 for(int y = 0; y < Gamma_BBT_CB.size(); y++){
727 sum_CB=sum_CB+Gamma_BBT_CB[y][x];
728 sum_VB=sum_VB+Gamma_BBT_VB[y][x];
729 sum_one_CB=sum_one_CB+Gen_BBT_CB[y][x];
730 sum_one_VB=sum_one_VB+Gen_BBT_VB[y][x];
731 }
732 gamma_sum_CB.push_back(sum_CB);
733 gamma_sum_VB.push_back(sum_VB);
734 gen_sum_CB.push_back(sum_one_CB);
735 gen_sum_VB.push_back(sum_one_VB);
736 }
737
738 gamma_final.push_back(depth_x);
739 gamma_final.push_back(gamma_sum_CB);
740 gamma_final.push_back(gamma_sum_VB);
741 transpose_matrix(gamma_final);
742
743 gen_final.push_back(depth_x);
744 gen_final.push_back(gen_sum_CB);
745 gen_final.push_back(gen_sum_VB);
746 transpose_matrix(gen_final);
747
748 }else{
749 gamma_final.push_back(depth_x);
750 for (int i=0 ; i<Gamma_BBT_CB.size() ; i++){
751 vector<double> copyRow( Gamma_BBT_CB[i].begin(),
Gamma_BBT_CB[i].end());
752 vector<double> copyRow_2( Gamma_BBT_VB[i].begin(),
Gamma_BBT_VB[i].end());
753 gamma_final.push_back(copyRow);
754 gamma_final.push_back(copyRow_2);
755 }
756 transpose_matrix(gamma_final);
757
758 gen_final.push_back(depth_x);
759 for (int i=0 ; i<Gen_BBT_CB.size() ; i++){
760 vector<double> copyRow( Gen_BBT_CB[i].begin(), Gen_BBT_CB[i].end());
761 vector<double> copyRow_2( Gen_BBT_VB[i].begin(),
Gen_BBT_VB[i].end());
762 gen_final.push_back(copyRow);
763 gen_final.push_back(copyRow_2);
764 }
765 transpose_matrix(gen_final);
766
767 }
768
769 // Creating text files for the results
770 print_file_from_2D_matrix(gamma_final,"Gamma_BBT_nonlocal.txt");
771 print_file_from_2D_matrix(gen_final,"Gen_BBT_nonlocal.txt");
772 cout << "The Band to Band Tunnelling process is finished and the
Generation result is
printed in your current directory folder";
773 return 0;
774 }
775
776 double Gamma_BBT_r(double r,double m,double Epsilon,vector<double>
E_x,double Tcv_u,double Tcv_l)
777 {
778 double q=1.602*pow(10.0,-19.0); // Charge constant
779 double h=6.582*pow(10.0,-16.0); // Dirac constant in eV
780 double integral_ans=0.0;
781 int n_intervals=E_x.size();
782 double dx=(r-0.0)/(n_intervals*2.0);
783 for (int i = 0; i < n_intervals; i++) {
784 if (i==0){
785 double area_under_integration=sqrt(2.0*m*abs(Epsilon-E_x[i]))*dx;
786 integral_ans=integral_ans+area_under_integration;
787 }else if (i==(n_intervals-1)){
788 double area_under_integration=sqrt(2.0*m*abs(Epsilon-E_x[i]))*dx;
789 integral_ans=integral_ans+area_under_integration;
790 }else{
791 double area_under_integration=sqrt(2.0*m*abs(Epsilon-E_x[i]))*dx;
792 integral_ans=integral_ans+(2*area_under_integration);
793 }
794 }
795 double gamma_r=Tcv_u*Tcv_l*exp(((-2.0)/(h))*integral_ans);
796 return gamma_r;
797 }
798
799 double Gen_BBT_r(double number,double A,double gamma_r,double
Vu,double Vl,double E,double
Efu,double Efl,double Tu,double Tl)
800 {
801 double q = 1.602*pow(10.0,-19.0);
802 double kb = 1.381*pow(10.0,-23.0);
803 double gen_r;
804 if (number==1.0){
805 gen_r =
((A*gamma_r*(Tu+Tl)*Vu*Vl)/(2.0*kb*q))*(pow(((1+exp((-q)*(Efu-
E)/(kb*Tu)))),-1.0)-pow((1+exp((-q)
*(Efl-E)/(kb*Tl))),(-1)));
806 }else if (number==2.0){
807 gen_r =
```

```
((A*gamma_r*(Tu+Tl)*Vu*Vl)/(2.0*kb*q))*(pow(((1+exp((-q)*(E-
Efu)/(kb*Tu)))),-1.0)-pow((1+exp((-q)
*(E-Efl)/(kb*Tl))),(-1)));
808 }else {
809 gen_r = 0.0;
810 }
811 return gen_r;
812 }
813
814 double V_BBT(double dy)
815 {
816 double V;
817 if (dy>0){
818 V=dy;
819 }else {
820 V=0.0;
821 }
822 return V;
823 }
824
825 void print_1D_vector(vector<double> matrix){
826 for (int i=0;i<matrix.size();i++){
827 cout << matrix[i] << " ";
828 }
829 cout << endl;
830 }
831
832 void print_2D_vector(vector<vector<double>> matrix){
833 for (int i = 0; i < matrix.size(); i++)
834 {
835 for (int j = 0; j < matrix[i].size(); j++)
836 {
837 cout << matrix[i][j] << " ";
838 }
839 cout << endl;
840 }
841 }
842
843 void transpose_matrix(vector<vector<double>> &matrix)
844 {
845 if (matrix.size() == 0)
846 return;
847
848 vector<vector<double>> trans_vec(matrix[0].size(), vector<double>());
849 for (int i = 0; i < matrix.size(); i++)
850 {
851 for (int j = 0; j < matrix[i].size(); j++)
852 {
853 trans_vec[j].push_back(matrix[i][j]);
854 }
855 }
856 matrix = trans_vec; // <--- reassign here
857 }
858
859 vector<double> find_index(vector<double> &matrix,double value){
860 vector<double> index_values;
861 for (int i = 0; i < matrix.size(); i++) {
862 if(abs(matrix[i]-value)<(0.001e-9)){
863 index_values.push_back(i);
864 }
865 }
866 return index_values;
867 }
868
869 vector<double> slice(vector<double> const &v, double m, double n)
870 {
871 auto first = v.cbegin() + m;
872 auto last = v.cbegin() + n + 1;
873 vector<double> vec(first, last);
874 return vec;
875 }
876
877 void extract_rows_from_matrix(vector<vector<double>> matrix_1, int
row, vector<double> &matrix_2)
878 {
879 vector<double> data;
880 for (int i=0; i<matrix_1.size(); i++){
881 for (int j=0; j<matrix_1[i].size(); j++){
882 if(i==row){
883 data.push_back(matrix_1[i][j]);
884 }
885 }
886 }
887 matrix_2 = data;
888 }
889
890 void extract_columns_from_matrix(vector<vector<double>> matrix_1, int
column, vector<double>
&matrix_2)
891 {
892 vector<double> data;
893 for (int i=0; i<matrix_1.size(); i++){
894 for (int j=0; j<matrix_1[i].size(); j++){
895 if(j==column){
896 data.push_back(matrix_1[i][j]);
897 }
898 }
899 }
900 matrix_2 = data;
901 }
902
903 void get_matrix_from_file(string filename,vector<vector<double>>
&matrix)
904 {
905 vector< vector<double> > data;
906
907 ifstream in( filename );
908 for ( string line; getline( in, line ); )
909 {
910 stringstream ss( line );
911 vector<double> row;
912 for ( double d; ss >> d; ) row.push_back( d );
913 data.push_back( row );
914 }
915 matrix = data;
916 }
917
918 void print_file_from_2D_matrix(vector<vector<double>> matrix,string
filename)
919 {
920 FILE * output;
921 output = fopen (filename.c_str(),"w");
922 for (int i=0; i<matrix.size(); i++){
923 for (int j=0; j<matrix[i].size(); j++){
924 if(j==(matrix[i].size()-1)){
925 fprintf (output, "%.6e",matrix[i][j]);
926 }else{
927 fprintf (output, "%.6e ",matrix[i][j]);
928 }
929 }
930 if(i!=(matrix.size()-1)){
931 fprintf (output, "\n");
932 }
933 }
934 fclose (output);
935 }
936
937 void print_file_from_1D_matrix(vector<double> matrix,string filename)
938 {
939 FILE * output;
940 output = fopen (filename.c_str(),"w");
941 for (int i=0; i<matrix.size(); i++){
942 if(i==(matrix.size()-1)){
943 fprintf (output, "%.6e",matrix[i]);
944 }else{
945 fprintf (output, "%.6e\n",matrix[i]);
946 }
947 }
948 fclose (output);
949 }
950
```

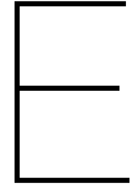

Input files for the validation of the tunnelling algorithms

E.1. ASA input file for the PN junction

```
1 # VALIDATION OF AN AMORPHOUS HYDROGENATED SILICON / CRYSTALLINE SILICON
P-N JUNCTION
SOLAR CELL;
2 # NAME - RAIYAN RIYAZ SHAIKH (Student no - 5267013);
3 # DAILY SUPERVISOR - Dr. ir. Carlos Ruiz Tobon;
4 # MAIN SUPERVISOR - Dr. ir. Rudi Santbergen;
5 # PVMD committee - Dr. ir. Olindo Isabella;
6
7 # Name Layer-f.1 TCO SnO-Asai;
8 # Name Layer-1 a-Si:H(P);
9 # Name Layer-2 c-Si;
10 # Name Layer-b.1 Al-Aluminium;
11
12 # DEFINITION OF SOLAR CELL STRUCTURE (LAYER THICKNESS AND OPTICAL
PROPERTIES);
13
14 layers front=1 electrical=2 back=1; # number of layers (front +
electrical +
back);
15
16 # Layer thickness and grid points (only for electrical layers);
17
18 grid[f.1] d= 70e-9; # TCO SnO-Asai;
19 grid[1] d= 30e-9 dx.t=0.5e-9 dx.c=1.0e-9 dx.b=0.5e-9; # a-Si:H(P);
20 grid[2] d=250e-6 dx.t=0.5e-9 dx.c=1.0e-6 dx.b=0.5e-9; # c-Si;
21 grid[b.1] d=300e-9; # Al;
22
23 # Import of optical properties (N and K);
24
25 optical[f.1] lnk.file=SnO-Asahi_PN.in; # TCO SnO-Asai;
26 optical[1] lnk.file=p-aSiC_PN.in; # a-Si:H(P);
27 optical[2] lnk.file=cSi-PN.in; # c-Si;
28 optical[b.1] lnk.file=Al_PN.in; # Al;
29
30 # DEFINITION OF ELECTRICAL PROPERTIES (IN ELECTRICAL LAYERS);
31
32 bands[1] e.mob=1.98 chi=3.620 nc=2.0E+26 nv=2.0E+26 epsilon=11.9; # a-
Si:H(P);
# Base Case;
33
34 # bands[2] e.mob=1.124 chi=3.950 nc=2.0E+26 nv=2.0E+26 epsilon=11.8; #
c-Si;
35 bands[2] e.mob=1.124 chi=4.050 nc=2.0E+26 nv=2.0E+26 epsilon=11.8; #
c-Si; #
Base Case;
36
37 # DEFINITION OF IMPURITY CONCENTRATION AND DOPING TYPE (IN ELECTRICAL
LAYERS);
38
39 doping[1] n.acc=1.035e25; # a-Si:H(P);
40 doping[2] n.don=1.0e22; # c-Si;
41
42 # DEFINITION OF ELECTRON AND HOLE MOBILITY (IN ELECTRICAL LAYERS);
43
44 mobility[1] mu.e=10.0e-4 mu.h=5.0e-4; # a-Si:H(P);
45 mobility[2] mu.e=0.13000 mu.h=0.0400; # c-Si;
46
47 # DEFINITION OF CARRIER LIFETIME -> ONLY IF AUGER AND/OR SHOCKLEY-
READ-HALL MODELS ARE
CALLED!;
48
49 recom[2] tau.e=10e-4 tau.h=10e-4 esrh.t=-0.5 esrhd.e=-0.4 esrhd.h=-0.4
nsrh.e=1e21
nsrh.h=1e21 caug.e=2.2e-43 caug.h=9.9e-43 caug.i=1.66e-42;
50
51 # DEFINITION OF DENSITY OF STATES (DoS) PARAMETERS -> ONLY FOR
AMORPHOUS SEMICONDUCTORS!;
52
53 vbtail[1] levels=20 c.neut=1.0e-17 c.pos=1.0e-15 e.range=0.5
n.emob=1e27
e.char=0.100; # a-Si:H(P);
54 cbtail[1] levels=15 c.neut=1.0e-17 c.neg=1.0e-15 e.range=0.5
n.emob=1e27
e.char=0.055; # a-Si:H(P);
55 dbond[1] levels=40 e.corr=0.2 ce.pos=5e-15 ce.neut=1e-15 ch.neg=3e-16
ch.neut=1e-16 e.neut=-0.6 n=2.5e21;
56
57 # DEFINITION OF MODEL SETTINGS;
58
59 model[all] poole.frenkel=off;
60 model[1] amorphous extended powell.deane.1996;
61 model[2] srh lifetime auger;
62
63 frontcon ohmic;
64 backcon ohmic;
65
66 # SETTINGS;
67
68 settings temp=300 eps.pois=1e-5 eps.cone=1e-5 eps.conh=1e-5
max.iter=20 damp=4
dv.max=10 gummel.starts=2 max.step.reduc=4 tunn.mass=0.25;
69 settings t.freeze.in=460 gru.factor=3 gru.steps=10 cap.dv=0.002
Rs=10e-4 Rp=4
D0=10e-9 newton;
70
71 # CALCULATING GENERATION PROFILE;
72
73 opticgen spectrum=am15_300-1500_NEW.in gp1;
74 print absorptance file=abs_flatPN.dat; # prints reflectance,
absorptance
(in each layer) and transmittance;
75
76 # CALCULATING SPECTRAL RESPONSE;
77
78 solve equil; # solves at
equilibrium;
79 solve sr wl.start=400e-9 wl.step=5e-9 wl.end=1100e-9 illum; #
calculates quantum
```

```
efficiency (between 300 nm and 1200 nm, every 5 nm);
80 print sr file=qe_flatPN.dat gnu; # prints quantum
efficiency;
81
82 # CALCULATING OTHER PARAMETERS;
83
84 solve jv v.start=0 v.end=1.2 n.step=50 illum; # calculates j-v
response
under illumination, between 0 V and 0.6 V with steps of 0.012 V;
85 print bands file=bands_flatPN.dat; # prints band diagram;
86 print sol.par file=ASA_PAR_flatPN.dat; # prints solar cell parameters
(Voc, Isc, Vmpp, Impp, FF, Pmax);
87 print jv file=jv_flatPN.dat; # prints j-v response;
88 print curr.e file=ASA_curr_e_flatPN.dat; # prints electron current
density;
89 print curr.h file=ASA_curr_h_flatPN.dat; # prints hole current
density;
90 print curr file=ASA_curr_T_flatPN.dat; # prints total current density;
91 print elec file=ASA_conc_e_flatPN.dat; # prints electron
concentration;
92 print hole file=ASA_conc_h_flatPN.dat; # prints hole concentration;
93 print efield file=ASA_efield_flatPN.dat; # prints electric field
magnitude;
94 print rec file=ASA_rec_flatPN.dat; # prints recombination rate;
95 print doping file=ASA_doping_flatPN.dat; # prints doping
concentration;
96 print potential file=ASA_potential_flatPN.dat; # prints electrostatic
potential;
```

E.2. ASA input file for the Silicon hetero-junction

```
1 # ASA SIMULATION INPUT FILE ;
2 # VALIDATION OF A SAMPLE SILICON HETEROJUNCTION SOLAR CELL;
3 # NAME - RAIYAN RIYAZ SHAIKH (Student no - 5267013);
4 # DAILY SUPERVISOR - Dr. ir. Carlos Ruiz Tobon;
5 # MAIN SUPERVISOR - Dr. ir. Rudi Santbergen;
6 # PVMD committee - Dr. ir. Olindo Isabella;
7
8 options ignore.bounds;
9
10 # Name Layer-f.1 Glass (0.1 mm);
11 # Name Layer-f.2 SiN (70 nm);
12 # Name Layer-f.3 TCO - SnO-Asahi (80 nm);
13 # Name Layer-1 p-aSi:H (20 nm);
14 # Name Layer-2 i-aSi:H (5 nm);
15 # Name Layer-2 c-Si (170 um);
16 # Name Layer-2 i-aSi:H (5 nm);
17 # Name Layer-1 n-aSi:H (20 nm);
18 # Name Layer-b.1 TCO - SnO-Asahi (80 nm);
19 # Name Layer-b.2 Al-Aluminium (300 nm);
20
21 # DEFINITION OF SOLAR CELL STRUCTURE (LAYER THICKNESS AND OPTICAL
PROPERTIES);
22
23 layers front=3 electrical=5 back=2; # number of layers (front +
electrical + back);
24
25 # Layer thickness and grid points (only for electrical layers);
26
27 grid[f.1] d=0.1e-3; # glass;
28 grid[f.2] d= 70e-9; # SiN;
29 grid[f.3] d= 80e-9; # TCO SnO-Asahi;
30 grid[1] d= 20e-9 dx.t=0.5e-9 dx.c=1.0e-9 dx.b=0.5e-9; # a-Si:H(P);
31 grid[2] d= 5e-9 dx.t=0.5e-9 dx.c=1.0e-9 dx.b=0.5e-9; # a-Si:H;
32 grid[3] d=170e-6 dx.t=0.5e-9 dx.c=2.0e-6 dx.b=0.5e-9; # c-Si;
33 grid[4] d= 5e-9 dx.t=0.5e-9 dx.c=1.0e-9 dx.b=0.5e-9; # a-Si:H;
34 grid[5] d= 20e-9 dx.t=0.5e-9 dx.c=1.0e-9 dx.b=0.5e-9; # a-Si:H(N);
35 grid[b.1] d= 80e-9; # TCO SnO-Asahi;
36 grid[b.2] d=300e-9; # Al;
37
38 # Import of optical properties (N and K);
39
40 optical[f.1] ext.coeff=0 ref.index=1.35 incoherent; # glass;
41 optical[f.2] lnk.file=nk/SiN.nk; # SiN;
42 optical[f.3] lnk.file=nk/tud_SnO-Asahi.nk; # TCO SnO-Asahi;
43 optical[1] lnk.file=nk/tud_p-aSiC.nk; # a-Si:H(P);
44 optical[2] lnk.file=nk/tud_i-aSi.nk; # a-Si:H;
45 optical[3] lnk.file=nk/cSi-HSJ-cmruiz.nk; # c-Si;
46 optical[4] lnk.file=nk/tud_i-aSi.nk; # a-Si:H;
47 optical[5] lnk.file=nk/tud_n-aSi.nk; # a-Si:H(N);
48 optical[b.1] lnk.file=nk/tud_SnO-Asahi.nk; # TCO SnO-Asahi;
49 optical[b.2] lnk.file=nk/tud_al.nk; # Al;
50
51 # interface scattering properties: Haze and AID calculated from AFM
scan;
52 # interface[i.4] adf.s.rf=cossq adf.s.rb=cossq adf.s.tf=cossq
adf.s.tb=cossq;
53 # interface[i.4] adf.h.rf=cossq adf.h.rb=cossq adf.h.tf=cossq
adf.h.tb=cossq
adf.h.file=sct_tco-p.nk;
54 # interface[i.5] adf.s.rf=user adf.s.rb=user adf.s.tf=user
adf.s.tb=user;
55 # interface[i.5] adf.h.rf=cossq adf.h.rb=cossq adf.h.tf=cossq
adf.h.tb=cossq;
56 # interface[i.10] adf.s.rf=cossq adf.s.rb=cossq adf.s.tf=cossq
adf.s.tb=cossq;
57 # interface[i.10] adf.h.rf=cossq adf.h.rb=cossq adf.h.tf=cossq
adf.h.tb=cossq
adf.h.file=sct_n-m.nk;
58
59 # DEFINITION OF ELECTRICAL PROPERTIES (IN ELECTRICAL LAYERS);
60
61 bands[1] e.mob=1.70 chi=3.900 nc=2.000E+26 nv=2.000E+26 epsilon=11.9;
#
a-Si:H(P);
62 bands[2] e.mob=1.70 chi=4.000 nc=2.000E+26 nv=2.000E+26 epsilon=11.9;
#
a-Si:H;
63 bands[3] e.mob=1.124 chi=4.050 nc=2.800E+25 nv=2.800E+25 epsilon=11.8;
#
c-Si;
64 bands[4] e.mob=1.70 chi=4.000 nc=2.000E+26 nv=2.000E+26 epsilon=11.9;
#
a-Si:H;
65 bands[5] e.mob=1.70 chi=3.900 nc=2.000E+26 nv=2.000E+26 epsilon=11.9;
#
a-Si:H(N);
66
67 # DEFINITION OF IMPURITY CONCENTRATION AND DOPING TYPE (IN ELECTRICAL
LAYERS);
68
69 doping[1] e.act.acc=0.300; # a-Si:H(P);
70 doping[3] n.don=5e21; # c-Si;
71 doping[5] e.act.don=0.150; # a-Si:H(N);
72
73 # DEFINITION OF ELECTRON AND HOLE MOBILITY (IN ELECTRICAL LAYERS);
74
75 mobility[1] mu.e=1.000E-03 mu.h=5.000E-04;
76 mobility[2] mu.e=2.000E-03 mu.h=1.000E-03;
77 mobility[3] mu.e=1.300E-01 mu.h=4.000E-02;
78 mobility[4] mu.e=2.000E-03 mu.h=1.000E-03;
79 mobility[5] mu.e=1.000E-03 mu.h=5.000E-04;
80
81 # Description of Density of states parameters - FOR AMORPHOUS SILICON
ONLY;
82
83 vbtail[1] levels=20 c.neut=1.0e-17 c.pos=1.0e-15 e.range=0.5
n.emob=1.1e27
e.char=0.070;
```

```
84 vbtail[2] levels=20 c.neut=1.0e-17 c.pos=1.0e-15 e.range=0.5
n.emob=1.0e27
e.char=0.045;
85 vbtail[4] levels=20 c.neut=1.0e-17 c.pos=1.0e-15 e.range=0.5
n.emob=1.0e27
e.char=0.045;
86 vbtail[5] levels=20 c.neut=1.0e-17 c.pos=1.0e-15 e.range=0.5
n.emob=1.1e27
e.char=0.080;
87
88 cbtail[1] levels=15 c.neut=1.0e-17 c.neg=1.0e-15 e.range=0.5
n.emob=1e27
e.char=0.040;
89 cbtail[2] levels=15 c.neut=1.0e-17 c.neg=1.0e-15 e.range=0.5
n.emob=1e27
e.char=0.030;
90 cbtail[4] levels=15 c.neut=1.0e-17 c.neg=1.0e-15 e.range=0.5
n.emob=1e27
e.char=0.030;
91 cbtail[5] levels=15 c.neut=1.0e-17 c.neg=1.0e-15 e.range=0.5
n.emob=1e27
e.char=0.040;
92
93 dbond[1] levels=40 e.corr=0.2 ce.pos=5e-15 ce.neut=1e-15 ch.neg=3e-16
ch.neut=1e-16
e.neut=-0.6 n=1e24;
94 dbond[2] levels=40 e.corr=0.2 ce.pos=5e-15 ce.neut=1e-15 ch.neg=3e-16
ch.neut=1e-16
e.neut=-0.9 n=1e23;
95 dbond[4] levels=40 e.corr=0.2 ce.pos=5e-15 ce.neut=1e-15 ch.neg=3e-16
ch.neut=1e-16
e.neut=-1.1 n=1e23;
96 dbond[5] levels=40 e.corr=0.2 ce.pos=5e-15 ce.neut=1e-15 ch.neg=3e-16
ch.neut=1e-16
e.neut=-1.2 n=5e23;
97
98 # DEFINITION OF CARRIER LIFETIME AND RECOMBINATION-> ONLY IF AUGER
AND/OR
SHOCKLEY-READ-HALL MODELS ARE CALLED!;
99
100 recom[3] tau.e=10e-3 tau.h=10e-3 esrh.t=-0.5 esrhd.e=-0.4 esrhd.h=-
0.4 nsrh.e=1e21
nsrh.h=1e21 caug.e=2.2e-43 caug.h=9.9e-43 caug.i=1.66e-42;
101
102 # DEFINITION OF MODEL SETTINGS;
103
104 model[1] amorphous powell.deane.1996.mod;
105 model[2] amorphous powell.deane.1996.mod;
106 model[3] srh lifetime auger ionscat;
107 model[4] amorphous powell.deane.1996.mod;
108 model[5] amorphous powell.deane.1996.mod;
109
110 # CONTACT PROPERTIES;
111
112 frontcon ohmic;
113 backcon ohmic;
114 frontopt reflect=0.1;
115 backopt reflect=0.8;
116
117 # NUMERICAL SETTINGS;
118
119 settings temp=300 eps.pois=1e-4 eps.cone=1e-4 eps.conh=1e-4
max.iter=99 damp=4
dv.max=10 gummel.starts=2 max.step.reduc=4 tunn.mass=0.25;
120 settings t.freeze.in=460 gru.factor=3 gru.steps=10 cap.dv=0.002
Rs=10e-4 Rp=4 D0=10e-9
newton field.lim=4e6 e0.fdme=1.2e7;
121
122 # CALCULATING GENERATION PROFILE;
123
124 opticgen spectrum=nk/am15_350-1200.in mult=1.20 gp3;
125
126 # CALCULATING SPECTRAL RESPONSE;
127 settings sr.flux=1.0e20;
128 solve equil; # Solve equilibrium;
129 solve sr wl.start=250nm wl.step=10nm wl.end=1200nm;
130 print opticgen file=HSJ_profile.gen;
131 print sr file=SR_HJS.dat gnu;
132
133 model poole.frenkel=off TAT=off;
134 solve equil;
135 print bands file=BANDS_SHJ_standard.dat;
136
137 # CALCULATING ILLUMINATED J-V (AM1.5 simulation);
138
139 model poole.frenkel=off TAT=off;
140 solve equil;
141 solve v.step=0.001 v.start=0.0 v.end=0.8 jv illum;
142 print sol.par file=par_standard.dat;
143 print jv file=JV_standard.dat;
144
```

E.3. ASA input file for the Perovskite-Silicon tandem

E.3.1. Genpro input file for the flat Perovskite-Silicon tandem

```
1 %GenPro-4 Validation of Flat Perovskite/Silicon Tandem device based on
2 %paper by Ashouri et.al.
3 %NAME - RAIYAN RIYAZ SHAIKH (Student no - 5267013)
4 %DAILY SUPERVISOR - Dr. ir. Carlos Ruiz Tobon
5 %MAIN SUPERVISOR - Dr. ir. Rudi Santbergen
6 %PVMD committee - Dr. ir. Olindo Isabella
7 %function [Lay,Int,rback,TYPE] = RT_2T_20210322
8 clear
9 clear Lay Int                          %clear variables
10
11 %===LAYERS===
12 Lay(1).med = 'air';                                     Lay(1).thi = inf;
13 Lay(2).med = 'perovskite-1.68eV-Man18-Eg-705-715';  Lay(2).thi = 0.532;         %↙
Lay(2).thi = 0:0.001:0.532;
14 Lay(3).med = 'c-Si-2015';                               Lay(3).thi = 300;           %↙
Lay(3).thi = 0:1:300;
15 Lay(4).med = 'air';                                     Lay(4).thi = inf;
16
17 %===INTERFACES===
18 Int(1).coat(1).med = 'LiF';                             Int(1).coat(1).thi = 0:0.001: ↙
0.085;
19 Int(1).coat(2).med = 'IZO';                             Int(1).coat(2).thi = 0:0.001: ↙
0.085;
20 Int(1).coat(3).med = 'SnO2-Man18';                      Int(1).coat(3).thi = 0:0.001: ↙
0.005;
21 Int(1).coat(4).med = 'C60';                             Int(1).coat(4).thi = 0:0.001: ↙
0.007;
22 %---
23
24 Int(2).coat(1).med = 'PTAA';                            Int(2).coat(1).thi = 0:0.001: ↙
0.023;
25 Int(2).coat(2).med = 'ITO';                             Int(2).coat(2).thi = 0:0.001: ↙
0.063;
26 Int(2).coat(3).med = 'n-SiOx-ncSi';                     Int(2).coat(3).thi = 0:0.001: ↙
0.111;
27 Int(2).coat(4).med = 'a-Si(i)';                         Int(2).coat(4).thi = 0:0.001: ↙
0.009;
28
29 %---
30 Int(3).coat(1).med = 'a-Si(i)';                         Int(3).coat(1).thi = 0:0.001: ↙
0.006;
31 Int(3).coat(2).med = 'a-Si(p)';                         Int(3).coat(2).thi = 0:0.001: ↙
0.012;
32 Int(3).coat(3).med = 'AZO';                             Int(3).coat(3).thi = 0:0.001: ↙
0.055;
33 Int(3).coat(4).med = 'Ag';                              Int(3).coat(4).thi = 0:0.001: ↙
0.3;
34
35 %---
36 Int(1).model = 'flat';             %use Flat-optics model
37 Int(2).model = 'flat';             %use Flat-optics model
38 Int(3).model = 'flat';             %use Flat-optics model
39 %===
40
41 % export_nkGPToASA(Lay,Int);
42
43 [Lay,Int,out] = GENPRO4(Lay,Int);            %run simulation
44 tc = min(Lay(2).cur,Lay(3).cur); %tandem current [mA/cm2]
45 title(['Perovskite-Silicon tandem current: ',num2str(tc,'%5.2f'),' mA/cm^2']) %add↙
title to graph
46
47 % mp=out.abp;save('matrix_profile_Korte_System_Textured_raiyan.dat','mp','-ascii')
48
49
50
```

E.3.2. Genpro input file for the bottom textured Perovskite-Silicon tandem

```
 1 %GenPro-4 Validation of bottom textured Perovskite/Silicon Tandem device based on
 2 %paper by Ashouri et.al.
 3 %NAME - RAIYAN RIYAZ SHAIKH (Student no - 5267013)
 4 %DAILY SUPERVISOR - Dr. ir. Carlos Ruiz Tobon
 5 %MAIN SUPERVISOR - Dr. ir. Rudi Santbergen
 6 %PVMD committee - Dr. ir. Olindo Isabella
 7 %function [Lay,Int,rback,TYPE] = RT_2T_20210322
 8 clear
 9 clear Lay Int                    %clear variables
10
11 load('AFM.mat','pyramids_20um')  %load texture hight map from file [um]
12 %height map of typical pyramid texture (~5um pyramid size)
13
14 %===LAYERS===
15
16 Lay(1).med = 'air';                               Lay(1).thi = inf;
17 Lay(2).med = 'perovskite-1.68eV-Man18-Eg-705-715';  Lay(2).thi = 0.532;         %↙
Lay(2).thi = 0:0.001:0.532;
18 Lay(3).med = 'c-Si-2015';                         Lay(3).thi = 300;           %↙
Lay(3).thi = 0:1:300;
19 Lay(4).med = 'air';                               Lay(4).thi = inf;
20
21 %===INTERFACES===
22
23 Int(1).coat(1).med = 'LiF';                       Int(1).coat(1).thi = 0:0.001: ↙
0.085;
24 Int(1).coat(2).med = 'IZO';                       Int(1).coat(2).thi = 0:0.001: ↙
0.085;
25 Int(1).coat(3).med = 'SnO2-Man18';                Int(1).coat(3).thi = 0:0.001: ↙
0.005;
26 Int(1).coat(4).med = 'C60';                       Int(1).coat(4).thi = 0:0.001: ↙
0.007;
27 %---
28 Int(2).coat(1).med = 'PTAA';                      Int(2).coat(1).thi = 0:0.001: ↙
0.023;
29 Int(2).coat(2).med = 'ITO';                       Int(2).coat(2).thi = 0:0.001: ↙
0.063;
30 Int(2).coat(3).med = 'n-SiOx-ncSi';               Int(2).coat(3).thi = 0:0.001: ↙
0.111;
31 Int(2).coat(4).med = 'a-Si(i)';                   Int(2).coat(4).thi = 0:0.001: ↙
0.009;
32 %---
33 Int(3).coat(1).med = 'a-Si(i)';                   Int(3).coat(1).thi = 0:0.001: ↙
0.006;
34 Int(3).coat(2).med = 'a-Si(p)';                   Int(3).coat(2).thi = 0:0.001: ↙
0.012;
35 Int(3).coat(3).med = 'AZO';                       Int(3).coat(3).thi = 0:0.001: ↙
0.055;
36 Int(3).coat(4).med = 'Ag';                        Int(3).coat(4).thi = 0:0.001: ↙
0.3;
37
38 %===MODEL SETTINGS===
39
40 Int(1).model = 'flat';           %Flat-optics model above Perovskite layer
41 Int(2).model = 'flat';           %Flat-optics model between Perovskite and Silicon ↙
layer
42 Int(3).model = 'ray';            %RAY-optics model below Silicon layer
43 Int(3).Z = -pyramids_20um;       Int(3).xy = [20,20];        %20x20um map - Base↙
Case Below cSo
44 %minus was added to get upside-down height map for rear
45
46 %===
47
48 rback = 0.90;
49 TYPE='Tan';
50
51 %===export_nkGPToASA(Lay,Int)===;
52
53 [Lay,Int,out] = GENPRO4(Lay,Int);           %run simulation
54 tc = min(Lay(2).cur,Lay(3).cur);            %tandem current [mA/cm2]
55 title(['Perovskite-Silicon tandem current: ',num2str(tc,'%5.2f'),' mA/cm^2']) %add↙
title to graph
56
57 % mp=out.abp;save('matrix_profile_Korte_System_Textured_raiyan.dat','mp','-ascii') ↙
% To extract the generation matrix profile to be imported into ASA
58
59
60
```

E.3.3. ASA input file for the bottom textured Perovskite-Silicon tandem

```
  1   # VALIDATION OF PEROVSKITE SILICON TANDEM SOLAR CELL - Al Ashouri et al;
  2   # NAME - RAIYAN RIYAZ SHAIKH (Student no - 5267013);
  3   # DAILY SUPERVISOR - Dr. ir. Carlos Ruiz Tobon;
  4   # MAIN SUPERVISOR - Dr. ir. Rudi Santbergen;
  5   # PVMD committee - Dr. ir. Olindo Isabella;
  6
  7   # options ignore.bounds suppress.warnings;
  8
  9   # Name Layer-f.1    LiF (85 nm);
 10   # Name Layer-1      IZO (85 nm);
 11   # Name Layer-2      SnO2 (5 nm);
 12   # Name Layer-3      C60 (7 nm);
 13   # Name Layer-4      Perovskite absorber (532 nm);
 14   # Name Layer-5      PTAA (23 nm);
 15   # Name Layer-6      ITO (63 nm);
 16   # Name Layer-7      nc  - SiOx (111 nm);
 17   # Name Layer-8      i   - aSi:H (9 nm);
 18   # Name Layer-9      base- c-Si (300 um);
 19   # Name Layer-10     i   - aSi:H (6 nm);
 20   # Name Layer-11     p   - aSi:H (12 nm);
 21   # Name Layer-12     AZO (55 nm);
 22   # Name Layer-b.1    Ag  - Silver (100 nm);
 23
 24   # DEFINITION OF SOLAR CELL STRUCTURE (LAYER THICKNESS AND OPTICAL PROPERTIES);
 25
 26   layers          front=2 electrical=10 back=2; # number of layers (front + electrical +
      back);
 27
 28   # Layer thickness and grid points (only for electrical layers);
 29
 30   grid[f.1]       d= 85e-9;                                     # LiF;
 31   grid[f.2]       d= 85e-9;                                     # IZO;
 32   grid[1]         d=  5e-9   spaces=200;                        # SNO2-Man18 (5 nm);
 33   grid[2]         d=  7e-9   spaces=200;                        # C60        (ETM 7 nm);
 34   grid[3]         d=532e-9   spaces=600;                        # Perovskite (330 nm);
 35   grid[4]         d= 23e-9   spaces=40;                         # PTAA       (HTM 23 nm);
 36   grid[5]         d= 63e-9   dx.t=0.5e-9;                       # ITO        (ETM 63
      nm);
 37   grid[6]         d=111e-9   dx.t=0.5e-9;                       # nc-SiOx    (111 nm);
 38   grid[7]         d=  9e-9   spaces=24;                         # a-Si:H;
 39   grid[8]         d=300e-6   dx.t=1.0e-9 dx.c=10e-9 dx.b=1.0e-9; # c-Si;
 40   grid[9]         d=  6e-9   spaces=24;                         # a-Si:H;
 41   grid[10]        d=12e-9    spaces=24;                         # a-Si:H(P);
 42   grid[b.1]       d= 55e-9;                                     # AZO;
 43   grid[b.2]       d=100e-9;                                     # Ag (300 nm);
 44
 45   # Import of optical properties (N and K);
 46
 47   # optical[f.1]    lnk.file=LiF.nk incoherent;                      # LiF;
 48   # optical[f.2]    lnk.file=IZO.nk;                                 # IZO;
 49   # optical[1]      lnk.file=SnO2-Man18.nk;                          # SNO2-Man18 (5 nm);
 50   # optical[2]      lnk.file=C60.nk;                                 # C60        (7 nm);
 51   # optical[3]      lnk.file=perovskite-1.68eV-Man18-Eg-705-715.in;  # Perovskite (330
      nm);
 52   # optical[4]      lnk.file=PTAA.nk;                                # PTAA (23nm);
 53   # optical[5]      lnk.file=ITO.in;                                 # ITO;
 54   # optical[6]      lnk.file=n-SiOx-ncSi.in;                         # nc-SiOx(111 nm);
 55   # optical[7]      lnk.file=tud_i-aSi.nk;                           # a-Si:H(i);
 56   # optical[8]      lnk.file=c-Si-2015.in;                           # c-Si (3000 nm);
 57   # optical[9]      lnk.file=tud_i-aSi.nk;                           # a-Si:H(i);
 58   # optical[10]     lnk.file=tud_p-aSiC.nk;                          # a-Si:H(P);
 59   # optical[b.1]    lnk.file=AZO.in;                                 # AZO;
 60   # optical[b.2]    lnk.file=Ag.in;                                  # Ag (300 nm);
 61
 62   # DEFINITION OF ELECTRICAL PROPERTIES (IN ELECTRICAL LAYERS);
 63
 64   bands[1]        e.mob=3.50  chi=4.00 nc=2.2e24 nv=1.8e25 epsilon= 9.0; # SNO2-Man18 (5
      nm);
 65   bands[2]        e.mob=2.00  chi=3.90 nc=8.0e25 nv=8.0e25 epsilon= 4.2; # C60  (7
      nm)(ETM);
 66   bands[3]        e.mob=1.68  chi=3.90 nc=4.4e23 nv=8.4e24 epsilon= 6.5; # Perovskite
      (330 nm);
 67   bands[4]        e.mob=3.30  chi=2.30 nc=2.2e24 nv=1.8e25 epsilon= 3.0; # PTAA(HTM 23 nm);
 68   bands[5]        e.mob=3.65  chi=4.80 nc=5.8e24 nv=1.0e24 epsilon= 8.9; # ITO (ETM 63 nm);
 69   bands[6]        e.mob=1.70  chi=3.90 nc=2.0e26 nv=2.0e26 epsilon=11.9; # nc-SiOx(111 nm);
 70   bands[7]        e.mob=1.75  chi=3.80 nc=2.0e26 nv=2.0e26 epsilon=11.9; # a-Si:H;
 71   bands[8]        e.mob=1.124 chi=4.05 nc=2.9e25 nv=3.1e25 epsilon=11.8; # c-Si;
 72   bands[9]        e.mob=1.75  chi=3.80 nc=2.0e26 nv=2.0e26 epsilon=11.9; # a-Si:H;
 73   bands[10]       e.mob=1.75  chi=3.80 nc=2.0e26 nv=2.0e26 epsilon=11.9; # a-Si:H(P);
 74
 75   # DEFINITION OF IMPURITY CONCENTRATION AND DOPING TYPE (IN ELECTRICAL LAYERS);
 76
 77   doping[1]       n.don= 2.00e25;  # SNO2 Lars Korte's data;
 78   doping[2]       n.don= 2.60e24;  # C60;
 79   #     [3]       n.don= 2.00e19;  # Perovskite (330 nm);
 80   doping[4]       n.acc=3.0e24;    # PTAA;
 81   doping[5]       n.don=1.0e27;    # ITO ;
 82   doping[6]       n.don=2.50e26;   # nc-SiOx(111 nm);
 83   #     [7]                        # a-Si:H(i);
 84   doping[8]       n.don=1.0e22;    # c-Si (3000 nm);
 85   #     [9]                        # a-Si:H(i);
 86   doping[10]      n.acc=2.00e26;   # p-a-SiC:H(P);
 87
 88   # DEFINITION OF ELECTRON AND HOLE MOBILITY (IN ELECTRICAL LAYERS);
 89
 90   mobility[1]    mu.e=10.0e-4   mu.h=1.0e-4;
 91   mobility[2]    mu.e=10.0e-4   mu.h=1.0e-4;
 92   mobility[3]    mu.e=20.0e-4   mu.h=5.0e-4;
 93   mobility[4]    mu.e=10.0e-4   mu.h=1.0e-4;
 94   mobility[5]    mu.e=50.0e-4   mu.h=3.0e-4;
 95   mobility[6]    mu.e= 2.0e-3   mu.h=1.0e-3;
 96   mobility[7]    mu.e=10.0e-4   mu.h=1.0e-4;
 97   mobility[8]    mu.e= 2.0e-3   mu.h=1.0e-3;
 98   mobility[9]    mu.e= 1.0e-3   mu.h=5.0e-4;
 99   mobility[10]   mu.e= 1.0e-3   mu.h=5.0e-4;
100
101   # Description of Density of states parameters - FOR AMORPHOUS SILICON ONLY;
102
103   vbtail[7]      e.range=0.9 levels=50 c.neut=0.7e-15 c.pos=0.7e-15;
104   vbtail[9-10]   e.range=0.9 levels=50 c.neut=0.7e-15 c.pos=0.7e-15;
105   vbtail[7]      n.emob=2.0e27 e.char=0.045;
106   vbtail[9]      n.emob=2.0e27 e.char=0.045;
107   vbtail[10]     n.emob=1.0e28 e.char=0.085;
108
109   cbtail[7]      e.range=0.9 levels=50 c.neut=0.7e-15 c.neg=0.7e-15;
110   cbtail[9-10]   e.range=0.9 levels=50 c.neut=0.7e-15 c.neg=0.7e-15;
111   cbtail[7]      n.emob=4.0e27 e.char=0.030;
112   cbtail[9]      n.emob=4.0e27 e.char=0.030;
113   cbtail[10]     n.emob=1.0e28 e.char=0.080;
114
115   dbond[7]       levels=40 e.corr=0.2 d.e=0.144 e.range=5.0;
116   dbond[9-10]    levels=40 e.corr=0.2 d.e=0.144 e.range=5.0;
117   dbond[7]       ce.neut=3.0e-15 ch.neut=3.0e-15 ce.pos=100.0e-15 ch.neg=100.0e-15;
118   dbond[9-10]    ce.neut=3.0e-15 ch.neut=3.0e-15 ce.pos=100.0e-15 ch.neg=100.0e-15;
119   dbond[7]       ep.def.pool=1.24 sigma.def.pool=0.18 ;
120   dbond[9]       ep.def.pool=1.24 sigma.def.pool=0.18 ;
121   dbond[10]      n=4.0e25  e.neut=-0.65;
122
123   # DEFINITION OF CARRIER LIFETIME -> ONLY IF AUGER AND/OR SHOCKLEY-READ-HALL MODELS ARE
      CALLED!;
124
125   recom[1]    tau.e=1e-5         tau.h=1e-6;     # caug.i=9.9e-41 direct.c=2e-16;
126   recom[2]    tau.e=1e-9         tau.h=1e-9;
127   recom[3]    tau.e=2.88e-7      tau.h=2.88e-7;  # esrh.t=-0.5 esrhd.e=-0.4 esrhd.h=-0.4
      nsrh.e=1e21 nsrh.h=1e21 caug.e=2.2e-43 caug.h=9.9e-43 caug.i=1.66e-42;
128   recom[4]    tau.e=1e-9         tau.h=1e-9;     # esrh.t=-0.5 esrhd.e=-0.4 esrhd.h=-0.4
      nsrh.e=1e21 nsrh.h=1e21 caug.e=2.2e-43 caug.h=9.9e-43 caug.i=1.66e-42;
129   recom[5]    tau.e=1e-6         tau.h=1e-6;     # esrh.t=-0.5 esrhd.e=-0.4 esrhd.h=-0.4
```

```
     nsrh.e=1e21 nsrh.h=1e21 caug.e=2.2e-43 caug.h=9.9e-43 caug.i=1.66e-42;
130  recom[6]    tau.e=1e-6          tau.h=1e-6;
131  # recom[7]  tau.e=1e-6          tau.h=1e-6;
132  recom[8]    tau.e=10e-3         tau.h=10e-3;    # caug.i=9.9e-41 direct.c=2e-16;
133  # recom[9]  tau.e=1e-6          tau.h=1e-6;
134  recom[10]   tau.e=1e-6          tau.h=1e-6;
135
136  # Numerical settings;
137
138  settings    gummel.starts=10 eps.pois=1e-6 eps.cone=1e-6 eps.conh=1e-6 update.rec
     dump.errors max.step.reduc=6 max.iter.eq=50;
139  settings    max.iter=99 damp=3 e0.fdme=2.0e7 field.lim=4e6 gru.factor=3 gru.steps=10
     tunn.mass=0.1; C gen.ramp.up=on;
140
141  # DEFINITION OF MODEL SETTINGS;
142
143  # model[all]    tat=on;
144  model[1]    srh lifetime;
145  model[2]    srh=on;
146  model[3]    srh lifetime;
147  model[4]    srh lifetime;
148  # model[5-6]              fdme=on;
149  model[5]    srh lifetime;
150  model[6]    srh lifetime;
151  model[7]    amorphous=on;
152  model[8]    srh lifetime;
153  model[9]    amorphous=on;
154  model[10]   amorphous=on;
155
156
157  # SOLUTIONS ;
158
159  solve        equil;
160  # opticgen   spectrum=am15_300-1500_NEW.in gp1;
161  opticgen     gen.file=matrix_profile_Korte_System_Textured_raiyan.dat; # GenPro4 (GP4)
     file;
162  # print      opticgen    file=matrix_gen.dat;
163  # print      absorption  file=absortion.dat;
164  # print      absorptance file=absortance.dat;
165
166  # solve      equil;
167  print        bands file=korte_bands_ITO27.dat gnu headers=off;
168  print        potential file=ASA_potential_pvk_cSi_tandem_Korte_ITO27.dat
     headers=off;       # prints electrostatic potential;
169  print        efield    file=ASA_efield_pvk_cSi_tandem_Korte_ITO27.dat headers=off;  #
     prints electric field magnitude;
170
171  solve        equil;
172  solve        jv v.start=-2.0 v.end=0.0 v.step=0.002 illum;
173  print        file=JV_ITO27.dat;
174
```

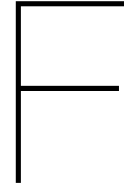

Input files for the simulation of Pvk/cSi tandem devices

F.1. Genpro input file for the improved textured Perovskite-Silicon tandem device

```
1 %GenPro-4 Validation of bottom textured Perovskite/Silicon Tandem device based on
2 %latest paper by Ashouri et.al.
3 %NAME - RAIYAN RIYAZ SHAIKH (Student no - 5267013)
4 %DAILY SUPERVISOR - Dr. ir. Carlos Ruiz Tobon
5 %MAIN SUPERVISOR - Dr. ir. Rudi Santbergen
6 %PVMD committee - Prof. ir. Peter Vaessen
7 %PVMD committee - Dr. ir. Paul Procel
8 %function [Lay,Int,rback,TYPE] = RT_2T_20210322
9 clear
10 clear Lay Int                    %clear variables
11
12 load('AFM.mat','pyramids_20um')  %load texture hight map from file [um]
13 %height map of typical pyramid texture (~5um pyramid size)
14
15 %===LAYERS===
16
17 Lay(1).med = 'air';                               Lay(1).thi = inf;
18 Lay(2).med = 'perovskite-1.68eV-Man18-Eg-705-715';  Lay(2).thi = 0.600;      % Lay↙
(2).thi = 0:0.001:0.600;
19 Lay(3).med = 'c-Si-2015';                         Lay(3).thi = 300;            %↙
Lay(3).thi = 0:1:300;
20 Lay(4).med = 'air';                               Lay(4).thi = inf;
21
22 %===INTERFACES===
23
24 Int(1).coat(1).med = 'LiF';                       Int(1).coat(1).thi = 0:0.001: ↙
0.109;      %Int(1).coat(1).thi = 0:0.001:0.110;
25 Int(1).coat(2).med = 'IZO_V3';                    Int(1).coat(2).thi = 0:0.001: ↙
0.085;      %Int(1).coat(2).thi = 0:0.001:0.090;
26 Int(1).coat(3).med = 'SnO2-Man18';                Int(1).coat(3).thi = 0:0.0001: ↙
0.010;      %Int(1).coat(3).thi = 0:0.001:0.010;
27 Int(1).coat(4).med = 'C60';                       Int(1).coat(4).thi = 0:0.0001: ↙
0.010;      %Int(1).coat(4).thi = 0:0.001:0.023;
28 %---
29 %
30 Int(2).coat(1).med = 'Glass';                     Int(2).coat(1).thi = 0: ↙
0.00001:0.001;      %Int(2).coat(1).thi = 0:0.001:0.005; % SAM
31 Int(2).coat(2).med = 'ITO';                       Int(2).coat(2).thi = 0:0.0002: ↙
0.020;      %Int(2).coat(1).thi = 0:0.001:0.005;
32 Int(2).coat(3).med = 'n-SiOx-ncSi';               Int(2).coat(3).thi = 0:0.001: ↙
0.107;      %Int(2).coat(2).thi = 0:0.001:0.107;
33 Int(2).coat(4).med = 'a-Si(i)';                   Int(2).coat(4).thi = 0:0.0001: ↙
0.005;      %Int(2).coat(3).thi = 0:0.001:0.005;
34 %---
35 Int(3).coat(1).med = 'a-Si(i)';                   Int(3).coat(1).thi = 0:0.0001: ↙
0.005;      %Int(3).coat(1).thi = 0:0.001:0.005;
36 Int(3).coat(2).med = 'a-Si(p)';                   Int(3).coat(2).thi = 0:0.0001: ↙
0.010;      %Int(3).coat(2).thi = 0:0.001:0.010;
37 Int(3).coat(3).med = 'ITO';                       Int(3).coat(3).thi = 0:0.0001: ↙
0.010;      %Int(3).coat(3).thi = 0:0.001:0.005;
38 Int(3).coat(4).med = 'SiO2';                      Int(3).coat(4).thi = 0:0.001: ↙
0.18;      %Int(3).coat(4).thi = 0:0.001:0.005;
39 Int(3).coat(5).med = 'Ag';                        Int(3).coat(5).thi = 0:0.001: ↙
0.4;       %Int(3).coat(5).thi = 0:0.001:0.4;
40
41 %===MODEL SETTINGS===
42 Lay(2).model = 'wave';           %Wave-optics model for Perovskite layer
43 Lay(2).Z = -pyramids_20um;       Lay(2).xy = [0.02,0.02];        %20x20nm map -↙
Base Case Below cSo
44 Lay(3).model = 'ray';            %Ray-optics model for Silicon layer
45 Lay(3).Z = -pyramids_20um;       Lay(3).xy = [20,20];        %20x20um map - Base↙
Case Below cSo
46
47 Int(1).model = 'flat';            %Wave-optics model above Perovskite layer
48 % Int(1).Z = -pyramids_20um;       Int(1).xy = [0.02,0.02];        %20x20um map
49 Int(2).model = 'wave';           %Wave-optics model below Perovskite and above↙
Silicon layer
50 Int(2).Z = -pyramids_20um;       Int(2).xy = [0.02,0.02];        %20x20nm map
51 Int(3).model = 'ray';            %RAY-optics model below Silicon layer
52 Int(3).Z = -pyramids_20um;       Int(3).xy = [20,20];        %20x20um map
53 %minus was added to get upside-down height map for rear
54
55 %===
56
57 rback = 1;
58 TYPE='Tan';
59
60 %===export_nkGPToASA(Lay,Int)===;
61 % S.wav = 0.300:0.001:1.200;                  % Wave length Range 300 to 1200 nm↙
with 0.001 nm step
62 % S.SM = 1;
63 [Lay,Int,out] = GENPRO4(Lay,Int);           %run simulation
64 tc = min(Lay(2).cur,Lay(3).cur);            %tandem current [mA/cm2]
65 title(['Perovskite-Silicon tandem current: ',num2str(tc,'%5.2f'),' mA/cm^2']) %add↙
title to graph
66
67 % mp=out.abp;save('matrix_profile_AlAshouri_298_System_Textured_raiyan.↙
dat','mp','-ascii') % To extract the generation matrix profile to be imported into↙
ASA
68
69
70
```

F.2. ASA input file for the improved textured Perovskite-Silicon tandem device

```
1   # VALIDATION OF LATEST (29.8% efficiency) PEROVSKITE SILICON TANDEM SOLAR CELL - Al
    Ashouri et al;
2   # NAME - RAIYAN RIYAZ SHAIKH (Student no - 5267013);
3   # DAILY SUPERVISOR - Dr. ir. Carlos Ruiz Tobon;
4   # MAIN SUPERVISOR - Dr. ir. Rudi Santbergen;
5
6   # Name Layer-f.1    LiF (109 nm);
7   # Name Layer-f.2    IZO (85 nm);
8   # Name Layer-1      SnO2 (10 nm);
9   # Name Layer-2      C60 (10 nm);
10  # Name Layer-3      Perovskite absorber (600 nm);
11  # Name Layer-4      SAM (1 nm);
12  # Name Layer-5      ITO (20 nm);
13  # Name Layer-6      nc  - SiOx (107 nm);
14  # Name Layer-7      i   - aSi:H (5 nm);
15  # Name Layer-8      base- c-Si (300 um);
16  # Name Layer-9      i   - aSi:H (5 nm);
17  # Name Layer-10     p   - aSi:H (10 nm);
18  # Name Layer-11     ITO (10 nm);
19  # Name Layer-b.1    SiO2 (180 nm);
20  # Name Layer-b.2    Ag  - Silver (400 nm);
21
22  # DEFINITION OF SOLAR CELL STRUCTURE (LAYER THICKNESS AND OPTICAL PROPERTIES);
23
24  layers      front=2 electrical=11 back=2;    # number of layers (front + electrical +
    back);
25
26  # Layer thickness and grid points (only for electrical layers);
27
28  grid[f.1]   d=109e-9;                                          # ARC - LiF;
29  grid[f.2]   d=85e-9;                                           # TCO - IZO;
30  grid[1]     d=10e-9     spaces=100;                            # SnO2;
31  grid[2]     d=10e-9     spaces=100;                            # C60;
32  grid[3]     d=600e-9    spaces=600;                            # Perovskite absorber;
33  grid[4]     d=1e-9      spaces=100;                            # SAM;
34  grid[5]     d=20e-9     spaces=100;                            # ITO;
35  grid[6]     d=107e-9    spaces=107;                            # nc  - SiOx;
36  grid[7]     d=5e-9      spaces=50;                             # i   - aSi:H;
37  grid[8]     d=300e-6    spaces=300;                            # base- c-Si;
38  grid[9]     d=5e-9      spaces=50;                             # i   - aSi:H;
39  grid[10]    d=10e-9     spaces=100;                            # p   - aSi:H;
40  grid[11]    d=10e-9     spaces=100;                            # TCO - ITO;
41  grid[b.1]   d=180e-9;                                          # SiO2;
42  grid[b.2]   d=400e-9;                                          # Ag-Silver;
43
44  # Import of optical properties (N and K);
45
46  optical[f.1]    lnk.file=LiF.in;                               # ARC - LiF;
47  optical[f.2]    lnk.file=IZO_V2.in;                            # TCO - IZO;
48  optical[1]      lnk.file=SnO2-Man18.in;                        # SnO2;
49  optical[2]      lnk.file=C60.in;                               # C60;
50  optical[3]      lnk.file=perovskite-1.68eV-Man18-Eg-705-715.in; # Perovskite absorber;
51  optical[4]      lnk.file=SAM_Glass.in;                         # SAM;
52  optical[5]      lnk.file=ITO.in;                               # ITO;
53  optical[6]      lnk.file=n-SiOx-ncSi.in;                       # nc  - SiOx;
54  optical[7]      lnk.file=a-Si(i).in;                           # i   - aSi:H;
55  optical[8]      lnk.file=c-Si-2015.in;                         # base- c-Si;
56  optical[9]      lnk.file=a-Si(i).in;                           # i   - aSi:H;
57  optical[10]     lnk.file=a-Si(p).in;                           # p   - aSi:H;
58  optical[11]     lnk.file=ITO.in;                               # TCO - ITO;
59  optical[b.1]    lnk.file=SiO2.in;                              # SiO2;
60  optical[b.2]    lnk.file=Ag.in;                                # Ag-Silver;
61
62  # DEFINITION OF ELECTRICAL PROPERTIES (IN ELECTRICAL LAYERS);
63
64  # bands[1]  e.mob=3.5   chi=4.65    nc=2.2e+24  nv=1.8e+25  epsilon=9.0;    # TCO - IZO;
65  bands[1]    e.mob=3.5   chi=4       nc=2.2e+24  nv=1.8e+25  epsilon=9.0;    # SnO2;
66  bands[2]    e.mob=2.0   chi=3.9     nc=8.0e+25  nv=8.0e+25  epsilon=4.2;    # C60;
67  bands[3]    e.mob=1.68  chi=3.9     nc=4.42E+23 nv=8.47E+24 epsilon=6.5;    # Perovskite
    absorber;
68  bands[4]    e.mob=3.1   chi=2.06    nc=1e+27    nv=1e+27    epsilon=3.5;    # SAM;
69  bands[5]    e.mob=3.65  chi=4.8     nc=5.8E+24  nv=1.0E+24  epsilon=8.9;    # ITO;
70  bands[6]    e.mob=1.7   chi=3.9     nc=2.0e+26  nv=2.0e+26  epsilon=11.9;   # nc  - SiOx;
71  bands[7]    e.mob=1.75  chi=3.8     nc=2.0e+26  nv=2.0e+26  epsilon=11.9;   # i   -
    aSi:H;
72  bands[8]    e.mob=1.124 chi=4.05    nc=2.86e+25 nv=3.1e+25  epsilon=11.8;   # base- c-Si;
73  bands[9]    e.mob=1.75  chi=3.8     nc=2.0e+26  nv=2.0e+26  epsilon=11.9;   # i   -
    aSi:H;
74  bands[10]   e.mob=1.75  chi=3.8     nc=2.0e+26  nv=2.0e+26  epsilon=11.9;   # p   -
    aSi:H;
75  bands[11]   e.mob=3.65  chi=4.8     nc=5.8E+24  nv=1.0E+24  epsilon=8.9;    # TCO - ITO;
76  # bands[13] e.mob=3.5   chi=4.65    nc=2.2e+24  nv=1.8e+25  epsilon=9.0;    # SiO2;
77
78  # DEFINITION OF IMPURITY CONCENTRATION AND DOPING TYPE (IN ELECTRICAL LAYERS);
79
80  # doping[1]       n.don=0.0;        # TCO - IZO;
81  doping[1]       n.don=2.0e25;   # SnO2;
82  doping[2]       n.don=2.6e24;   # C60;
83  doping[3]       n.don=2.0e16;   # Perovskite absorber;
84  doping[4]       n.acc=3.0e27;   # SAM - Changed doping from original 3e26;
85  doping[5]       n.don=3.0e27;   # ITO - Changed doping from original 1e26;
86  doping[6]       n.don=2.5e26;   # nc  - SiOx;
87  doping[7]       n.don=0.0;      # i   - aSi:H;
88  doping[8]       n.don=1.0e22;   # base- c-Si;
89  doping[9]       n.don=0.0;      # i   - aSi:H;
90  doping[10]      n.acc=2.0e26;   # p   - aSi:H;
91  doping[11]      n.acc=1.0e26;   # TCO - ITO;
92  # doping[13]      n.acc=1.0e26; # SiO2;
93
94  # DEFINITION OF ELECTRON AND HOLE MOBILITY (IN ELECTRICAL LAYERS);
95
96  # mobility[1]     mu.e=100e-4       mu.h=25e-4;         # TCO - IZO;
97  mobility[1]     mu.e=100e-4     mu.h=10e-4;         # SnO2;
98  mobility[2]     mu.e=0.08e-4    mu.h=0.0035e-4;     # C60;
99  mobility[3]     mu.e=1.62e-4    mu.h=1.62e-4;       # Perovskite absorber;
100 mobility[4]     mu.e=1e-7       mu.h=1e-7;          # SAM;
101 mobility[5]     mu.e=10e-4      mu.h=10e-4;         # ITO;
102 mobility[6]     mu.e=10e-4      mu.h=2.0e-4;        # nc  - SiOx;
103 mobility[7]     mu.e=20e-4      mu.h=5e-4;          # i   - aSi:H;
104 mobility[8]     mu.e=1300e-4    mu.h=400e-4;        # base- c-Si;
105 mobility[9]     mu.e=20e-4      mu.h=5e-4;          # i   - aSi:H;
106 mobility[10]    mu.e=10e-4      mu.h=1.0e-4;        # p   - aSi:H;
107 mobility[11]     mu.e=10e-4     mu.h=10e-4;         # ITO;
108 # mobility[13]    mu.e=100e-4       mu.h=25e-4;         # SiO2;
109
110
111 # Description of Density of states parameters - FOR AMORPHOUS SILICON ONLY;
112
113 vbtail[7]       e.range=0.9 levels=50 c.neut=0.7e-15 c.pos=0.7e-15; # i   - aSi:H;
114 vbtail[9-10]    e.range=0.9 levels=50 c.neut=0.7e-15 c.pos=0.7e-15; # i-p - aSi:H;
115 vbtail[7]       n.emob=2.0e27 e.char=0.045;                         # i   - aSi:H;
116 vbtail[9]       n.emob=2.0e27 e.char=0.045;                         # i   - aSi:H;
117 vbtail[10]      n.emob=1.0e28 e.char=0.085;                         # p   - aSi:H;
118
119 cbtail[7]       e.range=0.9 levels=50 c.neut=0.7e-15 c.neg=0.7e-15; # i   - aSi:H;
120 cbtail[9-10]    e.range=0.9 levels=50 c.neut=0.7e-15 c.neg=0.7e-15; # i-p - aSi:H;
121 cbtail[7]       n.emob=4.0e27 e.char=0.030;                         # i   - aSi:H;
122 cbtail[9]       n.emob=4.0e27 e.char=0.030;                         # i   - aSi:H;
123 cbtail[10]      n.emob=1.0e28 e.char=0.080;                         # p   - aSi:H;
124
125 dbond[7]        levels=40 e.corr=0.2 d.e=0.144 e.range=5.0;                          #
    i   - aSi:H;
126 dbond[9-10]     levels=40 e.corr=0.2 d.e=0.144 e.range=5.0;                          #
    i-p - aSi:H;
127 dbond[7]        ce.neut=3.0e-15 ch.neut=3.0e-15 ce.pos=100.0e-15 ch.neg=100.0e-15;  #
    i   - aSi:H;
128 dbond[9-10]     ce.neut=3.0e-15 ch.neut=3.0e-15 ce.pos=100.0e-15 ch.neg=100.0e-15;  #
    i-p - aSi:H;
129 dbond[7]        ep.def.pool=1.24 sigma.def.pool=0.18 ;                               #
    i   - aSi:H;
130 dbond[9]        ep.def.pool=1.24 sigma.def.pool=0.18 ;                               #
    i   - aSi:H;
131 dbond[10]       n=4.0e25  e.neut=-0.65;                                              #
    p   - aSi:H;
132
133 # DEFINITION OF CARRIER LIFETIME -> ONLY IF AUGER AND/OR SHOCKLEY-READ-HALL MODELS ARE
    CALLED!;
134
135 # recom[1]    tau.e=1e-7    tau.h=1e-7;     # TCO - IZO;
136 recom[1]    tau.e=1e-5      tau.h=1e-6;     # caug.i=9.9e-41 direct.c=2e-16; # SnO2;
137 recom[2]    tau.e=1e-9      tau.h=1e-9;     # C60;
138 recom[3]    tau.e=2.88e-7   tau.h=2.88e-7;  # esrh.t=-0.5 esrhd.e=-0.4 esrhd.h=-0.4
    nsrh.e=1e21 nsrh.h=1e21 caug.e=2.2e-43 caug.h=9.9e-43 caug.i=1.66e-42; # Perovskite;
139 recom[4]    tau.e=1e-9      tau.h=1e-9;     # esrh.t=-0.5 esrhd.e=-0.4 esrhd.h=-0.4
    nsrh.e=1e21 nsrh.h=1e21 caug.e=2.2e-43 caug.h=9.9e-43 caug.i=1.66e-42; # SAM;
140 recom[5]    tau.e=1e-6      tau.h=1e-6;     # esrh.t=-0.5 esrhd.e=-0.4 esrhd.h=-0.4
    nsrh.e=1e21 nsrh.h=1e21 caug.e=2.2e-43 caug.h=9.9e-43 caug.i=1.66e-42; # ITO;
141 recom[6]    tau.e=1e-6      tau.h=1e-6;     # nc  - SiOx;
142 # recom[7]      tau.e=1e-6      tau.h=1e-6; # i   - aSi:H;
143 recom[8]    tau.e=10e-3     tau.h=10e-3;    # caug.i=9.9e-41 direct.c=2e-16;
144 # recom[9]      tau.e=1e-6      tau.h=1e-6; # i   - aSi:H;
145 recom[10]   tau.e=1e-6      tau.h=1e-6;     # p   - aSi:H;
146 recom[11]   tau.e=1e-6      tau.h=1e-6;     # ITO;
147 # recom[13] tau.e=1e-6      tau.h=1e-6;     # SiO2;
148
149 # DEFINITION OF MODEL SETTINGS;
150
151 # model[1]     srh lifetime;
152 model[1]    srh lifetime; # auger direct;
153 model[2]    srh lifetime;
154 model[3]    srh lifetime; # auger;
155 model[4]    srh lifetime; # auger;
156 model[5]    srh lifetime; # auger;
157 model[6]    srh lifetime;
158 model[7]    amorphous srh lifetime; # auger direct;
159 model[8]    srh lifetime;
160 model[9]    amorphous srh lifetime; # auger;
161 model[10]   amorphous srh lifetime; # auger;
162 model[11]   srh lifetime; # auger;
163 # model[13]    srh lifetime; # auger;
164 model[4-5]   fdme=on;
165 model[all]   tat=on;
166
167 # frontcon  schottky e.bar=0.899;
168 # backcon   schottky e.bar=0.370;
169 frontcon    ohmic;
170 backcon     ohmic;
171 # frontopt  reflect=0.1;
172 # surfrec[i.2] surfrec.e=3500 surfrec.h=100;
173 # backopt       reflect=0.8;
174
175 # SETTINGS;
176
177 settings    temp=300 eps.pois=1e-6 eps.cone=1e-6 eps.conh=1e-6 update.rec ;
178 settings    max.iter=99 max.iter.eq=99 damp=2 dv.max=10 max.step.reduc=6 tunn.mass=0.25
    e0.fdme=1e6;
179 settings    t.freeze.in=460 gru.factor=3 gru.steps=10 cap.dv=0.002 Rs=10e-4 Rp=4
    D0=10e-9 gummel; # field.lim=1e5;
180 # gummel.starts=2;
181
182 # CALCULATING GENERATION PROFILE;
183
184 opticgen    gen.file=matrix_profile_AlAshouri_298_System_Textured_raiyan.dat;
185 # print     opticgen file=gen_NEW.dat headers=false;
186 # print     absorptance file=abs_pvk_cSi_tandem_Ashouri_298.dat;    # prints
    reflectance, absorptance (in each layer) and transmittance;
187 # print     absorption file=abt.dat;
188
189 # CALCULATING DARK PARAMETERS;
190
191 solve       equil;
192 print       bands     file=bands_pvk_cSi_tandem_dark_Ashouri_298.dat headers=on;    #
    prints band diagram;
193 print       potential file=ASA_potential_pvk_cSi_tandem_Ashouri_298.dat headers=on; #
    prints electrostatic potential;
194 print       efield    file=ASA_efield_pvk_cSi_tandem_Ashouri_298.dat headers=on;    #
    prints electric field magnitude;
195 # solve     v.start=-1.95 v.end=0 n.step=100;                          # calculates j-v
    response in dark, between -1.5 V and 1.5 V with steps of 0.01 V;
196 # print     jv        file=jv_pvk_cSi_tandem_dark_Ashouri_298.dat headers=on;       #
    prints dark j-v response;
197
198 # CALCULATING SPECTRAL RESPONSE;
199
200 # settings    sr.flux=1.0e20;
201 # solve       equil;                                                  # solves at
    equilibrium;
202 # solve       sr wl.start=400e-9 wl.step=5e-9 wl.end=1100e-9 illum; # calculates quantum
    efficiency (between 300 nm and 1200 nm, every 5 nm);
203 # print       sr file=qe_pvk_cSi_tandem_Ashouri_298.dat gnu;          # prints quantum
    efficiency;
204
205 # CALCULATING OTHER PARAMETERS;
206
207 # solve     jv        v.start=-1.95 v.end=0 n.step=100 illum;                        #
    calculates j-v response under illumination, between 0 V and 0.6 V with steps of 0.012 V;
208 # print     bands     file=bands_pvk_cSi_tandem_illum_Ashouri_298.dat headers=on;   #
    prints band diagram;
209 # print     sol.par   file=ASA_PAR_pvk_cSi_tandem_Ashouri_298.dat headers=on;       #
    prints solar cell parameters (Voc, Isc, Vmpp, Impp, FF, Pmax);
210 # print     jv        file=jv_pvk_cSi_tandem_Ashouri_298.dat headers=on;            #
    prints j-v response;
211 # print     curr.e    file=ASA_curr_e_pvk_cSi_tandem_Ashouri_298.dat headers=on;    #
    prints electron current density;
212 # print     curr.h    file=ASA_curr_h_pvk_cSi_tandem_Ashouri_298.dat headers=on;    #
    prints hole current density;
213 # print     curr      file=ASA_curr_T_pvk_cSi_tandem_Ashouri_298.dat headers=on;    #
    prints total current density;
214 # print     elec      file=ASA_conc_e_pvk_cSi_tandem_Ashouri_298.dat headers=on;    #
    prints electron concentration;
215 # print     hole      file=ASA_conc_h_pvk_cSi_tandem_Ashouri_298.dat headers=on;    #
    prints hole concentration;
216 # print     efield    file=ASA_efield_pvk_cSi_tandem_Ashouri_298.dat headers=on;    #
    prints electric field magnitude;
217 # print     rec       file=ASA_rec_pvk_cSi_tandem_Ashouri_298.dat;                  #
    prints recombination rate;
218 # print     doping    file=ASA_doping_pvk_cSi_tandem_Ashouri_298.dat;               #
    prints doping concentration;
219 # print     potential file=ASA_potential_pvk_cSi_tandem_Ashouri_298.dat headers=on; #
    prints electrostatic potential;
220 # print     rho       file=ASA_rho_pvk_cSi_tandem_Ashouri_298.dat;                  #
    prints space charge density;
221
```